



FERMILAB-Conf-01/390-T

# **Proceedings of a Workshop on Beam-beam Effects in Circular Colliders**

Fermilab, June 25-27, 2001

P.O. Box 500, Batavia, Illinois 60510

Editors  
T.Sen and M.Xiao

# Table of Contents

<b>Preface</b>	3
<b>List of Participants</b>	4
 <b>Observations of beam-beam phenomena in colliders</b>	
W. Herr, <i>Beam-beam issues in the LHC and relevant experience from LEP and the SPS collider</i>	6
M. Tawada, <i>Beam-beam performance and experience at KEKB</i>	17
M. Boscolo, <i>Beam-beam experience at DAΦNE</i>	22
J. Rogers, <i>Beam-beam observations at CESR and CESRc</i>	27
I. Nesterenko and Y. Shatunov, <i>Experimental studies of coherent beam-beam effects, flip-flop and dynamic beta at VEPP-2M</i>	36
W. Fischer, <i>RHIC as a test bench for beam-beam studies</i>	43
A. Temnykh, <i>Summary of the observation session</i>	48
 <b>Beam-beam compensation</b>	
V. Shiltsev, <i>Tevatron electron lens for beam-beam compensation: First experimental results</i>	52
Y. Alexahin, D. Shatilov, and V. Shiltsev, <i>Analytical study and tracking simulations of the beam-beam compensation at the Tevatron</i>	58
J.P. Koutchouk, <i>Correction of the long-range beam-beam effect in LHC using electromagnetic lenses</i>	63
F. Zimmermann, <i>Weak-strong simulation studies for the LHC long-range beam-beam compensation</i>	66
W. Herr, <i>Summary of the session on beam-beam compensation schemes</i>	71
 <b>Weak-strong phenomena</b>	
F. Schmidt, <i>Beam-beam simulations for the LHC at injection and collision energies</i>	74
T. Sen, M. Xiao, and N. Gelfand, <i>Beam-Beam study for Tevatron Run IIa</i>	79

Y. Alexahin, T. Sen, and M. Xiao, <i>Beam-Beam excited synchro-betatron resonances in the Tevatron Run II lattice</i>	86
A. Burov, <i>Beam rounders for circular colliders</i>	92
M. Syphers, <i>Excerpts from the VLHC design study - accelerator physics issues</i>	96
J.P. Koutchouk, <i>Summary of the session on weak-strong phenomena</i>	103

## **Strong-strong phenomena**

W. Herr, <i>Self-consistent closed orbit caused by beam-beam effects in the LHC</i>	107
F. Zimmermann, <i>Beam sizes in collision at KEKB</i>	111
Y. Alexahin, <i>Spectra of coherent transverse oscillations in colliding bunches of finite length</i>	117
J. Rogers, M. Vogt, <i>Summary of coherent phenomena</i>	121

## **Theory and simulations of strong-strong interactions**

R. Warnock and J. Ellison, <i>Integral equation for the equilibrium state of colliding electron beams</i>	125
J. Ellison and M. Vogt, <i>An averaged Vlasov equation for the strong-strong beam-beam</i>	130
J. Rogers, <i>ODYSEUS, an adaptive 3D strong-strong beam-beam simulation code</i>	136
W. Herr, <i>Beam-beam simulations using a fast multipole method</i>	139
M. Vogt, J. Ellison, T. Sen and R. Warnock, <i>Two methods for simulating the strong-strong beam-beam in hadron colliders</i>	149
L. Jin and J. Shi, <i>Effect of electron beam compensation of beam-beam tune spread on beam size growth in the Tevatron</i>	157
J. Ellison, M. Vogt, <i>Summary of coherent theory and simulations session</i>	162

# Preface

A workshop on beam-beam interactions in circular colliders was held at Fermilab from June 25-27, 2001. Twenty five participants from eleven different institutions representing hadron and electron-positron accelerators, and universities attended. This workshop was a direct successor to a similar workshop held at CERN in April 1999. It was motivated by the emergence of new regimes of interest in present and future colliders and the need to review the progress made since 1999. In the Tevatron and the LHC, long-range interactions and schemes to compensate them have emerged as the key theme. In  $e^+ - e^-$  colliders, the beam-beam limit and lattice modifications to increase this limit are active areas of interest. Coherent phenomena are very important in  $e^+ - e^-$  colliders and they are expected to be significant in future hadron colliders. All of these topics were addressed by the speakers. After plenary talks on the opening day, talks and discussions were organized into five working groups:

- Observations at existing colliders, chaired by A. Temnykh
- Beam-beam compensation schemes, chaired by W. Herr
- Coherent phenomena, co-chaired by J. Rogers and M. Vogt
- Weak-strong phenomena, chaired by J.P. Koutchouk
- Theory and simulations of strong-strong interactions, chaired by J. Ellison

The workshop closed with summary talks from the session chairs. The talks and written reports may be found at the website:

<http://www-ap.fnal.gov/~meiqin/beambeam01/beambeam01.html>

We thank all the participants for making this workshop a success. We also thank S. Holmes, J. Cooper and M. Shaevitz from the Fermilab directorate for providing the financial support that made the workshop possible. Finally, it is a pleasure to thank the workshop secretaries: V. Stazak, R. Becker, C. Kowalik and J. Sullivan for their able administrative help and for ensuring that the workshop ran smoothly.

Tanaji Sen and Meiqin Xiao  
Editors



# Participants

Name	Institution	Email address
Y. Alexahin	FNAL	alexahin@fnal.gov
M. Boscolo	INFN	manuela.boscolo@lnf.infn.it
A. Burov	FNAL	burov@fnal.gov
J. Ellison	Univ. of New Mexico	ellison@math.unm.edu
W. Fischer	BNL	wolfram.fischer@bnl.gov
N. Gelfand	FNAL	gelfand@fnal.gov
W. Herr	CERN	zwe@mail6.cern.ch
L. Jin	Univ. of Kansas	jinlh@ukans.edu
J.P. Koutchouk	CERN	jean-pierre.koutchouk@cern.ch
I. Nesterenko	BINP	nesterenko@inp.nsk.su
J. Rogers	CESR	jtr1@cornell.edu
F. Schmidt	CERN	frank.schmidt@cern.ch
T. Sen	FNAL	tsen@fnal.gov
D. Shatilov	BINP	d.n.shatilov@inp.nsk.su
Y.M. Shatunov	BINP	shatunov@inp.nsk.su
J. Shi	Univ. of Kansas	shi@kubeam.phsx.ukans.edu
V. Shiltsev	FNAL	shiltsev@fnal.gov
M. Syphers	FNAL	syphers@fnal.gov
M. Tawada	KEK	masafumi.tawada@kek.jp
S. Temnykh	CESR	abt6@cornell.edu
S. Tzenov	Princeton Plasma Physics Lab	stzenov@pppl.gov
M. Vogt	Univ. of New Mexico	vogtm@math.unm.edu
R. Warnock	SLAC	warnock@slac.stanford.edu
M. Xiao	FNAL	meiqin@fnal.gov
F. Zimmermann	CERN	frank.zimmermann@cern.ch

## Organizing Committee

T. Sen (Chair)    Y. Alexahin    V. Shiltsev    M. Syphers    M. Xiao

## Workshop Secretaries

V. Stazak    R. Becker    C. Kowalik    J. Sullivan

## **SECTION I: Observations of beam-beam phenomena in colliders**

# Beam-beam issues in the LHC and relevant experience from the SPS proton antiproton collider and LEP

W. Herr CERN, SL Division

## Abstract

The beam-beam effects observed in SPS and LEP in various operational modes are reviewed. Special emphasis is put on effects relevant for the LHC. This includes orbit effects, crossing angle and PACMAN effects.

## 1 INTRODUCTION

In the LHC we have to expect numerous effects due to the beam-beam interactions. It is worthwhile to consider the experience gained running the SPS collider and LEP and use it in LHC studies where relevant knowledge is available [1, 2, 3]. The SPS was run approximately 10 years as a proton antiproton collider and the first hadron collider where long range beam-beam effect became important. LEP as an electron positron collider is very different from the LHC. The strong damping at its highest energy of 94.5 GeV allows beam-beam strength parameters up to 0.075, i.e. approximately 20 times larger than the expected values for the LHC of around 0.0034.

In SPS and LEP the two colliding beams had unlike signs, i.e. they travel in the same vacuum chamber on (a priori) identical orbits. However, both machines were run in various modes of operation and some of the observed features can be found again in the LHC, such as:

- Parasitic crossings for all modes of operation
- Orbit effects due to beam-beam kicks
- Effects from bunch trains
- PACMAN effects due to different types of beam-beam interactions
- Strong-strong beam-beam effects
- Coherent beam-beam effects
- Crossing angles

One can therefore hope that the concepts developed and tested for SPS and LEP can be applied to the LHC.

## 2 LHC LAYOUT

The conceptual layout of the LHC is shown in Fig.1. The two beams travel in two separate rings and cross over in the four experimental areas in interaction regions 1, 2, 5 and 8. To avoid unwanted interactions, crossing angles are used in these areas. To compensate first order long range effects, the crossing takes place in the horizontal plane in

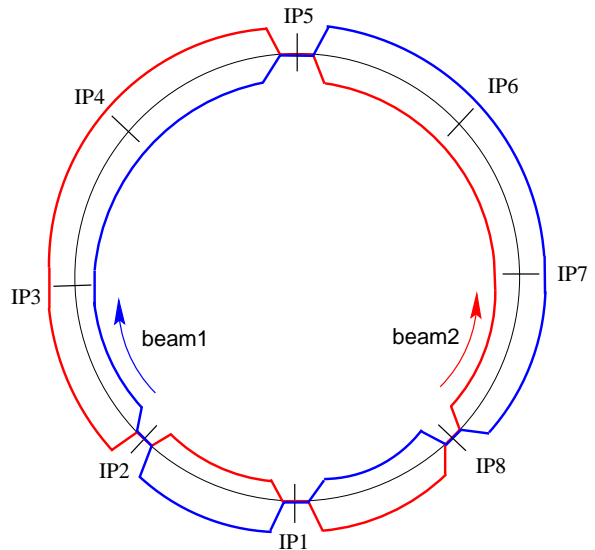


Figure 1: Layout of LHC beams and collision points.

interaction regions 5 and 8 and the crossings in 1 and 5 are in the vertical plane.

## 3 SPS, LEP AND LHC PARAMETERS

A comparison of the most important SPS, LEP and LHC parameters is made in Tab.1. A few significant differences can be seen from Tab.1. The number of bunches per beam in the LHC is orders of magnitude larger than in SPS or LEP and consequently also the number of parasitic encounters. The damping time in both hadron machines, SPS and LHC, can be neglected compared to the very fast damping time in LEP of less than 4 ms at its highest energy. Another feature of the LHC is a finite crossing angle that is required to separate the beams. In SPS and LEP the crossing angles were unintentional and very small, except in dedicated experiments. The number of experiments is comparable and the 2+(1) for the SPS indicates 2 experimental areas plus one unavoidable head on collision. The SPS collider was also operated with 3 bunches per beam without separation, i.e. 6 head on collisions, but this mode of operation will not be considered here since it is not relevant for LHC studies.

Table 1: Comparison of SPS, LEP and LHC parameters at high energy in collision

	SPS	LEP	LHC
Bunches per beam	6	4 - 16	2808
Experiments	2+(1)	4	4
Parasitic interactions	9	4 - 28	120
$\Delta Q (\xi)/IP$	0.0050	0.0450 (0.0700)	0.0033
Damping time	-	0.004 s	$10^{-5}$ s
Full crossing angle $\alpha$	small	small	$300 \mu\text{rad}$

## 4 SPS AND LEP MODES OF OPERATION

### 4.1 SPS operation with pretzel scheme

When the SPS collider was operated with 6 bunches per beam, a horizontal pretzel scheme was used to separate the beams at the unwanted collision points (Fig.2). This pretzel

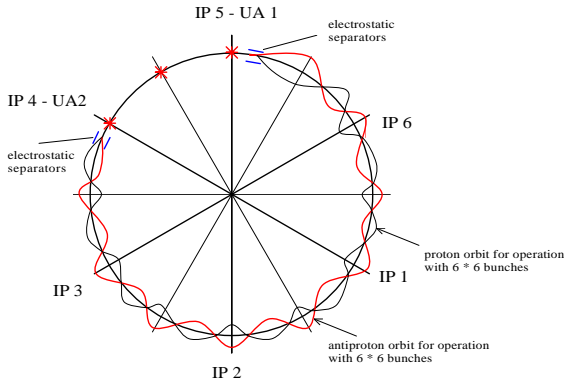


Figure 2: SPS operation with horizontal pretzel scheme and 6 bunches per beam.

zel extended over 5 of the 6 sectors and allowed head on collisions in the two main experiments UA1 and UA2 and an unwanted head on collision in between. During colliding beam conditions the beams were separated by about  $6\sigma$  at the unwanted collision points. For injection a single separator created a orbit distortion around the whole ring providing separation between 1.5 to  $6\sigma$  at the 12 crossing points.

### 4.2 LEP operation with bunch trains

During the last 6 years of its operation, LEP operated with bunch trains and although it also successfully used a horizontal pretzel scheme with 8 bunches per beam, I shall concentrate on its operation with bunch trains since this scenario gives more information relevant for the LHC.

To allow more than eight bunches per beam, a bunch train scheme was developed and installed in LEP [17, 18]. The basic idea is to start from the original four bunch scheme and to replace a single bunch by a short train of bunches. This requires a local separation at the unwanted collisions around the nominal collision point. A horizontal crossing angle was abandoned for background considerations and a local vertical separation was installed, using already existing separators in the interaction area. The principle of this

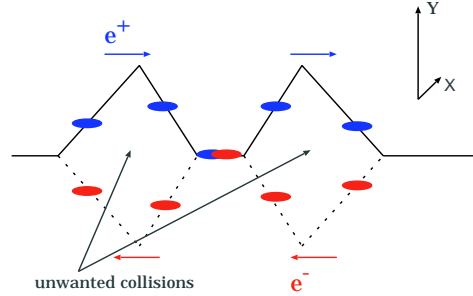


Figure 3: Principle of bunch train separation in LEP.

mode of operation is shown in Fig.3.

## 5 HEAD-ON BEAM-BEAM EFFECTS

The most basic beam-beam effects are due to the (wanted) head on collisions. Some of the results from the SPS collider are worth mentioning here. The working diagram of the SPS together with the tune footprints is shown in Fig.4. At injection energy the tune spread of the protons is dominated by the space charge tune spread of about  $\Delta Q_h \approx -0.03$  and  $\Delta Q_v \approx -0.05$  which is much larger than their beam-beam tune spread. The tune spread of the antiprotons is mainly due to the beam-beam effects from the protons and has opposite sign (Fig.4). In collision the total spread was about 0.015 to 0.018 and the life time was limited by high order beam-beam resonances since the footprint in collision is crossing the 13th and 16th order resonances. This is true in particular when the beam sizes of the two beams were not equal.

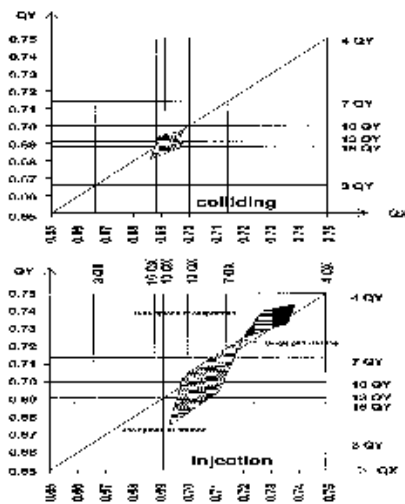


Figure 4: SPS working diagram at injection and in collision.

### 5.1 Unequal beam sizes

Without damping, the emittances of protons and antiprotons are determined by the injectors. On a single occasion, the emittances of the three antiproton bunches (X, Y, Z) were significantly different. It was noticed that the bunch with the largest emittance had a lower lifetime, suggesting a loss of particles from the tails of the distribution (Fig. 5). After these large amplitude particles were lost, the lifetimes

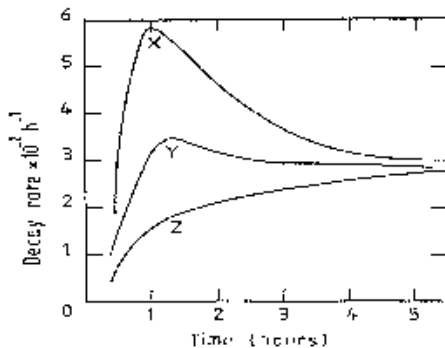


Figure 5: Decay rate for antiprotons with unequal beam size.

of the bunches became similar. The antiproton emittances were typically a factor two smaller ( $\epsilon^* \approx 3$  mm mrad) than the emittances of the protons ( $\epsilon^* \approx 6$  mm mrad). The large amplitude particles of the proton bunches now oscillate in the very non-linear part of the antiproton beam-beam force and are more sensitive to high order resonances. In

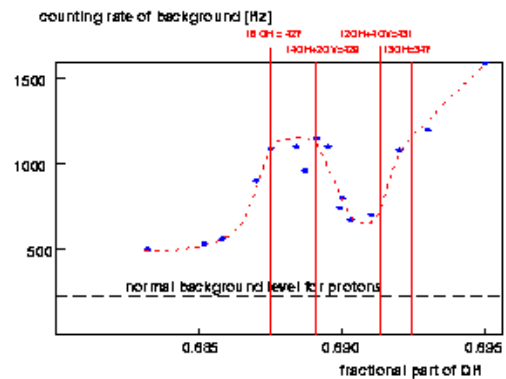


Figure 6: Resonance scan across 13th and 16th order resonances in the SPS.

the Fig.6 the result of a resonance scan is shown and the proton losses correlate with the 13th and 16th order resonance. This demonstrates the importance of resonances of very high order under such conditions. In another, dedi-

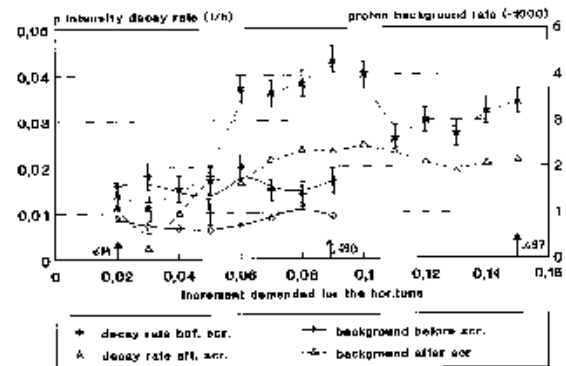


Figure 7: Tune scan with protons before and after scraping of antiprotons.

cated experiment the decay rate of a single proton bunch was measured and shown in Fig.7 as a function of the proton tune for two different sizes of the antiproton bunch (before and after scraping to smaller emittance). While for approximately equal beam sizes no significant effect is visible, the decay rate increases strongly in the neighbourhood of the 16th order resonance when the size of the antiproton bunch was decreased. The protons at large amplitudes experience now the very non-linear beam-beam force of the antiprotons and high order resonances are excited.

In the LHC we have to expect bunch to bunch emittance variations and for the reasons explained above they must be kept as small as possible. We presently allow a 10%

variation in our calculations.

### 5.2 Dynamic $\beta$ effects

The beam-beam force changes the  $\beta$ -function at the collision point and as a result the optics is modified. The real tune shift  $\Delta Q$  depends on this 'dynamic  $\beta$ ' effect which depends on the optical parameters. Only in the limit of small values of the beam-beam parameter  $\xi$  and for tunes well above the integer the tune shift can be approximated by  $\xi$ . During the last few years of LEP operation this dynamic  $\beta$  effect became important. The unperturbed beam-beam parameter was in the order of 0.07 to 0.08 per interaction point and the phase advance between two interaction points was just above the integer (fractional tune 0.19 and 4 interaction points). The actual tune shift was therefore in the order of 0.04 [4]. The beating introduced around the machine was rather substantial leading to a reduction of  $\beta^*$  from 5 to  $\approx 2.5$  cm. Together with small phase advance errors (a few degrees are sufficient) between the interaction regions, a substantial difference of  $\beta^*$  between the interaction points has to be expected, and was manifested in a regularly observed luminosity imbalance between the four experiments. With the nominal parameters a noticeable dynamic  $\beta$  effect is not expected in the LHC.

### 5.3 Synchrobetatron resonances

The finite crossing angle or a non-zero dispersion at the collision point can couple the longitudinal and transverse motion via the beam-beam interaction. This leads to the excitation of synchro-betatron resonances. The strength of the coupling due to a crossing angle can be expressed through the normalized crossing angle (or Piwinski angle) which is  $\frac{\alpha \cdot \sigma_s}{2\sigma_z} \approx 0.7$  for the nominal crossing angle of  $300 \mu\text{rad}$  for the LHC. Resonances of the type  $nQ_x + mQ_y \rightarrow nQ_x + mQ_y + rQ_s$  are excited and should show as additional lines in the tune spectrum. The ef-

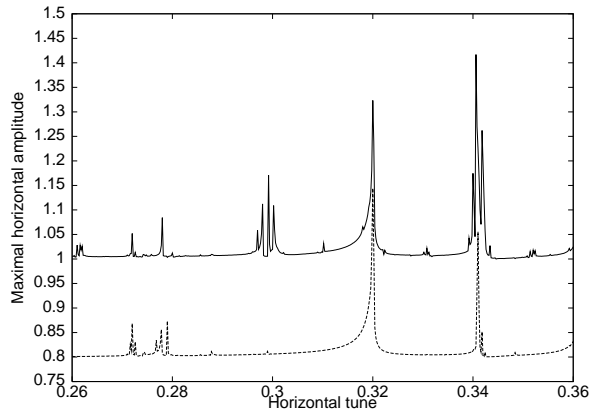


Figure 8: Simulation of synchrobetatron resonances due to finite crossing angle.

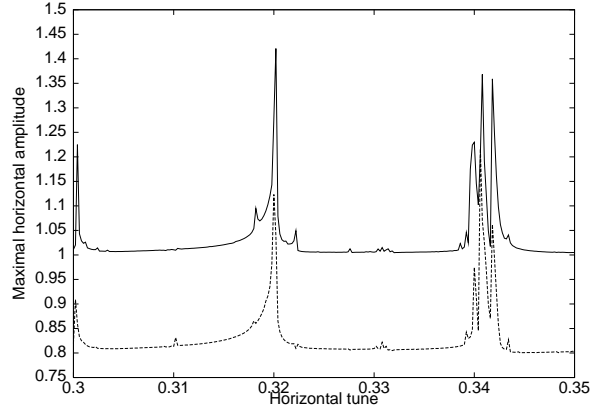


Figure 9: Simulation of synchrobetatron resonances due to finite dispersion at interaction point.

fect of the crossing angle was simulated [5] and a tune scan with and without a crossing angle is shown in Fig.8. This simulation shows the appearance of synchrotron sidebands next to the main resonance lines but also a new resonance can be observed. For a strictly head-on beam-beam collision of round beams only even order resonances can be excited due to the symmetry of the system. This symmetry is broken either by long range interactions or by a crossing angle as demonstrated in Fig.8. The Fig.9 shows a similar scan but now for a non-zero dispersion at the collision point ( $D_x = 0.10$  m). It can be derived [5] that a residual dispersion of 0.10 m is equivalent to a crossing angle of  $300 \mu\text{rad}$ , i.e. excites synchro-betatron resonances with the same strength. Although these resonances have to be expected in the LHC, the synchrotron tune ( $Q_s = 0.00212$ ) is very small compared to lepton accelerators (e.g. LEP  $Q_s = 0.10$ ) and therefore the sidebands are very close to the main resonance line. The required space in the tune diagram is therefore hardly increased.

## 6 LONG RANGE BEAM-BEAM EFFECTS

Around the experimental regions the LHC beams travel in a common vacuum chamber and therefore experience the fields of the opposing beams, so-called long range interactions. The number of these parasitic encounters depends on the lengths of the common regions before the beams are sufficiently separated by dipole magnets and the bunch spacing. For the LHC we calculate 15 long range interactions on either side of the four collision points, i.e. we have approximately 120 distant interactions.

The effect of these interaction depends mainly on the separation, normalized to the transverse beam size. It can be shown that in the drift space between the collision point and the first focussing element this normalized separation

is constant:

$$d_{sep} \approx \frac{\alpha\beta^*}{\sigma^*} = \frac{\alpha\sqrt{\beta^*}\sqrt{\gamma}}{\sqrt{\epsilon^*}} = const. \quad (1)$$

The long range interactions are therefore most important in the high luminosity, i.e. low  $\beta^*$  interaction regions. Although increasing the crossing angle  $\alpha$  can improve the separation easily, other considerations have to be taken into account which limit this angle. Too large angles reduce the luminosity, require more aperture, strongly excite synchrotron resonances and bring the beams into the more non-linear part of the quadrupole fields of the insertion magnets. The present crossing angle of  $300 \mu\text{rad}$  is a compromise between the different requirements.

### 6.1 Beam separation

To provide the required crossing angles, dedicated dipole magnets are used which act either on both or individual beams [6, 7]. An example of such a crossing angle bump is given for one beam in Fig.10. The orbit of the counter-rotating beam is antisymmetric around the central collision point. During injection, the beams are also separated in

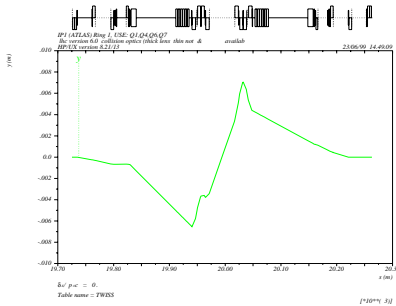


Figure 10: Vertical bump for crossing angle.

the second plane by a parallel bump of a few mm, ensuring that the normalized separation is never smaller than approximately  $14 \sigma$ . Such a parallel bump is shown in Fig.11.

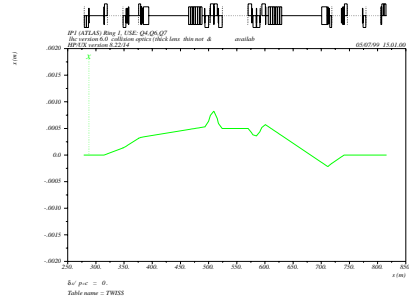


Figure 11: Horizontal bump for parallel bump at injection.

so-called PACMAN effects. The nominal bunch filling pattern of the LHC is shown in Fig.12. The pattern exhibits a

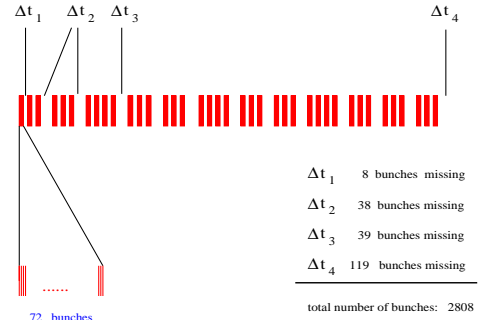


Figure 12: Bunch filling scheme for the LHC.

fourfold symmetry and has 39 batches of 72 bunches each, i.e. in total 2808 bunches of a maximum possible of 3564 are filled. The gaps between the batches are required for the injection and extraction kickers of the LHC injectors and a large gap at the end is needed to allow for the rise-time of the kicker of the beam dumping system. Ideally

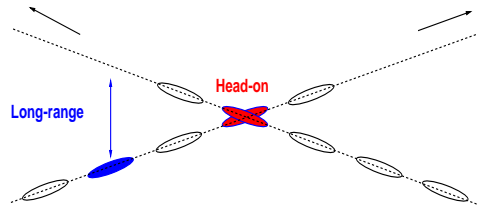


Figure 13: Origin of PACMAN effects.

the holes in the bunch train of one beam should meet holes of the other beam. This is true for the head-on collisions in interaction points 1 and 5. However the bunches at the beginning and end of a batch miss long range interaction either before or after the head-on collision (see Fig.13). This

### 6.2 Dynamic aperture

The beam-beam effects decrease the available dynamic aperture of the LHC beams at injection and in collision, either alone or in combination with the non-linearities of the LHC lattice. Since this subject is treated in a different presentation [13] as well as simulations of the improvement of the dynamic aperture [14] using a long range compensation scheme [15], I do not give details on that subject in this report.

### 6.3 PACMAN effects

An effect which is expected to play a very important role is caused by the bunch filling pattern of the LHC, leading to

left-right asymmetry cannot be avoided. In the worst case, i.e. for the first or last bunch of a batch, only half of the long range interactions are encountered [16]. Furthermore, in collision points 2 and 8 the large dump gap will meet a full batch and reduce the number of long range collisions of some bunches further. The maximum and minimum numbers of parasitic encounters become 120 and 40, respectively. Due to this gap some bunches will miss also head-on collisions. The interaction point 8 is moved longitudinally by 3 half bunch spacings, adding further missing head-on collisions to the interaction schedule and leaving bunches with only 2 out of 4 nominal head-on collisions. It is clear that all these bunches experience a very different accumulated beam-beam effect which may lead to different dynamics and, in the worst case, different life times. For beam measurements it is also important to have a reproducible reference and ideally one should use the nominal bunches.

To evaluate the strength of beam-beam interactions, a standard tool is to compute the tune footprint, i.e. the two dimensional tune shift as a function of the amplitude. Such footprints are shown in Fig.14 where I show the foot-

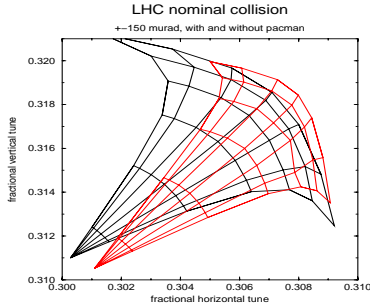


Figure 14: Footprints for head-on and long range interactions for nominal (black) and PACMAN bunches (red).

print for nominal bunches (i.e. bunches with all head-on and long range interactions) and the extreme PACMAN bunches (i.e. minimum number of long range interactions). The footprints are computed for the nominal parameters and bunch intensities. Although not visible, the effect of alternating horizontal and vertical crossing is all important since they compensate for the first order tune shift [1]. With all crossings in one plane the footprint of PACMAN bunches would be shifted rather far from the nominal and thus produce a very large operational tune spread. The bunches with one or more missing head-on collisions do not show in Fig.14 since for those the overall head-on part of the footprint just scales down and is therefore inside the nominal area.

## 6.4 PACMAN effects with bunch trains in LEP

It can be shown that operating LEP with bunch trains exhibits all properties of PACMAN effects. The separated

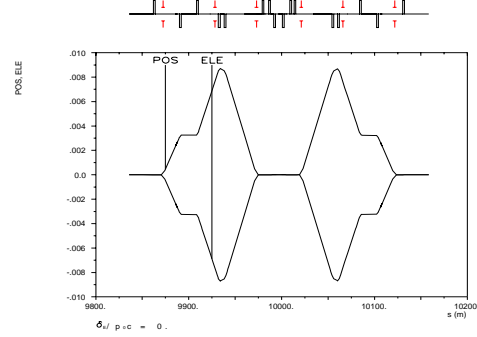


Figure 15: Vertical separated orbits for bunch train operation around IP 4 for 45.6 GeV and central collision

orbits of electrons and positrons around an experimental region is shown in Fig.15. While the central collision is head-on, the parasitic encounters have to be accommodated inside the separation bumps (Fig.15). This determines the parameters such as bunch spacing and number of bunches per train. The design allows a maximum of four bunches per train, spaced by 87 RF wavelengths, i.e. three parasitic collisions have to fit into the separation bumps on each side.

The left half of such a bump in an experimental region is shown again in Fig.16 together with the position of the parasitic encounters and the separation, normalized to the local horizontal beam size  $\sigma_x$ . The central collision point is at the right hand side of the figure and the horizontal axis gives the distance from the collision point. The figure

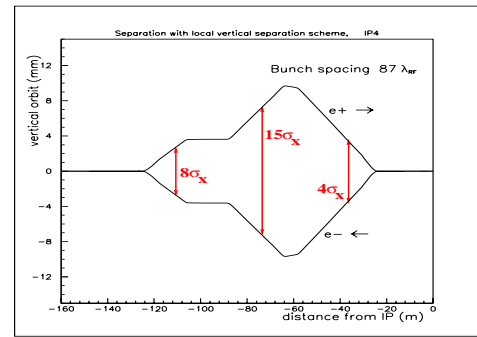


Figure 16: Vertical separated orbits and normalized separation for bunch train operation around IP 4

shows the situation when the bunches collide in the centre and for 45.6 GeV. For injection, the central collision has to be separated as well, imposing some constraints on the choice of the separation scheme. It further has to allow the fine adjustment of the head-on collision. Contrary to the



Table 2: *Separation and parasitic beam-beam strength  $\xi$  for parasitic collisions around IP 4 (for:  $\epsilon_x = 30$  nm,  $I_b = 500$   $\mu$ A)*

	3	2	1
$d/\sigma_x$	$\approx 8$	$\approx 15$	$\approx 4$
$\xi_x (10^{-3})$	$\approx 0.8$	$\approx 0.2$	$\approx 3.6$
$\xi_y (10^{-3})$	$\approx -4.8$	$\approx -0.7$	$\approx -0.3$

four bunch case, the separation bumps cannot be switched off during physics fills. The separation and the parasitic beam-beam tune shift is summarised for the three parasitic collisions in Tab.2. A horizontal emittance of 30 nm and a bunch current of 500  $\mu$ A was used for the calculation. It is shown that in particular the outmost collision point gives the largest vertical tune shift while the other encounters give significantly smaller values. The Fig.17 and Tab.3

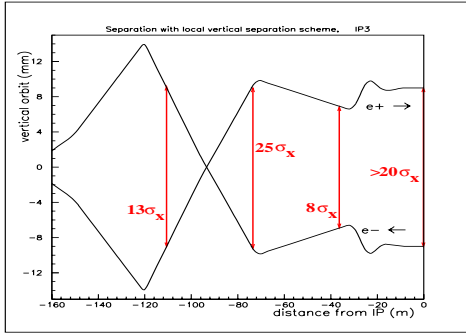


Figure 17: *Vertical separated orbits and normalized separation for bunch train operation around IP 3*

Table 3: *Separation and parasitic beam-beam strength  $\xi$  for parasitic collisions around IP 3 (for:  $\epsilon_x = 30$  nm,  $I_b = 500$   $\mu$ A)*

	3	2	1	0
$d/\sigma_x$	$\approx 13$	$\approx 25$	$\approx 8$	$\geq 20$
$\xi_x (10^{-3})$	$\approx 0.3$	$\leq 0.1$	$\approx 0.7$	$\approx 0.1$
$\xi_y (10^{-3})$	$\approx -0.2$	$\approx -0.5$	$\approx -0.2$	$\approx -0.1$

show the bump and tune shifts for a typical unused (i.e. odd) interaction region. The interaction at the central collision point is now also avoided. The separations are generally larger and the tune shifts smaller than for the experimental (even) regions. We therefore expect more problems from the parasitic encounters in the even than in the odd points.

**Interaction schedule** For four equal bunches and a high degree of symmetry of the optical layout of LEP, all bunches experience practically the same beam-beam effects. For not equally spaced bunches or finite bunch trains the interaction schedule can become rather complex. The extreme case of LHC with closely spaced bunches and gaps of different sizes leads to so-called PACMAN bunches [16] with a very complicated interaction schedule. The scheme with bunch trains in LEP shows a similar behaviour, although with fewer bunches. While the first bunch of a train has a head-on collision followed by the three parasitic encounters shown in Fig.16, the second bunch will first experience a parasitic encounter on the incoming side, followed by the head-on collision and two parasitic encounters on the outgoing side of the interaction point. Similar considerations can easily be made for all bunches of a train. As a consequence of this schedule every bunch of a train has a different sequence of beam-beam interactions and therefore experiences different effects. Some bunches may have very unfavourable encounters, e.g. those with small separation, and are likely to be most sensitive to unstable behaviour. One can therefore identify at least four different classes of bunches according to their beam-beam interactions, showing a "PACMAN-like" effect *within the beams*. In addition to the differences within a train, a residual non-closure of the separation bumps due to imperfections or energy mismatch causes a global offset that needs correction at each interaction point and can cause additional parameter splits *between the beams*.

**Offsets and orbit separation** The beam-beam kicks of the parasitic interactions distort the orbits of the individual bunches and since the collision pattern is different for different bunches, the orbits of all bunches are slightly different. As a consequence, the orbits at the interaction points are different and the bunches collide with a small offset. In the design of the bunch train separation scheme care was taken to make use of possible compensation effects to reduce these unwanted offsets [17, 18]. However, small offset of the order of  $\mu$ m are unavoidable. Furthermore, the orbit at the parasitic encounters itself is changed by the beam-beam kicks and a self-consistent calculation is required to give the correct answer. A program TRAIN was developed [19] to compute the individual orbits of all bunches in a train and the relevant parameters, such as tune, chromaticity, dispersion, offsets and crossing angles. The

Table 4: *Orbit offsets and separation (at central collision point) for 300  $\mu$ A per bunch at 45.6 GeV*

	a	b	c	d
$e^+ [\mu\text{m}]$	+5.75	+1.10	-1.65	-0.30
$e^- [\mu\text{m}]$	+0.30	+1.65	-1.10	-5.75
$d [\mu\text{m}]$	+5.45	-0.55	-0.55	+5.75

orbit offsets and resulting separation of a train with four bunches is shown in Tab.4 for an experimental interaction point. An antisymmetry between the forward and backward beam can be observed as expected. The calculated separation amounts to more than the vertical r.m.s. beam size and it is clear that it is impossible to adjust the collision such that all bunches of a train collide head-on. The above example was computed for 45.6 GeV and bunch intensities of 500  $\mu\text{A}$ , i.e. above what was actually achieved, but demonstrates the importance of this effect. The Fig.16

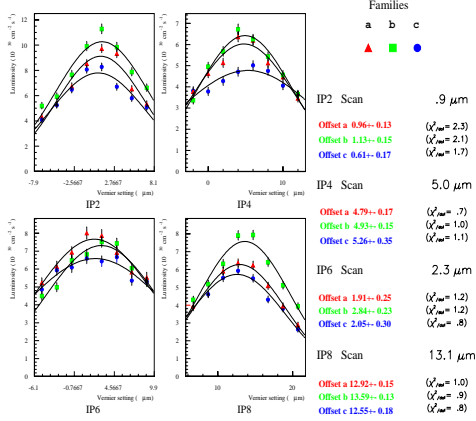


Figure 18: Result of separation scans for three bunches per train

shows the result of a vertical separation scan with simultaneous measurements of the luminosity for three bunches per train, the preferred operational scenario in 1995. The maximum luminosity, i.e. full bunch overlap, is reached at different vertical positions for the three bunches within a train, in full agreement with the calculation.

For four bunches per train this information is not available since most of the time LEP was operated with three bunches per train, i.e. 12 bunches total. This small offset proved to be an important performance limitation and the best tune shifts obtained were always smaller than in previous years, leading to a performance that was lower than expected. Nevertheless, the optimization of the bunch overlap was essential for a good performance. It should be mentioned, that from symmetry considerations a running with two bunches per train is most favourable since the symmetry of the collision is fully restored and both bunches of the train can be collided head-on, although possibly in different vertical position.

In the LHC the calculation of self-consistent orbits would be necessary for almost 3000 bunches and it is not obvious whether this is feasible nor whether a self-consistent solution exists.

**Tune and chromaticity splits** Once the self-consistent orbits were calculated, this information was used to compute the tune and chromaticity of the individual bunches in

a train. The result is summarized in Tab.5 where  $q$  indi-

Table 5: Fractional tunes and chromaticities are split inside a train for 300  $\mu\text{A}$  per bunch at 45.6 GeV

	a	b	c	d
$q_x$	0.3548	0.3612	0.3613	0.3547
$q_y$	0.2127	0.2235	0.2234	0.2133
$Q'_x$	0.4526	0.5000	0.5025	0.4848
$Q'_y$	0.1872	-0.2218	-0.2259	0.0053

cates the fractional part of the tune and  $Q'$  the chromaticity. The example was computed for 300  $\mu\text{A}$  per bunch and 45.6 GeV and four bunches per train. The maximum tune difference was up to 0.010 and the chromaticity difference 0.41 units in the vertical plane. This is a significant limitation to the operational parameter space for the optimization of the performance.

When the machine was operated with four bunches per train, some bunches always had a lower life time, usually those who experienced a beam-beam interaction at small separation. This was confirmed in dedicated tests.

## 6.5 Closed orbit effects in the LHC

The TRAIN program [19] originally developed for the maximum 16 bunches of LEP was re-written to handle two beams with almost 3000 bunches each. Furthermore it must be able to handle different optics for the two beams. Details about the algorithm and its performance can be found in [8].

For the nominal bunch filling scheme the horizontal offset in interaction point 1 (IP1) is shown in Fig.19. The off-

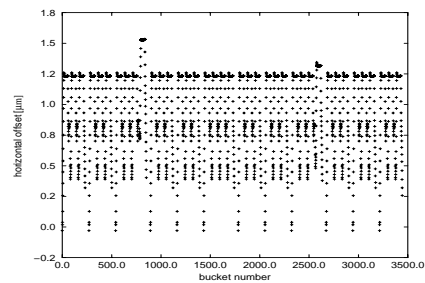


Figure 19: Closed orbit along bunch structure in the LHC.

set is shown in  $\mu\text{m}$  as a function of the bunch number, starting the count with the bunch following the large gap. The first bunch of beam one is assumed to collide with the first bunch of beam two in IP1. For symmetry reasons they also collide in IP5. In Fig.20 I show a zoom into the first part of Fig.19. Clearly visible are the nominal bunches in the middle of each batch (approximately 40). At both ends of

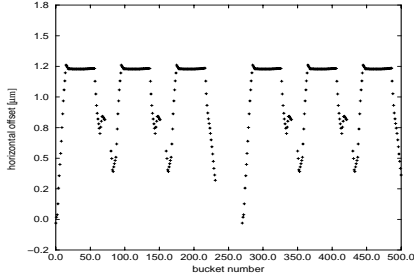


Figure 20: Closed orbit along bunch structure in the LHC, zoomed into 3 batches.

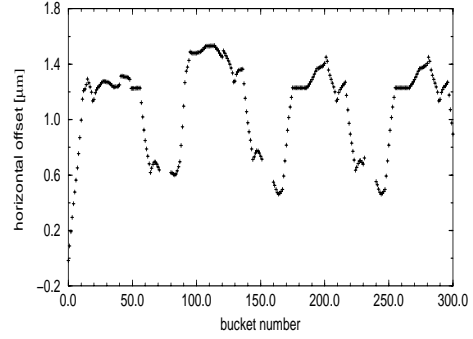


Figure 22: Closed orbit along bunch structure in the LHC, zoomed into 3 batches. No fourfold symmetry.

a batch the orbit offsets change due to the decreasing number of long range dipole kicks. The spread of the offset is in the order of 0.1 to 0.2 transverse beam sizes. Although this small offset has practically no effect on the luminosity, it needs to be studied whether quasi head-on collisions with a crossing angle and a small offset lead to an emittance growth or other unwanted side effects. In the Figs.21 and

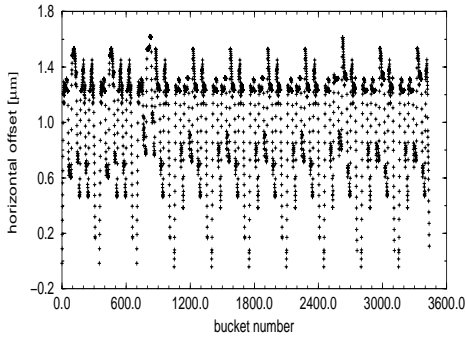


Figure 21: Closed orbit along bunch structure in the LHC. No fourfold symmetry.

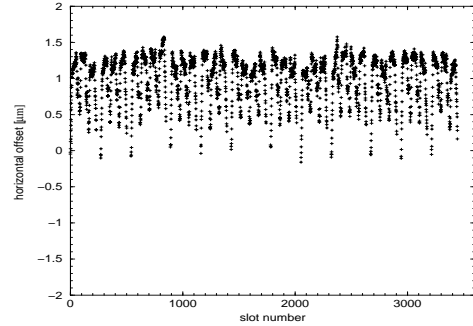


Figure 23: Closed orbit along bunch structure in the LHC. 20% intensity variation between bunches.

## 7 COHERENT EFFECTS

### 7.1 Coherent effects in LEP

22 I show similar data for an alternative filling scheme [9] which optimizes the number of bunches, however it does not have a fourfold symmetry. The effect is immediately visible: the offset is slightly increased but not dramatic, however practically no nominal bunches can be identified. This may lead to unwanted difficulties and uncertainties for beam measurements. As a further complication, we have to expect bunch to bunch intensity variations of 10 to 20%. In the TRAIN program this intensity variation can be considered and the result of such a variation is shown in Figs.23 and 24, again for the nominal filling scheme. The additional offset variation is clearly visible [9], and close to the acceptable level.

Coherent beam-beam modes were frequently observed in LEP and due to the large beam-beam strength parameter the separation between the main modes, i.e. the  $\sigma$ - and  $\pi$ -mode is rather large allowing only a limited area in the tune space. Some background problems experienced in 1998 were attributed to the excitation of the horizontal  $\pi$ -mode near the half integer resonance. A clear demonstration of the two principal modes is shown in Fig.25 [20]. The tune spectra of two colliding bunches were recorded separately and the sum of the spectra is plotted. From the top to the bottom of the picture the phase of one spectrum is shifted in steps of one degree from zero to 360 degrees and the sum signal is shown. For zero and 360 degrees this corresponds to an in-phase signal and the  $\sigma$ -mode is observed. For a phase difference of 180 degrees the out-of-phase signal corresponds to the  $\pi$ -mode. Both modes are very clearly visible, a clear demonstration that the modes observed at the corresponding frequencies can be associated to an in-phase and an out-of-phase motion of the two bunches.

A coherent quadrupole mode was observed once at LEP,

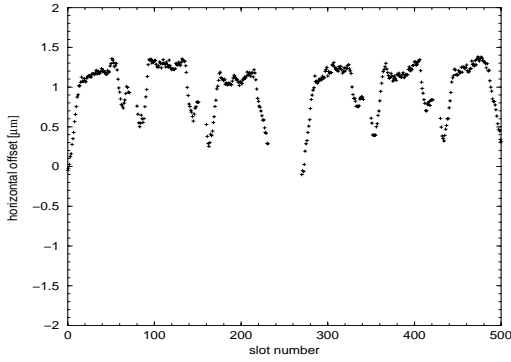


Figure 24: Closed orbit along bunch structure in the LHC, zoomed into 3 batches. 20% intensity variation between bunches.

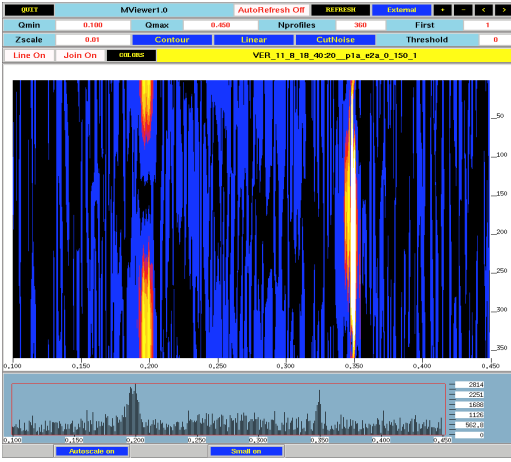


Figure 25: Demonstration of coherent beam-beam modes in LEP

however was never reproduced afterwards.

## 7.2 Coherent effects in LHC

Possible excitation of coherent dipole modes in the LHC were studied using new simulation techniques and details can be found in [10, 11, 12].

## 8 CONCLUSION

Amongst the numerous information on beam-beam effects we have obtained at LEP, some are of importance for the evaluation of LHC beam-beam effects although a quantitative application is not possible. The orbit effects caused by beam-beam kicks have been identified as a severe problem. A self-consistent treatment was vital to understand the observations quantitatively and the PACMAN like effects have limited the performance. The experience has shown that parameter splits between the beams or the bunches within a beam must be kept as small as possible

and self-compensation of these effects must be used wherever possible in the design process.

## 9 REFERENCES

- [1] W. Herr; *Experience with beam-beam effects in LEP* Proc. workshop on beam-beam effects in hadron colliders LHC99, (CERN, Geneva 1999) CERN SL/99-039 (AP) (1999) 7.
- [2] R. Schmidt; *Beam-beam observations in the SPS proton antiproton collider* Proc. workshop on collective effects in large hadron colliders, (Montreux, 1994) Part. Accelerators Vol.50, Number 1-3, p. 47, (1995).
- [3] K. Cornelis; *Beam-beam effects in the SPS proton antiproton collider* Proc. workshop on beam-beam effects in hadron colliders LHC99, (CERN, Geneva 1999) CERN SL/99-039 (AP) (1999) 2.
- [4] D. Brandt, W. Herr, M. Meddahi and A. Verdier; *Is LEP beam-beam limited at its highest energy ?* Proceedings of 1999 Part.Acc.Conf., New York, 29.3.-2.4. 1999.
- [5] L. Leunissen; *Influence of vertical dispersion and crossing angle on the performance of the LHC* Proc. workshop on beam-beam effects in hadron colliders LHC99, (CERN, Geneva 1999) CERN SL/99-039 (AP) (1999) 81.
- [6] O. Brüning, W. Herr, R. Ostojic, *A beam separation and collision scheme for IP1 and IP5 at the LHC for optics version 6.1*, CERN LHC Project Report 315
- [7] O. Brüning, W. Herr, R. Ostojic, *A beam separation and collision scheme for IP2 and IP8 at the LHC for optics version 6.1*, CERN LHC Project Report 367
- [8] H. Grote; *Self-consistent closed orbits caused by beam-beam effects in the LHC* Proc. Europ. Part. Acc. Conf. 2000, (Vienna, 2000) 1202.
- [9] H. Grote and W. Herr; *Self-consistent closed orbits caused by beam-beam effects in the LHC* Proc. this workshop, (FNAL, 2001).
- [10] Y. Alexahin, H. Grote, W. Herr and M.P. Zorzano, *Coherent beam-beam effects in the LHC* Proc. International Conf. on High Energy Accel. HEACC 2001, (Tsukuba, 2001) and LHC Project Report 466 (2001).
- [11] W. Herr, M.P. Zorzano and F. Jones; *Beam-beam simulations using a Hybrid Fast Multipole Method*. Phys. Rev. ST Accel. Beams **4**, 054402 (2001).
- [12] W. Herr, M.P. Zorzano and F. Jones; *Beam-beam simulations using a Hybrid Fast Multipole Method*. Proc. this workshop, (FNAL, 2001).
- [13] Y. Luo and F. Schmidt; *Beam-beam simulations for the LHC at injection and collision energies*. Proc. this workshop, (FNAL, 2001).
- [14] F. Zimmermann; *Weak-strong simulation studies for the LHC long-range beam-beam compensation*. Proc. this workshop, (FNAL, 2001).
- [15] J.P. Koutchouk; *Correction of the Long-Range Beam-Beam Effect in LHC using Electromagnetic Lenses*. Proc. this workshop, (FNAL, 2001).
- [16] W. Herr; *Effects of PACMAN bunches in the LHC*; CERN LHC Project Report 39 (1996).

- [17] W. Herr; *Bunch trains without a crossing angle*; Proc. 4th workshop on LEP performance, (Chamonix 1994) CERN SL/94-06 (DI) (1994) 323.
- [18] B. Goddard *et al.*; *Bunch trains for LEP*; Part. Accelerators Vol.**57**, Number 4, p. 237, (1998).
- [19] E. Keil; *Truly selfconsistent treatment of the side effects with bunch trains*; CERN SL/95-75 (AP) (1995).
- [20] G. Morpurgo; *Private communication*;

# Beam-Beam experience at KEKB

M. Tawada, K. Akai, N. Akasaka, K. Bane\*, A. Enomoto, J. W. Flanagan, H. Fukuma, Y. Funakoshi, K. Furukawa, J. Haba, S. Hiramatsu, K. Hosoyama, N. Huang†, T. Ieiri, N. Iida, H. Ikeda, T. Kamitani, S. Kato, M. Kikuchi, E. Kikutani, H. Koiso, S. -I. Kurokawa, M. Masuzawa, T. Matsumoto, S. Michizono, T. Mimashi, T. Nakamura, Y. Ogawa, K. Ohmi, Y. Ohnishi, S. Ohsawa, N. Ohuchi, K. Oide, E. A. Perevedentsev‡, D. Pestrikov‡, K. Satoh, M. Suetake, Y. Suetsugu, T. Suwada, M. Tejima, M. Tobiyama, S. Uno, Y. Z. Wu†, N. Yamamoto, M. Yoshida, S. Yoshimoto, M. Yoshioka, C. H. Yu†, F. Zimmermann§, KEK, 1-1 Oho, Tsukuba-shi, Ibaraki-ken 305-0801, Japan

## Abstract

KEKB has achieved the peak luminosity of  $4.1 \times 10^{33} \text{ cm}^{-2} \text{ sec}^{-1}$  and the present capability for delivering integrated luminosity is  $224 \text{ pb}^{-1}/\text{day}$ . This paper describes (1) the recent performance and the problems of KEKB and (2) the comparison of beam-beam simulations with experiments at KEKB.

## 1 INTRODUCTION

KEKB is a double ring electron-positron collider to study B-meson physics. One ring is an 8 GeV electron ring (HER) and the other is a 3.5 GeV positron ring (LER). The HER and LER rings cross at the interaction point (IP) with a  $\pm 11$  mrad crossing angle. To study B-meson physics, which deals with very rare processes, KEKB has a high design luminosity of  $1 \times 10^{34} \text{ cm}^{-2} \text{ sec}^{-1}$  and high vertical beam-beam parameters ( $\xi_y$ ) of 0.05. The general outline and overall parameters of the KEKB accelerator are given in [1].

Recently, there has been excellent progress in commissioning of the KEKB accelerator. Figure 1 shows the luminosity history of KEKB from the beginning of the commissioning with the Belle detector. The peak luminosity of  $4.1 \times 10^{33} \text{ cm}^{-2} \text{ sec}^{-1}$  was achieved and the present capability for delivering integrated luminosity is  $224 \text{ pb}^{-1}/\text{day}$ ,  $4.7 \text{ fb}^{-1}/\text{month}$ . The total integrated luminosity of  $30 \text{ fb}^{-1}$  was accumulated[2]. Table 1 summarizes the present parameters which are related to the luminosity with the design parameters.

## 2 RECENT IMPROVEMENT OF KEKB PERFORMANCE

KEKB performance has been improved by several means: (1) installation of solenoids to LER, (2) a shift of the vertical tunes above a half integer for both rings, (3) increasing the HER bunch current after the replacement of HER movable masks to those of a new type of mask and (4) a continuous tune monitor of pilot bunch.

\* visiting from SLAC, U.S.A

† visiting from IHEP, China

‡ visiting from BINP, Russia

§ visiting from CERN, Switzerland

	LER	HER	unit
Horizontal emittance	18	24	nm
Beam current	885 (2600)	748 (1100)	mA
No. of bunches/ring	1154 (5120)	1154 (5120)	
Bunch current	0.77 (0.5)	0.65 (0.2)	mA
Bunch spacing	2.4 (0.6)	2.4 (0.6)	m
Bunch trains	1	1	
$\sigma_x^*$	103	123	$\mu\text{m}$
$\sigma_y^{*1)}$	2.9	2.9	$\mu\text{m}$
$\epsilon_y/\epsilon_x$	4.2	3.2	%
$\beta_x/\beta_y$	0.59/0.0065 (0.33/0.01)	0.63/0.007 (0.33/0.01)	m
$\xi_x/\xi_y^{2)}$	0.072/0.045 (0.039/0.052)	0.050/0.028 (0.039/0.052)	
$\nu_x/\nu_y$	45.51/44.57 (45.52/44.08)	44.519/42.517 (44.52/42.08)	
Beam lifetime	166@854 mA	210@675 mA	min.
Bunch length	5.9@8.0	6.4@11	mm@MV
Luminosity (CsI)	$4.1 \times 10^{33}$	$(1 \times 10^{34})$	/cm <sup>2</sup> /sec
Luminosity records per day/ 7 days / month	224/1336/4703		/pb

Table 1: The present machine parameters and performance of the KEKB (June 13, 2001). The values in a parenthesis are the design values. 1) Vertical beam sizes of the two beams are assumed to be equal. 2) An effect of dynamic beta and dynamic emittance is not considered.

### 2.1 Installation of solenoid to LER

A vertical beam blowup has been observed in LER since early operation. The main characteristics of the blowup are explained by single-beam head-tail instability caused by an electron cloud. About 4600 solenoids were installed to LER in order to suppress the electron cloud. Its total length is about 1.23 km and about 40 % of the ring circumference was covered by solenoid field. The calculated field strength was 45 Gauss at the center of the solenoid when the maximum current of 5 A was applied. Figure 2 shows the luminosity as a function of the bunch current product with and without solenoid field.

The averaged vertical beam size over all bunches are

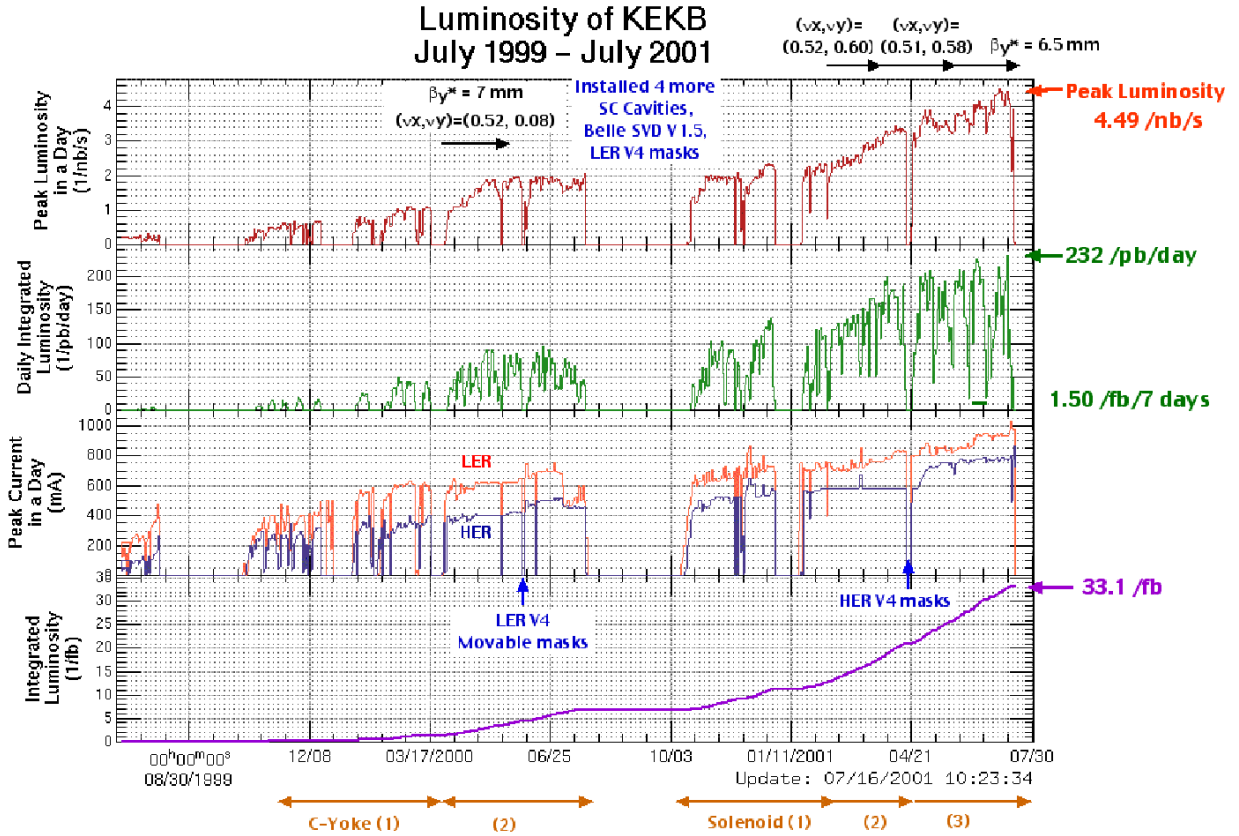


Figure 1: This figure shows the luminosity history from the beginning of the commissioning with Belle detector (July 16, 2001).

measured by a synchrotron radiation interferometer [3]. The beam size is transformed from the source point of the synchrotron radiation to IP. The threshold current of blowup was also increased when solenoids were excited[4]. The problem is improved but not solved yet. The vertical beam size is still large at the higher beam current than 700 mA with 1154 bunch mode.

## 2.2 Tune Survey and Continuous Tune Monitor

We have moved to the vertical tune above the half integer for both rings at February, 2001. The reason is as follows. (1) The closed orbit at the tune above the half integer is not so sensitive to the machine errors as that with a tune just above the integer. (2) The strong-strong beam-beam simulations have predicted a tune region above the half integer would bring a better luminosity[5].

The machine stability was also improved by the continuous tune monitor of pilot bunches. This monitor can measure the tune during both injection and physics time by using un-collided bunches.

## 2.3 HER current

The movable mask is a device that cuts off spent electrons/positrons just near the beam orbit and reduces back-

ground of a detector. Sixteen movable masks were installed for each ring of KEKB. Heating problems of movable masks have limited the stored beam currents for HER. New movable masks have been designed employing RF technologies for HOM damping[6].

After replacement of the HER movable masks to a new type[7] at April, 2001, we could increase the beam currents gradually.

## 3 PRESENT LUMINOSITY LIMITATION AND PROBLEM AT KEKB

The luminosity of KEKB has been limited by the several problems. (1) Installation of the solenoids to suppress the electron cloud instability has improved the problem as described before but not resolved it completely. (2) It turned out that the LER single beam blowup is sensitive to the filling pattern. We have tried various filling patterns to increase the number of bunches. But we could not get higher luminosity than that with 4 rf bucket spacing. (3) The total beam current is limited by the heating of vacuum components due to the synchrotron radiation or HOM. And the bunch current is also limited by the heating of the HOM damper of the superconducting cavity for HER. (4) beam background for Belle detector.



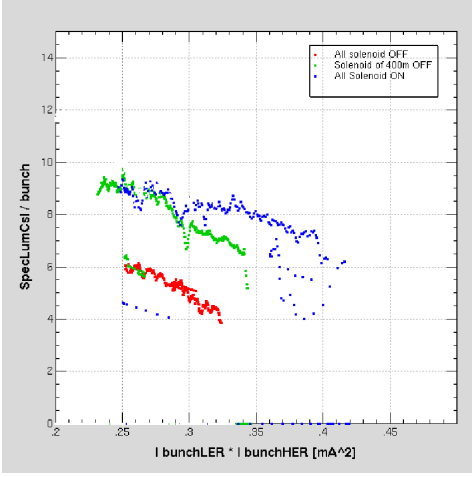


Figure 2: Specific luminosity per bunch as a function of the bunch current product in the case of all solenoid OFF(●), solenoid of 400 m OFF(●) and All solenoid ON(●)

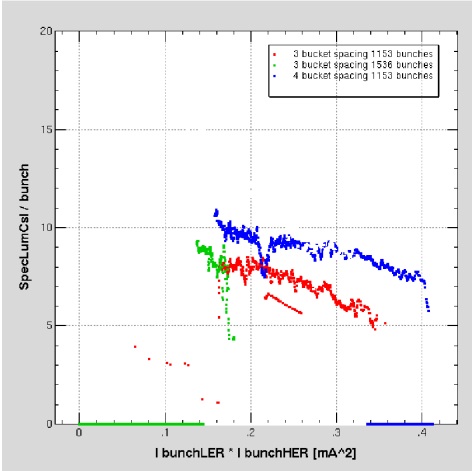


Figure 3: The data for the 3 rf bucket (●,●) spacing pattern show lower specific luminosity than that for the 4 rf bucket (●) pattern.

### 3.1 "Egure" problem

Sudden drops of the luminosity, so called "Egure" at KEKB, are frequently observed. Figure 4 shows a typical "Egure" pattern. The "Egure" accompanies the LER horizontal beam size growth. (sometimes accompanies vertical beam size growth.) When "Egure" is occurred, we make the horizontal beam separation ( $\sim 50 \mu\text{m}$ ) for short time and

then the luminosity is recovered.

F. Zimmermann have explained that "egure" problem comes from a significant tune dependence and the existence of flip-flop solutions for head-on collisions by evaluating a simplified linear model of beam-beam interaction[8].

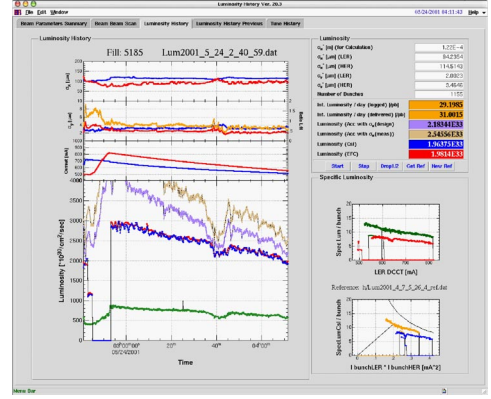


Figure 4: This figure shows a typical "Egure" pattern.

## 4 BEAM-BEAM SIMULATION

Newly, a strong-strong beam-beam simulation code was developed by K. Ohmi[9] to study beam-beam effect. In that simulation, both of the colliding beams are represented by macro-particles. The electron-magnetic fields of each relativistic beam are obtained by solving the Poisson equation for the charge distribution of the macro-particles. At each turn, the electron-magnetic fields are calculated for each beam, and then these beams are allowed to interact with each other through the fields. A transformation of the collided bunch across one revolution through the ring is calculated by using a beam transfer matrix. The effects of radiation damping and quantum excitation are included in this code. The machine errors can be included.

We have carried out simulations for the KEKB parameters which were used in operation and compared these results with experiments. A  $64 \times 128$  mesh with horizontal and vertical sizes of  $20 \times 0.4 \mu\text{m}$  mesh was used, respectively. Both beams are represented by 100,000 macro-particles, typically. The macro-particles are tracked for 45,000 turns. Due to the fast progress in computing power, the strong-strong beam-beam simulation becomes feasible. But it still requires a large amount of computer resources.

Figure 5 shows the longitudinal slice number dependence of specific luminosity. Although the slice number should be bigger than 20, but we usually used 5 longitudinal slices due to the limited computing resources. Even if longitudinal slice number is 5, the simulation results are in reasonable agreement with measurements qualitatively in many cases. For a simulation for one tune point, it takes



about 5 days on the Unix workstation of AP3000 (Sun) and about 4 hours on the supercomputer of SR8000F1 (Hitachi), which have 12 GFLOPS for each node under above conditions.

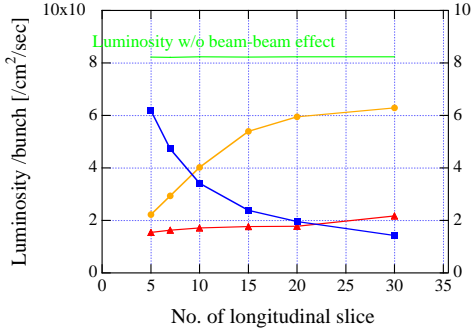


Figure 5: Longitudinal slice number dependence of specific luminosity. They were tracked for 20,000 turns, respectively. The yellow filled circle (●) is the luminosity per bunch, the red filled triangle (▲) and the filled box (■) is the vertical beam size of LER and HER, respectively.

#### 4.1 Tune Survey

Since the luminosity at KEKB is sensitive to the tune, the tune survey is a very important tuning issue. We have shifted the vertical tunes above a half integer for both rings as described before.

The beam-beam simulation without errors shows that  $\nu_x \sim 45.51$ ,  $\nu_y \sim 44.64$  is the best point in that area (the upper graph of Figure 6). We have tried the LER vertical tune of 44.64 several times. But the luminosity with that tune is lower than that with the present working point ( $\nu_x \sim 45.51$ ,  $\nu_y \sim 44.57$ ), which is found by a trial and error method.

The simulation with the error of vertical crossing angle explains the lower luminosity at the tune of  $\nu_x \sim 45.51$ ,  $\nu_y \sim 44.64$  is caused by machine error (the bottom graph of Figure 6).

#### 4.2 Specific luminosity versus current product

Beam-beam effects cause an increase in vertical beam size and subsequent decreases in specific luminosity. Figure 7 shows the simulation of the specific luminosity versus the beam current products. The measured bunch current and bunch length are also used as input parameters for simulations. The simulation is in good agreement with the experiment.

#### 4.3 Vertical emittance dependence of Luminosity

As shown in the Figure 8, the beam-beam simulation predicted that (1) the vertical emittance of HER can be optimized to get a higher luminosity and (2) the vertical emittance

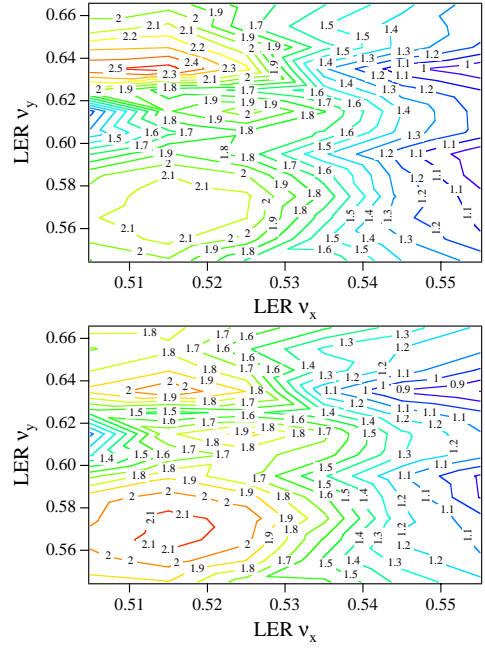


Figure 6: The result of LER tune survey by the strong-strong beam-beam simulation without errors (Top graph) and with the error of the vertical crossing angle of 0.1 mrad (Bottom graph).

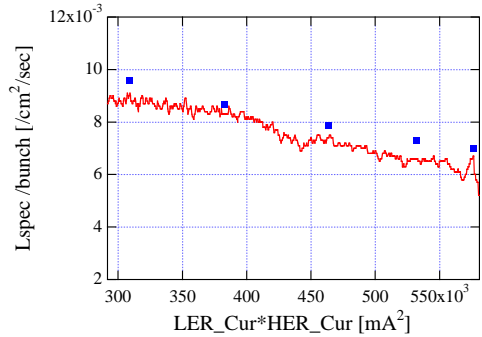


Figure 7: Specific luminosity/bunch as a function of the current products. The red solid line is the experimental result (May 2, 2001, Fill 4811) and the blue filled box (■) is the simulation result. The longitudinal slice number is 10 in this simulation.

tance dependence of the luminosity for KEKB is stronger than that for the case of zero-crossing angle.

The vertical emittance feedback system is realized by so-called "iSize" feedback system at KEKB[10]. At one of the strongest non-interleaved sextupole pairs in the arc section of HER, an anti-symmetric bump is made by three dipole correction magnets. This bump converts the horizontal dispersion to the vertical. It leaks out around the whole of the ring. The created xy-coupling is closed in the bump. This dispersion enlarges the vertical emittance. "iSize" system at KEKB works well.

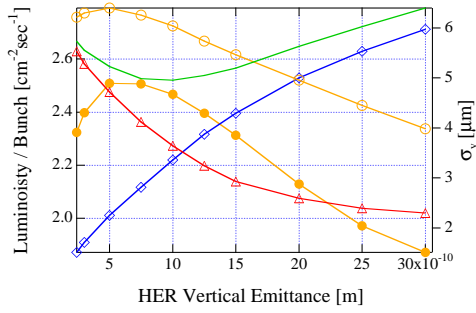


Figure 8: Vertical emittance dependence of luminosity. Vertical beam size of LER( $\Delta$ ), HER( $\diamond$ ), and  $\Sigma$ (blue solid line), Luminosity with a crossing angle of  $\pm 11$  mrad ( $\bullet$ ), Luminosity without a crossing angle( $\circ$ ).

## 5 SUMMARY

The peak luminosity of  $4.1 \times 10^{33} \text{ cm}^{-2} \text{ sec}^{-1}$  was achieved at KEKB and the present capability for delivering integrated luminosity is about  $4.7 \text{ fb}^{-1}/\text{month}$ . Installation of the solenoids to suppress the electron cloud instability has improved the situation but not resolved the problem. The machine stability has been improved by moving to the tune above a half integer and the continuous tune monitor of pilot bunches. The beam-beam simulation is in reasonable agreement with measurement in many cases.

## 6 FUTURE PLAN

(1) Since KEKB has a crossing angle, a shorter bunch length is favorable for a geometrical luminosity reduction. But we are afraid that the shorter bunch for HER may cause more heating of HOM dampers. Anyway, we will try to do machine study to shorten the LER bunch length.

(2) As we mentioned above, installation of the solenoids to suppress the electron cloud instability has improved the problem but not resolved it. During this summer shutdown, we will add more solenoid to LER.

(3) The injection rate for positron beams is 1.5 mA, which is the design value. We will try to introduce the two-bunch acceleration in order to minimize injection time. This plan would almost double the injection rate, and the injection time would be reduced by 1/2.

## 7 ACKNOWLEDGEMENTS

The authors would like to acknowledge the members of KEKB accelerator group and Belle group.

## 8 REFERENCES

- [1] KEKB B-Factory Design Report, KEK Report 95-7, (1995).
- [2] <http://www-acc.kek.jp/WWW-ACC-exp/KEKB/KEKB-home.html>
- [3] J. W. Flanagan et. al. PAC97.
- [4] H. Fukuma et. al., HEACC2001, Tsukuba, March (2001).

- [5] Y. Z. Wu, Y. Funakoshi, M. Tawada, K. Ohmi "A new working point for the KEKB", HEACC2001, Tsukuba, March (2001).
- [6] K. Kanazawa, K. Sato, N. Akasaka, T. Kageyama, Y. Suetsugu, Y. Takeuchi, "Development of the Movable Mask System for KEKB", EPAC2000, 2301 (2000).
- [7] Y. Suetsugu et. al., HEACC2001, Tsukuba, March (2001).
- [8] F. Zimmermann, in these proceedings.
- [9] K. Ohmi, K. Hirata and K. Oide, Phys. Rev. **E49** 751, 1994.
- [10] N. Iida et. al. , HEACC2001, Tsukuba, March (2001)

# BEAM-BEAM EXPERIENCE AT DAΦNE

M. Boscolo, for the DAΦNE Team<sup>1</sup>

INFN, Laboratori Nazionali di Frascati, C.P. 13, 00044 Frascati (Rome), Italy

## Abstract

DAΦNE, the Frascati LNF  $\Phi$ -factory [1], is providing a higher peak and integrated luminosity for the KLOE experiment since July 2000 [2,3]. Such improvements, together with a background reduction in the KLOE detector, have been obtained after continuous machine studies. An increase of the single bunch luminosity has been achieved essentially by the reduction of the effects of the machine non-linearities. These studies are described, and the present beam-beam limitations are reported, with an analysis of the coupling between the machine non-linearities and the beam-beam interaction. The integrated luminosity did greatly benefit by the capability of topping up the beam currents while keeping the KLOE detector on, together with an increase of the stored currents.

## 1 INTRODUCTION

DAΦNE is a high luminosity and low energy electron-positron collider, working at the center of mass energy of the  $\Phi$  resonance (1.02 GeV) to produce a high rate of K mesons to study CP violation. Two 97 m long independent rings lay in the same horizontal plane, crossing at a small horizontal angle (25 mrad) in two interaction regions (IRs), where the two experiments KLOE and DEAR are placed. The first one consists of a large detector with a high solenoidal field integral of 2.4 Tm, that gives a strong perturbation to the machine optics at its relatively low beam rigidity ( $B\rho=1.7\text{Tm}$ ). KLOE aims at measuring the CP violating parameter  $\text{Re}(\epsilon'/\epsilon)$ . The second experiment is small and non-magnetic, it studies the properties of kaonic atoms and will eventually be replaced by the magnetic detector FINUDA, for the study of hypernuclear physics.

In March 2001 a peak luminosity of  $10^{30}\text{cm}^{-2}\text{s}^{-1}$  in single bunch mode has been reached, after dedicated machine nonlinearities studies, discussed in more details in sections 2 and 4.

A peak luminosity of  $3.3 \cdot 10^{31}\text{cm}^{-2}\text{s}^{-1}$  has been achieved in the multibunch mode, with 47 bunches separated by one bucket and beam currents of  $\approx 700$  mA, as reported in section 3. The maximum daily integrated luminosity is  $1.7\text{pb}^{-1}$ , and the total integrated luminosity by KLOE is  $\approx 100\text{pb}^{-1}$  (see figure 1).

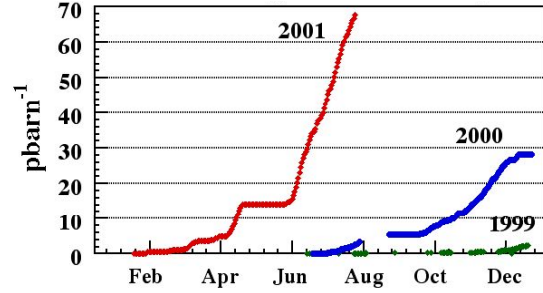


Figure 1: KLOE Integrated Luminosity.

## 2 SINGLE BUNCH LUMINOSITY

To increase the single bunch (SB) luminosity, in the past years many physics runs have been dedicated to working point tuning, coupling correction, measurement and reduction of the effects of nonlinearities [4].

Table 1 shows the improvements in the SB luminosity in such period. The first entry in the table, a SB luminosity of about  $0.2 \cdot 10^{30}\text{cm}^{-2}\text{s}^{-1}$  obtained with a bunch current of about 10 mA, has been measured after the optimisation of both the collision parameters and coupling.

The working points are different for the two rings since May 2000: they are (5.15;5.21) for the positron ring and (5.12;5.17) for the electron one. A strong coupling reduction ( $\kappa \approx 0.3\%$ ) has enhanced the SB luminosity to  $\approx 0.5 \cdot 10^{30}\text{cm}^{-2}\text{s}^{-1}$  (with a bunch current of about 15 mA). In this configuration in November 2000 a luminosity of  $1.8 \cdot 10^{31}\text{cm}^{-2}\text{s}^{-1}$  with 45 bunches and  $\approx 600$  mA current has been achieved.

Table 1. Single bunch maximum luminosity and corresponding beam-beam tune shift.

time	$L_{\text{SB}}$ ( $10^{30}\text{cm}^{-2}\text{s}^{-1}$ )	$I_{\text{perbunch}}$ (mA)	$\xi_x$
Nov.'99	0.2	10	0.01
May'00	0.5	15	0.015
March'01	1	20	0.02

A non-linear term in the wiggler magnets has been demonstrated last November, so machine time has been dedicated to systematic studies of the effect of nonlinearities, as it is discussed in more details in section 4.

A new optics, called 'detuned', with no low- $\beta$  in the DEAR IR, has been applied to DAΦNE [5]. With this structure the machine is tuned to collide only at the KLOE IP. As a consequence, the lattice has lower

<sup>1</sup> D.Alesini, G.Benedetti, S.Bertolucci, C.Biscari, R.Boni, A.Clozza, G. Delle Monache, S. Di Mitri, G. Di Pirro, A.Drago, A.Gallo, A.Ghigo, S.Guiducci, F.Marcellini, G.Mazzitelli, C.Milardi, L.Pellegrino, E.Perevedentsev (BINP), P. Raimondi(SLAC), M.A.Preger, R.Ricci, C.Sanelli, F.Sgamma, F.Sannibale, M.Serio, A.Stecchi, A.Stella, C.Vaccarezza, M.Vescovi, G. von Holtey(CERN), M.Zobov.

chromaticity, so smaller sextupole strengths are needed to compensate it. Since a large vertical separation at the second IP is introduced, parasitic interactions at the second IP are avoided. Moreover, the “detuned” lattice is adjusted to have smaller  $\beta$ -functions in the wiggler decreasing the effect of their octupole terms. As this optics is less sensitive to machine nonlinearities, it has been possible to obtain a single bunch luminosity of  $10^{30} \text{ cm}^{-2} \text{ s}^{-1}$  at currents of  $\approx 20 \text{ mA}$  per bunch, as reported in the last row of Table 1.

### 3 MULTIBUNCH PERFORMANCE

#### 3.1 Peak Luminosity

The collision parameters achieved in DAΦNE operation for KLOE are listed in Table 2.

Table 2: DAΦNE Collision Parameters.

Beam Energy [GeV]	0.51
Half Crossing Angle [mrad]	12.5
Luminosity [ $\text{cm}^{-2} \text{ s}^{-1}$ ]	$3.3 \cdot 10^{31}$
Number of bunches	47
Longitudinal separation [RF buckets]	2
Harmonic number	120
e+ current [mA]	$\approx 900$
e- current [mA]	$\approx 800$
$\beta_y/\beta_x$ @IP [m]	0.045/4.5
Emittance [ $10^{-6} \text{ m}$ ]	0.8
Rms beam size $\sigma_y/\sigma_x$ @IP [mm]	0.011/19
Damping time $\tau_y/\tau_x$ [ms]	17.8/36
Injection time [min]	3
Max integrated luminosity/day [ $\text{pb}^{-1}$ ]	1.7
Total integrated luminosity [ $\text{pb}^{-1}$ ]	$\approx 100$

An improvement of the peak luminosity has been possible by increasing the single bunch luminosity, the total beam currents and the number of bunches. Presently 47 bunches spaced at 2 RF buckets are used for KLOE runs with a gap to avoid ion trapping in the electron ring, and they are injected in collision. In figure 2 the increase of the peak value from February to July 2001 is shown.

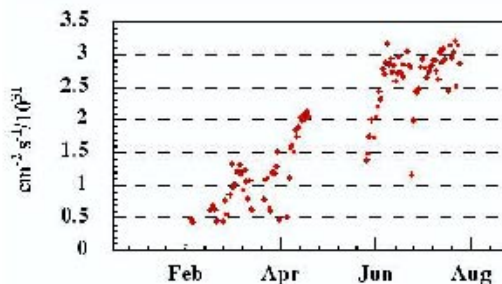


Figure 2 Daily peak luminosity in the first months of 2001 after the winter shutdown.

The peak luminosity is usually obtained with total currents of 600-700 mA per beam, corresponding to currents per bunch lower than the ones giving the maximum SB luminosity.

At the beginning of operation the maximum luminosity could not be delivered to KLOE due to the high background level, which limited the stored beam currents. A great effort has been spent in order to reduce the machine induced background. In a low energy machine like DAΦNE it arises mainly from the Touschek effect. In particular this background reduction has been obtained by tuning orbits and optical functions in the IRs, by adjusting the sextupoles strengths and the  $\beta_x$  value upstream the IR's. Efforts to reduce the remaining particle backgrounds have been spent by optimising the scrapers configuration [6]. Present KLOE background rate is nearly the same as in July 2000 but with a five times larger daily-integrated luminosity.

#### 3.2 Average Luminosity

Improvement of average luminosity and beam lifetime has been obtained by carefully tuning the working point, the machine coupling and the optimization of sextupoles configuration.

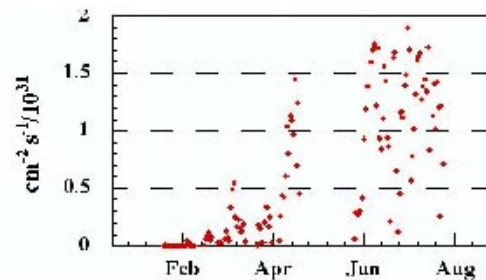


Figure 3: KLOE Daily Average Luminosity in the first months of 2001 after the winter shutdown.

The data taking efficiency has increased by keeping the KLOE detector on during injection. The average luminosity is maintained close to the peak value by a frequent refill of the rings currents (about every 10-15 minutes). The increase of the average luminosity from February to July 2001 is shown in figure 3.

### 4 NON-LINEARITIES

Non-linearities have been intensively studied in order to improve the beam lifetime and the beam-beam performance. The largest source of non-linearity has been found in wigglers: the tune shift on amplitude (measured by applying local orbit bumps [7]) shows a parabolic behaviour well reproduced by an octupole term originated by the combination of a decapole term in the wiggler field and the oscillating beam path, leading to a large cubic non-linearity.

An analysis has been performed in order to study the impact of cubic non-linearity on beam-beam performance [8]. The machine non-linearity has been measured using a



dynamic tracking system [9] and the relative luminosity performances have been compared to simulations.

The non-linear variation of the beam-beam force with the distance from the beam center causes a tune shift dependent on the particle betatron oscillations amplitude and a tune spread in the beams and it induces non-linear resonances, usually studied by the Hamiltonian perturbation theory. When the two non-linear forces (cubic lattice non-linearity and beam-beam interaction) are considered together, the tune shift is given by the sum of the tune shift on amplitude due to the cubic non-linearity  $\Delta Q_x = 2c_{11}J_x$  and the beam-beam tune shift. In fact, the single particle Hamiltonian taking into account the beam-beam interaction and the cubic non-linearities can be expressed in the following way:  $H = H_0 + (H_{CUB} + V_{BB})$ .  $H_0$  is the unperturbed Hamiltonian, which is proportional to the unperturbed betatron tune  $Q_{x0}$  and to the action variable  $J_x$  ( $H_0 \propto Q_{x0} J_x$ ), in one degree of freedom.  $V_{BB}$  is the beam-beam potential. The Hamiltonian cubic term  $H_{CUB}$  can be expressed as  $c_{11}J_x^2$ .

The coefficient  $c_{11}$  characterizing the cubic non-linearity strength, is measured by the dynamic tracking system. A single bunch is excited horizontally by pulsing one of the injection kickers. The dynamic tracking system allows to store and to analyse the position of the kicked bunch turn-by-turn. The coherent betatron oscillation amplitude is recorded over more than 2000 turns, providing informations on betatron tune shifts with amplitude.  $c_{11}$  is derived from the analysis of the coherent oscillation amplitude decay due to nonlinear filamentation. The decoherence signal envelope at small currents decays with time  $t$  in the following way [10]:

$$S(t) \propto \exp\left(-\frac{t^2}{2\tau^2}\right) \exp\left(-\left(\frac{\partial\omega_x}{\partial E} \frac{\sigma_E}{\Omega_s}\right)^2 (1 - \cos \Omega_s t)\right)$$

$$\text{where } \tau = \left(2 \frac{\partial\omega_x}{\partial A_x^2} \Delta x \sigma_x\right)^{-1}.$$

The cubic nonlinearity can be determined from  $\tau$  if the kick amplitude  $\Delta x$  and the horizontal beam size  $\sigma_x$  are known at the pick-up position.  $\partial\omega_x / \partial E$  and is the chromaticity,  $\sigma_E$  is the energy spread and  $\Omega_s$  the synchrotron frequency. The coefficient  $c_{11}$  is related to the cubic nonlinearity  $\partial\omega_x / \partial A_x^2$  by the following relation:  $c_{11} = (\partial\omega_x / \partial A_x^2)(\beta_x / \omega_0)$ , where  $\beta_x$  is the horizontal beta function at the pick-up position and  $\omega_0$  is the angular revolution frequency and it is found directly from the signal envelope by fitting it by the exponential function. Practically:  $c_{11} = (\beta_x / 2\epsilon_x)^{1/2} / (2\pi N_t \Delta x)$ , where  $N_t$  is the number of turns after which the amplitude of the coherent signal drops by  $1/e$  and  $\epsilon_x$  is the horizontal emittance.

During collider tune up for collisions it has been found that the cubic nonlinearity can change widely depending on lattice functions and orbit. In fact values of  $c_{11}$  have been measured between  $-6 \cdot 10^2$  and  $+4 \cdot 10^2$ , as reported in

Table 3. It is worth remarking that the sign of the non-linearity changes when the wigglers are switched off.

A different behaviour of signal decoherence is expected when  $c_{11}$  is positive or negative. In fact, for  $c_{11} < 0$  the resonance width can be small and there is decoherence, but on the other hand the beam-beam footprint enlarges, so that the beam tails cross more resonances. For  $c_{11} > 0$  the resonance width can be very large and no decoherence is predicted, but in this case the cubic non-linearities tend to compensate the beam-beam footprint.

So, it is not obvious to say whether it is preferable to have  $c_{11}$  positive or negative. It has been found experimentally in DAΦNE that the best situation from the beam-beam point of view was with  $c_{11}$  negative and in absolute value less than about  $|2 \cdot 10^2|$ , as the highest value of SB luminosity ( $10^{30} \text{cm}^{-2} \text{s}^{-1}$ ) has been measured when  $c_{11}$  was about  $-1.7 \cdot 10^2$ .

From the analysis on the measurements reported in Table 3 we conclude that the highest negative contribution to  $c_{11}$  comes from the wigglers and its effect depends strongly on the  $\beta$ -value where the non-linearity is positioned; the sextupoles give a negative contribution to  $c_{11}$ , but less than the wigglers.

The combined effect of the cubic non-linearities and the beam-beam interaction depends on betatron tunes, on beam-beam tune shifts, on the non-linearity strength and on the sign of  $c_{11}$ .

The new ‘detuned’ optics presently used reduces the effect of non-linearities in wigglers by a smaller value of the  $\beta_x$ -function at their location. The reduction of the wiggler octupole contribution helps to increase the single bunch luminosity, but at the same time the Landau damping needed to suppress transverse multibunch instabilities is reduced.

In order to correct and optimise the effect of the octupole term on beam-beam and instabilities the installation of octupole magnets in foreseen in Fall 2001.

Table 3. Measured non-linear coefficient for different lattice configurations.

Optics	$c_{11} \cdot 10^2 [\text{m}^{-1}]$
last year KLOE runs	-6
Wigglers off and sextupoles off	+4
Wigglers off	+2
Wiggler's B field reduced by 15%	-3
‘detuned’	-3

## 5 BEAM-BEAM SIMULATIONS

### 5.1 Effect of cubic nonlinearities on Single Bunch Luminosity

The weak-strong code LIFETRAC [11] has been used to perform beam-beam simulations including the cubic non-linearity implicitly through the coefficient  $c_{11}$ . In this way it is possible to investigate the dependence of beam-beam tails, beam blow-up and lifetime on the cubic non-linearity. Simulations have been done on the present

positron working point (5.15;5.21) assuming equal tune shift parameter for the two transverse planes  $\xi_x=\xi_y=0.03$  and  $c_{11}$  has been varied from  $-6 \cdot 10^2$  to  $+6 \cdot 10^2$  corresponding to the measured values. Dynamic aperture is assumed rectangular with boundaries at  $10 \sigma_x$  and  $70 \sigma_y$ .

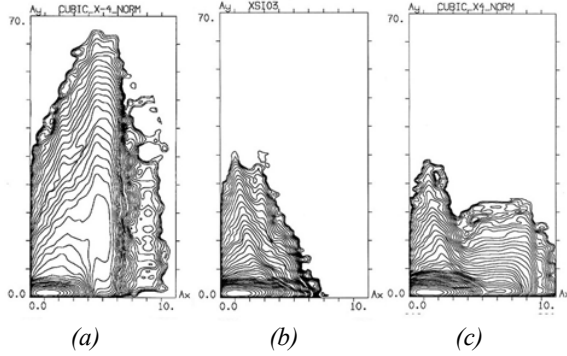


Figure 4. Equilibrium distributions for different cubic nonlinearities in space of normalised betatron amplitudes: (a):  $c_{11}=-4 \cdot 10^2$ ; (b):  $c_{11}=0$ ; (c):  $c_{11}=+4 \cdot 10^2$ .

Table 4 summarises the simulations performed for different  $c_{11}$  values, where the horizontal and vertical blow-up and the expected beam-beam lifetimes are reported. The beam distributions in the space of normalised betatron amplitudes shown in Figure 4 evidence that both positive and negative nonlinearities are harmful for the beam-beam effects. Above  $|c_{11}| > 2 \cdot 10^2$  the distribution tails start growing and the bunch core blows up in both cases. According to simulations, the nonlinearity strength can be considered acceptable when  $c_{11}$  is within  $-2 \cdot 10^2$  and  $+2 \cdot 10^2$ , as inside this range the beam tails are inside the dynamic aperture and no blow up is expected. This expectation agrees with our observations, where the highest single bunch luminosity of  $10^{30} \text{ cm}^{-2} \text{ s}^{-1}$  has been reached with  $c_{11} = -1.7 \cdot 10^2$ , while a low single bunch luminosity of about  $6 \cdot 10^{30} \text{ cm}^{-2} \text{ s}^{-1}$  was obtained when  $c_{11}$  was  $-6 \cdot 10^2$ , for which blow up and short lifetime are predicted.

Table 4. Simulated beam-beam blow up and lifetime versus cubic non-linearity strength.

$c_{11} \cdot 10^2 [\text{m}^{-1}]$	$\sigma_x/\sigma_{x0}$	$\sigma_y/\sigma_{y0}$	$\tau_{\text{beam-beam}}$
-6	1.06	2.43	2.4 h
-4	1.05	1.30	9.9 h
-2	1.07	1.04	$\infty$
0	1.07	1.05	$\infty$
+2	1.11	1.05	$\infty$
+4	1.16	1.04	7.7 h
+6	1.40	1.11	4 min

In the present electron ring structure  $c_{11}$  is about  $-3 \cdot 10^2$  while in the positron one is about  $-3.5 \cdot 10^2$ , so it is higher than the above discussed ‘limit’ at  $|2 \cdot 10^2|$  in both cases. This is due to the increase of the  $\beta$ -function in the wigglers, in order to handle background. In fact, it has

been found both experimentally and from simulations that Touschek particles could be stopped inside the wigglers by enhancing the  $\beta_x$ -value at their location. These particles would otherwise be lost inside the experiments. Values of  $c_{11}$  around  $-3 \cdot 10^2$  seem to balance well background problems with nonlinearities. In fact with the present configuration a single bunch luminosity of about  $8 \cdot 9 \cdot 10^{29} \text{ cm}^{-2} \text{ s}^{-1}$  has been measured by KLOE.

## 5.2 Effects of parasitic crossings and cubic nonlinearities

A reduction of the average single bunch luminosity by about 15% has been observed experimentally when going from single bunch to multibunch operation, as the luminosity does not scale linearly with the number of bunches. In fact, the peak luminosity is  $3.3 \cdot 10^{31} \text{ cm}^{-2} \text{ s}^{-1}$  with 47/60 bunches, giving an average single bunch luminosity of  $7 \cdot 10^{29} \text{ cm}^{-2} \text{ s}^{-1}$  with  $\approx 18 \text{ mA}$  per bunch current. One of the reasons is that the maximum beam currents cannot be stored simultaneously, since both rings are filled by the same injector chain. Few minutes are necessary to convert the injector between the two beams and the lifetimes are of the order of 2000 s. We have not observed yet a limit in the maximum of the luminosity as a function of the beam currents. Presently, the maximum electron beam current suitable for luminosity delivery is limited to  $\approx 850 \text{ mA}$  by ion trapping and longitudinal instabilities. The positron maximum beam current is limited to  $\approx 800 \text{ mA}$  by the KLOE background. Above such current we also observe a rapid decrease of the electron lifetime, due to strong beam-beam effects. The optimum number of bunches is found during operation.

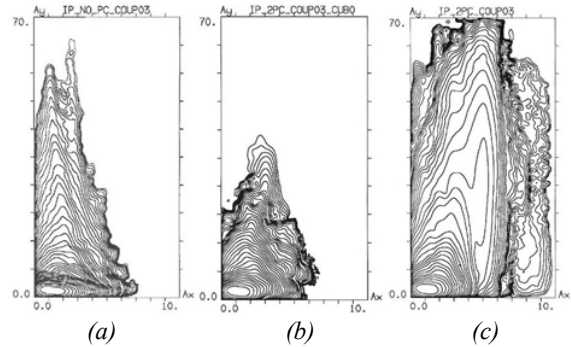


Figure 5. Equilibrium distributions in space of normalised betatron amplitudes: (a): no nonlinearity, no parasitic crossings included; (b): no nonlinearity and two parasitic crossings at  $10 \sigma_x$ ; (c): cubic nonlinearity with  $c_{11}=-350$  and two parasitic crossings.

One source of luminosity limitation in multibunch operation can derive from parasitic crossings (PC) enhanced by the cubic nonlinearity. In fact, a linear scaling with the number of bunches has been observed when they were separated by three empty buckets instead than only by one. Possible cures to parasitic crossings are

the decrease of  $\beta_x$  at the PC position, the decrease of emittance or an increase of the crossing angle.

Beam-beam interaction with two parasitic crossings at each side of the IP in the presence of cubic nonlinearity have been simulated by LIFETRAC. The PCs have been placed at 81 cm from the IP (about  $10\sigma_x$ ), which corresponds to the presently used fill pattern with one empty bucket between bunches. For these simulations the bunch current was 25 mA,  $c_{11}$  has been set to  $-3.5 \cdot 10^2$ , coupling has been set to the present value 0.3% and the horizontal and vertical emittance at  $10^{-6}$  m and  $0.3 \cdot 10^{-8}$  m respectively.

As it is shown in Figure 5 the PCs enhanced by the nonlinearity strongly affect the bunch tails reducing the beam lifetime.

## 6 CONCLUSIONS

Peak luminosities of  $10^{30} \text{ cm}^{-2}\text{s}^{-1}$  and of  $3.3 \cdot 10^{31} \text{ cm}^{-2}\text{s}^{-1}$  have been reached in single and multi-bunch mode respectively. Measurements and simulations have been performed in order to understand and control nonlinearities. The DAΦNE optics has been modified to reduce their impact on the luminosity performances.

The numerical simulations of beam-beam effects taking into account the measured cubic nonlinearities have shown that they have a strong effect on the collider luminosity performance, in agreement with experimental observations.

Experimentally it has been found that the negative sign for  $c_{11}$  is preferable, as in this case decoherence seems to play a stabilizing role for the beams. In agreement with simulations it has also been found experimentally that the nonlinearity strengths are acceptable for values below  $\approx [2 \cdot 10^2]$ .

The optimisation of the beam-beam performance with nonlinearities will be carried out when tunable octupoles will be installed on the two main rings next fall. Long term plans foresee major hardware modifications: wiggler nonlinearities are planned to be corrected by means of pole shimming.

## 7 REFERENCES

- [1] G.Vignola and DAΦNE Project Team, "DAΦNE, The Frascati Φ-factory", PAC93, Washington, 1993.
- [2] M.Preger for the DAΦNE Team, "Status of DAΦNE", HEACC2001, March 2001, Tsukuba, Japan.
- [3] S.Guiducci *et al.*, "Status report on DAΦNE", PAC01, Chicago, June 2001.
- [4] M.Zobov *et al.*, "Beam-Beam Experience at DAΦNE", PAC01, Chicago, June 2001.
- [5] C.Biscari, "Detuned Lattice for DAΦNE Main Rings", DAΦNE Technical Note L-32, Frascati, March 2001.
- [6] M.Boscolo, S.Bertolucci, C.Curceanu, S.Guiducci and G.von Holtey "Experience with beam induced backgrounds in the DAΦNE detectors" PAC01, Chicago, June 2001.
- [7] C.Milardi *et al.*, "Effects of nonlinear terms in the wiggler magnets at DAFNE", PAC01, Chicago, June 2001.
- [8] M. Zobov, "Crosstalk between beam-beam effects and lattice nonlinearities in DAΦNE", DAΦNE Technical Note G-57, Frascati, July 2001.
- [9] A.Drago and A.Stella, "A Dynamic Tracking Acquisition System for DAΦNE e+e- collider", to be published in Proc. Of DIPAC2001.
- [10] G.N. Kulipanov *et al.*, "The influence of chromaticity and cubic nonlinearity on the kinematics of betatron oscillations", Preprint INP 76-87, Novosibirsk 1976.
- [11] D.N.Shatilov, "Beam-Beam simulation at Large Amplitudes and Lifetime Determination", Part.Acc. 52,65 ('96).

# BEAM-BEAM SIMULATION STUDIES OF CESR-c AND OBSERVATIONS IN CESR

Joseph T. Rogers, Mark A. Palmer, and Antonella P. Romano, Laboratory of Nuclear Studies, Cornell University, Ithaca, NY 14853, USA

Christopher R. Jones, Department of Physics, University of Iowa, Iowa City, IA 52242, USA

## Abstract

CESR-c is a possible modification of CESR to operate in a beam energy range of 1.5 to 2.5 GeV for charm, QCD, and tau physics. Control of the horizontal emittance, energy spread, and synchrotron radiation damping at these low energies requires the installation of new wiggler magnets. We present the results of beam-beam simulations for CESR-c using the ODYSSEUS strong-strong simulation code. Evidence of a coherent beam-beam effect is seen.

## 1 CESR-c: AN $e^+e^-$ FACTORY FOR CHARM AND QCD PHYSICS

CESR-c is a proposed  $e^+e^-$  factory for charm and QCD physics based on CESR [1]. To be able to run at energies as low as 1.55 GeV and as high as the 5.3 GeV energy used by CESR for Y(4s) physics and synchrotron radiation, significant modifications of CESR are needed. These are:

- Replacement of the present permanent magnet IR quads with superconducting quads (including a short, vertically focusing permanent magnet nosepiece) to expand the operating energy range and lower  $\beta_y^*$  at the interaction point.
- An upgrade of the rf cavity complement to shorten the bunch length so that it is compatible with lower  $\beta_y^*$ .
- Installation of ~18 m of 2.1 Tesla wiggler magnets to control emittance and damping.

The control of horizontal emittance through the use of wiggler magnets is necessary to maintain a high bunch current without exceeding the maximum beam-beam parameter that the beams can tolerate. The luminosity, written in terms of horizontal emittance  $\epsilon_x$  and limiting beam-beam parameters  $\xi_x$  and  $\xi_y$ , is:

$$L = (1+r)^2 \frac{\pi f_c \gamma^2 \epsilon_x \xi_x \xi_y}{r_0^2 \beta_y^*}$$

where  $r = \sigma_y^*/\sigma_x^* \ll 1$ ,  $f_c$  is the collision frequency, and  $r_0$  is the classical electron radius.  $E$  is fixed by the high-energy physics requirements, and  $\xi_y$  and  $\xi_x$  are limited by beam dynamics in a way that's not fully understood. One wants to increase the number of bunches and decrease  $\beta_y^*$  as much as possible given the accelerator lattice and interaction region optics. The remaining parameter that can be changed is the horizontal emittance  $\epsilon_x$ , which should be increased as much as possible within the

constraints imposed by the physical and dynamic apertures.

The goals for manipulating synchrotron radiation effects are:

- to increase the horizontal emittance  $\epsilon_x$ ;
- to keep the energy spread  $\Delta E/E_0$  within tolerable limits; and
- to minimize the transverse damping time  $\tau_{y,x}$  to facilitate multi-turn injection.

Minimization of the transverse damping time may also be beneficial for  $\xi_y$ . A survey of past experience in many  $e^+e^-$  colliders suggests that a larger damping decrement is associated with a larger maximum beam-beam parameter. We used a particle-tracking simulation, described in the next section, to estimate the effect of damping decrement on  $\xi_y$ .

Some parameters of CESR-c are listed in Table 1.

Table 1: CESR-c and CESR parameters.

$E_0$ [GeV]	1.55	1.88	2.5	5.3
$L$ [ $10^{33} \text{ cm}^{-2} \text{ s}^{-1}$ ]	0.150	0.300	0.500	1.250
$i_{\text{bunch}}$ [mA/bunch]	2.8	4.0	5.1	8.2
$I_{\text{beam}}$ [mA/beam]	130	180	230	360
$\xi_y$	0.035	0.04	0.04	0.06
$\xi_x$	0.028	0.036	0.034	.028
$\Delta E/E_0$ [ $10^{-3}$ ]	0.75	0.81	0.79	0.67
$\tau_{y,x}$ [ms]	69	55	52	22
$B_{\text{wiggler}}$ [Tesla]	2.1	2.1	1.75	0
$\beta_y^*$ [cm]	1.0	1.0	1.0	1.8
$\epsilon_x$ [nm-rad]	230	220	215	205

## 2 BEAM-BEAM SIMULATION

### 2.1 Simulation Code: ODYSSEUS

ODYSSEUS [2,3] is a strong-strong beam-beam particle-in-cell code which includes longitudinal dynamics; and broadband and narrowband resonator wake fields.

Its speed has been optimized by:

- using different approximations for the electromagnetic field calculations in different parts of the beam (core vs. tails);
- using an adaptive mesh; and
- using FFT methods for the electromagnetic field calculation.



## 2.2 Benchmarking the Code with CESR at 5.3 GeV

Under simulation conditions that included only a perfectly linear lattice and no vertical radiation excitation, ODYSSEUS was used to simulate CESR at 5.3 GeV with its known operating parameters. Because there was no source of natural vertical emittance, the beam was allowed to find its own equilibrium vertical size due to the beam-beam effect.

The results of a  $7 \times 7$  tune scan are shown in Figure 1. The best operating point found in the simulation tune scan is nearly identical to the one used in CESR operation, and the maximum luminosity in the simulation ( $1.33 \times 10^{33} \text{ cm}^{-2} \text{ s}^{-1}$ ) is nearly the same as the observed maximum luminosity ( $1.3 \times 10^{33} \text{ cm}^{-2} \text{ s}^{-1}$ ).

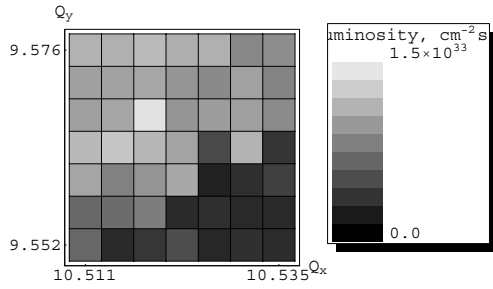


Figure 1. Simulation results: luminosity vs. tune in CESR at 5.3 GeV.

## 2.3 Simulation of CESR at 1.55, 1.89, and 2.5 GeV

The same code was used to simulate the equilibrium luminosity of CESR-c for the parameters of Table 1, at energies of 1.55, 1.89, and 2.5 GeV. The results of the tune scans are shown in Figures 2, 3, and 4.

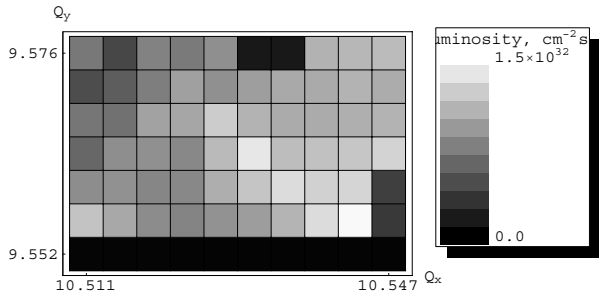


Figure 2. Simulation results: luminosity vs. tune in CESR-c at 1.55 GeV.

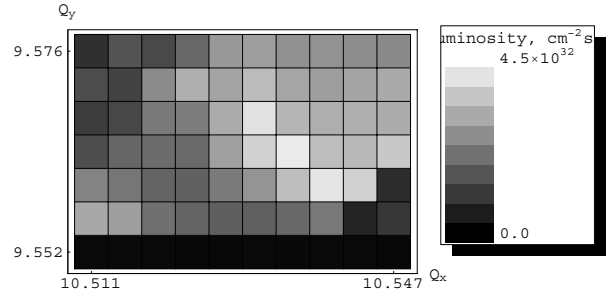


Figure 3. Simulation results: luminosity vs. tune in CESR-c at 1.89 GeV.

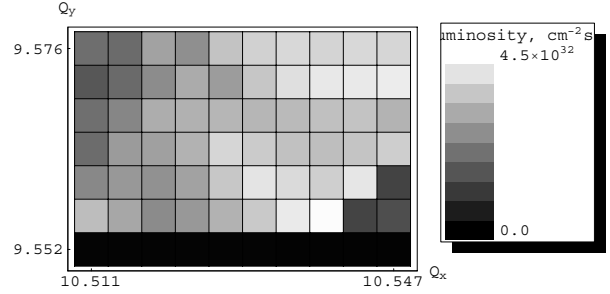


Figure 4. Simulation results: luminosity vs. tune in CESR-c at 2.50 GeV.

The regions of good luminosity in the tune plane are significantly different for these parameters than for the 5.3 GeV parameters. This is probably due to the difference in synchrotron tune, which is approximately twice as large for the low energy parameter sets as for the 5.3 GeV set. The dark horizontal band at the bottom of Figures 2, 3, and 4 appears to be due to a synchrotron resonance.

Table 2 summarizes the luminosity at best operating point for the four different energies. The luminosity indicated by the simulation is, in each case, similar to the luminosity goal in the parameter list of Table 1. The maximum achievable  $\xi_y$  appears to be very sensitive to the synchrotron tune (compare, for example,  $\xi_y$  for 1.89 GeV with that for 2.5 and 1.55 GeV). Further simulation is needed to determine the optimum value of all three tunes.

Table 2: Summary of simulation luminosity results.

$E$ (GeV)	$Q_s$	$I_{\text{bunch}}$ (mA)	$L$ ( $\text{cm}^{-2} \text{ s}^{-1}$ )	$\xi_y$
5.30	0.056	7.68	$1.33 \times 10^{33}$	0.060
2.50	0.104	5.10	$4.45 \times 10^{32}$	0.036
1.89	0.110	4.06	$4.13 \times 10^{32}$	0.055
1.55	0.105	2.82	$1.46 \times 10^{32}$	0.034

## 2.4 Effect of Damping Time

To investigate the effect of the transverse damping time on the maximum achievable beam-beam parameter  $\xi_y$ , we simulated the case of CESR-c at 1.89 GeV with a single 1.3 m wiggler rather than an 18 m set of wigglers. The simulation parameters are listed in Table 3, and the luminosity vs. tune plot for the long (320 ms) damping

time is shown in Fig. 5.

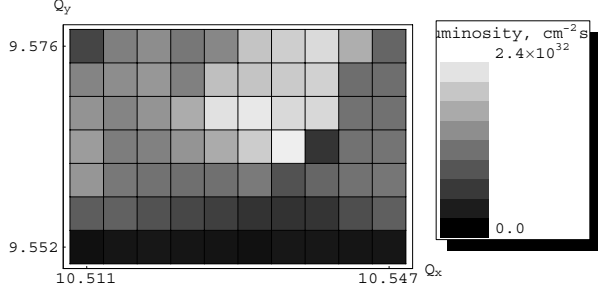


Figure 5. Simulation results: luminosity vs. tune in CESR-c at 1.89 GeV with a 320 ms transverse damping time.

Table 3: Simulation results: variation of damping time.

$E$ (GeV)	$\tau_{x,y}$ (ms)	$Q_s$	$I_{bunch}$ (mA)	$L$ (cm <sup>-2</sup> s <sup>-1</sup> )	$\xi_y$
1.89	55	0.110	4.06	$4.13 \times 10^{33}$	0.055
1.89	320	0.075	4.06	$2.23 \times 10^{32}$	0.030

The tune plane plots of Fig. 3 and Fig. 5 cannot be compared directly, because the synchrotron tunes are different. However, the maximum luminosity shows only a mild dependence on damping time. If the luminosity  $L$  has a power-law dependence on damping time  $\tau$ , then the simulation indicates  $L \propto \tau^{-0.35}$ .

### 3 IS THE BEAM-BEAM LIMIT A COHERENT OR INCOHERENT PHENOMENON?

In flat-beam  $e^+e^-$  colliders, the beam-beam parameter  $\xi_y$  tends to increase linearly with current until it reaches some limiting value, and then remains constant at higher current. Two alternative explanations are possible for this beam-beam limit. The first is that resonances caused by the nonuniformity of the beam-beam focusing produce an increase of the vertical amplitude of individual particles. The second explanation is that the beam-beam interaction couples the collective motion of both beams, and that some coupled modes of oscillation are unstable. It is not known whether the observed beam-beam limit is due primarily to single-particle (incoherent) or collective (coherent) instability. There is evidence from DCI [4] that the limiting  $\xi_y$  with charge neutralization is similar to that in other colliders. That observation favors coherent instability as the dominant mechanism for the beam-beam limit. We have examined the simulation results for CESR for evidence of a coherent instability.

#### 3.1 Flip-flop in the simulation results

Perhaps the most familiar type of coherent instability in circular colliders is the “flip-flop” effect, in which the equilibrium beam size of one beam shrinks while that of the other beam grows. Some of the regions of poor

luminosity in Fig. 1 are due to flip-flop. The ratio of the vertical beam size of the small beam to that of the large beam, for the simulation results of Fig. 1, is plotted in Fig. 6. Areas of severe flip-flop are adjacent to areas with good luminosity.

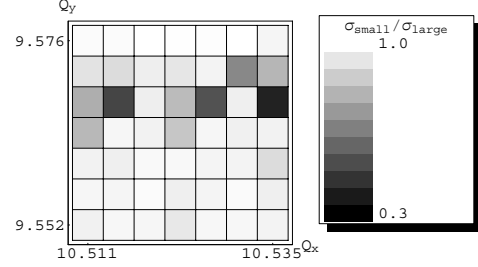


Figure 6. Simulation results: vertical beam size ratio  $\sigma_{y,small}/\sigma_{y,large}$  vs. tune in CESR at 5.3 GeV.

#### 3.2 Fluctuations in the simulation results

Figure 7 shows the vertical centroid of both beams vs. turn number for the simulation corresponding to CESR 5.3 GeV operating conditions. Because of the limited number of macroparticles ( $N_p = 5000$ ) used in the simulation, there must be a random root-mean-square fluctuation of the centroid  $y_{rms} = \sigma_y / \sqrt{N_p}$ . The actual fluctuation of the centroid in the simulation is 4.4 times larger, indicating a departure from random motion. The two beams are oscillating in phase (*i.e.*, in the  $\sigma$ -mode) with an oscillation amplitude much less than the vertical beam size. The power spectrum of the vertical centroid motion of one of the beams (Figure 8) shows a spike at the bare tune frequency, as expected for  $\sigma$ -mode oscillations.

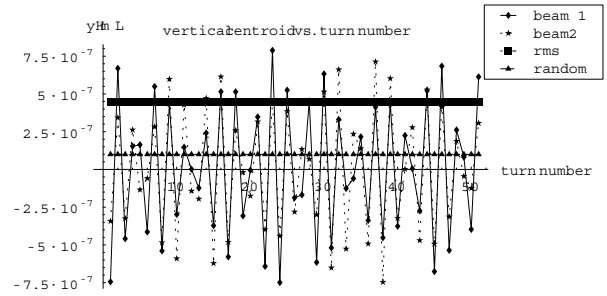


Figure 7. Simulation results: vertical centroid vs. turn number.

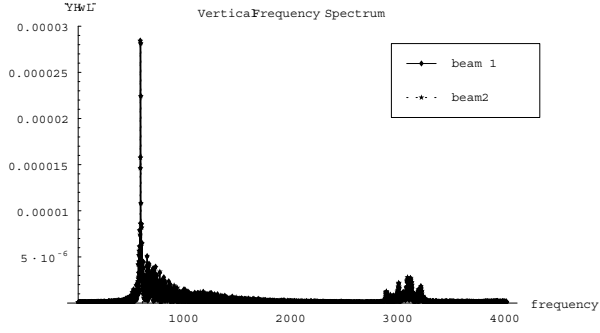


Figure 8. Simulation results: power spectrum of the vertical centroid motion.

### 3.3 Correlations in the Simulation Results

Figure 9 shows the amplitude of the vertical centroid motion of beam 1 and beam 2 for 60,000 turns, corresponding to 7 transverse radiation damping times. Initial random correlations must disappear after several damping times, so this strong correlation indicates that the oscillations are coherent.

Figure 10 shows the rate of change of the phase,  $(d\phi/dn)/2\pi$ , of the vertical oscillation of each beam. This quantity can be thought of as the instantaneous coherent tune of the oscillation. A Gaussian smoothing function of width  $\sigma_n = 200$  turns has been applied to this time series. The instantaneous tune is also very strongly correlated between beams and shows correlated brief jumps from one tune to another.

Plots of the instantaneous vertical tune *vs.* horizontal tune are shown in Figures 11 and 12. Figure 11 plots the same simulation results as Figs. 9 and 10, *i.e.*, CESR operating conditions. Excursions in the vertical and horizontal tune are visible, but are not obviously correlated with each other. Figure 12 shows the simulation output for a value of the tunes where the luminosity is low, but there is no flip-flop. The horizontal band at  $0.57 < Q_y < 0.58$  is due to strong vertical head-tail motion.

When plots of the tune space trajectories for a variety of bare machine tunes are superimposed, structure becomes evident. Fig. 13 shows the tune space trajectories (plotted as points) of the motion of the centroid of the beam for  $7 \times 7$  values of the bare tunes. The lines on the plot correspond to resonance conditions: the vertical, horizontal, and diagonal lines represent  $2Q_x - 2Q_y = n$ ,  $4Q_y - 6Q_x = n'$ , and  $4Q_x - Q_y + 6Q_y = n''$ , respectively. A horizontal band at  $Q_y \approx 0.574$  does not meet such a resonance condition. This line is due to vertical head-tail motion. The power spectrum of  $\langle yz \rangle$  for  $(Q_x, Q_y) = (0.519, 0.568)$  shown in Fig. 14 indicates a large head-tail amplitude.

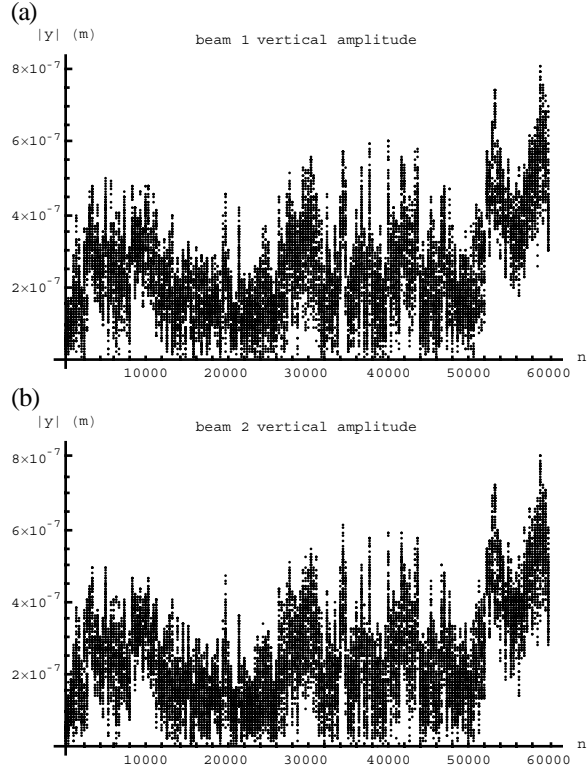


Figure 9. Simulation results: amplitude of the vertical centroid motion *vs.* turn number for (a) beam 1 and (b) beam 2.

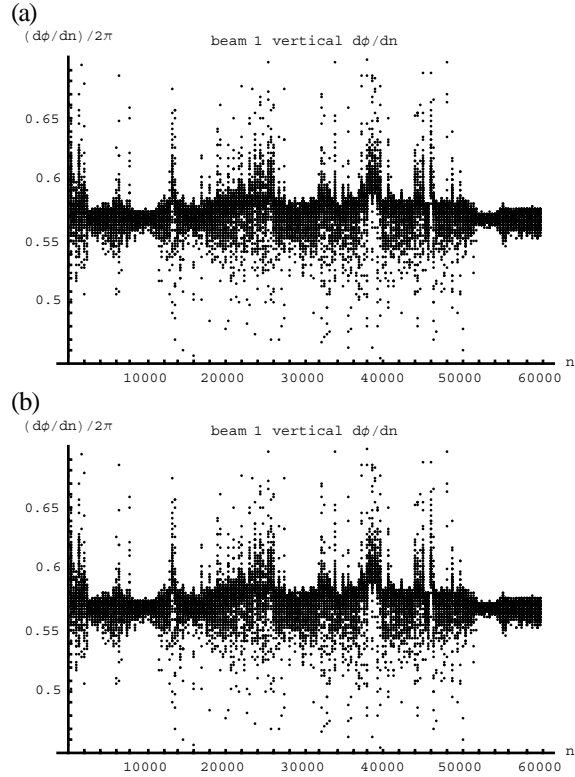


Figure 10. Simulation results:  $(d\phi/dn)/2\pi$  (instantaneous tune) of the vertical centroid motion *vs.* turn number for (a) beam 1 and (b) beam 2.

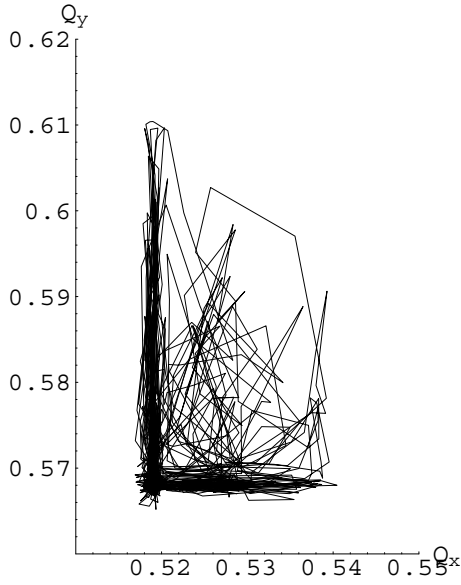


Figure 11. Simulation results: Tune space trajectory of the motion of the centroid of the beam for bare tunes  $(Q_x, Q_y) = (0.519, 0.568)$ .

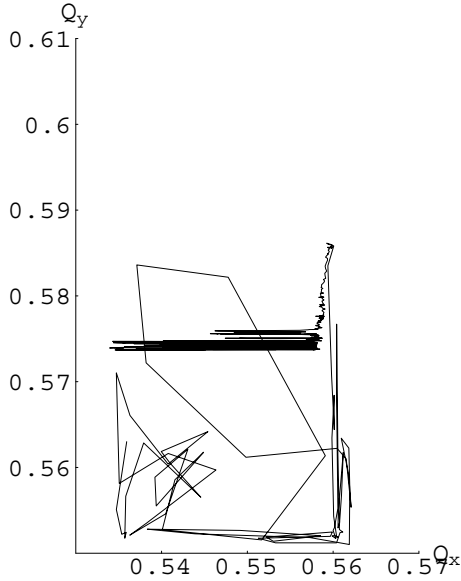


Figure 12. Simulation results: Tune space trajectory of the motion of the centroid of the beam for bare tunes  $(Q_x, Q_y) = (0.535, 0.552)$ .

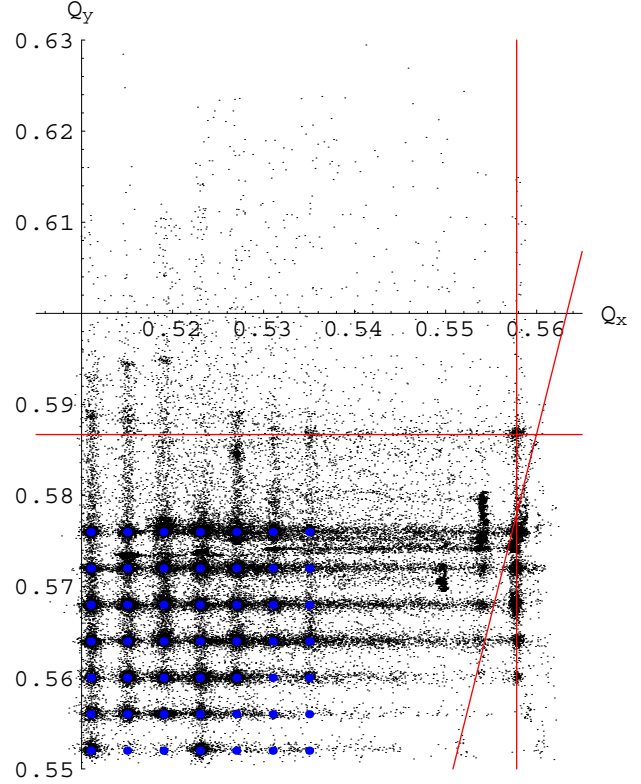


Figure 13. Simulation results: Superimposed tune space trajectories (plotted as points) of the motion of the centroid of the beam for  $7 \times 7$  values of the bare tunes.

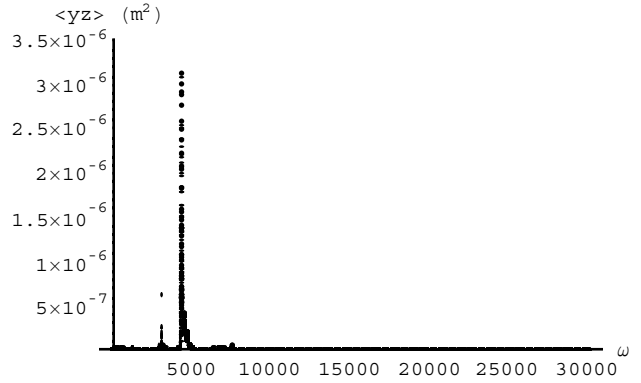


Figure 14. Simulation results: power spectrum of  $\langle yz \rangle$  for  $(Q_x, Q_y) = (0.519, 0.568)$ .

The observation that the simulated beam has low amplitude coherent oscillations leads us to a conjecture about the nature of the beam-beam limit for favorable tunes: the beams are neither stable (*i.e.*, subject only to single-particle dynamics), nor unstable (*e.g.*, undergoing oscillations comparable to the beam size), but instead are at the threshold of stability. That is, the beams seek a size where they are just on the edge of stability. Smaller beams would be unstable with a significant growth rate, and would grow. Larger beams are stable and would shrink due to radiation damping.

## 4 OBSERVATIONS IN CESR AT 5.3 GEV

### 4.1 Beam-Beam Performance

The luminosity achieved by CESR at 5.3 GeV was the result of a long-term program to improve beam-beam performance. Since both beams share the same vacuum chamber, they are separated electrostatically and cross at the interaction point with a  $\pm 2.3$  mrad angle. The history of the vertical beam-beam parameter in CESR can be summarized as:

- Head-on collisions, 2 interaction points:  $\xi_y \approx 0.02$
- Head-on collisions, 1 interaction point:  $\xi_y \approx 0.04$
- First 7-bunch crossing angle collisions:  $\xi_y \approx 0.03$
- First 9-bunch crossing angle collisions:  $\xi_y \approx 0.023$
- 45-bunch crossing angle collisions:  $\xi_y \approx 0.07$

In going from two interaction points to one, the beam-beam parameter (per interaction point) doubled. In going to 7-bunch collisions and then to 9-bunch collisions with a crossing angle, the effect of the large orbit displacement in and near the interaction region severely limited the beam-beam parameter. At the end of its 5.3 GeV operation, CESR operated with 9 trains of 5 bunches, each with a  $\xi_y$  that was three times as large as it was in the first 9-bunch collisions, even though the number of parasitic beam-beam interactions had increased. The improvement in  $\xi_y$  was due to:

- elimination of multipoles in the wigglers used for producing synchrotron radiation;
- improvement in operating point;
- reduction of the higher multipole fields of the sextupole magnets by altering the pole tips;
- improvement in the measurement and correction of betatron phase, local coupling, dispersion, and interaction point parameters (*e.g.*,  $\alpha^*$  and  $\beta^*$ );
- improvement in the distribution of sextupole magnet strengths;
- survey and alignment of quadrupole and dipole magnet rolls;
- rewiring of dipole magnet backleg windings to eliminate a skew sextupole moment.

Careful attention to the closed orbit, coupling,  $\beta$  function errors, operating point, interaction point errors and multipole errors resulted in a large increase in the beam-beam performance. CESR shows the typical behavior of a  $\xi_y$  that increases with current up to a maximum value, after which it no longer increases (see Figure 15 below) [5]. The fact that the beam-beam simulation code predicts the observed  $\xi_y$  in CESR may indicate that, at 5.3 GeV, CESR reached its limiting  $\xi_y$  for its choice of operating parameters.

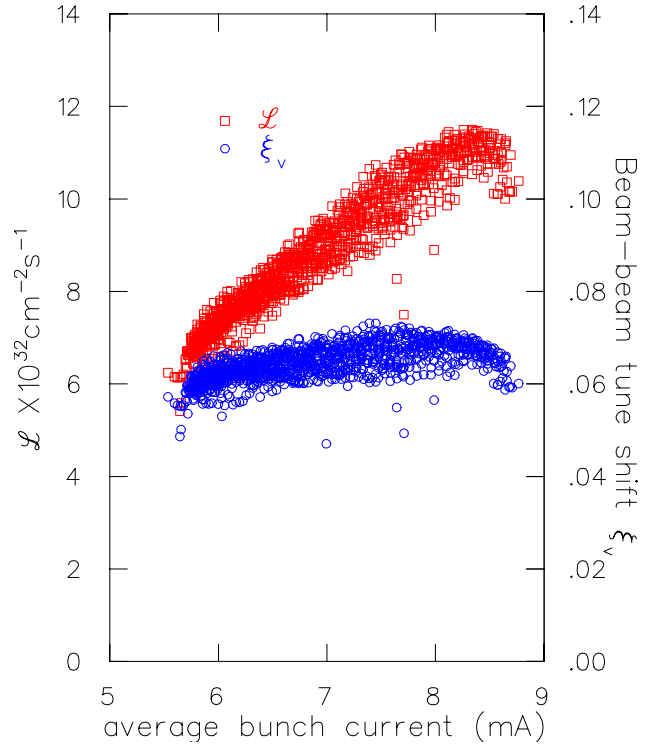


Figure 15. Luminosity and vertical beam-beam parameter  $\xi_y$  for high-energy physics operation at 5.3 GeV in CESR.

### 4.2 Long-Range Beam-Beam Interaction

In CESR, the beams share a single vacuum chamber, and are separated electrostatically to produce a “pretzel”. The long-range beam-beam interaction (LRBBI) causes closed orbit errors and tune shifts. The closed orbit and tune are different for different bunches, because the bunches are not uniformly spaced

The beams are vertically displaced in interaction region due to the helical orbit produced by the detector solenoid, so the LRBBI produces kicks with a vertical component. A significant differential vertical displacement of the bunches at interaction point results. The orbit and tune error is mostly due to parasitic collision points within interaction region. The calculated displacements and tune shifts [5] are shown in Figure 16.

The differential vertical beam displacements for each bunch, averaged over trains, have been measured in CESR. Figure 17 shows these displacements *vs.* time during a single run. Compensation of the differential vertical displacements has been attempted using a transverse feedback kicker as a feed-forward device, with partial success [6].

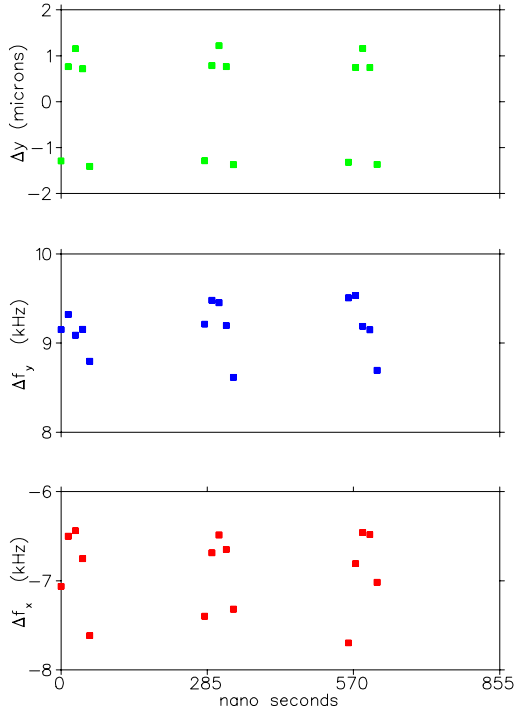


Figure 16. Calculated vertical beam displacement (at the interaction point) and tune shift due to LRBBI in CESR at 5.3 GeV.

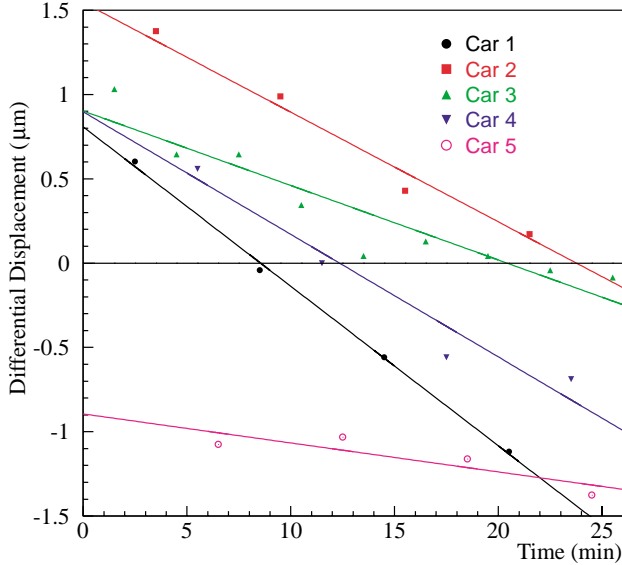


Figure 17. Measured vertical differential beam displacement vs. time in CESR at 5.3 GeV. The five sets of symbols represent the average over 9 trains of each car in the train.

### 4.3 Round-Beam Experiments

Electron storage rings tend to have flat beams, in which the horizontal emittance is much larger than the vertical emittance, because of synchrotron radiation excitation of the horizontal motion. By coupling the horizontal and vertical motion of the beam particles and making the horizontal and vertical beta functions equal at the interaction point, the beams may be made round in

collision. The luminosity of a collider with equal parameters for both (short) Gaussian beams is:

$$L[\text{cm}^{-2}\text{s}^{-1}] = 2.17 \times 10^{34} (1+r) \frac{\xi_y E[\text{GeV}] I[\text{A}]}{\beta_y^*[\text{cm}]}$$

where  $r = \sigma_y/\sigma_x$ ,  $\xi_y$  is the vertical beam-beam parameter,  $E$  is the beam energy,  $I$  is the current per beam, and  $\beta_y^*$  is the vertical beta function at the interaction point. For flat beams  $(1+r) \approx 1$ , but for round beams  $(1+r) = 2$ . From this geometric factor alone, one can gain a factor of 2 in luminosity with all other parameters being held the same. One might also expect that the limiting value of the beam-beam parameter would be higher for round beams than for flat beams, since round beams possess a greater degree of symmetry than flat beams and are immune to some of the resonances that affect flat beams.

Past experiments with resonantly coupled round beams in CESR [7, 8] demonstrated a beam-beam parameter  $\xi = 0.09$ , larger than the best beam-beam parameter ( $\xi_y = 0.07$ ) achieved with flat beams. The parameter set for one of these experiments is shown in Table 4. The single-bunch luminosity was small, because  $\beta^*$  was limited by the interaction region optics. The value of the beam-beam parameter was determined from the measured collision rate and from the beam-beam tune split, shown in Figure 18.

Table 4: Past round beam experiment parameters

parameter	value	
energy	$E$	5.30 GeV
horizontal $\beta$ function at IP	$\beta_x^*$	300 mm
vertical $\beta$ function at IP	$\beta_y^*$	300 mm
horizontal tune	$Q_x$	10.77
vertical tune	$Q_y$	9.77
h emittance (uncoupled)	$\epsilon_{x,\text{unc.}}$	124 nm
emittance (coupled)	$\epsilon_x, \epsilon_y$	62 nm
beam-beam parameter	$\xi_x, \xi_y$	0.09, 0.09
bunch current	$I_b$	22 mA
single-bunch luminosity	$L$	$1.0 \times 10^{31} \text{ cm}^{-2}\text{s}^{-1}$

Another approach to round beams is the Möbius lattice of Talman [9]. The Möbius lattice uses a set of skew quadrupoles to exchange vertical and horizontal degrees of freedom at one point in the ring. Horizontal oscillations become vertical at this point and horizontal again after a second turn. In this way the vertical and horizontal emittances become exactly equal. The Möbius ring has the unusual property of possessing a single transverse tune.

A skew quadrupole Möbius section was set up opposite the interaction point in CESR. The single tune was demonstrated and portions of tune plane mapped, but problems from the sextupole distribution, injection, and aperture prevented achieving significant luminosity.

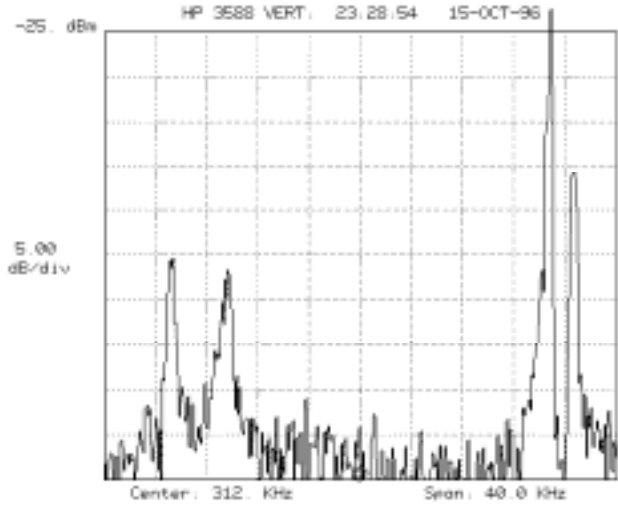


Figure 18. Spectrum analyzer plot of the tunes of resonantly coupled round beams in CESR. The two  $\sigma$ -modes are at the left and the two  $\pi$ -modes are on the right.

## 5 PLANS FOR FUTURE WORK

### 5.1 Simulation

We plan to incorporate the nonlinear lattice and the long-range beam-beam interaction into ODYSSEUS via calls to BMAD [10], a particle-tracking code. We plan to determine as cleanly as possible the effect of synchrotron radiation damping rate on  $\xi_y$  by running simulations where the tunes and beam geometry parameters are held fixed while the damping times are changed. We also plan to simulate the effect of unequal electron and positron tunes on  $\xi_y$ .

### 5.2 Experiments

The superconducting/permanent magnet interacting region magnets recently installed in CESR will make it possible to conduct round-beam experiments with  $\beta_x^* = \beta_y^* = 30$  mm, an order of magnitude smaller than in the past CESR experiments. The experiment parameters are listed in Table 5:

Table 5: Future round beam experiment parameters.

parameter		value
energy	$E$	1.88 GeV
solenoid field	$B$	1.0 T
horiz. $\beta$ function at IP	$\beta_x^*$	30 mm
vertical $\beta$ function at IP	$\beta_y^*$	30 mm
horizontal tune	$Q_x$	8.75
vertical tune	$Q_y$	9.75
h emittance (uncoupled)	$\epsilon_{x,unc.}$	52.8 nm
emittance (coupled)	$\epsilon_x, \epsilon_y$	26.4 nm
beam-beam parameter	$\xi_x, \xi_y$	0.10, 0.10
bunch current	$I_b$	2.76 mA
single-bunch luminosity	$L$	$0.76 \times 10^{31} \text{ cm}^{-2} \text{ s}^{-1}$

Superconducting quadrupoles Q1 and Q2 will have their polarities reversed so that they become horizontally focusing and vertically focusing, respectively. Together with the vertically focusing permanent magnet quadrupole, they comprise a triplet, with a small  $\beta^*$  in both transverse planes. The optics in the arcs of the machine together with the existing electrostatic separators can support a seven-bunch pretzel with zero crossing angle at the interaction point. The aperture will accommodate particles out to  $12 \sigma_{x,y}$  when the emittances are four times the nominal coupled emittance of 26.4 nm, and the long-range beam-beam interaction will allow bunch currents up to four times the nominal bunch current of 2.76 mA.

A second set of experiments will use the CESR-c damping wigglers to increase the emittance, and thus the bunch current, by a factor of four, maintaining the same beam-beam parameter. With seven bunches in CESR-c, a luminosity of  $2.1 \times 10^{32} \text{ cm}^{-2} \text{ s}^{-1}$  is expected. This luminosity is nearly that which we expect with flat beams ( $L = 3.0 \times 10^{32} \text{ cm}^{-2} \text{ s}^{-1}$ ), but the specific luminosity  $L/I_{tot}$  would be a factor 1.6 higher than with flat beams. Perhaps more importantly, the round beam optics relaxes the requirement for small bunch length imposed by the “hourglass effect” while maintaining high luminosity. In the example given,  $\beta_y^*$  is 3 times larger for round beams than for flat beams, and the required bunch length would be a factor of 3 longer. This allows a very large relaxation of impedance and accelerating voltage requirements compared with flat beam operation.

We plan to operate CESR at low energy without and with damping wigglers to study beam-beam behavior as the damping decrement is varied, and to further benchmark ODYSSEUS code.

## ACKNOWLEDGMENTS

We gratefully acknowledge the contributions of the members of the CESR Operations Group to this work. This work was supported by the National Science Foundation.

## REFERENCES

- [1] D. Rice *et al.*, “Parameters for Low Energy Operation of CESR”, to be published in Proc. 2001 Particle Accelerator Conf., Chicago (2001).
- [2] E.B. Anderson, T.I. Banks, and J.T. Rogers, Proc. 1999 Particle Accelerator Conf., New York (1999) 1686.
- [3] E.B. Anderson, Ph.D. dissertation, Cornell University (1998).
- [4] J. LeDuff *et al.*, Proc. 11th International Conference on High Energy Accelerators (1980) 707.
- [5] D.L. Rubin *et al.*, “CESR Status and Performance”, to be published in Proc. 2001 Particle Accelerator Conf., Chicago (2001).
- [6] D. Sagan, M. Billing, and M. Palmer “Effect on Luminosity from Bunch-to-Bunch Orbit Displacements at

CESR”, to be published in Proc. 2001 Particle Accelerator Conf., Chicago (2001).

[7] E. Young *et al.*, Proc. 1997 Particle Accelerator Conference, Vancouver (1997) 1542.

[8] E. Young, Ph.D. dissertation, Cornell University (1998).

[9] R. Talman, Phys. Rev. Lett. **74** (1995) 1590.

[10] D.L. Rubin and D. Sagan, “CESR Lattice Design”, to be published in Proc. 2001 Particle Accelerator Conf., Chicago (2001).



# EXPERIMENTAL STUDIES OF BEAM-BEAM EFFECTS AT VEPP-2M

P.M. Ivanov, I.N. Nesterenko, E.A. Perevedentsev, Yu.M. Shatunov, A.A. Valishev  
Budker Institute of Nuclear Physics, Novosibirsk, 630090, Russia

## Abstract

In this work we present the last experimental results of coherent dipole synchro-betatron beam-beam modes observation at the VEPP-2M storage ring, flip-flop phenomena and so-called dynamic beta effect. Experimental results are compared with analytical and numerical models. A split of coherent beam-beam modes related to the beam-beam parameter is evaluated. An influence of the bunch length and beta-function at IP on the flip-flop phenomena and the dynamic beta effect is discussed.

## 1 OBSERVATION OF THE DYNAMIC BETA EFFECT FOR VARIOUS BUNCH LENGTHS.

In the first approximation the beam-beam interaction can be considered as an additional focusing lens which perturbs the initial lattice functions of a storage ring. The distortion of the lattice function results in reduction of the beam life time and essentially influences the background loading of the detector. The influence of dynamic beta effect on CESR operation has initiated a series of papers [1, 2], in which the feasible methods of this effect reduction are discussed. Distortion of the storage ring lattice functions leads to change in the beam emittance generation conditions. Therefore it is necessary to take this effect into consideration in simulation of the beam-beam interaction and provide dynamic perturbation of the emittance in the presence of counter-beam as well as correct generation of its initial value. Paper [3] gives analytical calculation of this effect.

In this work the experimental results of the dynamic beta effect observation at different bunch lengths and  $\beta$ -functions at IP are presented. They were received at the VEPP-2M collider (Novosibirsk) [4] in summer, 2000. A computer simulation of this effect for various values of the parameter  $\sigma_s/\beta^*$  (ratio of the longitudinal bunch size to the  $\beta$ -function at IP) has been carried out and the results have been compared to the experiment.

### 1.1 Basic formulae

For particles with small betatron oscillation amplitudes ( $< \sigma$ ,  $\sigma$  being the Gaussian beam size) the opposite bunch can be considered as a focusing lens with the gradient which depends only on longitudinal coordinate  $s$ :

$$g_{x,y}(s) = g_{x,y}^* \cdot \exp\left(-\frac{s^2}{2\sigma_{eff}^2}\right) / \sqrt{1 + \frac{s^2}{\beta_{x,y}^{*2}}}. \quad (1)$$

Here  $\sigma_{eff} = \sigma_s/2$  is the effective length of beam-beam interaction region. Exponential dependence results from the Gaussian distribution of particles in a bunch and the term  $\sqrt{1 + s^2/\beta_{x,y}^{*2}}$  is related to the change of vertical/horizontal beam size caused by the  $\beta$ -function variation in experimental straight section. Coefficient  $g_{x,y}^*$  is derived from the normalizing condition:

$$\oint \beta_{x,y}(s) \cdot g_{x,y}(s) ds = 4\pi\xi_{x,y}, \quad (2)$$

$\xi_{x,y}$  is the beam-beam space charge parameter.

Calculation of the  $\beta$ -function distortion in the storage ring VEPP-2M has been done using the RING code. The beam was sliced in longitudinal direction in 30 parts (lenses) with equal lengths. The gradient value in each lens varied vs. its position relative to the IP according to the formula (1). The  $4 \times 4$  matrix which transforms the betatron coordinates through a slice has a block-diagonal structure:

$$\begin{pmatrix} G_x & 0 \\ 0 & G_y \end{pmatrix}.$$

Here  $G_{x,y}$  are  $2 \times 2$  matrices of the focusing quadrupole lens.

### 1.2 Experimental results

The vertical beam size was measured by digital cameras with linear CCD-sensor, one for the positron bunch and two for the electron bunch. One of the electron cameras was located in a place similar to the positron camera (the  $\beta$ -function value and the betatron phase with respect to IP). The betatron phase between the observation and interaction points equals to  $\pi/2$ . Another electron camera was located in an additional place with the betatron phase difference with respect to IP equal to  $\pi$  (Fig. 1).

If the beam size is measured in two proper points (with the betatron phases difference of  $\pi/2$ ) then it is possible to receive information about the space charge parameter  $\xi$  value without any external influence on the beam.

Observations were carried out at the beam energy  $E=392$  MeV in strong-weak operation mode. The positron beam always had greater current. Such option eliminates possible additional focussing of electrons due to the presence of ion clouds. The electron beam current value was considered small if relative change of the strong positron beam size was less than 10%.

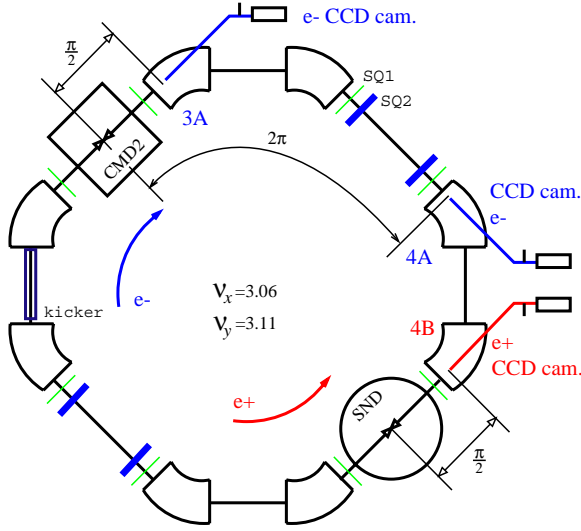


Figure 1: Layout of the experiment. SQ1 (8 thin green lines) is the family of skew-quadrupoles for the betatron coupling compensation. SQ2 (4 thick blue lines) is the family of skew-quadrupoles for creating dispersion function in bending magnets. CMD2 and SND are particle detectors.

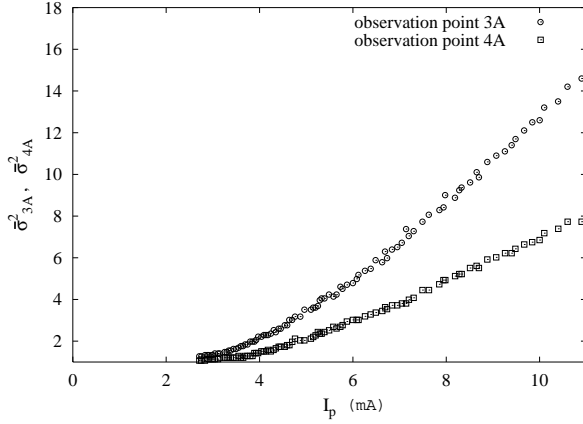


Figure 2: Normalized sizes of the electron beam at two observation points vs. the positron beam current.

We have chosen the following ratio as the value describing dynamic beta effect:

$$\frac{\tilde{\sigma}_{3A}^2 / \sigma_{3A}^2}{\tilde{\sigma}_{4A}^2 / \sigma_{4A}^2} = \frac{\tilde{\beta}_{3A} / \beta_{3A}}{\tilde{\beta}_{4A} / \beta_{4A}}.$$

Here  $\sigma_{3A}$ ,  $\sigma_{4A}$ ,  $\beta_{3A}$ ,  $\beta_{4A}$  are the electron beam sizes and beta-functions in the absence of positron beam at observation points 3A, 4A, accordingly, and  $\tilde{\sigma}_{3A}$ ,  $\tilde{\sigma}_{4A}$ ,  $\tilde{\beta}_{3A}$ ,  $\tilde{\beta}_{4A}$  are these values with the presence of the positron beam. This ratio does not depend any more on the beam emittance and can describe the "clean" dynamic beta effect. Normalization on  $\sigma_{3A}^2 / \sigma_{4A}^2$  is done for equal scaling of all results.

In Fig. 2 the normalized beam sizes vs. the positron

beam current are shown. The beam size in 4A observation point grows regardless of the fact that  $\delta\beta_{4A}$  (distortion of  $\beta$ -function) is negative. This fact shows that the beam emittance growth is much more than dynamic distortion of the  $\beta$ -function at this point.

Ratio  $\sigma_s / \beta^*$  is the key parameter influencing the dynamic distortion of storage ring lattice functions. It is possible to provide various values of this parameter in two ways:

- by regulating voltage of the accelerating RF field
- by changing value of the  $\beta$ -function at IP.

We used both ways of this parameter variation to expand the range of its accessible values.

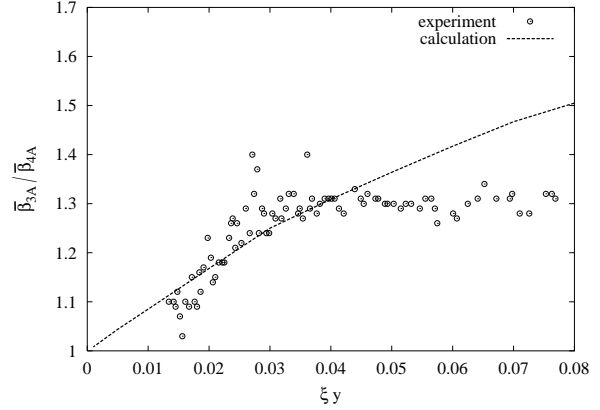


Figure 3: Ratio of the dynamic  $\beta$ -functions at two observation points (3A and 4A in Fig. 1) vs. the beam-beam parameter  $\xi$ . Initial  $\beta_{3A} / \beta_{4A} = 2.0$ , ratio of the longitudinal size and beta-function at the IP ( $\sigma_s / \beta^*$ ) was 1.2. Relative beta distortion at the IP ( $\delta\beta^* / \beta^*$ ) at  $\xi = 0.08$  was 0.31.

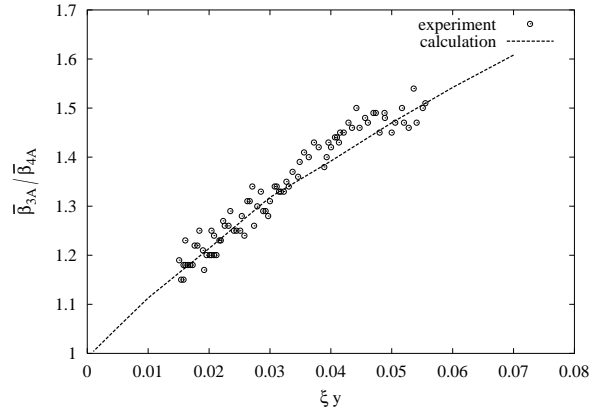


Figure 4: Ratio of the dynamic  $\beta$ -functions at two observation points vs. the beam-beam parameter  $\xi$ . Initial  $\beta_{3A} / \beta_{4A} = 2.0$ ,  $\sigma_s / \beta^* = 0.5$ ,  $\delta\beta^* / \beta^* = 0.36$ .

In Figs. 3, 4, 5, 6 the experimental data and the numerical calculation results of the dynamic beta effect for some

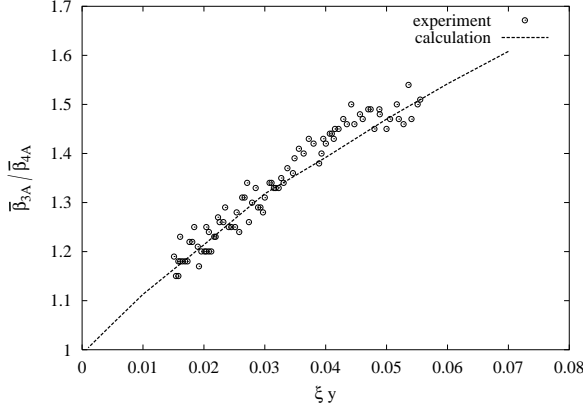


Figure 5: Ratio of the dynamic  $\beta$ -functions at two observation points vs. the beam-beam parameter  $\xi$ . Initial  $\beta_{3A}/\beta_{4A} = 1.6$ ,  $\sigma_s/\beta^* = 1.0$ ,  $\delta\beta^*/\beta^* = 0.29$ .

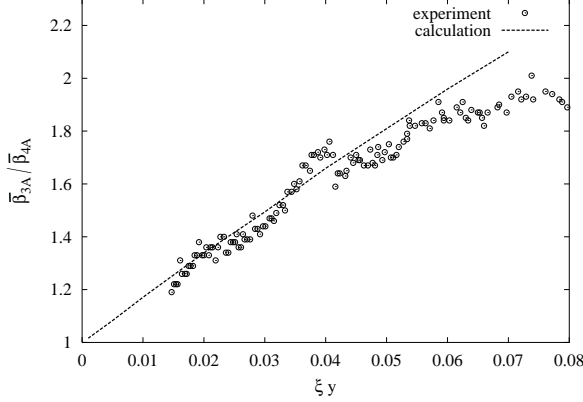


Figure 6: Ratio of the dynamic  $\beta$ -functions at two observation points vs. the beam-beam parameter  $\xi$ . Initial  $\beta_{3A}/\beta_{4A} = 1.6$ ,  $\sigma_s/\beta^* = 0.4$ ,  $\delta\beta^*/\beta^* = 0.35$ .

typical values of parameter  $\sigma_s/\beta^*$  and two different values of the  $\beta^*$ -function at IP ( $\beta^* = 4.2$  cm and  $\beta^* = 4.8$  cm) are demonstrated. Satisfactory agreement of the simulation results with received experimental data is observed. Visible deviations of the simulation from the experimental data in Fig. 3 in the range of high  $\xi$  are apparently connected with the nonlinearity of the beam-beam interaction which is not taken into account in simulation. Distinctions revealed in the experimental dependencies of the dynamic beta effect require further interpretation. In the future it is planned to compare the experimental data with results of strong-weak beam-beam simulation codes.

## 2 FLIP-FLOP PHENOMENON OBSERVATION.

Typically the beam-beam interaction at modern colliders results in the vertical beam size increase with the growth of counter beam current. Sometimes an essential difference

in vertical size of the counter-bunches is observed even at equal bunch intensities (the so-called “flip-flop” effect). In this case one bunch has the size close to the initial one while the other is much greater. If an external perturbation is applied the bunch sizes may interchange. The flip-flop effect appears only at bunch intensities exceeding some threshold value. In paper [5] the phenomenological model of the flip-flop effect is investigated. Using the given model it is possible to predict the appearance and the threshold value for the flip-flop effect.

In this work a comparison of the phenomenological model with experimental data is presented. The experimental data were received at VEPP-2M in summer, 2000. The effect of two different conditions of the vertical emittance buildup on the flip-flop stability is considered. It is shown that the non-resonant generation of the vertical emittance (i.e. by excitation of the vertical dispersion in bending magnets) permits to increase the blowup threshold in comparison with the mode when the emittance is determined by coupling of vertical and horizontal betatron oscillations or by vicinity of the betatron tune to coupling resonance.

### 2.1 Phenomenological model of the flip-flop effect.

To predict a possibility and conditions of the flip-flop appearance we consider properties of the self-consistent solution for the system:

$$\begin{cases} \sigma_p = f(\xi_e) \\ \sigma_e = f(\xi_p) \end{cases} \quad (3)$$

Here each equation describes change of the vertical beam size vs. the space charge parameter of the counter bunch  $\xi$  in strong - weak operation mode. It is assumed that  $\xi$  depends on current ( $I$ ) and size ( $\sigma$ ) of the counter bunch at IP. Thus the equations (3) can be rewritten in the following way (with equal beam currents):

$$\begin{cases} \sigma_p(I) = f(I, \sigma_e(I)) \\ \sigma_e(I) = f(I, \sigma_p(I)) \end{cases} \quad (4)$$

The obvious solution of system (4) is the solution with equal sizes  $\sigma_p(I) = \sigma_e(I)$ . In the case when  $\partial f/\partial \sigma > 1$  the solution with equal sizes becomes unstable. The threshold current value can be found from condition  $\partial f(I^*, \sigma)/\partial \sigma = 1$ , where we denote  $\sigma = \sigma_p(I^*) = \sigma_e(I^*)$ .

### 2.2 Experimental results.

For observation of the flip-flop effect the diagnostics system described in section 1.2 was used. Measurements were carried out in two different modes of the vertical emittance buildup. These optics modifications were created as follows:

1. The initial optics with minimally possible betatron coupling  $\epsilon_y/\epsilon_x < 0.01$  and vertical dispersion function  $\eta_y \approx 0$  was tuned. This optics then was a basis for modes described in items 2 and 3.

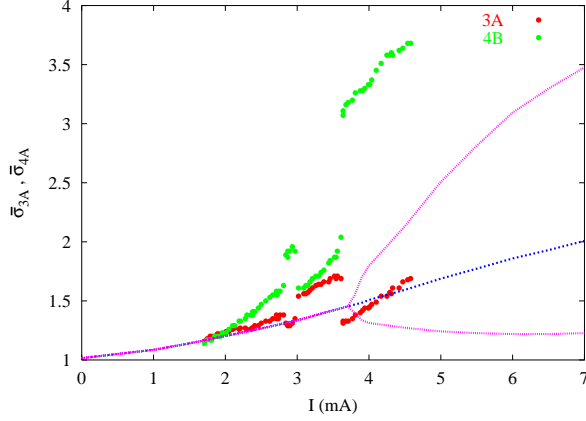


Figure 7: Normalized size at two observation points vs. the beam current, simulation and experiment. Resonant vertical emittance forming.

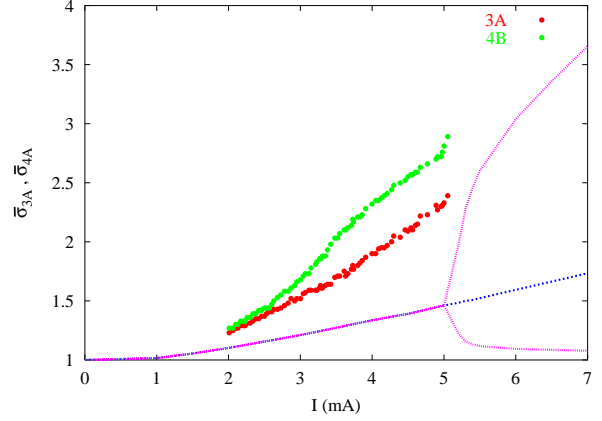


Figure 8: Normalized size at two observation points vs. the beam current, simulation and experiment. Non-resonant vertical emittance forming.

2. The optics with vertical dispersion  $\eta_y \neq 0$  in bending magnets was created using skew-quadrupole family SQ2 (see Fig. 1) without excitation of the betatron coupling. This way of vertical emittance buildup is named *non-resonant*.
3. The optics with vertical emittance equal to one in the previous mode was done using another skew-quadrupole family SQ1. In this case the emittance was generated only due to betatron coupling and without excitation of  $\eta_y$ .

Equality of vertical emittances in the two optics was controlled by monitoring the vertical beam size without the counter beam with CCD cameras.

Experimental dependencies of the beam size vs. the colliding beam current received in two optics modifications in strong-weak mode were used for generation of system (4). The received system of equations was solved numerically.

In Figs. 7, 8, the experimental data and numerical solutions of the system (4) are presented at the two different options of emittance generation. In the resonant case at currents higher than 3.6 mA the flip-flop effect is observed. The threshold predicted by the phenomenological theory coincides well with the observed in experiment. In the non-resonant regime the flip-flop threshold is essentially increased.

Although the phenomenological theory is in good agreement with the experiment in prediction of the threshold intensity value the self-consistent solution itself shows an essential difference with experimental dependencies obtained in strong-strong mode. The theory does not explain why optics with non-resonant vertical emittance formation is more robust to flip-flop. The obtained experimental data show the preference of non-resonant optics for circular colliders, especially for round beam operation.

### 3 OBSERVATION OF COHERENT SYNCHRO-BETATRON BEAM-BEAM MODES.

Among the beam-beam phenomena there is a large group of effects concerning the coherent motion of colliding bunches [6]-[9]. It has been recently proposed that a finite length of colliding bunches can lead to the coupling of synchro-betatron modes in the beam-beam system (Fig.9) and affect the beam stability [10]. However, there was no experimental evidence of existence of such modes at the present colliders. This paper gives an outline of the theory and presents the experimental investigation of the synchro-betatron beam-beam modes at the VEPP-2M collider, comparing the measured data with theoretical predictions.

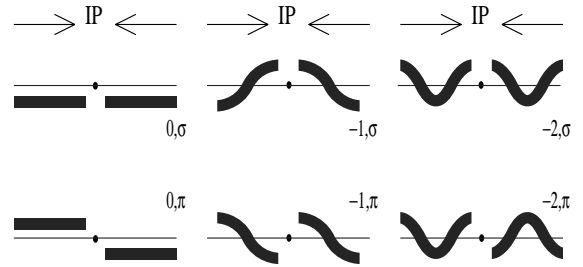


Figure 9: Naming convention for the synchro-betatron beam-beam modes.

#### 3.1 Theory: Mode Spectrum

The dipole motion of bunches, coupled via the beam-beam force can be expressed in terms of coherent synchro-betatron modes. Usually the betatron coupling between the transverse degrees of freedom is small, and therefore a separate treatment of horizontal and vertical synchro-betatron oscillations is a good approximation. Since the rise time of

the head-tail instability is much shorter than the radiation damping time in  $e^+e^-$  machines, we can drop the radiative effects in what follows.

For the case of small betatron oscillation amplitudes it is often allowable to linearize the transverse force exerted by the beams on each other. This linearized beam-beam interaction is considered here.

We study the dipole moments as functions of the longitudinal position in the bunch. Discrete approximation of the appropriate eigen-functions allows to reduce the task to linear algebra.

We use the so-called “hollow beam” model. It assumes that all particles of the bunch have equal synchrotron amplitudes and are evenly spread over the synchrotron phase, forming a circle in the synchrotron phase space. This circle is divided into  $N$  mesh elements, each characterized by its transverse dipole moment (2 variables) and its number corresponding to its synchrotron phase. In the arcs synchro-betatron oscillations of the elements forming a bunch are represented by the  $2N \times 2N$  matrix  $M = C \otimes B$ , where  $\otimes$  denotes the outer product,  $B$  is the betatron oscillation matrix of dimension  $2 \times 2$ ,  $C$  is the  $N \times N$  circulant matrix [11], which transports the dipole moment around the circle formed by the mesh elements with fixed synchrotron phases and thus performs a synchro-betatron mapping of  $2N$  variables for each of the colliding bunches.

The linearized beam-beam interaction is described by a  $4N \times 4N$  matrix  $M_{bb}$  consisting of consecutive short kicks and drifts between interactions of macroparticles sitting in each mesh, and assumed to be transversely-rigid Gaussian disks [7].

The complete one-turn matrix is the product of the arc matrix  $M$  and the beam-beam matrix  $M_{bb}$ . Its  $\xi$ -dependent eigenvalues and eigenvectors completely characterize the synchro-betatron modes of the beam-beam system and can be obtained numerically using a computer algebra system [12], see an example in Fig.10.

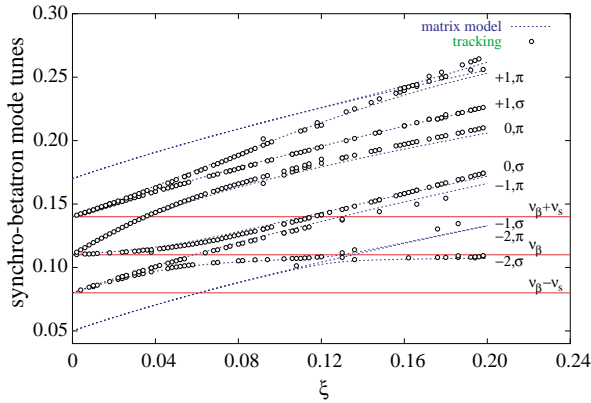


Figure 10: Synchro-betatron mode tunes vs. the beam-beam parameter  $\xi$ . Comparison of the circulant matrix model and tracking. Equal bunch intensities,  $\nu_\beta = 0.11$ ,  $\nu_s = 0.03$ , and the bunch length is  $0.7\beta^*$ .

### 3.2 Observation techniques

Vertical coherent oscillations of the bunches were observed using the beam synchrotron radiation from the dipoles. The optical image of the beam was focused into the movable screen plane (Fig. 11). The screen was cutting off a portion of the light in the beam image plane. For a fixed edge position, a displacement of the beam centroid resulted in modulation of the light flux.

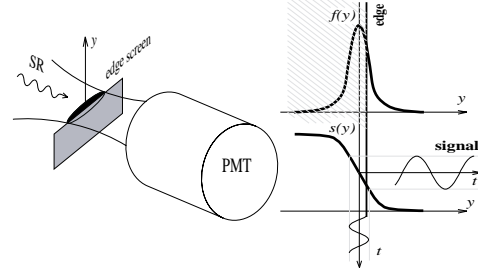


Figure 11: Edge detector scheme.

The light which passed through the optical system then fell on the PMT (Fig. 12). The PMT signal, with modulation proportional to the beam displacement, was fed to the fast ADC input. In our system we used the CAMAC-standard 8-bit ADC with the 8k read buffer and minimum transform time of 10 ns. The PMT bandwidth was adjusted to observe separate turns of the bunch in the storage ring. The ADC clock rate was exactly equal to the beam revolution frequency and the phase was locked to the RF phase of the bunch. Timing of the ADC start with the high voltage beam excitation pulse was performed using the multichannel time interval generator (TIG in Fig.12): the TIG trigger signals were passed to both the ADC and the HV generator.

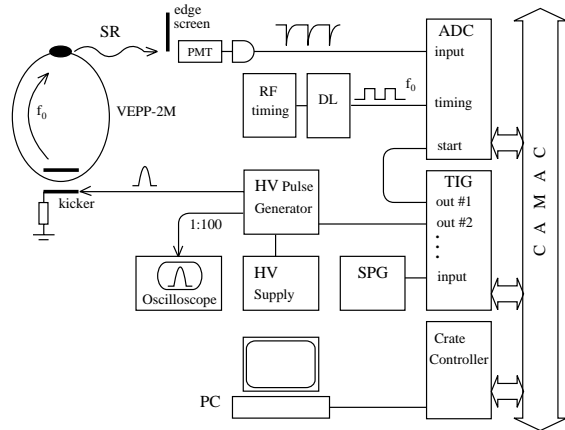


Figure 12: Block diagram of the experimental setup.

The similar observation channel was implemented for the positron beam. For synchronization of the electron and

positron channels the clock pulse splitter was used with the delay correction tuned by means of the additional cable in the positron channel.

The HV pulse generator gave a one-turn kick to the bunch, with an adjustable amplitude of the excited oscillations. A minimum amplitude was equal to  $0.2\sigma$ ,  $\sigma$  being the Gaussian vertical beam size. The kicker plate terminated in a matched load, to kick only the electron bunch.

### 3.3 Experimental results

The center of mass positions of the colliding bunches were sampled turn-by-turn. The Fourier transform of the collected data gave the coherent mode spectrum, where the proposed synchro-betatron modes of the beam-beam system were experimentally detected, and their spectrum was measured as a function of the beam-beam parameter at different synchrotron tunes.

The complete results of the coherent beam-beam mode spectra calculation with the account of the finite bunch length are presented in [10, 12]. Since VEPP-2M had a negligible transverse impedance, we compare these experimental data with the simulation results for the case where the collective interaction is completely due to beam-beam. Fig.13 shows the dependence of the measured and calculated synchro-betatron mode tunes on the beam current for equal electron and positron bunch intensities.

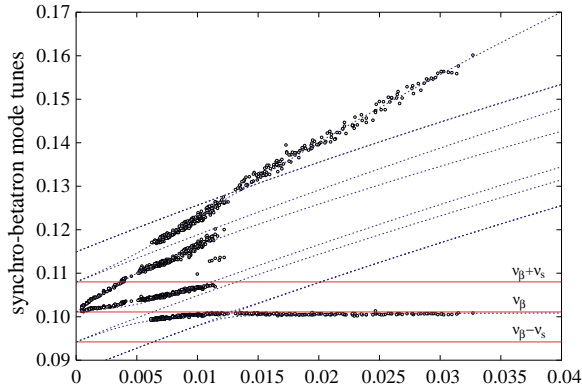


Figure 13: Measured(circles) and calculated (lines) synchro-betatron mode tunes vs the beam-beam parameter  $\xi$ . VEPP-2M was operated with one  $e^+$  and one  $e^-$  bunches colliding at two IPs,  $\nu_\beta = 0.101$ ,  $\nu_s = 0.0069$ ,  $\beta^* = 6$  cm, and the bunch length was 3.5 cm.

In perfect agreement with the theoretical model, the measurement has shown that besides the leading  $\sigma$  and  $\pi$  modes a number of synchro-betatron modes coupled via the beam-beam force exist in the dipole mode spectrum. These modes show up and disappear with the beam current change due to  $\xi$ -dependence of the beam-beam mode eigen-states. For the  $\xi$  value less than the synchrotron tune  $\nu_s$ , the state excited with the kick consists of only two beam-beam modes,  $\sigma$  and  $\pi$ , with the synchrotron

wavenumber  $m = 0$ . In the range  $\nu_s < \xi < 2\nu_s$  the initial condition is the combination of four eigenmodes:  $-1\sigma$ ,  $0\sigma$ ,  $0\pi$ ,  $+1\pi$ . Here the first index labels the synchrotron wavenumber, the second labels the coherent beam-beam eigenmodes with even and odd symmetry between the two colliding bunches, respectively. With larger  $\xi$  the dipole moment passes on to  $-2\sigma$ ,  $+2\pi$  and later to  $-3\sigma$ ,  $+3\pi$   $\sigma$  modes. Because of small coupling of modes with large synchrotron wavenumber these transitions do not show an apparent tune split.

An important parameter in the coherent beam-beam effect is the ratio  $Y$  between the coherent beam-beam  $\sigma$  and  $\pi$  modes tune split  $\Delta\nu$  and  $\xi$ . The rigid Gaussian beam model [7] predicts the ratio  $\Delta\nu/\xi = 1.0$ . With non-rigid beams, solution of the Vlasov equation [9] gives for our case of flat beam and vertical oscillations  $\Delta\nu/\xi = 1.21$ .

In our experiment  $\Delta\nu(I)$  was evaluated by fitting the theoretical mode spectrum to the whole dataset of the measured spectrum, using a *single fitting parameter*,  $Y\xi$ . Then  $\xi(I)$  was evaluated from the luminosity measurement:

$$\xi_y = \frac{2er_e\beta_y}{\gamma I} L.$$

The main inaccuracy in  $\xi$  thus evaluated is due to statistical straggling of on-line  $L$  data and equals to  $\sim 10\%$ . A good linearity of  $L$  vs  $\sqrt{I}$  evidenced for current-independent beam sizes at the IP, i.e. we had  $\xi \propto I$  without saturation, in the whole range of currents used. From our experiment we have found  $Y = \Delta\nu/\xi = 1.05$ .

This result can be related to our experimental procedure. Indeed, after the kick the transverse beam density distribution does not change during the measurement period of 8192 turns (or effectively less, limited by decoherence). This is much less than the radiation damping time. For this reason the situation appears to be equivalent to interaction of two transversely-rigid Gaussian bunches.

The observation system allowed to discover the synchro-betatron modes in the spectrum of coherent oscillations of colliding bunches at the VEPP-2M collider. The measured spectra dependence on the beam current is in excellent agreement with analytical and numerical models [10, 12]. The measured coherent beam-beam mode tune split is  $1.05\xi$ . This is close to the value expected from the rigid Gaussian model which seems to be adequate to the used experimental technique.

The above presented experimental evidence of the synchro-betatron beam-beam modes adds confidence to the conclusions of their theory. One of them is that for the negligible transverse impedance the mode system remains stable unless some of the mode tunes reach a half-integer resonance.

On the other hand, calculations involving the machine impedance predict a coherent beam-beam *instability* without a threshold. Some, though not all, of the synchro-betatron modes can be damped by optimizing the betatron tune chromaticity. Since the theoretical models [10, 12] used the linearized beam-beam interaction, their prediction

of instability is not as conclusive as the above prediction of stability. In a realistic nonlinear beam-beam system one can expect saturation of such an instability at amplitudes of the order of the vertical beam size. However, this mechanism can cause a vertical emittance blowup detrimental to the high performance of the flat-beam colliders.

## 4 REFERENCES

- [1] D. Sagan, "The Dynamic Beta Effect in CESR", CBN 94-06, Cornell 1994.
- [2] A. Temnykh, "The Dependence of Dynamic Beta Effect on Bunch Length", CON 96-14, Cornell, June 1996.
- [3] A.V. Otboev, E.A. Perevedentsev, "Self-consistent beta function and emittances of round colliding beams", PRST-AB, vol.2, 104401, 1999.
- [4] P.M. Ivanov, I.A. Koop, E.A. Perevedentsev, Yu.M. Shatunov and I.B. Vasserman, "Luminosity and the beam-beam effects in the electron-positron storage ring VEPP-2M with superconducting wiggler magnet", in Proc. 3rd Advanced ICFA Beam Dyn. Workshop, May 29 - June 3, Novosibirsk, 1989, p. 26 (1989).
- [5] A.B. Temnykh. "Phenomenological model of flip-flop effect in colliding beams". Preprint INP 82-148. Novosibirsk, 1982.
- [6] H. Koiso et al., *Particle Accelerators* **27**, 83 (1990).
- [7] K. Hirata, *Nucl. Instr. Meth. A* **269**, 7 (1988).
- [8] A.W. Chao and R.D. Ruth, *Particle Accelerators* **16**, 201 (1985).
- [9] K. Yokoya and H. Koiso, *Particle Accelerators* **27**, 181 (1990).
- [10] E.A. Perevedentsev, in Proc. 1999 Particle Accelerator Conf., New York (1999), vol. 3, p.1521;  
E.A. Perevedentsev, in Proc. Int. Workshop on Electron-Positron Factories, Sept. 21-24 1999, Tsukuba, KEK Proceedings 99-24, Feb. 2000.
- [11] V.V. Danilov, E.A. Perevedentsev, *Nucl. Instr. Meth. A* **391**, 77 (1997).
- [12] E.A. Perevedentsev and A.A. Valishev, *Phys. Rev. ST-AB* **4**, 024403 (2001);  
E.A. Perevedentsev and A.A. Valishev, in Proc. 2000 European Particle Acc. Conf., Vienna (2000), p. 1223;  
E.A. Perevedentsev and A.A. Valishev, in Proc. 2000 Int. Computational Acc. Phys. Conf., Darmstadt (2000).



# RHIC AS A TEST BENCH FOR BEAM-BEAM STUDIES \*

W. Fischer and S. Peggs, Brookhaven National Laboratory, Upton, NY 11973, USA

## Abstract

The Relativistic Heavy Ion Collider (RHIC) is the only existing hadron collider where strong-strong beam-beam effects may occur. It is therefore a good test bench for future hadron colliders for which these effects are relevant. RHIC now approaches its design parameters and its instrumentation is sufficiently developed to allow for beam-beam experiments.

## 1 INTRODUCTION

The Relativistic Heavy Ion Collider (RHIC) went into operation in 2000. The machine has six interaction points (IPs) and supports currently four experiments (see Fig. 1). With gold beams, 10% of the design luminosity was reached in 2000 [1] and more than 25% in 2001. The main machine parameters are summarized in Tab. 1 (a complete list can be found in Ref. [2]).

Beams of equal species collide nominally without a crossing angle. The beams are split horizontally by dipoles (DX) about 10m from the interaction point (see Fig. 2). With 120 or less bunches, symmetrically filled, there are no parasitic beam-beam crossings. Because of this, only a limited number of bunches in both rings are coupled together through beam-beam interactions. With six interaction points, a group of 3 symmetrically distributed bunches in one ring is coupled to a group of 3 bunches in the

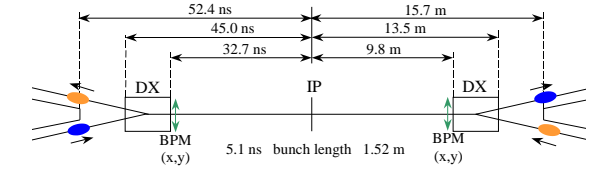


Figure 2: RHIC interaction region layout. The bunches shown correspond to a fill pattern of 120 equally spaced bunches.

other ring, also symmetrically distributed. Every bunch of one group interacts with every bunch of the other group. This can be inferred from Fig. 1. If there is a small difference between the radio frequencies of both rings (see below), all bunches can be coupled together by beam-beam interactions.

When two identical Gaussian beams collide, the horizontal and vertical beam-beam parameters are given by

$$\xi_{x,y} = \frac{r}{2\pi\gamma} \frac{N_b \beta_{x,y}}{\sigma_{x,y}(\sigma_x + \sigma_y)} \quad (1)$$

where  $N_b$  is the single bunch population, the classical radius  $r$  is  $r_p = 1.5347 \times 10^{-18}$  meters for protons and  $r_{Au} = 48.992 \times 10^{-18}$  meters for gold.  $\beta_{x,y}$  is the beta function,  $\sigma_{x,y}$  the transverse rms beam size, and  $\gamma$  is the Lorentz factor. Assuming round beams ( $\beta_x = \beta_y = \beta_t$ ), ( $\sigma_x = \sigma_y = \sigma$ ) and using as definition for the normalized emittance

$$\epsilon_N = (\beta\gamma) \frac{6\sigma^2}{\beta_t}, \quad (2)$$

Eq. (1) can be written as

$$\xi = \frac{3N_b r}{2\epsilon_N}. \quad (3)$$

Note that the beam-beam parameter is independent of energy ( $\gamma$ ), and independent of the lattice function  $\beta_t$ . The tune shift of small amplitude particles due to each collision is equal to the parameter  $\xi$  no matter what the azimuthal location of the collision, if the beams are round and if they collide head-on. Expected beam-beam parameters are listed in Tab. 1. It may be convenient to parameterize the gold and proton beam-beam parameters as

$$\xi_{Au} = 0.0023 \frac{N_b}{10^9} \frac{10\mu\text{m}}{\epsilon_N} \quad (4)$$

and

$$\xi_p = 0.0074 \frac{N_b}{10^{11}} \frac{10\mu\text{m}}{\epsilon_N}. \quad (5)$$

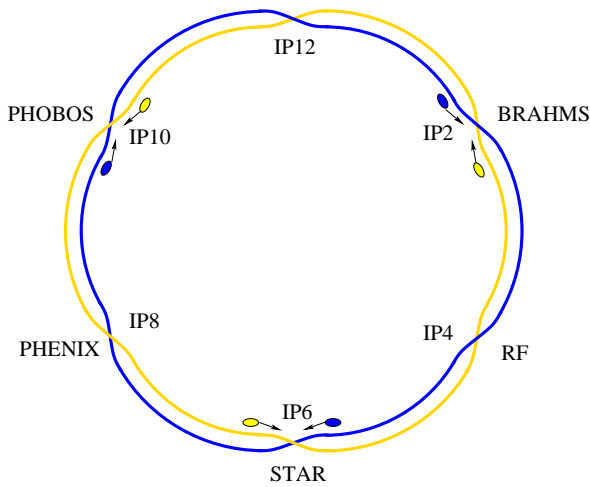


Figure 1: RHIC layout. In stores, only 6 bunches, 3 symmetrically distributed in each ring, are coupled together through the beam-beam interaction.

\* Work supported by U.S. Department of Energy under contract No DE-AC02-98CH10886.



Table 1: RHIC principal machine parameters. The column labeled Au2001 shows machine parameters that were achieved with gold beams. The columns labeled A2001+ and p2001+ show machine parameters expected to be approached in the foreseeable future with gold and polarized proton beams respectively.

parameter	symbol	unit	Au design	Au2001	Au2001+	p design	p2001+
collisions per turn	...	...	2–6	2–6	2–6	2–6	2–6
kinetic energy range	$E$	GeV/u	10-100	9–100	9–100	25-250	25-250
harmonic number	$h$	...	$7 \times 360$	360	$7 \times 360$	$7 \times 360$	$7 \times 360$
gap voltage	$V$	MV	6.0	0.3	3.0	6.0	3.0
number of bunches	$N$	...	60	56	110	60	110
ions per bunch	$N_b$	...	$10^9$	$0.5 \cdot 10^9$	$10^9$	$10^{11}$	$10^{11}$
normalized emittance (95%) <sup>†</sup>	$\epsilon_{N\ x,y}$	$\mu\text{m}$	10	10	10	20	10
bunch area	$S_{95\%}$	$\text{eV} \cdot \text{s/u}$	0.5	1.0	0.5	0.5	0.5
average luminosity	$L$	$\text{cm}^{-2} \text{s}^{-1}$	$2 \cdot 10^{26}$	$2 \cdot 10^{25}$	$2 \cdot 10^{26}$	$10^{31}$	$2 \cdot 10^{31}$
beam-beam parameter, per IP	$\xi_{x,y}$	...	0.0023	0.0012	0.0023	0.0037	0.0074

<sup>†</sup> At the beginning of stores.

With  $a_{x,y}$  denoting the betatron amplitudes at the IP and defining the variables  $\alpha_{x,y} = (a_{x,y}/\sigma_{x,y})^2/4$ , the weak-strong amplitude dependent tune shift due to head-on collisions can be written as [3]

$$\Delta Q_{x,y} = -\xi_{x,y} \int_0^1 du \exp[-(\alpha_x + \alpha_y)u] \times (6) \\ \times I_0(\alpha_{y,x}u) [I_0(\alpha_{x,y}u) - I_1(\alpha_{x,y}u)],$$

where  $I_0$  and  $I_1$  denote the modified Bessel functions of zero and first order respectively.

## 2 EXPECTED BEAM-BEAM EFFECTS

### 2.1 Weak-Strong Effects

The beam-beam interaction leads to incoherent and coherent tune shifts [4]. These can put limitations on the working point. Furthermore, nonlinear resonances may be driven that lead to emittance growth and beam loss. These effects can be further enhanced through nonlinear magnetic field errors and tune modulation. In Fig. 3 a tune footprint is shown for the Au2001+ scenario (see Tab. 1) at the tunes  $(Q_x, Q_y) = (28.22, 29.23)$ , which are close to the ones currently used in operation. It is assumed, that beams are colliding in four IPs and are transversely separated in the other two IPs. Sum resonances up to order 9 are added. In Fig. 4 a tune footprint for the p2001+ scenario is shown for collisions at two IPs and transverse separation at the other four IPs. A working point that avoids the resonances is likely to improve the lifetime.

For comparison, significant beam-beam effects are noticed in proton colliders when  $\xi = 0.004$ , with 6 head-on collisions per turn [5]. Increased background rates were observed in the SPS when the tune approached resonances of order 13 and 16 [6].

### 2.2 Strong-Strong Effects

With beams of high and almost equal intensities coherent modes of transverse oscillation ( $\sigma$  and  $\pi$  modes) may

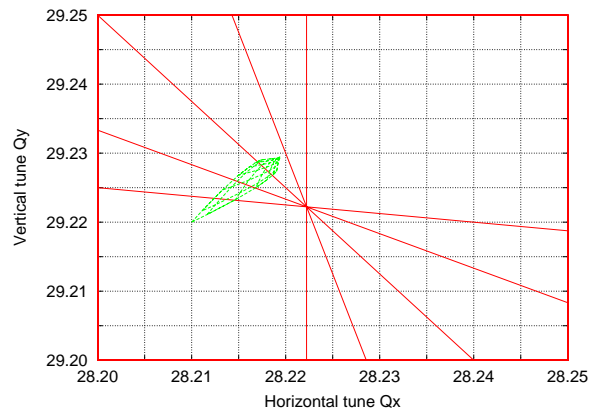


Figure 3: Beam-beam footprint for amplitudes up to 6 rms beam sizes with the Au2001+ parameters and four IPs. The working point is  $(Q_x, Q_y) = (28.22, 29.23)$ . Also shown are sum resonances of order 9.

become visible. The simulation in Ref. [7] clearly shows these modes in the transverse spectra for a single bunch of beam in each ring at the gold design parameters (see Tab. 1). Should the  $\pi$  mode be outside the continuum spectrum, it will not be damped.

A simulation in Ref. [8] showed unstable beam centroid oscillations when the beam-beam parameter becomes larger than a critical value,  $\xi > \xi_c$ . The growth rate of the unstable amplitude oscillations is enhanced through nonlinear field errors in the lattice. Furthermore, transverse emittance growth is strongly enhanced under these conditions.

## 3 BEAM-BEAM OBSERVATIONS DURING OPERATION

Up to now colliding beams were only achieved in gold operation. A coherent tune shift of about  $10^{-3}$  was measured when beams with  $0.3 \times 10^9$  ions were brought in and

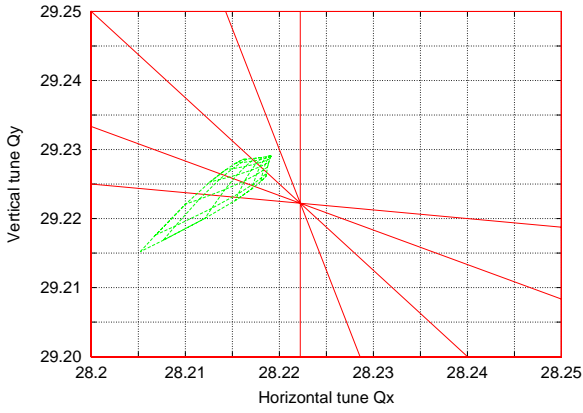


Figure 4: Beam-beam footprint for amplitudes up to 6 rms beam sizes with the p2001+ parameters and two IPs.

out of collision longitudinally. This seems to indicate a relatively minor effect. However, frequently a lifetime deterioration is observed when the beams are brought into collision. Fig. 5 shows such a case at storage energy. Usually the lifetime can be improved by adjusting the general beam conditions such as closed orbit, tune and chromaticity.

In RHIC, the rf systems of both rings are independent since it is planned to accelerate different ion species, which may require different radio frequencies. Thus, the radio frequencies of the Blue and Yellow ring can differ when the phase and radial loops are closed. The small radio frequency difference results in beam-beam collisions with longitudinally moving crossing locations. At injection, this leads reproducibly to lifetime problems in one of the two beams and a scheme was implemented to enforce equal radio frequencies and separate the beams longitudinally [9].

More recently, beam losses along the ramp (when the rf loops are closed and a small difference in the radio frequencies exist) were also attributed to the beam-beam interaction [10], and a transverse separation was implemented in the interaction regions along the ramp to ameliorate the effect [11].

The deterioration of lifetime when both beams have different radio frequencies can be explained by tune modulation that is caused through the longitudinal movement of the interaction point through the interaction region [12]. Typical differences in the radio frequencies lead to tune modulation frequencies of the order of 1 Hz with modulation depth of up to a few  $10^{-3}$ .

During stores a transverse emittance growth was observed that is much larger than expectations from intra-beam scattering [13, 14], which may be caused by beam-beam interactions. Furthermore, there are indications that the transverse emittance growth increases during vernier scans (in which the luminosity is recorded as a function of the transverse beam separation) when the beams collide with a transverse offset [5, 14, 15].

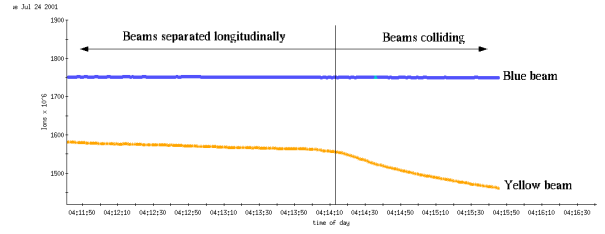


Figure 5: Observed lifetime deterioration due to beam-beam effect in gold operation.

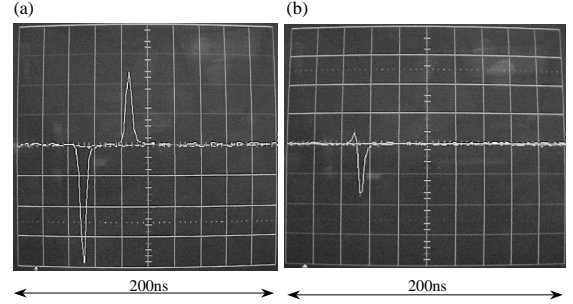


Figure 6: One Blue (upper) and one Yellow (lower) bunch seed with a wall current monitor located at an IP. Due to the different current directions of both beams, the wall current has a positive sign for one and a negative sign for the other beam. In part (a) the beams are not colliding at the IP, in part (b) they do.

#### 4 POSSIBLE BEAM MANIPULATIONS IN INTERACTION REGIONS

At storage the beam positions in the interaction regions are manipulated longitudinally and transversely. Longitudinally the beam can be separated or brought into collision (see Fig. 6). The IP can be moved to any location between the crotches (see Fig. 2). By shifting the IP between the DX magnet and the crotch a crossing with up to 90mm horizontal separation ( $80\sigma$  at storage energy for  $\epsilon_N=10\mu\text{m}$  and  $\beta^*=5\text{m}$ ) can be achieved. The IP location can be changed in steps of 30mm. With a small radio frequency difference between the rings the IP can also be shifted continuously. This happens routinely during ramps when both rings run with independent phase and radial loops.

Transversely any of the two beams can be moved laterally in steps of  $10\mu\text{m}$ . The crossing angle can be changed in steps of  $1\mu\text{m}$  (see Fig. 7). The beam movement is observable in the dual plane DX BPMs (see Fig. 2). Transverse separations of more than 100 transverse rms beam sizes and beam-to-beam crossing angles of at least 2mrad can be implemented [16].

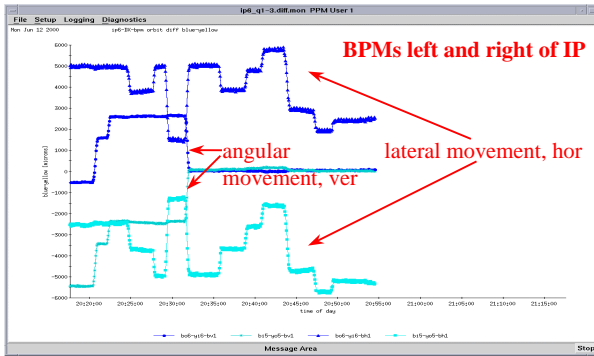


Figure 7: Transverse beam manipulations seen in the DX BPMs. Shown is the angular and lateral movement of the Blue beam at IP6.

## 5 INSTRUMENTATION FOR EXPERIMENTS

The instrumentation for beam observations has been developed and commissioned over the last few years. The current and future capabilities of the main systems are listed below.

**Beam Position Monitors** In the arcs every quadrupole is equipped with a single plane beam position monitor (BPM). In the interaction regions every quadrupole is equipped with a dual plane beam position monitor. Dual plan BPMs are also located at the inner sides of the beam splitting DX magnets (see Fig. 2) with only a drift space in between. With a trigger signal 128 or 1024 consecutive turns can be read out from every BPM. In the future, two BPMs per plane and ring may deliver  $10^5$  to  $10^6$  turns.

**Wall Current Monitor** Several wall current monitors (WCMs) are available. Typically a full turn can be recorded every 4s with a resolution of 0.25ns (accelerating buckets are 36ns, storage buckets 5ns long).

**Ionization Profile Monitor** Horizontal and vertical beam profile monitors are available from ionization profile monitors (IPMs) [22]. Currently profiles are obtained from single bunch stores every 4s. With more R&D it may be possible to get profiles from an arbitrary bunch in a regular store (56 or 110 bunches) every 4s. An IPM may also be able to record up to 125000 consecutive turns of a single bunch.

**Tune Meters** Tunes are available from a system that excites the beam with a small number of small kicks, reads out the beam response in a BPM and computes the Fast Fourier Transform [20]. The resolution of this system is  $10^{-4}$ . At injection, the tune can also be determined from the spectrum of the injection oscillations. In addition, the tune and tune spread can be measured with a Schottky monitor [21].

**Kickers** Several kickers are available to excite coherent beam oscillations. The tune kickers [20] can provide a  $0.2\sigma$  horizontal and a  $0.1\sigma$  vertical kick at injection. The injection kicker could provide a vertical kick of more than  $5\sigma$  at injection. At storage energy the kick strength is reduced accordingly.

**AC Dipole** AC dipoles for both the horizontal and vertical plane will be installed in RHIC. These devices excite coherent dipole oscillation through an AC dipole field running close to the betatron frequencies. With such a resonant drive, in principle, any amplitude can be excited. The AC dipoles can be switched off in about 10 turns to provide free coherent betatron oscillations like through a kicker. The AC dipoles are located close to an interaction point and shared by both beams.

**Pulsed Quadrupole** A pulsed quadrupole will be available in the future, also shared by both beams. This quadrupole is intended for transverse echo measurements [24] and would provide a one turn quadrupole kick. The pulsed quadrupole would change the tune by about 0.002 when run continuously at injection.

## 6 POSSIBLE BEAM-BEAM EXPERIMENTS

Beam-beam experiments can be done at injection as well as at storage since the beam-beam parameter  $\xi$  is independent of the energy (see Eq. (3)). Experiments at storage energy may be more convenient since orbits are already prepared for collision. However, destructive measurements are best done at injection, since the beam can be restored in a few seconds.

As a basic measurement the coherent tune shift with bunches longitudinally separated or in collision can be determined. Furthermore, the coherent tune shift can be measured as a function of transverse separation, once the bunch intensity is high enough to allow this, given the resolution of the tune measurement. The Schottky system allows to measure the tune and tune spread in the beam. Schottky measurements can also identify beam trapped in resonance islands.

### 6.1 Weak-Strong Effects

To measure weak-strong effects one beam should have a large and one a small intensity. The weaker beam is used for the measurements. In addition to the tune measurements described above, emittance growths can be measured as a function of several parameters such as the tune or the transverse offset. The transverse offset can be made as large as  $80\sigma$  (see above). With IPMs or a scraper, amplitude dependent diffusion may also be determined.

## 6.2 Strong-Strong Effects

Tune measurements and emittance growth can also be measured with both beams at high intensity. But in addition, coherent modes may be studied. For this only one interaction is desirable with the maximum intensity possible in both beams. A coherent excitation reveals if the  $\pi$ -mode is damped. In addition, with many-turn BPM observation it can be revealed if the center-of-mass undergoes chaotic motion as predicted in Ref. [8].

## 7 SUMMARY

With RHIC operational and its instrumentation developed, the machine can serve as a test bench for beam-beam effects. Better than any other existing machine, it is suited to investigate strong-strong effects in hadron colliders.

## 8 ACKNOWLEDGEMENTS

The authors wish to thank M. Furman, W. MacKay, W. Herr, S. Tepikian, J. Shi and F. Zimmermann for discussions and help in the preparation of this report.

## 9 REFERENCES

- [1] D. Trbojevic, L. Ahrens, M. Blaskiewicz, M. Brennan, M. Bai, P. Cameron, J. Cardona, R. Connolly, J. DeLong, A. Drees, R.P. Fliller, W. Fischer, G. Ganetis, W. Glenn, H. Hahn, T. Hayes, A. Lehrach, W. MacKay, J. Kewisch, S. Peggs, V. Ptitsyn, T. Roser, T. Satogata, T. Shea, K. Smith, S. Tepikian, N. Tsoupas, J. van Zeijts, "Commissioning of the Relativistic Heavy Ion Collider", proceedings of the 2001 Particle Accelerator Conference, Chicago, BNL-67969 (2001).
- [2] H. Hahn (editor), "RHIC Design Manual", revision of October 2000, <http://www.rhichome.bnl.gov/NT-share/rhicdm/00-toc1i.htm>.
- [3] J.D. Jackson (editor), "Conceptual Design of the Superconducting Super Collider", SSC Central Design Group, SSC-SR-2020 (1986).
- [4] E. Keil, "Beam-beam Dynamics", CERN Accelerator School, Rhodes, Greece, CERN 95-06 (1995), CERN SL/94-78 (1994).
- [5] D. Siergiej, "Beam-Beam Interaction Effects in the Fermilab Collider", PhD thesis, University of New Mexico (1995).
- [6] W. Herr, these proceedings.
- [7] M.A. Furman, "Beam-Beam Simulations for Separated Beams", proceedings of the US-LHC Collaboration Meeting on Accelerator Physics Experiments for Future Hadron Colliders, Upton, New York, BNL-52601; LBNL-4563, CBP Note 333 (2000).
- [8] J. Shi and D. Yao, "Collective Beam-Beam Effects in Hadron Colliders", Phys. Rev. E, Vol. 62, Number 1, p. 1258 (2000).
- [9] J. DeLong, J.M. Brennan, private communication (2001).
- [10] A. Drees, D. Trbojevic, "RHIC Logbook" 18 August 2001.
- [11] V. Ptitsyn, private communication (2001).
- [12] W. Fischer, "Tune Modulation from Beam-Beam Interaction and Unequal Radio Frequencies in RHIC", unpublished note (2001).
- [13] W. Fischer, A. Drees, J.M. Brennan, R. Connolly, R. Fliller, S. Tepikian, and J. van Zeijts, "Beam Lifetime and Emittance Growth Measurements of Gold Beams in RHIC at Storage", proceedings of the 2001 Particle Accelerator Conference, Chicago, BNL-67975 (2001).
- [14] A. Drees, Z. Xu, "Results from Luminosity Scans during the RHIC 2000 Run", proceedings of the 2001 Particle Accelerator Conference, Chicago (2001).
- [15] A. Drees, private communication (2001).
- [16] After a problem in one of the IP2 DX magnets was discovered its current was reduced and a beam-to-beam crossing angle of 1.81 mrad implemented temporarily.
- [17] S. Peggs, "Parasitic Beam-Beam Collisions and Crossing Angles in RHIC", BNL RHIC/AP/68 (1995).
- [18] S. Peggs, "Beam-beam Collisions and Crossing Angles in RHIC", proceedings of the 1999 LHC Beam-Beam Workshop at CERN, BNL RHIC/AP/169 (1999).
- [19] T. Satogata and S. Peggs, "Hadron Beam-Beam Diffusion in 2.5-D", proceedings of the 1999 LHC Beam-Beam Workshop at CERN, BNL RHIC/AP/170 (1999).
- [20] P. Cameron, R. Connolly, A. Drees, T. Ryan, H. Schmickler, T. Shea, D. Trbojevic, "ARTUS: A Rhic TUNE monitor System", BNL RHIC/AP/156 (1998).
- [21] P. Cameron, J. Cupolo, C. Degen, L. Hammons, M. Kesselman, R. Lee, A. Meyer, R. Sikora, "Schottky Measurements During RHIC 2000", proceedings of the 2001 Particle Accelerator Conference, Chicago (2001).
- [22] R. Connolly, P. Cameron, R. Michnoff, S. Tepikian, "Performance of the RHIC IPM", proceedings of the 2001 Particle Accelerator Conference, Chicago (2001).
- [23] M. Bai, M. Meth, C. Pai, B. Parker, S. Peggs, T. Roser, R. Sanders, D. Trbojevic, A. Zaltsman, "RHIC AC Dipole Design and Construction", proceedings of the 2001 Particle Accelerator Conference, Chicago (2001).
- [24] W. Fischer, B. Parker and O. Brüning, "Transverse Echos in RHIC", proceedings of the US-LHC Collaboration Meeting on Accelerator Physics Experiments for Future Hadron Colliders, Upton, New York, BNL-52601 (2000).
- [25] W. Fischer and F. Zimmermann, "RHIC Beam Experiments for the LHC Era", BNL RHIC/AP/179 (1999).

# Summary of Observation Session.

A. Temnykh \*

Laboratory of Nuclear Studies, Cornell University, Ithaca NY 14953, USA

## Abstract

Here is given a short summary of data presented on "Observation" session on Beam-Beam workshop held at FNAL from June 25 to June 28 2001.

## 1 INTRODUCTION

Since the beginning of colliding beams era the beam-beam interaction phenomenon attracted much attention because of the role of this phenomenon in colliders performance limitation. Theory developing, numerical simulations and experimental studies in the past decades provided significant progress in understanding of the phenomenon. The most recently built B - factories, Pep-II and KEKB, even though having complicated beam colliding scheme (different colliding beams energies, crossing angle) reached excellent beam-beam performance ( $\xi \sim 0.05$ ) and high luminosity in very short period of time.

However, many features of the beam-beam interaction such as dependence  $\xi$  on damping, coupling, machine non-linearity and etc. still are not well understood. Better understanding may lead to a significant progress in efficiency of the existing and future colliders.

One task of the "Observation" session was to review a recently collected experimental data in order to evaluate recommendations which can be useful in future planning.

The data presented on the session came from two low energy lepton colliders VEPP-2M (Novosibirsk) and DAΦNE (Frascati) and from ion-ion collider RHIC (Brookhaven).

## 2 RECENT BEAM-BEAM OBSERVATION ON VEPP-2M [1]

Three recent experiments were reported from VEPP-2M.

- *Dynamic Beta Effect.* This effect is in fact distortion of the linear machine optics caused by interaction of one beam particles with an opposite beam. In the study, vertical beam size of weak electron beam collided with strong positron beam was monitored at two different locations along the beam trajectory. The distortion of vertical beta-function was calculated from the change of ratio of beam heights at these locations. Beta function distortion was measured as a function of positron beam intensity for various positron bunch length and beta function at interaction point. Under certain condition, the vertical beta function was changed by a factor two. The experimental data are in good agreement with theoretical model.

It should be mentioned that even though the effect of linear optics distortion by beam-beam interaction was known for a long time, there were only several documented experimental studies related to this phenomenon, see for example [2]. Thus, the reported data which confirm theoretical model in wide range of parameters is of great significance.

- *Flip-Flop Phenomenon* study was in line with phenomenological models described in references [3], [4] and [5].

Often in lepton colliders beam-beam interaction causes the equal intensity colliding beams to have very different beam sizes. This effect, called flip-flop phenomenon, may occur when colliding beam intensities exceed the threshold. Like it was done in previous work, the authors assume that the vertical size of one beam is a function of ratio of intensity to vertical size of other beam, i.e.,  $\sigma_1 = f(I_2/\sigma_2)$ . Note that the  $I_2/\sigma_2$  is proportional to  $\xi_v$  parameter. Using measured dependence of the weak beam vertical size on intensity of strong beam, one can write down the system of two equations and find solution  $\sigma_{1,2}(I_1, I_2)$  numerically. In the case of two equal intensity beams  $I_1 = I_2 = I$ , there will be single solution  $\sigma_1(I) = \sigma_2(I)$  for low intensity  $I \leq I_{tr}$ , and, if function  $f$  is steep enough, there will be more then one solutions with  $\sigma_1(I) \neq \sigma_2(I)$  for higher intensity,  $I \geq I_{tr}$ .  $I_{tr}$  is a threshold current. The multiple solution indicates appearance of the flip-flop effect.

In general, experimental data fit well the model prediction. However, there is good agreement between modeled and measured flip-flop threshold current, but only qualitative correspondence between measured and predicted dependence of vertical beam sizes on beams intensity.

Results of this study confirm that the simple model using beam-beam parameter  $\xi_v \sim I/\sigma_v$  and weak-strong approximation can only qualitatively describe the dynamics of colliding beams. For more realistic description one should use more complicated model with more parameters involved.

- *Coherent Synchro-Betatron Beam-Beam Modes* study was another interesting experiment reported from VEPP-2M on this session. In this experiment two synchrotron light monitors with edge screens were aimed on both counter colliding beams. The horizontal edges of the screens were positioned to cut out part of the SR beam images projected on PMT cathode. In this scheme, the signal from PMT was very sensitive to vertical position of the bunches. In the process of measurement, one bunch (there was one bunch per beam) was excited by a short pulse and then signals from both PMTs were recorded on turn-to-turn base. Fourier analysis of the recorded signals revealed the excited modes.

\* e-mail: abt6@cornell.edu

At least 6 (!) synchro - betatron modes  $0\pi, 1\pi, 2\pi$  and  $0\sigma, -1\sigma, -2\sigma$  (first index means dipole, quadrupole and etc. distribution in synchrotron space,  $\sigma$  and  $\pi$  refer to the betatron motion of the bunches) were seen. At low beams intensity ( $\xi_v \leq 0.005$ ) two "classical"  $0\pi$  and  $0\sigma$  modes were detected, while at higher intensity ( $\xi_v \geq 0.015$ ) two other modes  $-2\sigma$  and  $-2\pi$  were dominating. This observation is in good agreement with the theory developed early in [6] and [7].

Note that linear theory of beam-beam interaction predicts relation between the  $\sigma$  and  $\pi$  mode tune difference and  $\xi$  parameter:  $\delta Q_{\pi-\sigma} = C \cdot \xi$  with  $C = 2$ . Calculation accounting for nonlinearity of beam-beam force and transverse density distribution gives  $C \simeq 1.4$ . This is confirmed by tracking. However, experimental data for  $C$  reported from different machines vary from 1 to 2. The reported experiments suggested the explanation of this diversity. On different machines different types of synchro-betatron modes may be observed. Together with synchrotron tunes varying from one machine to another it can explain the observed variation in  $C$  value.

Understanding of the relation between the  $\sigma/\pi$  modes tune split and  $\xi$  may have a great practical importance. The tune split is easy to measure. If one can establish reliable relation between the tune split and  $\xi$ , then, using correlation between luminosity and  $\xi$  ( $\mathcal{L} = \frac{\gamma}{2\epsilon r_e \beta} \xi$ ), one can use this measurement for *quantitative* luminosity monitoring.

### 3 BEAM-BEAM OBSERVATION ON DAΦNE [8]

DAΦNE is a recently commissioned low energy ( $\sim 0.5\text{GeV}$ ) lepton collider. It started operation in May 1999 and since then is rapidly progressing by doubling luminosity approximately every 6 months. In the report the machine upgrades which provided the beam-beam performance and luminosity enhancement were discussed.

- *Optimization of general machine parameters* such as collision parameters and global coupling shortly after commissioning allowed to reach luminosity  $0.2 \times 10^{30} \text{ cm}^{-2} \text{ sec}^{-1}$  per bunch and  $\xi_v \sim 0.01$ . Further improvement in coupling ( $\epsilon_y/\epsilon_x \sim 0.3\%$ ) and better working point ( $Q_x = 5.15/5.10, Q_y = 5.21/5.14$  for  $e+/e-$  beams) resulted in luminosity doubling,  $\mathcal{L} \sim 0.5 \times 10^{30} \text{ cm}^{-2} \text{ sec}^{-1}$  per bunch.

- *Cubic machine nonlinearity* attracted attention after the strong octupole-like component was detected in wigglers. That promoted intensive study of influence of machine cubic nonlinearity on the machine beam-beam performance.

Early it was found that the topology of the phase space resulted from beam-beam interaction is very sensitive to sign and value of machine cubic nonlinearity [9]. Changing the dependence of tune on amplitude the machine cubic nonlinearity can increase or decrease the width of resonance islands generated by beam-beam interaction. It results in growing or in diminishing of beam tails effecting

beam life time.

Numerical simulation made for DAΦNE showed the dramatic effect of the cubic nonlinearity generated in wigglers on particle density distribution in the beam tails. A new optics with reduced beta function in the wiggler locations was designed and implemented to decrease the machine cubic nonlinearity. It helped to improve beam-beam performance,  $\xi_v \sim 0.02$ , and provided luminosity growth,  $\mathcal{L} \sim 1.0 \times 10^{30} \text{ cm}^{-2} \text{ sec}^{-1}$  per bunch. The future plans call for octupole lenses installation for better control of machine cubic nonlinearity.

The beam-beam experience obtained on DAΦNE proved the importance of the machine cubic nonlinearity control and demonstrated that the cubic nonlinearity tuning may lead to substantial gain in luminosity and beam-beam performance.

### 4 RHIC AS A TEST BENCH FOR BEAM-BEAM STUDIES [11]

In the report presented by Wolfram Fisher, Relativistic Heavy Ion Collider (RHIC) was described as a potential test bench for future hadron colliders such as LHC and VLHC. Flexibility in manipulation with beams in longitudinal and transverse spaces together with well developed beam diagnostics make possible to study many features of beam-beam phenomenon. Although the time available for the study is limited because of strong competition with other programs, RHIC team is very interested and ready to test new theories of beam-beam interaction.

### 5 CONCLUSION

Many interesting observations of beam-beam phenomenon were reported on the session. Two of them, observation of coherent synchro-betatron modes on VEPP-2M and dependence of beam-beam performance and luminosity on machine cubic nonlinearity observed on DAΦNE (similar were reported in [10]) are of especial importance and it is very desirable to carry out analogous experiments on other machines.

### 6 REFERENCES

- [1] I. Nesterenko, Last experimental studies of beam-beam effects at VEPP-2M, These proceedings.
- [2] D. Cinabro et al., Observation of the Dynamic Beta Effect at CESR with CLEO, CLNS 97/1496.
- [3] G. Voss, Proc. XI Intern. Conf. On High Energy Accel., p.148
- [4] A. Temnykh, Phenomenological Model of Flip-Flop Effect in Colliding Beams. Preprint INP 82-148. Novosibirsk, 1982
- [5] A.V Otboev and E.A. Perevedevtsev, On Self-Consistent  $\beta$  - function of Colliding Bunches. Proceedings of the 1999 Particle Accelerator Conference, New York, 1999, pp. 1524-1525.

- [6] E. A. Perevedentsev and A.A. Valishev, Characteristics and Possible Cures of The Head-Tail Instability of Colliding Bunches. Proceedings of EPAC 2000, Vienna, Austria, pp. 1223-1225.
- [7] E. A. Perevedentsev, Simplified Theory of The Head-Tail Instability of Colliding Bunches. Proceedings of the 1999 Particle Accelerator Conference, New York, 1999, pp. 1521-1523.
- [8] M. Boscolo on behalf of the DAΦNE team, Beam-Beam Experience at DAΦNE, These proceedings.
- [9] A. B. Temnykh, Influence of Cubic Nonlinearity of Storage Ring Magnetic Field on Beam-Beam Effects on VEPP-4, Proceedings of XIII International Conference on High Energy Accelerators, Novosibirsk, 1986, V1. pp. 78-81.
- [10] A. B. Temnykh, Observation of Beam-Beam Effects on VEPP-4, Proceedings of Third Advanced ICFA Beam Dynamics Workshop on Beam-Beam Effects in Circular Collider, Novosibirsk, 1989, pp. 5-11
- [11] W. Fischer, RHIC as a Test Bench for Beam-Beam Studies, These proceedings.

## **SECTION II: Beam-beam compensation**



# FISRT EXPERIMENTS WITH ELECTRON LENS FOR BEAM-BEAM COMPENSATION IN TEVATRON

V. Shiltsev, G.Kuznetsov, N. Solyak, D. Wildman, X.L. Zhang, FNAL, Batavia, IL 60510, USA  
Yu.Alexahin, JINR, Dubna, Russia; and K.Bishofberger, UCLA, Los-Angeles, CA 90095, USA

## Abstract

The project of beam-beam compensation (BBC) in the Tevatron using electron beams [1] has passed a successful first step in experimental studies. The first Tevatron electron lens (TEL) has been installed in the Tevatron, commissioned, and demonstrated the theoretically predicted shift of betatron frequencies of a high energy proton beam due to a high current low energy electron beam. After the first series of studies in March-April 2001 (total of 7 shifts), we achieved tuneshifts of 980 GeV protons of about  $dQ=+0.007$  with some 3 A of the electron beam current while the proton lifetime was in the range of 10 hours (some 24 hours at the best). Future work will include diagnostics improvement, beam studies with antiprotons, and fabrication of the 2nd TEL.

## 1 BRIEF DESCRIPTION OF BEAM-BEAM COMPENSATION AND THE 1<sup>ST</sup> TEVATRON ELECTRON LENS

In the Tevatron, the antiproton bunches suffer a tuneshift due to their interactions with the more intense proton bunches. In multibunch operation, the tuneshifts vary from antiproton bunch to antiproton bunch, leading to an effective spread in tune. An electron lens, consisting of a short, low energy, electron beam colliding with antiprotons, can induce a tuneshift on the antiproton bunches, which has the opposite sign to that, which they experience, from the protons. With appropriate choice of parameters two such lenses could provide effective beam-beam tuneshift compensation. An R&D program has resulted in the construction and, recently, the successful testing of a single such device. If results continue to be positive the use of such devices could lead to a longer luminosity lifetime in the Tevatron and hence to a large integrated luminosity. Another potential luminosity improvement may come from compensation of non-linear tune spread within each antiproton bunch (footprint compression) by using electron beams with Gaussian profiles [2].

Fig.1 depicts a general layout of the TEL. The magnetic system of the TEL (see details in [3]) consists of a 65 kG SC main solenoid, four 8 kG and two 2 kG SC dipole correctors in the same cryostat, and 4 kG gun and collector solenoids. The TEL cryostat is part of the Tevatron magnet string cooling system. Strong  $\Pi$ -shaped magnetic field is needed to guide 10 kV electron beam from an electron gun thru an interaction region, where electrons collide with high energy (anti)protons, to a water cooled collector. SC dipole correctors allow precise

steering in position and angle of the electron beam onto the Tevatron beams. A number of precautions have been taken during SC magnets fabrication in order to achieve very high linearity of magnetic field lines inside the main solenoid. The reason is that as the electron beam goes along magnetic field lines it should not deviate around the straight Tevatron beam trajectory, otherwise the effectiveness of the TEL would be deteriorated.

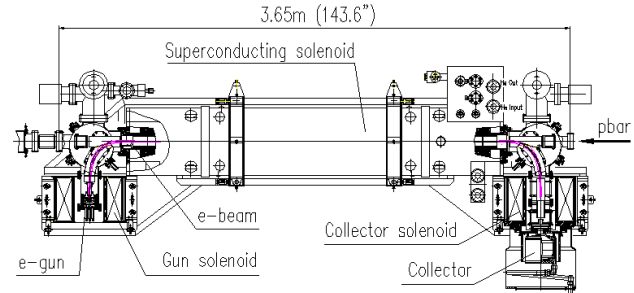


Figure 1: General layout of the Tevatron Electron Lens.

Measured rms deviations of the lines are 15  $\mu\text{m}$  in the vertical plane and 50  $\mu\text{m}$  in the horizontal plane (which is the plane of the bends) [4]. This is 10% of the Tevatron beam size in the location of the electron lens. It was found experimentally that the electron beam can be steered to pass through the main solenoid if the gun solenoid field is in the range of  $B_{\text{Gun}}=1.9\text{-}4.2$  kG for  $B_m=35\text{ kG}$  (outside the range, the beam touches parts of the vacuum system) [5].

The electron gun employs a 10 mm diameter convex thermo-cathode and can provide up to 6A of pulsed current and 3A DC of up to 15kV electrons. Perveance of the gun is  $5.6 \mu\text{A}/\text{V}^{3/2}$ . Electron current profile is close to rectangular, but can be changed to a more smooth one if a negative potential (w.r.t. the cathode) is applied to a special near-cathode electrode. Water cooled collector is characterized by high-perveance of about  $10 \mu\text{A}/\text{V}^{3/2}$ , high absorbing efficiency exceeding 99.5%, and dissipation up to 50 kW of electron beam power. See details on the gun and collector in [5].

In order to vary electron current at the scale of the bunch-to-bunch spacing (396ns in the Tevatron at present Run IIa) high-voltage pulses are applied to the gun anode. During the first studies a 8 kV, 800 ns FWHM modulator based on RF tube has been used to provide electron pulses synchronized with a single Tevatron bunch at the repetition frequency of 47.7 kHz (see [6] for details).

The TEL is equipped with 4 BPMs: one vertical and horizontal at the beginning and at the end of the main solenoid. The BPMs are supposed to measure transverse positions of electron, proton and antiproton beams passing through and thus, allow the electron beam to be centered on the antiproton or the proton one. 100  $\mu\text{m}$  diameter

tungsten wires, vertical and horizontal, can be introduced into the very middle of the interaction region for electron current profile measurements. They are remotely controlled and removed when high energy beams circulate in the machine. Electron currents leaving the cathode, into the collector and onto the collector entrance electrode are measured by 3 inductive coils. There are 10 HV electrodes around the electron beam trajectory which can be used for ion or secondary electron cleaning (though most of the time there are grounded). Beams diagnostics employed in the TEL is described in detail in [7].

The TEL vacuum under working conditions with 3 ion pumps with a total pumping speed of 300 l/s ranges from 4 to 10 e-8 Torr. Table 1 summarizes main parameters of the TEL.

Table 1: TEL operational parameters

electron beam energy,	$U_e$ , kV	6-12
maximum peak electron current	$J_e$ , A	2-3.5
magnetic field in main solenoid	$B_m$ , kG	35
in gun solenoid	$B_g$ , kG	3.7
e-beam radius in main solenoid	$a_e$ , mm	1.75
cathode radius	$a_c$ , mm	5
e-pulse width, FWHM	$\tau_e$ , mm	~800
current stability, peak-to-peak	$\Delta J_e/J_e$ , %	< 0.1
effective interaction length	$L_e$ , m	2.0
valve-to-valve length	$L_{tot}$ , m	3.65

We observed very minimal effects of the magnetic fields of the lens on 980 GeV proton beam. Tunes are shifted by less than 0.001 in both planes, the tune split  $Q_x - Q_y$  varies from 0.0072 to 0.0077, no coupling correctors are needed to operate the Tevatron, and the orbit distortion around the ring stays within about 1 mm. Measurements with the proton beam have shown that numerous electrodes of the TEL (BPMs, HV electrodes) and discontinuities of the beam pipe all together generate a broadband impedance  $|Z/n| < 0.1$  Ohm, that is a very small contribution to the total Tevatron impedance estimated to be some 2-8 Ohm.

In March-April 2001 there were total of seven 8-hour beam shifts dedicated to studies with the Tevatron Electron Lens. Most experimental results were obtained with a single coalesced proton bunch in the ring at the energy of 980 GeV and everywhere below we assume that proton energy if not specifically stated. Total proton bunch length was less then 19 ns, bunch intensity varied from 6 to 60  $\times 10^9$ . The only shift at 150 GeV on March 23 was the very first one and to our great satisfaction a decent betatron frequency shift was observed, breaking the path for application of electron lenses in high-energy accelerators.

## 2 PROTON TUNE SHIFT DUE TO THE ELECTRON LENS

According to [1], a perfectly steered round electron beam with a constant current density distribution will shift the betatron tune by:

$$dQ_{x,y} = \mp \frac{\beta_{x,y}}{2\pi} \cdot \frac{1 \pm \beta_e}{\beta_e} \cdot \frac{J_e L_e r_p}{e \cdot c \cdot a_e^2 \cdot \gamma_p} \quad (1)$$

where the sign reflects defocusing for antiprotons and focusing for protons,  $\beta_e = v_e/c$  is the electron beam velocity,  $\beta_x = 101$  m and  $\beta_y = 28$  m are beta functions at the location of the lens (the first TEL is installed in the Tevatron sector F48),  $a_e$ ,  $J_e$  and  $L_e$  stand for the electron beam size, current and effective interaction length,  $r_p$  is the classical proton radius,  $\gamma_p = 1044$  relativistic Lorentz factor for 980 GeV protons. Electron beam is assumed to be much wider than (anti)proton beam, so, all high-energy particles acquire the same  $dQ$ . Factor  $1 \pm \beta_e$  reflects the fact that contribution of the magnetic force is  $\beta_e$  times the electric force contribution and depends on the direction of the electron velocity. So far we operated only with protons only (while the actual goal is to operate with antiproton bunches) which move in the same direction as the TEL electrons, so the magnetic force reduces the total tuneshift.

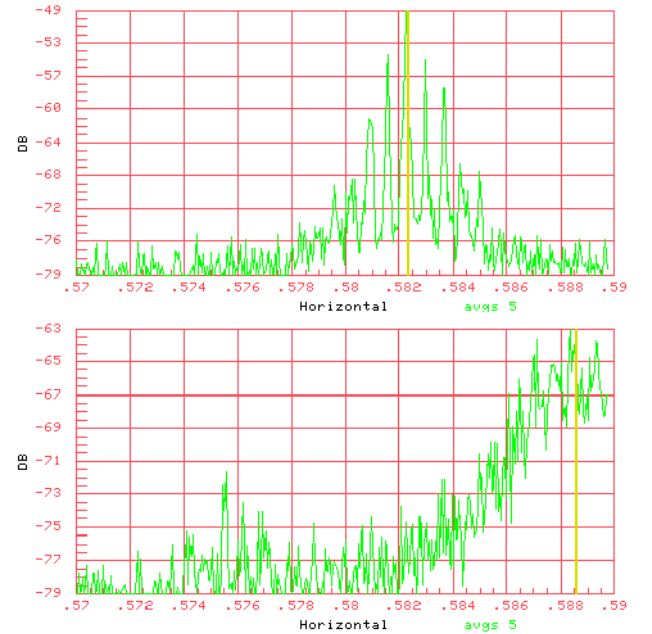


Figure 2: Schottky spectra of horizontal motion of protons without electron current (top) and with 3A of electron current (bottom), cathode potential  $U_c = 7.6$  kV.

Fig.2 shows an example of the Schottky spectra of horizontal proton beam oscillations without electron current and with 3 A electron current. One can see that the horizontal tune is shifted positively by about  $dQ_x = +0.0065$  from 20.5824 to 20.5889. One should expect that the same electron beam would shift the horizontal tune of antiprotons  $(1 + \beta_e / 1 - \beta_e) = 1.5$  times this amount, i.e., by -0.01 given that  $\beta_e \approx 0.2$ . Besides a central peak corresponding to the betatron frequency (highlighted by

marker line), the spectra consist of several synchrotron sidebands, separated by the synchrotron tune  $Q_s \approx 0.0007$ . Total power in the peaks depends on proton intensity and noise level exciting the beam motion. Application of the electron beam may or may not cause spectra shape variation as in Fig.2. The shape also depends on the machine tuning, working point, etc. The shape variations sometimes make precise tuneshift measurements rather difficult, and we estimate typical error to be  $\delta Q \approx \pm 0.0001$ .

Fig.3 shows how the proton tune shifts depend on the time delay between the 2A electron pulse and the arrival of the proton bunch. One can see that a) the tune shift follows the electron pulse shape and, therefore, it's possible to shift the tune for any bunch without touching neighbors 400 ns aside, and b) horizontal tune shift is some 4 times the vertical one  $dQ_x/dQ_y = 0.0037/0.0008 = 4.6$  that is close to the beta function ratio  $\beta_x/\beta_y = 101/28 = 3.6$ . The remaining discrepancy can be explained by either uncertainty in beta-functions, which is known to be  $\pm 10\%$ , small ellipticity of the electron beam, mis-steering of the electron beam, which might play role if compared with  $a_e$ .

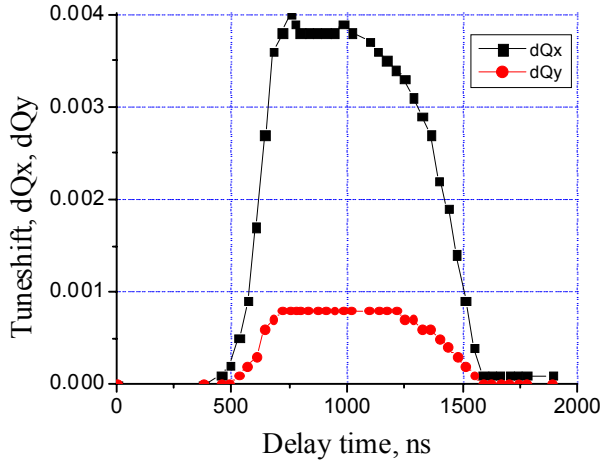


Figure 3: Shift of the horizontal (black) and vertical proton tunes vs delay between the proton bunch and 800 ns long, 1.96 A peak electron pulse,  $U_e = 6.0$  kV.

Having the electron beam properly synchronized for maximum effect, we have studied dependence of  $dQ_x$  on the peak electron current. The results are presented in Fig.4 and compared with Eq.(1). The theoretical dependence is non-linear because the electron energy inside the vacuum pipe and, thus,  $\beta_e$ , goes down with the current due to electron space charge,  $U_e = U_c - gQ_{sc}$ , where  $g$  is the geometry dependent factor. As seen in Fig.4, the maximum discrepancy is about 20% at  $J_e = 2$  A. There are systematic errors in a number of parameters used for calculations, e.g.,  $a_e^2$  is known within  $\pm 10\%$ , effective length  $L_e$  depends on precision of the steering and may vary within  $\pm 10\%$ , and the electron current calibration each contribute some  $\pm 5\%$  error. In addition there might

be some  $\pm 5\%$  uncertainty in the electron velocity  $\beta_e$  due to formation of an ion cloud which shields some fraction of the electron space-charge  $Q_{sc}$ . An indication of that is that maximum electron current allowed to propagate through the beam pipe at a given cathode potential of 7.5 kV goes down by 25% if the pulse repetition rate is reduced from 47.7 kHz (standard regime of operation with a single proton bunch) to about 50 Hz. On the other hand, ions do not change *charge density* and thus do not contribute to  $dQ$  directly most probably because of larger transverse size of the cloud.

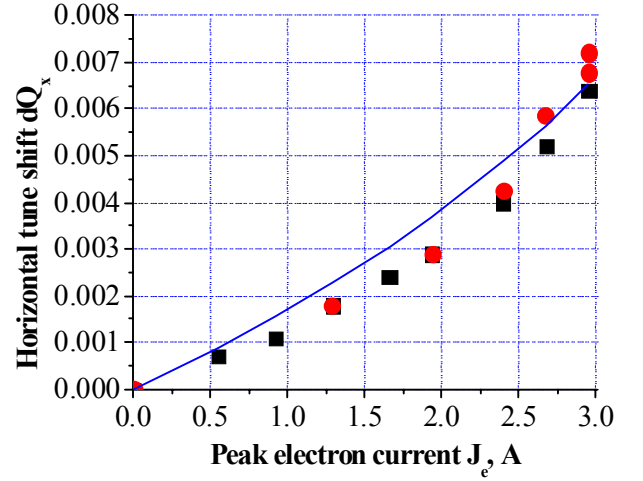


Figure 4: Shift of the horizontal proton tune vs the electron current,  $U_e = 7.5$  kV. Circles and squares – experimental data, solid line – Eq.(1).

It might be of interest to mention, that horizontal tune shift for protons coming just after the electron pulse (delay times from 0 to 400 ns in Fig.3) is slightly lower than  $dQ_x$  for protons arriving right before the electron beam enters the interaction region (delay times above 1600 ns). The little difference of about  $-0.0001$  electrons (if one believes that it is not just a measurement error) can be associated with defocusing effect due to ions freshly attracted inside the electron beam.

As long as the proton beam travels inside a wider electron beam, the proton tune shift does not depend much on the electron beam position, e.g., for the case 1 A electron beam  $dQ_x(d_x, d_y=0) = dQ_{max} = 0.0021$  if  $|d_{x,y}| < 2$  mm – see Fig.5. But when distance between centers of the two beams exceeds the electron beam radius then one should expect  $dQ_x(d_x, d_y=0) \approx -dQ_{max}/(d_x/a_e)^2$ ,  $|d_x| \gg a_e$ , and  $dQ_x(d_x=0, d_y) \approx +dQ_{max}/(d_y/a_e)^2$ ,  $|d_y| \gg a_e$  (note the sign). Theoretical predictions  $dQ_x(d_x, d_y)$  – see smooth curves in Fig.5 – are in a good agreement with experimental data. The only visible discrepancy is an asymmetry in  $dQ_x(d_x, d_y=0)$ . At negative horizontal displacements,  $d_{x,y} < -2.5$  mm, the tuneshift does not change sign as it does at  $d_{x,y} > +2.5$  mm. The effect is, most probably, due to the asymmetric  $\Pi$ -shape of the electron beam (see Fig.1), which results in additional positive contribution to  $dQ_x$ .

from the bending portions of the beam if the protons propagate through them.

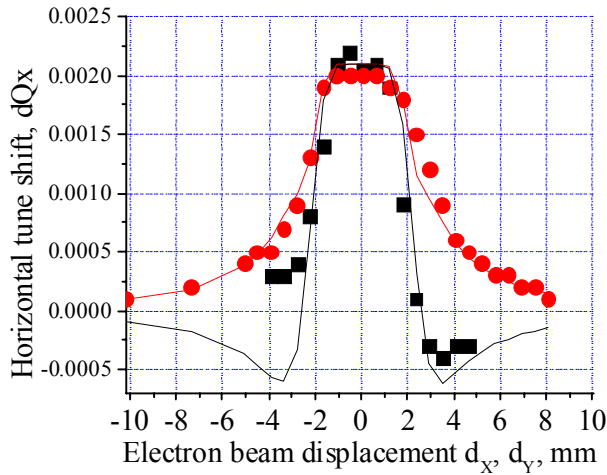


Figure 5: Horizontal tune shift vs horizontal (squares) and vertical (circles) displacement of the electron beam,  $J_e = 1A$ ,  $U_c = 6.0$  kV.

To summarize, we can say that experimentally observed tunes shifts agree reasonably well with theory.

### 3 TEVATRON BEAM LIFETIME WITH ELECTRON LENS

There is no formula to estimate the (anti) proton beam lifetime  $\tau = (dN/dt/N)^{-1}$  under impact of the TEL. Nevertheless, analytical studies [2] and numerical tracking [8] predict the following phenomena concerning the lifetime: 1)  $\tau$  depends on non-linear resonances in the vicinity of the machine working point; 2) it should decrease if the electron beam is mis-steered and protons experience non-linear forces of the electron beam; but if the beam-beam separation is very large, then the electron beam should not affect the lifetime; 3) one should expect better lifetime for the same  $dQ$  if the electron beam is wider and its current density profile is a smooth, bell-like function.

We found that without collisions the Tevatron proton beam lifetime is very good over a broad range of the beam parameters and the machine working points (WP)  $Q_x, Q_y$ . Because of the limited time of the studies, we measured lifetimes based on 15 minutes records of the beam intensity records. This resulted in some 50% error in  $1/\tau$  when typical lifetime was some  $\tau_0 = 90$  hours.

Collisions with the multi-Ampere electron beam did always cause certain deterioration of the  $\tau$ , but the best lifetime was observed at good WPs. Fig.6 shows the set of resonances up to 12<sup>th</sup> order over the range  $Q_{x,y} = 20.55$ -20.60 which is typical for the Tevatron collider operation. Arrows represent the tunes shift due to the TEL. The longest one reflects the result of the very first beam study shift, the very first attempt to operate the TEL with 150

GeV protons. All others were obtained with 980 GeV protons on different shifts. Numbers near each arrow show the best lifetime achieved at that WP with the maximum electron current. Electron and proton currents and beam sizes were about the same for all these observations while we can not guarantee that the electron beam was always steered with the same precision (see next Section).

One can see, that the smallest lifetimes of 1.5-6 hrs were observed when the Tevatron operated at the 7<sup>th</sup> order resonances at  $Q_x, Q_y = 0.573, 0.567$ , better lifetimes of 6-13 hours at the 12<sup>th</sup> order resonances  $Q_x, Q_y = 0.583, 0.577$ , and the best lifetime of 24 hours was achieved away from resonances at  $Q_x, Q_y = 0.564, 0.555$ .

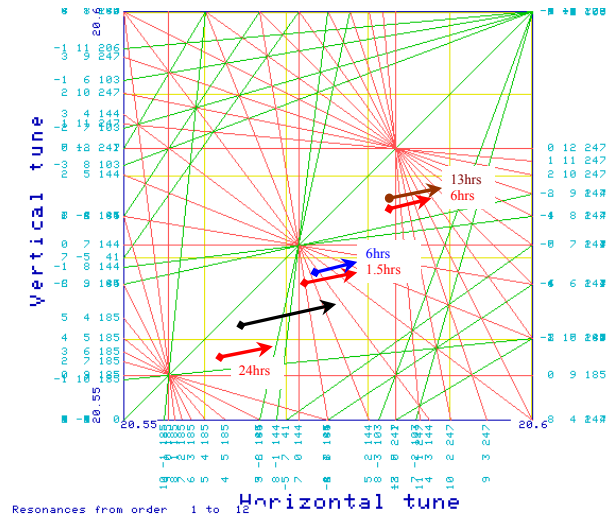


Figure 6: Proton bunch tunes shifts due to the TEL and corresponding lifetimes.

Our experience shows that mis-steering of the electron beam is by far the most important factor affecting the lifetime. It can affect  $\tau$  even at comparatively small electron currents. For example, Fig.7 shows a 20 minute record of the proton bunch population (top curve) which originally was about  $2.6 \times 10^{10}$  and the average electron beam current which was constant at 35mA.

The record was taken during the measurement of the tunes shift vs the electron beam position presented in Fig.5 ( $J_e = 1A$ ,  $U_c = 6.0$  kV) at the “better WP” of  $Q_x, Q_y = 0.583, 0.577$ . One can see that intensity does not go down smoothly, drops occur while we cross the electron beam edges. One may associate these with excitation of non-linear resonances. At very large electron currents we also detected significant proton emittance blow-up, which sometime made a good lifetime impossible after that.

On the other hand, if electron and proton beams are separated by some 5 mm (about 3 times the electron beam radius  $a_e$ ), then no deterioration of the proton beam intensity has been observed and the measured lifetime is about  $\tau_0$ .



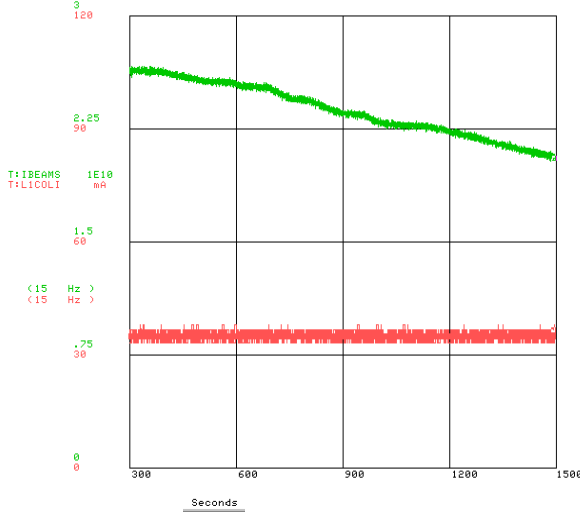


Figure 7: Proton beam intensity and electron current during the electron beam steering.

We did not have enough time to study the effect of the electron beam size and/or electron current density profile yet. The only indication that relative size matters is that when the proton emittance is 1.5-2 times larger than usual, e.g.  $40\text{-}60\pi$  mmmrad (95%) instead of  $25\pi$  mmmrad (corresponding to a rms horizontal beam size at the TEL location of 0.8-0.9 mm instead of typically 0.7 mm – compare with  $a_e = 1.75\text{mm}$ ), the lifetime becomes very poor.

#### 4 FUTURE STUDIES, IMPROVEMENTS

Topics for our further studies include: effects of the electron beam size and shape on the tunes and lifetime, emittance growth vs electron beam current and position stabilization, effects of ions, TEL operation with the Tevatron antiproton beam, and, finally, the TEL operation with many bunches. The ultimate goal of the studies is to achieve the same or better beam lifetime with the TEL at  $dQ$  comparable with the Tevatron beam-beam tune shift and around typical working points.

Further studies will require (in order of urgency): better electron beam steering, better proton beam diagnostics, and better quality electron beam. To achieve more precise steering we are currently working on the BPM hardware and electronics improvement (the existing ones gave unreliable readings of the proton bunch position).

Using “tickling” of the proton orbit with the electron beam can potentially improve the steering as well. The idea is similar to the “K-modulation” in the beam based alignment: variation of the electron current in the electron lens should cause variations in the proton beam orbit around the ring if the electron lens beam is not centered. Fig. 8 shows the rms amplitude of the vertical proton orbit variation at the Tevatron BPM located at A0 sector vs vertical displacement of the electron beam at F48 which had the current modulation of  $J_e = 1.02 +$

$0.18\sin(2\pi \cdot 107\text{Hz})$  A. The amplitude becomes equal to 0 if the proton beam goes through the center of the electron beam. The 7 mm distance between the two peaks reflects an effective diameter of the electron current distribution, and, thus, indicates angular misalignment of the electron beam because it exceeds the electron beam diameter of about 3.5 mm. Therefore, steering by the orbit tickling should concentrate not only on the search of the minimum orbit response, but also on having two maxima closer to each other. In the first experiments, such a tickling measurements took about 2-3 hours, and now we are looking for a faster automated system.

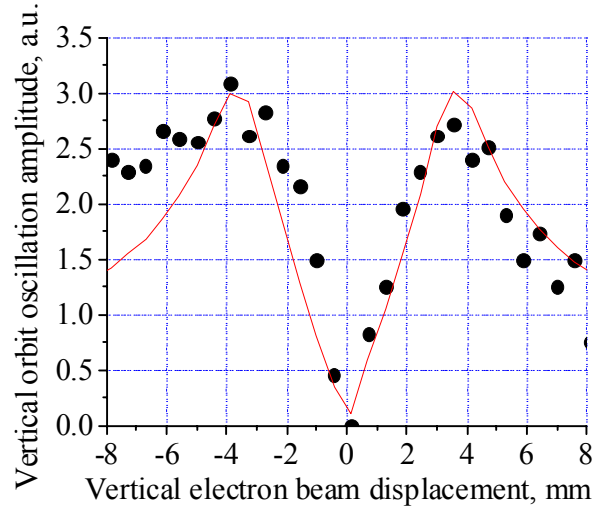


Figure 8: Rms amplitude of vertical proton orbit variation vs vertical position of AC electron beam.

We also look forward to having more reliable proton diagnostics for the emittance measurements (e.g., synchrotron light system instead of flying wires) and an automated tune measurement system for the multi-bunch measurements. R&D on the better electron beam for the TEL include a wider beam with smooth edges from new 10A, 30kV electron gun pulsed by 100ns solid-state HV FID-pulser [6], a better stabilization of the beam current and position, and a better control system

#### 5 CONCLUSION

We have experimentally demonstrated feasibility and operation of an electron lens. Experimental studies of the beam-beam effects in the electron-proton collisions have been performed and shown a decent agreement with theory. We will continue our studies on the beam-beam compensation with TELs. We found no “show-stoppers” yet, and we know what we have to do on each of the problems. Our studies with the 1<sup>st</sup> TEL should demonstrate that the electron lens does not deteriorate luminosity lifetime of the Tevatron. After the demonstration we will start fabrication of the 2<sup>nd</sup> TEL which will be installed at A10 sector of the Tevatron. The 2<sup>nd</sup> lens will complete the system for linear beam-beam

compensation which is supposed to start working routinely already in the Tevatron Run IIa (approximately at the end of 2003 – early 2004). The next step would be to study compensation of non-linear beam-beam effects. For that we will develop electron lenses with non-uniform (close to Gaussian) transverse electron current profile. If successful, the non-linear BBC can allow substantial increase of the collider luminosity. The increase may double if the non-linear BBC will allow to get rid of some 200  $\mu$ rad crossing angle at the Tevatron interaction points that is going to be introduced as soon as the Tevatron collider starts operation with 3 times shorter bunch spacing in the Run IIb (namely, 132 ns).

Besides linear and non-linear BBC, electron lenses - a novel type of accelerator element - can be used for cleaning, dumping and shaping high-energy beams, for space-charge compensation in low-energy proton boosters [9], for selective slow extraction from particular bunches

[10], for increasing transverse impedance and TMCI studies.

We sincerely thank all the people who contributed to the TEL design, fabrication, commissioning, and operation.

## 6 REFERENCES

- [1] V.Shiltsev, et.al, Phys.Rev. ST-AB, 2,071001(1999)
- [2] Y.Alexahin, et.al, Proceedings IEEE PAC 2001.
- [3] A.Ageev, et.al, Proceedings IEEE PAC 2001.
- [4] K.Bishofberger, et.al, Proceedings IEEE PAC 2001.
- [5] N.Solyak, et.al, Proceedings IEEE PAC 2001.
- [6] D.Wildman, et.al, Proceedings IEEE PAC 2001.
- [7] N.Solyak, et.al, Proceedings IEEE PAC 2001.
- [8] D.Shatilov, et.al, Proceedings IEEE PAC 2001.
- [9] A.Burov, et.al, Proceedings IEEE PAC 2001.
- [10] V.Shiltsev, J.Marriner, Proceedings PAC IEEE 2001.

# ANALYTICAL STUDY AND TRACKING SIMULATIONS OF THE BEAM-BEAM COMPENSATION AT TEVATRON

Y.Alexahin, V.Shiltsev, FNAL, Batavia, IL 60510,  
D.Shatilov, BINP, Novosibirsk, Russia

## Abstract

Compensation the beam-beam effect with the help of electron lenses [1] is considered, that includes elimination of the  $\bar{p}$  bunch-to-bunch tunespread due to the PACMAN effect (linear beam-beam compensation) and compression of the intrabunch nonlinear beam-beam tunespread (nonlinear compensation). It is shown that the influence of adverse side-effects of such compensation (excitation by the electron beams of the high order resonances remaining within the residual tunespread, reduction in the stabilizing tune dependence on amplitudes) can be minimized by an appropriate choice of the electron beam configuration and the working point in the tune diagram. Compression of the beam-beam tunespread by a factor of two is shown to be feasible.

## 1 INTRODUCTION

Owing to a number of reasons - a larger number of protons per bunch and a smaller proton emittance, a factor of seven larger number of the parasitic long-range interactions (see Table 1) - the beam-beam driven resonances (the synchro-betatron ones in particular) can present in the Tevatron Run IIa configuration [2] a greater danger for stability of antiprotons [3] than previously.

Another complication associated with the parasitic interactions is the so-called PACMAN effect: dependence of the tuneshifts on the bunch position in a train as illustrated by Fig.1a which shows the distribution of antiprotons in the tune diagram with the traditional for Tevatron choice of the bare lattice tunes,  $\nu_{x0}=20.585$ ,  $\nu_{y0}=20.575$ . Each of the 12 bunches in a train is represented by 3000 particles, tunes were calculated analytically using formulae of Ref.[3].

As can be seen from Fig.1a it is impossible to accommodate all particles in the area free of the

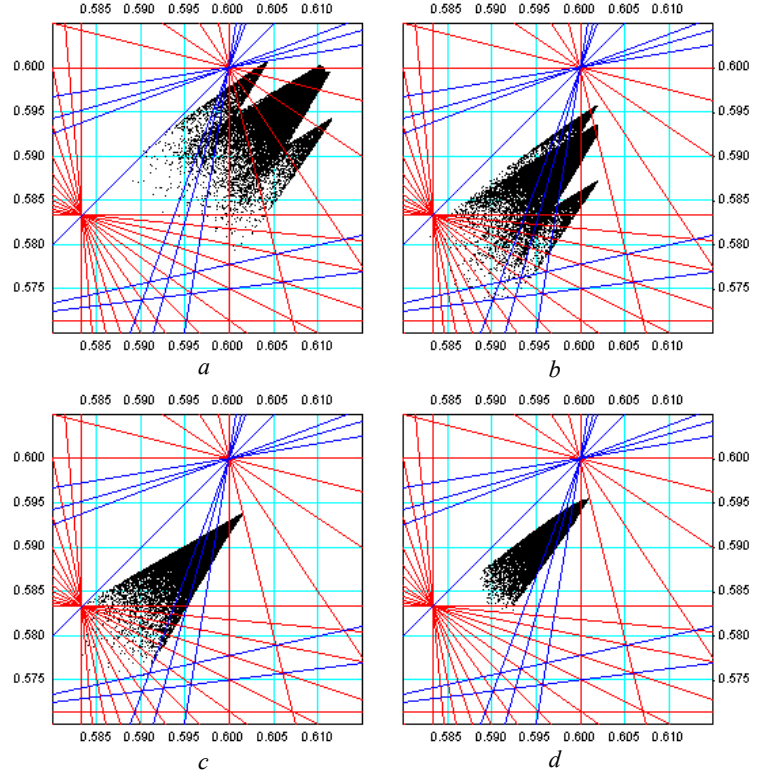


Figure 1: Antiproton beam footprint in the betatron tunes plane with: *a* – no BBC, *b* – linear BBC with 1 Tevatron electron lens (TEL), *c* – linear BBC with 2 TELs, *d* – nonlinear BBC with 2 TELs

resonances of the order lower than 13 which are shown with red and blue lines for the sum and difference resonances respectively.

The beam-beam tuneshift can be compensated with the help of electron lenses [1]. Two linear lenses created by electron beams of constant charge density can completely eliminate the bunch-to-bunch tunespread (linear beam-beam compensation), by choosing a bell-like shape it is possible to reduce the intrabunch nonlinear tunespread as well (nonlinear compensation). The question arises whether this will really improve the stability of antiprotons since the electron beams themselves may contribute to excitation of high order resonances remaining within the residual tunespread.

## 2 LINEAR COMPENSATION

Round electron beam of constant charge density acts as a linear lens on the antiprotons with amplitudes smaller than its radius  $a_e$  producing negative tuneshift in both transverse planes in proportion to the corresponding betatron function:

	Run Ib	Run IIa	Run IIb
$N_p/\text{bunch}$ , $10^{11}$	2.32	2.7	2.7
$\epsilon_p$ (95% norm.), $\pi \cdot \mu\text{m} \cdot \text{rad}$	23	20	20
$\xi/\text{nominal IP}$	0.0074	0.01	0.01
$N$ parasitic IPs	10	70	278
$\xi$ , total	$\sim 0.015$	$\sim 0.025$	$\sim 0.025$
$\epsilon_{p\text{bar}}$ (95% norm), $\pi \cdot \mu\text{m} \cdot \text{rad}$	13	15	15

Table 1. Parameters for different Tevatron runs.

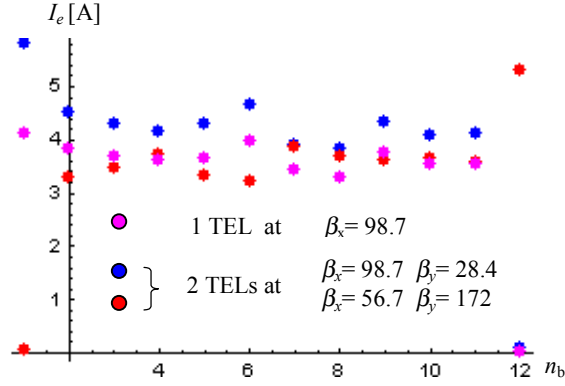


Figure 2: Electron beam currents needed for equalization of the horizontal tunes with one TEL (violet) and both horizontal and vertical tunes with two TELs (blue and red).

$$\Delta v_{x,y} = -\frac{1+\beta_e}{\beta_e} \cdot \frac{I_e L_e r_p}{2\pi \gamma_p e c a_e^2} \beta_{x,y} \quad (1)$$

where  $I_e$ ,  $L_e$  and  $\beta_e = v_e/c$  are respectively the electron beam current, length and velocity.

By modulation of the current in one electron lens (TEL1) placed at a location where  $\beta_x \gg \beta_y$  it is possible to equalize the horizontal tunes in all bunches without increasing the bunch-to-bunch vertical tunespread. Circles with violet fill in Fig.2 show what current the antiproton bunches should see in order to have equal horizontal tunes for small amplitude particles in the case of electron beam with  $a_e = 1.8$  mm,  $\beta_e = 0.2$ ,  $L_e = 2$  m at location where  $\beta_x = 98.7$  m,  $\beta_y = 28.4$  m. The resultant distribution in tunes (after some trimming of the bare lattice tunes as well) is shown in Fig.1b.

Adding a second electron lens (TEL2) at a location where  $\beta_x \ll \beta_y$  permits to equalize both horizontal and vertical tunes. The electron currents which are needed in this case are shown in Fig.2 by circles with blue and red fill. The radius of the second beam is  $a_e = 2.35$  mm, at its location  $\beta_x = 56.7$  m,  $\beta_y = 172$  m. The resultant tunespread is shown in Fig.1c.

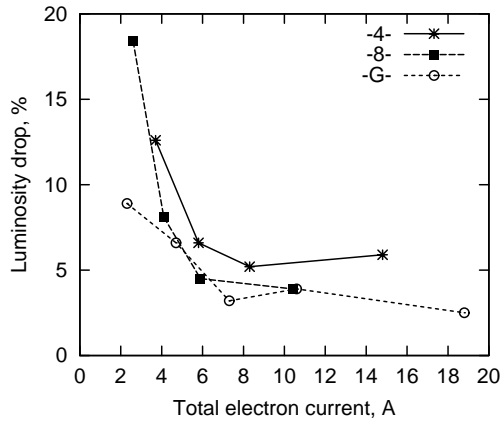


Figure 3: Luminosity drop vs. the electron current for different e-beam profiles: G – Gaussian, 4 and 8 – given by eq.(2) with  $\alpha = 0$  and  $n = 4$  and 8.

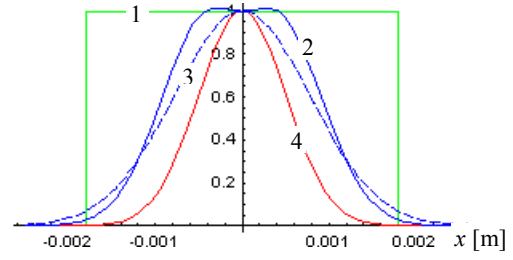


Figure 4: Space charge distribution: 1 – linear TEL, 2 – TEL with “profiler”, 3 – Gaussian distribution with the same current, 4 – antiproton beam at TEL1.

## 2.1 Numerical simulations

Though the electron beam radii were chosen sufficiently large (more than  $3\sigma_{pbar}$ ) the stability of tail particles which see the sharp edges of the electron beams is not guaranteed. Effect of the electron beam size and profile was a subject of extensive numerical simulations with the LIFETRAC code [4]. In these simulations only one TEL was considered which was located, as planned initially for the demonstration experiment, in the region with approximately equal betatron functions.

A few electron beam density profiles were taken: a Gaussian and ones described by the formula

$$\rho(r) = \rho_0 \frac{1 + \alpha(r/R_0)^2}{1 + (r/R_0)^n} \quad (2)$$

with  $\rho_0$  adjusted so that to keep  $\Delta v_{x,y} = -0.01$  at different values of parameters  $\alpha$  and  $n$ . The bare lattice tunes, after some scanning, were chosen to be  $v_{x0} = 20.566$ ,  $v_{y0} = 20.556$ .

Tracking with noise showed high sensitivity to and complicated dependence on the electron beam profile, however, some general trends can be established.

Fig.3 shows the relative luminosity reduction after  $3 \cdot 10^6$  turns as a function of the electron current for different space charge distributions. One can see that smoother the distribution, the lesser the observed drop in luminosity (i.e. the Gaussian one is the best of the three). However the total peak electron current required to keep the luminosity high is approximately the same for all three distribution functions: about 7A (that corresponds to

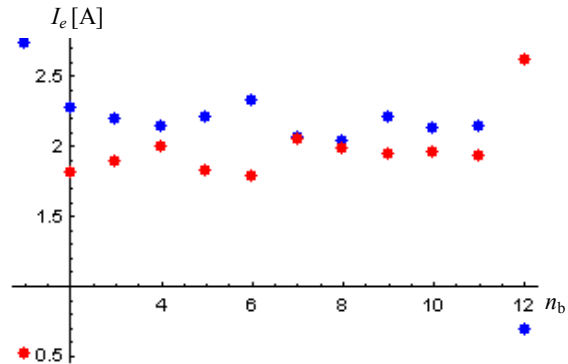


Figure 5: Electron beam currents needed for nonlinear beam-beam compensation with two TELs



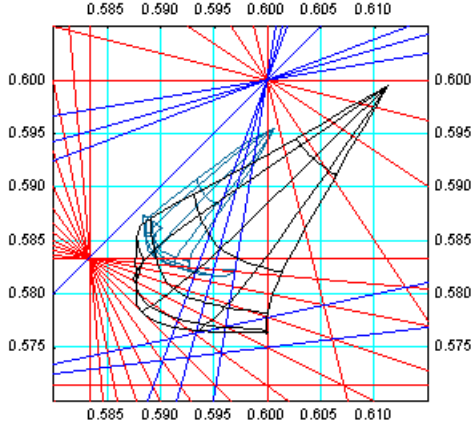


Figure 6: Original and compressed antiproton bunch #6 footprint in the vicinity of the standard working point.

$R_0 \sim 3\sigma_{pbar}$ .

A number of other issues were addressed in the simulations with one TEL: effect of the e-beam misalignment (meanders and offsets) and noise as well as the transient effect while aligning the e-beam with the orbit of antiprotons. The results can be briefly summarized as follows:

- Stationary offsets of up to  $0.2 R_0$  are tolerable.
- Meandering of the electron beam around the  $\bar{p}$  orbit with amplitude of  $0.25 R_0$  produce no harmful effect; this opens a possibility to vary the e-beam effective aspect ratio by deliberately bending the beam with correctors.
- The process of the electron beam alignment, if started from large initial offsets ( $\geq R_0$ ), destroys the antiproton beam. Therefore it has to be done in a few steps, each time with a new  $\bar{p}$  bunch and/or using initially lower electron beam current.
- The  $\bar{p}$ -beam emittance dilution due to random turn-by-turn fluctuations in the e-beam position and current is found to be in a good agreement with the previous analytical estimates [1], for example, the relative current fluctuation of  $2.2 \cdot 10^{-3}$  gives 10 hrs growth time.

### 3 NONLINEAR COMPENSATION

There are several disadvantages inherent to the linear beam-beam compensation (BBC):

- the intrabunch nonlinear tunespread is much larger than the bunch-to-bunch tunespread being compensated; therefore it is still difficult to accommodate the total footprint in a resonance free area;
- there is strong excitation of high order resonances for antiprotons with large betatron amplitudes which see the steep edges of the electron beam;
- the electron beam current, owing to a large beam radius, should be high ( $\geq 6A$ ) easily reaching the electrostatic limit in the Tevatron beam pipe [1]; a high-current electron beam may also produce an unwanted effect on the protons.

These problems can be simultaneously solved by shaping the electron beam in the gun with a Pierce-like

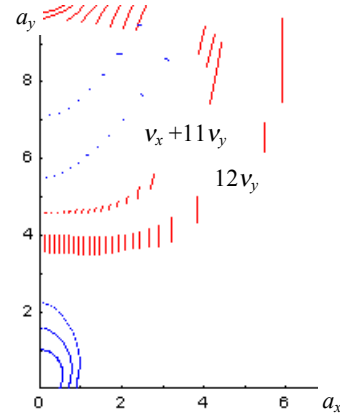


Figure 7: Swing of the betatron amplitudes due to resonances encountered by particle of bunch #6 at the nominal working point with BBC.

electrode [5] (a “profiler”) so that it had a smaller r.m.s. size and smoother edges as shown in Fig.4 with the solid blue line.

#### 3.1 Footprint compression

With the electron and antiproton beam sizes becoming comparable, the tuneshift produced by the electron lens acquires the amplitude dependence which is similar to that of the tuneshift from the head-on collisions with the proton beam. In the result the total tunespread within a single antiproton bunch can be compensated to the extent determined by the contribution of the long-range interactions.

Obviously, to benefit from such compensation one should eliminate the bunch-to-bunch tunespread first, so again two electron lenses are necessary. We assume them to be at locations with the betatron function values cited in the previous section and to have the HWHM sizes  $r_e = 1$  mm in TEL1 and  $r_e = 1.3$  mm in TEL2. The electron currents that provide a complete compensation of the bunch-to-bunch tunespread and compress the intra-bunch nonlinear tunespread by a factor of two are shown in Fig.5. Due to smaller e-beam sizes they are twice lower than those needed for the linear BBC.

The effect of TELs on the total tunespread is shown in Fig.1d; compensation of the nonlinear tunespread in a particular bunch is illustrated by Fig. 6. It shows the antiproton bunch #6 footprint in the tune diagram without BBC (black) and with it (teal blue). The bare lattice tunes (assumed nominally to be  $\nu_x = 20.585$ ,  $\nu_y = 20.575$ ) were slightly trimmed in the latter case. The arc lines correspond to equidistant with step 2 values of the total transverse amplitude

$$a_{\perp} = \sqrt{a_x^2 + a_y^2}, \quad (3)$$

where  $a_{x,y}$  are taken in the  $\bar{p}$  r.m.s. sizes, the radial lines correspond to constant values of  $a_x/a_y$ .

It can be seen that the footprint “folding”, which is caused by the long-range interactions with the proton beam and without BBC happens at amplitudes  $\sim 8\sigma$ , with BBC takes place at amplitudes as low as  $5\sigma$ . Since even very weak high order resonances may lead to a fast

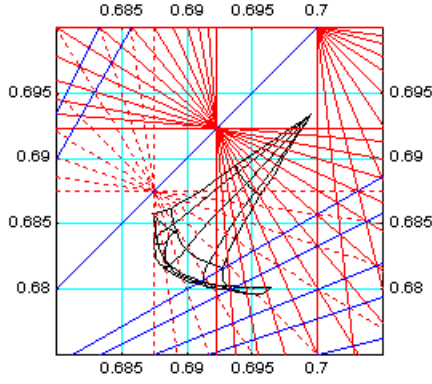


Figure 8: Bunch #6 footprint at the SPS WP with BBC by two Gaussian TELs

particle transport over the region of folding thus reducing the particle lifetime, this effect sets a natural limit on the degree of the footprint compression.

Another limitation comes from the requirement that the tune modulation by the synchrotron motion due to finite dispersion at the TEL locations was small:  $r_e \gg D_x \sigma_E \approx 1.7 \text{ m} \times 9 \cdot 10^{-5} \approx 0.15 \text{ mm}$ , to avoid strong excitation of the synchrotron satellites of betatron resonances.

### 3.2 Resonance excitation

The electron beams of TELs can themselves contribute to excitation of resonances. Fig.7 shows beatings of the betatron amplitudes (calculated analytically in a single resonance approximation) due to resonances encountered by antiprotons of bunch #6 whose footprint with BBC was shown in Fig.6 in teal blue.

Due to the TEL contribution the width of the  $12\nu_y$  resonance is much larger than that of the  $\nu_x + 11\nu_y$  resonance which, in the absence of misalignments, is excited exclusively by the long-range interactions.

For off-momentum particles the effective resonance width is even larger owing to the synchrotron satellites.

#### 3.2.1 Choice of the working point

The compressed with TELs footprint can fit into other areas in the tune diagram which are surrounded by less dangerous resonances. One such possibility, with the

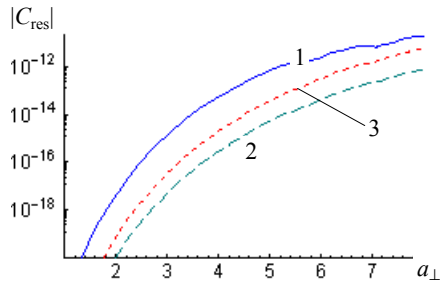


Figure 9: The  $10\nu_x + 6\nu_y$  resonance driving term for  $a_x = a_\perp/2^{1/2}$ : 1 – 2 TELs with flat-top e-beam (Fig.4, curve 2), 2 – 2 TELs with Gaussian e-beam, 3 – 1 TEL with Gaussian e-beam at location with  $\beta_x = \beta_y$ .

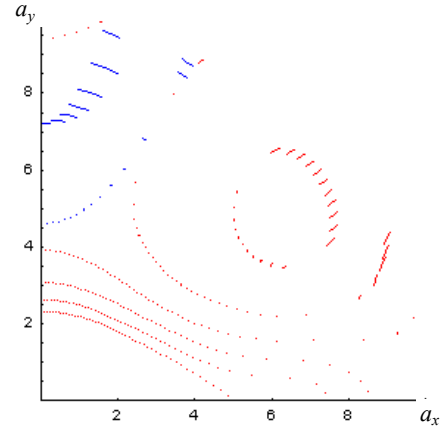


Figure 10: Swing of the betatron amplitudes due to resonances at the SPS WP with BBC by two Gaussian TELs.

tunes around  $\nu_x = 20.563$ ,  $\nu_y = 20.557$ , was considered for the linear BBC [4]. However, this area is not wide enough to avoid setting some particles on either 7<sup>th</sup> or 9<sup>th</sup> order resonances. Another option is the SPS working point [6]. The compressed with TELs footprint at the bare lattice tunes  $\nu_x = 20.689$ ,  $\nu_y = 20.682$  (which we refer to as the SPS WP) is shown in Fig.8.

#### 3.2.2 Effect of the electron beam profile

Excitation of the 16<sup>th</sup> order resonances (and its satellites) by TELs can facilitate diffusion of antiprotons, especially in the region of amplitudes where the footprint folding occurs. As the example of  $10\nu_x + 6\nu_y$  resonance shows (Fig.9), excitation of high order resonances by TELs can be reduced by making the e-beam charge distribution more monotonous (e.g. Gaussian). One more advantage is that the footprint folding occurs at somewhat larger amplitudes with the Gaussian e-beams (compare the compressed footprints in Figs.6 and 8).

Analytical calculation of the beatings of the betatron amplitudes at the SPS working point in the case of Gaussian e-beams predicts only moderate effect of the difference resonance  $3\nu_x - 6\nu_y$  on the tail particles (Fig.10).

#### 3.2.3 Effect of the number of TELs

There is an additional argument (besides compensation of the PACMAN effect) in favor of using two TELs at points with  $\beta_x \gg \beta_y$  and  $\beta_x \ll \beta_y$ , rather than one TEL at a location with equal  $\beta$ 's. From the resonances excited by TELs the high-order sum resonances are the most dangerous (the WP can always be chosen so that the uni-dimensional ones were reached at too small amplitudes to be noticeable or not reached at all). Since the driving term of the  $k\nu_x + l\nu_y = n$  resonance contains the factor  $\beta_x^{k/2} \beta_y^{l/2}$ , its excitation is significantly suppressed in the case of two TELs, as illustrated by Fig.9 (curves 2,3). In all cases TELs provided the same horizontal tuneshift  $\Delta\nu_x = -0.014$ .

#### 3.2.4 Effect of the finite dispersion

Owing to the finite dispersion TELs can contribute to excitation of the synchro-betatron resonances (SBRs)

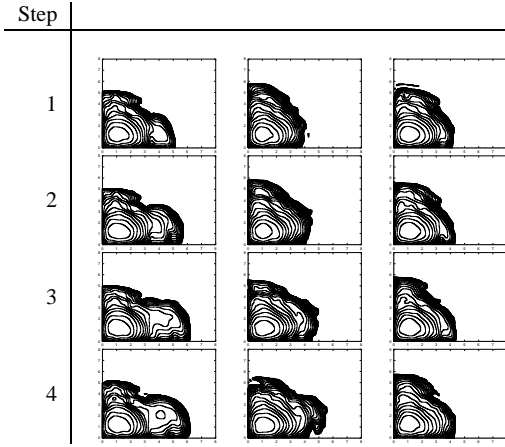


Figure 11: Evolution (from top to bottom) of the density of antiprotons in the  $(a_x, a_y)$  space with the step of  $10^5$  turns in the cases described in the text.

two-fold: via the tune modulation arising from the steep fall-off of the instantaneous tunes with the displacement  $D_x \delta_p$ , and via variation of the nonlinear component of the TEL field seen by an antiproton in the course of the synchrotron motion.

According to the estimates the second effect should not be important, whereas the first one, *the TEL second order chromaticity*, is big: TEL tunes shift is modulated by more than 20% at  $a_s = 3$ . Both effects can be reduced, if necessary, by increasing the e-beam radius.

### 3.3 Numerical simulations

All the above presented results were obtained in the single resonance approximation using analytical formulae of Ref.[3]. More realistic picture can be obtained by tracking simulations with the code LIFETRAC which can take into account the cooperative action all beam-beam and TEL nonlinearities and the external noise.

Fig.11 shows evolution of the bunch #6 density at the SPS WP with the BBC by two Gaussian TELs which provide zero-amplitude tunes shifts of  $\Delta v_x^e \approx -0.0144$ ,  $\Delta v_y^e \approx -0.0115$ . With the bare lattice tunes 20.689, 20.682 the 13<sup>th</sup> order resonances proved to be strong enough to affect the core particles (left column). With tunes shifted down by 0.005 (center column) the core was not affected, still some tails had developed which were not seen in the test run with linear lenses instead of TELs. Weakening the TELs nonlinearity by a 15% increase in the e-beam sizes diminishes the tails (right column). In all three cases neither luminosity nor lifetime had suffered.

## 4 CONCLUSIONS

- With the help of two electron lenses it is possible to completely compensate the bunch-to-bunch tunespread (PACMAN effect) and partially reduce the intrabunch nonlinear tunespread.
- The degree of nonlinear BBC is limited by the footprint “folding” due to the long-range contribution and the electron lens chromaticity due to finite dispersion.

- The possibility to eliminate the footprint folding by additional compensation of the long-range interactions (e.g. with pulsed wires) should be studied.
- Excitation of high order resonances by TELs can be reduced by choosing a smooth electron beam charge distribution (e.g. Gaussian) and using two TELs at points with strongly unbalanced  $\beta$ -functions.
- Compression of the footprint by a factor of two permits to fit it in the areas free of resonances of orders lower than 13, the neighborhood of the SPS working point being a promising candidate.
- Compensation of the beam-beam effect appears to be a viable method to achieve and surpass the Run II design goals.

## 5 REFERENCES

- [1] V.Shiltsev et al., PRST-AB, v.2, 071001 (1999).
- [2] <http://www-bd.fnal.gov/runII/index.html>
- [3] Y.Alexahin, FERMILAB-TM-2148 (2001).
- [4] D.Shatilov, V.Shiltsev, FERMILAB-TM-2124 (2000)
- [5] A.Shemyakin et al., Proc. EPAC 2000, Vienna, p.1271.
- [6] K.Cornelis, Proc. LHC99, CERN-SL-99-039 AP, p.2

# CORRECTION OF THE LONG-RANGE BEAM-BEAM EFFECT IN LHC USING ELECTRO-MAGNETIC LENSES

J.P. Koutchouk, CERN, Geneva, Switzerland

## Abstract

The beams in LHC collide head-on in at most four experimental points. Due to the small bunch spacing, the beams experience more than one hundred ‘near-misses’ on either side of the collision points. The transverse beam separation at these places, limited by the quadrupole aperture, is in the range of 7 to  $13\sigma$ . The non-linear part of these ‘long-range’ interactions appears to be the dominant mechanism for beam blow-up or beam loss in simulation. A simple non-linear model of the long-range interactions can be devised. It shows that the latter may be locally corrected with good accuracy using wires as correcting lenses. The non-linearity measured by the tune footprint is reduced by one order of magnitude. Pulsing the correcting lenses cancels the so-called PACMAN effect.

## 1 THE LONG-RANGE BEAM-BEAM INTERACTIONS IN LHC

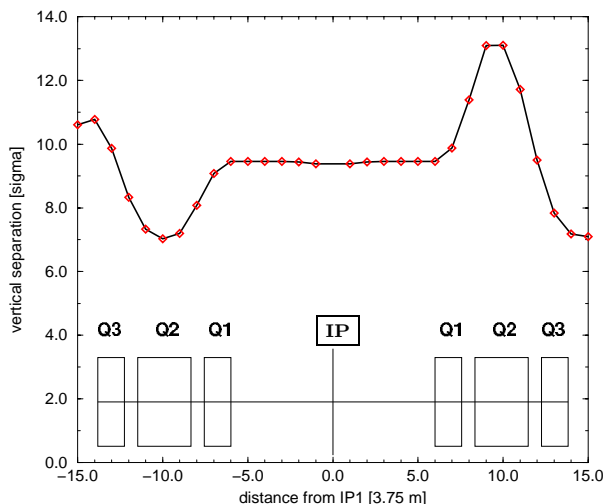


Figure 1: Beam separation in the crossing angle ( $\pm 150 \mu\text{rad}$ ) plane of IP1 in  $\sigma$ 's

With a 25 ns bunch spacing, there would be 31 head-on collisions per experimental insertion in the absence of the  $\pm 150 \mu\text{rad}$  crossing angle. The aperture of the single-bore low- $\beta$  quadrupoles does not allow to increase it much above its nominal value. In the high-luminosity proton mode, the beam size is squeezed in two of the four collision points (IP1 and IP5). The larger beam divergence sets the normalized beam separation to  $9.5\sigma$  on average (Figure 1). In the other two collision points, the normalized separation

is much larger. Their contribution to the long-range (LR) beam-beam effect can be neglected.

The machine parameters were chosen to limit to 0.01 the tune spread due to the beam-beam effect. This criterion, successfully tested in the Sp $\bar{p}$ S for the head-on beam-beam effect, is extended, for LHC to its LR component as well. In spite of the crossing angle, the footprint of the latter is still 65% of that due to the head-on collision.

Tracking studies using as a criterion the dynamic aperture [1] [2], the diffusion in tune or amplitude [4] [3] [5] have demonstrated the importance of the LR interactions. Even-though the footprint criterion is fulfilled, losses of particles occurs at  $8.5\sigma$  and a significant diffusion in amplitude and tune is observed at lower amplitudes. The LR effect acts as the dominant destabilizing mechanism.

The alternating crossing angles [6] in IP1 and IP5 minimize the tune footprint by a compensation of the linear detunings. We propose in this paper a correction principle able to cope with the non-linear part as well.

## 2 MODEL OF THE LONG-RANGE BEAM-BEAM KICKS

We consider a slightly simplified model of the LR beam-beam interactions for the design of the correction system. The test of its efficiency is carried out without these simplifications. Only one of the two identical insertions is considered without losing generality. Following the tradition, the sample particle of one beam is called the weak beam. It suffers from the perturbation of the second ‘strong’ beam.

### 2.1 Layout and Strength of the LR Effect

Due to the strong focusing of the low- $\beta$  quadrupoles, the 15 LR kicks experienced by the weak beam on each side of an IP are very close in betatron phase. Their average and rms phase shifts from the IP are  $88.5^\circ$  and  $2.0^\circ$ . For 80% of the kicks, the rms phase difference is  $0.4^\circ$  only. We can therefore lump the kicks.

The anti-symmetric optics of the low- $\beta$  section causes the Twiss parameters to be unchanged when changing simultaneously the plane and the side of the IP. Figure 1 shows that the beams are round to within 10% in about 60% of the cases. The largest aspect ratio is about 1.8 as compared to a beam separation of at least 7 in the same units. We therefore assume in the model round beams.

The nominal number of particles per bunch is  $1.1 \cdot 10^{11}$  for a rms bunch length of 7.7 cm. Assuming a total bunch length  $\sqrt{2\pi}\sigma_s$ , the instantaneous beam current is 27.36 A (43.77 A for the ultimate performance).

## 2.2 Model of the Beam Magnetic Field

For ultra-relativistic counter-rotating beams, the forces exerted by the electric and magnetic fields are equal. The interaction time is half the bunch length. The kick is the same when integrating the magnetic force only over the full bunch length. Assuming a Gaussian cylindrical charge distribution, the expression of the magnetic field is:

$$B_\theta = \frac{\mu_0}{2\pi} \frac{I_b}{r} (e^{-r^2/2\sigma_s^2} - 1) \quad (1)$$

$I_b$  is the beam current,  $r$  the distance between the center of the strong beam and the weak beam,  $\sigma_s$  the transverse beam size of the strong beam.

The largest amplitude of the betatron oscillation allowed by the collimation system is  $6\sigma$ . In the worst case where this amplitude is fully in the plane of the beam separation, the exponential term in Eq. 1 accounts for 4% of the integrated magnetic field over the 30 LR interactions. Averaging over the betatron phase, it is reduced to 1%.

An electric current in a wire is therefore a good model for the strong beam in the LHC LR interactions. The multipole expansion of this model magnetic field is given by:

$$B_y + iB_x = \frac{\mu_0 I_b}{2\pi r_0} \sum_{n=1}^{\infty} (-\cos n\phi - i \sin n\phi) \frac{(x + iy)^{n-1}}{r_0^{n-1}} \quad (2)$$

where  $r_0$  is the closed orbit difference between the beams,  $\phi$  the azimuthal angle and  $x$  and  $y$  the betatron coordinates of the weak beam. A naive calculation of e.g. the integrated  $b_{10}$  shows an integral much larger than that due to the low- $\beta$  quadrupole field imperfections and may give a clue to the seriousness of the LR effect.

## 2.3 Scaling of the LR Perturbation

The perturbation of the motion is proportional to:

$$\int_{l_{LR}} \sqrt{\beta_{x/y}} \frac{B_{y/x}}{B\rho} ds \quad (3)$$

If  $r_0$ ,  $x$  and  $y$  scale with the same  $\sqrt{\beta}$ , the perturbation does not depend on the  $\beta$ -function. This is the case for about all LR encounters in the experimental straight-section (about 50% of the total).

# 3 LR CORRECTION SCHEME

## 3.1 Principle of the Correction

The model of the LR beam-beam kicks points clearly to the possibility of correcting the LR beam-beam effect (linear and non-linear) by means of an electric current in a conductor running parallel to the weak beam. Assuming such a corrector on each side of the IP, the integrated intensity shall be  $27.36\text{A} \times \sqrt{2\pi} \times 7.7\text{cm} \times 15 \approx 80\text{ A m}$  with a sign opposite of that of the strong beam.

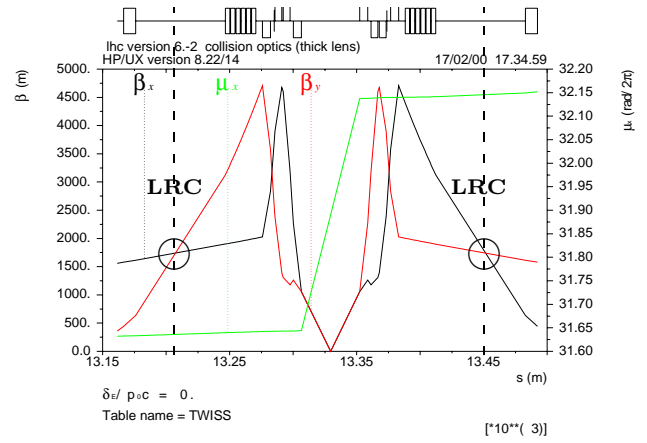


Figure 2: Twiss parameters in IR5 and schematic positions of the correctors for a horizontal crossing.

## 3.2 Transverse Position of the Correctors

The respective transverse positions of the corrector and weak beam should be the same as that of the strong and weak beams at the LR interaction points. For a horizontal crossing, the correctors should be placed between the two beams. For a vertical crossing, they should be placed above or below the weak beam. Eq. 3 remains invariant if the beam-corrector separation  $r_0$  scales with the  $\beta$ -function. Hence the correctors shall be placed at  $9.5\sigma$  from the weak beam. This provides an exact correction of the LR interactions occurring in the straight-section and an approximate one for the others. This approximation is later investigated numerically. Eq. 3 shows further that any other scaling, i.e.  $I$  versus  $r_0$  does not allow the simultaneous compensation of all linear and non-linear terms. The separation of  $9.5\sigma$  puts the corrector in the shadow of the secondary collimator. Figure (2) shows a schematics of the corrector set-up.

## 3.3 Longitudinal Position of the Correctors

Positions with equal  $\beta$ -functions in the two planes may be found on the other side of the triplet versus the IP (Figure 2). At these positions (112m from the IP's), the beam separation is almost nominal ( $\approx 100\sigma$ ) and sufficient to install instrumentation acting on a single beam. The betatron phase shift between these positions and the LR interaction points is  $2.6^\circ$ , owing to the very large  $\beta$ -functions. This small phase shift should guaranty that the phase-dependent non-linear terms are well compensated (e.g. factors of 5 and 2 for 5th and 11th-order resonances).



## 4 NUMERICAL SIMULATIONS

### 4.1 Model for the Simulation

LHC v6 is used in its full complexity. To allow a faster evaluation in the MAD tracking, the part of the lattice which does not include LR interactions or correctors is mapped at the order 3 in the Hamiltonian. The LR corrector is represented by a beam-beam lens whose beam size is artificially reduced ( $\sigma/100$ ), providing a field in  $1/r$  with great accuracy. The correctors are positioned on each side of the IP at a position where the  $\beta$ -functions are the same in the two planes on the unperturbed machine. They are transversely displaced by  $9.5\sigma$ . The criteria used to judge on the efficiency of the correction are: the betatron tunes, the closed orbit at another collision point and the largest extent of the tune footprint. The latter is calculated by tracking a set of initial conditions on circles in the  $x, y$  plane with radii ranging from  $\sqrt{x^2 + y^2} = 1\sigma$  to  $6\sigma$ . By symmetry, there is no orbit perturbation at the IP under consideration.

### 4.2 Test of the Correction

This artificial example allows an exact correction. Only the LR interactions occurring in the experimental straight-section are retained (12 in total) and their strength increased to keep the same integrated kick. Table 1 shows a practically perfect correction.

Name	$Q_x$	$Q_y$	$\Delta Q(6\sigma)$
no beam-beam	.2800	.3100	.0033 $10^{-3}$
12 LR's	.2820	.3080	2.2 $10^{-3}$
after correction	.2800	.3100	.0092 $10^{-3}$

Table 1: Results of the correction test

### 4.3 A Realistic Correction in IP5

The LR interactions in the quadrupoles are now added. Table 2 and Figure 3 show that the compensation is almost exact for the orbit and reduces the footprint by a factor of 5. If the current in the correctors is empirically increased

Name	$Q_x$	$Q_y$	$x_{IP1}$ $\mu\text{m}$	$\Delta Q(6\sigma)$ $10^{-3}$
no beam-beam	.2800	.3100	0	.0033
All LR's	.2824	.3076	2.6	3.5
Nominal correction	.2802	.3098	.09	.65
Optimized correction	.2799	.3100	.25	.275

Table 2: Results of a realistic correction in IP5

by 13%, the footprint is further reduced by a factor 2 and the orbit perturbed in a negligible way. Given the small betatron phase shift between perturbation and correction, the tune footprint should be a rather faithful image of the other non-linear terms.

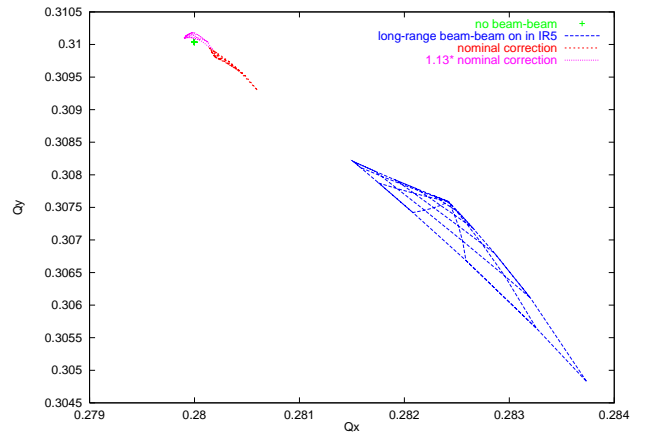


Figure 3: Tune footprints before and after corrections

### 4.4 Robustness

Due to the summation of the LR kick over 15 bunches, the expected 20% bunch intensity spread is reduced to a 5% effect. The scheme is insensitive to a change of the closed orbit of the weak beam. The dependence on the exact corrector current appears non critical (Table 2).

## 5 CONCLUSION

We show that the long-range beam-beam interactions, presently considered as the most drastic limitation of LHC performance, can be rather accurately corrected for both their linear and non-linear perturbations. The principle of the corrector is simple and considered challenging but feasible by the experts. A dc operation of the correctors compensates the LR effect for nominal bunches. The so-called PACMAN bunches can be taken care off by pulsing the system at 1/15 of the bunch frequency.

## 6 ACKNOWLEDGEMENTS

To S. Fartoukh, H. Grote, J.M. Jowett and G. Schröder.

## 7 REFERENCES

- [1] W. Chou, D. Ritson, 'Dynamic aperture studies during collisions in the LHC', CERN LHC Project Report 123, 1997.
- [2] J. Miles in M. Boege *et al.*, 'Overview of the LHC dynamic aperture studies', LHC Project Report 106, 1997.
- [3] T. Sen *et al.*, 'Effect of the beam-beam interactions in the LHC', CERN-SL-99-039 AP, 1999.
- [4] Y. Papaphilippou, F. Zimmermann, 'Weak-strong beam-beam simulations for LHC', CERN-SL-99-039 AP, 1999.
- [5] H. Grote *et al.*, 'LHC Dynamic Aperture at Collision', LHC Project Note 197, 1999.
- [6] W. Herr and J. Miles, 'Optimizing the LHC Interaction Region for Luminosity', LHC Project Report 40, 1996.
- [7] H. Grote, O. Meincke, 'Tune Footprints for Collision Optics 5.0', LHC Project Note 161, 1998.

# Weak-Strong Simulation Studies for the LHC Long-Range Beam-Beam Compensation

F. Zimmermann, CERN, Geneva, Switzerland

## Abstract

Using weak-strong computer simulations, we study the improvement of LHC tune footprints and dynamic aperture by electromagnetic lenses, *i.e.*, pulsed wires, which compensate for the long-range beam-beam interaction. In particular, we explore the robustness of this compensation scheme to linear optics imperfections as well as to errors in wire strength and position.

## 1 INTRODUCTION

The long-range or parasitic collisions are expected to limit the dynamic aperture of the LHC [1, 2, 3]. A compensation scheme for the effect of the long-range collisions, proposed by J.-P. Koutchouk, is presently under investigation at CERN [4, 5, 6]. The compensation employs an electric wire on each side of each interaction point (IP). The wire carries an integrated current of about 80 Ampere meter, and it is placed at a horizontal or vertical distance from the beam that equals the effective beam-beam separation at the long-range encounters, about  $9.5\sigma$  at top energy. If the current is pulsed or ramped at the start of each bunch train the correction can work even for the so-called PACMAN bunches [7], *i.e.*, for bunches which do not experience the full set of long-range encounters, due to gaps in the opposing beam.

In this report, we report weak-strong simulation results for the wire compensation scheme. The simulation program is the same as described in Ref. [2], except that two electric wires have been added. Considering two head-on collisions with alternating crossing and the parasitic collisions around each head-on IP, the simulation yields the tune footprints and the action diffusion rate at various betatron amplitudes. Using this simulation, we study the sensitivity of the wire compensation to various errors, such as to errors in the wire position, the wire strength, or the betatron phase advance between the wire and the collision point.

Section 2 describes the simulation model in more detail. Results are presented in Section 3. Conclusions are drawn in Section 4.

## 2 MODEL

The simulation study follows John Irwin's approach for the SSC [2, 8]. It is a 4-dimensional code, without synchrotron oscillations. However, tune modulation can be included as an option.

We consider two IPs, one with horizontal crossing, the other with vertical. This models the two main IPs in the

Table 1: Parameters.

parameter	symbol	value
number of particles per bunch	$N_b$	$1.1 \times 10^{11}$
beam energy	$E_b$	7 TeV
rms beam size at IP	$\sigma_{x,y}^*$	$16 \mu\text{m}$
rms divergence at IP	$\theta_{x,y}^*$	$31.7 \mu\text{rad}$
IP beta function	$\beta_{x,y}^*$	50 cm
full crossing angle	$\theta_c$	$300 \mu\text{rad}$
number of main collision points	$n_{IP}$	2
parasitic collisions per side	$n_{\text{par}}$	16
bunch spacing	$L_{\text{sep}}$	7.48 m
beam-beam parameter	$\xi$	0.00342
revolution frequency	$f_{\text{rev}}$	11.25 kHz

LHC. Simulation parameters are summarized in Table 1. At the parasitic collision points the beams are separated by  $\theta_c/\theta_{x,y}^* \approx 9.5$  rms beam sizes. The fractional tunes are set to the LHC design values of 0.31 and 0.32. The phase advance between IPs is taken to be exactly half the total phase advance per turn.

At each IP we apply a series of 3 kicks representing, respectively,

- the lumped effect of long-range collisions and wire compensation on the incoming side,
- a head-on collision,
- the lumped effect of long-range collisions and wire compensation on the outgoing side.

### 2.1 Head-On Collision

The head-on collision with a round Gaussian beam is parametrized as

$$\Delta x' = \frac{2r_p N_b}{\gamma} \frac{x}{r^2} \left( 1 - e^{-\frac{x^2}{2\sigma^{*2}}} \right) \quad (1)$$

$$\Delta y' = \frac{2r_p N_b}{\gamma} \frac{y}{r^2} \left( 1 - e^{-\frac{x^2}{2\sigma^{*2}}} \right) \quad (2)$$

where  $\sigma^* \equiv \sigma_x = \sigma_y$ ;  $r = \sqrt{x^2 + y^2}$  is the radial distance to the origin,  $r_p$  the classical proton radius,  $\gamma$  the Lorentz factor, and  $N_b$  the bunch population. The phase-space coordinates  $x$ ,  $x'$ ,  $y$ , and  $y'$  refer to the IP.

### 2.2 Long-Range Interactions

All parasitic collisions ( $n_{\text{par}}$ ) on one side of the IP are lumped into a single deflection. Assuming a perfect  $\pi/2$

distance in phase advance between head-on and parasitic collision points, the kick is approximately expressed as a change in the IP coordinate (while the IP angle stays unchanged). For the IP with horizontal crossing, the IP coordinates and slopes are changed according to

$$\Delta x = n_{\text{par}} \frac{2r_p N_b}{\gamma} \left[ \frac{x' + \theta_c}{\theta_t^2} \left( 1 - e^{-\frac{\theta_t^2}{2\theta^{*2}}} \right) - \frac{1}{\theta_c} \left( 1 - e^{-\frac{\theta_t^2}{2\theta^{*2}}} \right) \right] \quad (3)$$

$$\Delta y = n_{\text{par}} \frac{2r_p N_b}{\gamma} \frac{y'}{\theta_t^2} \left( 1 - e^{-\frac{\theta_t^2}{2\theta^{*2}}} \right) \quad (4)$$

where

$$\theta_t \equiv ((x' + \theta_c)^2 + y'^2)^{1/2} \quad (5)$$

and  $\theta^* \equiv \theta_x^* = \theta_y^*$  is the rms IP beam divergence. At the LHC, the effective number of parasitic crossings per side is  $n_{\text{par}} \approx 16$ . The expression for the kick is the same on both sides of the IP. The second IP, with vertical crossing, is treated analogously.

### 2.3 Wire Compensation

The new feature of the code is the electric wire. For a horizontal crossing, the effect of a thin wire is represented as:

$$\begin{aligned} \Delta x &= \frac{\mu_0 I_w l_w}{2\pi(B\rho)} \left[ \frac{x' + \theta_{c,w} \pm \phi_x x / \beta_x^*}{\theta_{tw}^2} - \frac{1}{\theta_{c,w}} \right] \quad (6) \\ \Delta x' &= -(\pm 1)\phi_x \Delta x / \beta_x^* \\ \Delta y &= \frac{\mu_0 I_w l_w}{2\pi(B\rho)} \frac{y' \pm \phi_y y / \beta_y^*}{\theta_{tw}^2} \\ \Delta y' &= -(\pm 1)\phi_y \Delta y / \beta_y^* \end{aligned}$$

where

$$\theta_{tw} \equiv ((x' + \theta_{c,w} \pm \phi_x x / \beta_x^*)^2 + (y \pm \phi_y y / \beta_y^*)^2)^{1/2}, \quad (7)$$

and  $l_w$  is the length of the wire,  $\theta_{c,w}$  is the angle at the IP representing the transverse distance between the beam and the wire,  $I_w$  the wire current, and  $(B\rho)$  the magnetic rigidity of the beam. The  $\pm$  signs refer to the two sides of the IP. Again the vertical crossing is treated in analogy. The errors  $\phi_x$  and  $\phi_y$  represent the deviation in phase advance from the IP with respect to the ideal value  $\pi/2$ . Simultaneously they also give the differences in phase advance from the location of the long-range collisions. At the wire location presently contemplated, the phase errors are about  $2-3^\circ$  in the design optics [4]. For perfect compensation, the wire current must be chosen as

$$I_w = -4\pi(B\rho)N_b r_p n_{\text{par}} / (\mu_0 \gamma l_w). \quad (8)$$

The ideal distance between wire and beam is  $d_w \approx (\theta_c / \theta_{x,y}^*) \sigma$ , where  $\sigma$  denotes the rms beam size at the wire. This corresponds to  $\theta_{c,w} = \theta_c$ .

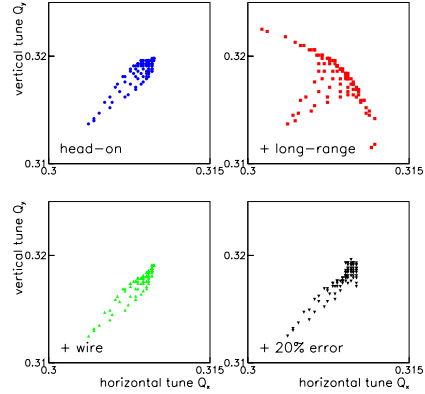


Figure 1: Tune footprints for various cases, for initial horizontal and vertical amplitudes extending to  $7\sigma_{x,y}$ . Top left: head-on collisions only; top right: head-on plus long-range collisions; bottom left: head-on plus long-range collisions and a perfect wire; bottom right: head-on plus long-range collisions and a wire with 20% strength error.

### 2.4 Compensation Errors

We consider five types of errors, namely,

- a simultaneous symmetric betatron phase error  $\phi_{x,y}$  on both sides of each IP,
- a static wire strength error,
- a random wire strength error,
- a wire position error,
- a betatron phase error  $\phi_{x,y}$  with only one wire per IP.

Simulation results for each case are discussed next.

## 3 RESULTS

Figure 1 shows tune footprints computed for initial amplitudes extending to  $7\sigma_{x,y}$ . The tunes were calculated by applying a fast Fourier transform to particle positions sampled over 4096 turns. The top left picture shows the tune footprint for the two head-on collisions alone, the top right the enhancement of the footprint by the long-range collisions. The bottom left picture demonstrates that an ideal wire reduces the footprint to a size equal to or even smaller than that for head-on collisions only. The compensation still works even with a significant static strength error, as illustrated in the last picture.

Diffusion rates are calculated by launching groups of 100 particles at identical start amplitudes in the horizontal and vertical plane, but with random initial betatron phase. The spread in linear action values is averaged over 1000 consecutive turns to reduce fluctuations due to regular



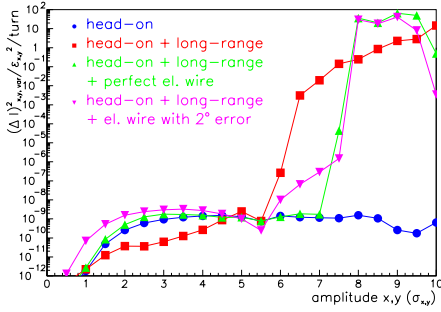


Figure 2: The diffusion per turn as a function of the start amplitude. Different cases are compared.

phase deformations, and to more clearly pronounce chaotic behavior. The mean increase per turn in the action variance measures the strength of the diffusion.

Figure 2 shows the simulated diffusion rates as a function of start amplitude. The vertical axis is on a logarithmic scale. It represents the increase in the action variance per turn, in units of the rms design emittance. Any value larger than  $10^{-8}$  could indicate a significant diffusion over  $10^8$  turns. It is most noteworthy, that at an amplitude of about  $6\sigma$  the diffusion rate increases by 7–9 orders of magnitude, if long-range collisions are present (the red curve, squares). The strong diffusion is absent when only head-on collisions are accounted for (the blue curve, circles). This is consistent with the results of Ref. [2]. When the electric compensating wire is added (green curve, upright triangles), the amplitude of the steep increase moves outwards by  $1.5\text{--}2\sigma$ , to about  $7.5\text{--}8\sigma$ . This remarkable improvement confirms the efficiency of the wire. Even with an imperfect wire ( $2^\circ$  phase error - the pink curve, inverse triangles), the diffusion rates in the intermediate amplitude range  $6\text{--}8\sigma$  is still several orders of magnitude lower than without the wire. Note that a  $2\sigma$  improvement of the dynamic aperture, in both planes, might greatly improve the operating margin of the LHC.

That the wire compensation fails for amplitudes larger than  $8\sigma$  is understandable. At amplitudes above  $8\sigma$  the particles start passing through the core of the opposing beam, where the beam force strongly deviates from the  $1/r$  force of the wire.

Figure 3 shows a more systematic study of the effect of a phase error. The same phase error with respect to the head-on collision point was assumed for the wires on either side of the IP and in both planes. Results are compared for three different amplitudes. Since, for phase errors of about  $\pm 10^\circ$ , the diffusion rate at  $7.5\sigma$  increases to the uncompensated level, we may consider this value as the phase tolerance. In practice, the phase errors are confined to less than  $2 \pm 1^\circ$  [4], *i.e.*, phase errors due to optical imperfections will have a negligible effect on the beam-beam compensa-

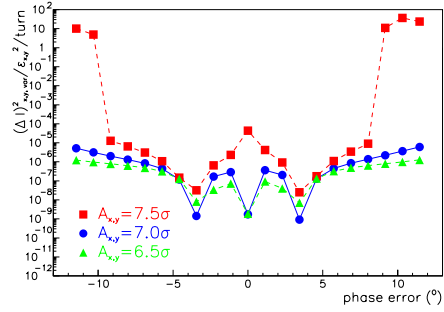


Figure 3: Variation of diffusion rate with symmetric betatron phase error at various amplitudes. The phase errors for the wires on either side and for the two planes are all assumed to be equal.

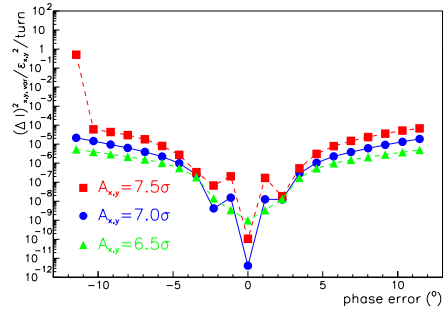


Figure 4: Variation of diffusion rate with betatron phase error at various amplitudes, if there is a compensating wire only on one side of each IP.

tion.

Alternatively, we consider the case that there is only one wire per IP and study the sensitivity to betatron phase errors in this configuration. The results are shown in Fig. 4. They are similar to, or even lower than, those in Fig. 3, despite of the reduced symmetry. Since it is not possible to choose a location with a phase error less than  $1^\circ$  also here we take  $\pm 10^\circ$  as the tolerance. The differences in the diffusion rates for one and two wires depend on the working point.

If the wire current is not perfect, the compensation degrades. This is studied in Fig. 5 (again for two wires per IP), depicting diffusion rates at  $6.5$ ,  $7$  and  $7.5\sigma$  as a function of the wire strength error in percent. Especially at the largest amplitude, the dependence is rather erratic, presumably indicating the existence of resonance islands. Static strength errors in the range between  $0$  and  $-10\%$  appear acceptable.

The effect of a random change in the wire strength from turn to turn is illustrated in Figs. 6 and 7. The strength of

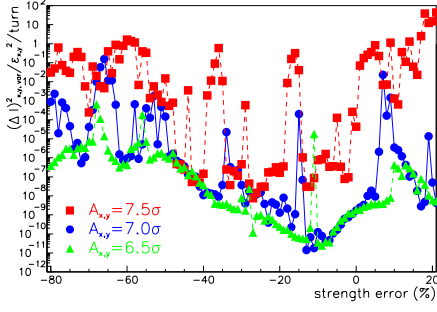


Figure 5: Variation of diffusion rate with static wire strength error (in units of percent) at various amplitudes.

each wire is assumed to fluctuate from turn to turn. Plotted along the horizontal axis is the normalized peak value  $\Delta I_w/I_w$  of the random fluctuation in wire current. The latter is uniformly distributed between  $-\Delta I_w$  and  $\Delta I_w$ . Then the diffusion rates should be symmetric around zero, and deviations from the mirror symmetry reflect the uncertainty of the simulation result, due to the choice of random seed.

In the simulation of Fig. 6, we have assumed that the fluctuation in wire strength does not give rise to dipolar deflections. This means, that in Eq. (6) all three terms containing the factor  $\theta_{c,w}$  were varied simultaneously. For the corresponding results in Fig. 7, only the average dipole deflection, *i.e.*, not including the fluctuating part, was subtracted from the wire force. In this case, the beam experiences random dipole kicks in addition to fluctuating focusing forces, and higher order terms. Since no fast orbit feedback is foreseen for the LHC at top energy the second simulation is more realistic. The difference in the computed diffusion rates is small, however, which suggests that the random quadrupolar excitation is more harmful than the dipolar one. Both figures indicate that the tolerance on the turn-to-turn stability of the wire is less than 0.1%.

Finally, Fig. 8 shows simulated diffusion rates as a function of an error in the transverse distance between beam and wire. We observe that errors in the wire position towards larger amplitudes are preferred, presumably because the  $1/r$  field increases strongly in the vicinity of the thin wire. Note that the sharp increase in the diffusion rates for smaller distances is consistent with the steep rise at an amplitude of  $7.5\sigma$ , in Fig. 2, and that the preservation of a low diffusion rate for distances 10–20% larger than nominal is compatible with the dependence on the static strength error in Fig. 5. We deduce from Fig. 8 that the tolerable range of distances extends approximately between 0 and 20% of the optimum distance.

In LHC operation, the relative distance of beam and wire can be determined with sufficient precision by detecting the effect of the wire current on the closed orbit.

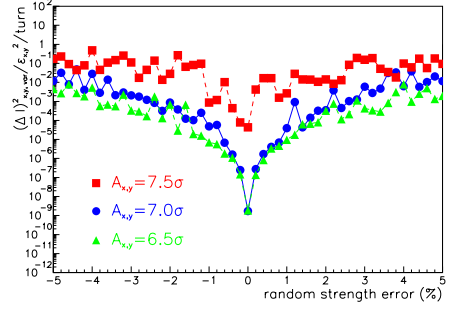


Figure 6: Variation of diffusion rate with peak value of turn-to-turn random wire strength error at various amplitudes. The dipolar deflection by the wire is subtracted including its fluctuation.

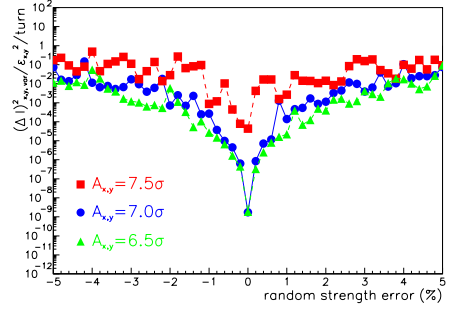


Figure 7: Variation of diffusion rate with random wire strength error at various amplitudes. The average dipole deflection is subtracted.

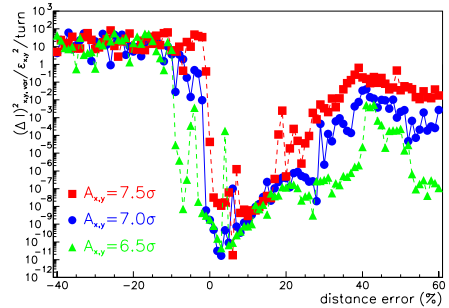


Figure 8: Variation of diffusion rate with wire position error at various amplitudes. Zero on the horizontal axis refers to a beam-wire distance of  $(\theta_c/\theta_{x,y}^*)\sigma \approx 9.5\sigma$ .

## 4 CONCLUSIONS

Weak-strong simulation studies show that at amplitudes between  $6$  and  $8\sigma$  the wire compensation reduces the diffusion rate by many orders of magnitude. The tolerance to betatron phase errors is about  $10^\circ$ . The tolerable range of static strength errors extends between  $0$  and  $-10\%$ . Transverse distance errors between  $0$  and  $20\%$  are acceptable. The most critical tolerance appears to be that to turn-to-turn fluctuation of the wire strength. Here a stability better than  $0.1\%$  must be achieved.

## 5 ACKNOWLEDGEMENTS

I thank O. Brüning, W. Herr, J.-P. Koutchouk and F. Ruggerio for suggesting this study, support, helpful discussions, and a careful reading of the manuscript.

## 6 REFERENCES

- [1] T. Sen, et al., “Effect of the Beam-Beam Interactions on the Dynamic Aperture and Amplitude Growth in the LHC,” CERN-SL-99-039 AP (1999).
- [2] Y. Papaphilippou and F. Zimmermann, “Weak-Strong Beam-Beam Simulations for the LHC,” Proc. of the Workshop on Beam-Beam Effects in Large Hadron Colliders — LHC99, Geneva, April 12-17, CERN-SL-99-039 AP (1999) (J. Poole and F. Zimmermann eds.); published in Physical Review Special Topics – Accelerators and Beams 2, 104001 (1999).
- [3] H. Grote, et al., “LHC Dynamic Aperture at Collision,” LHC Project Note 197 (1999).
- [4] J.-P. Koutchouk, “Principle of a Correction of the Long-Range Beam-Beam Effect in the LHC using Electromagnetic Lenses,” LHC Project Note 223 (2000).
- [5] J.-P. Koutchouk, “Correction of the Long-Range Beam-Beam Effect in LHC using Electro-Magnetic Lenses,” presented at IEEE PAC 2001 Chicago (2001).
- [6] J.-P. Koutchouk, these proceedings.
- [7] W. Herr, “Effects of PACMAND Bunches in the LHC,” CERN-LHC-Project-Report-39 (1996).
- [8] J. Irwin, “Diffusive Losses from SSC Particle Bunches due to Long Range Beam-Beam Interactions,” SSC-233 (1989).

# Summary of session on beam-beam compensation schemes

W. Herr CERN, SL Division

## Abstract

This paper summarizes the presentations and discussions in the session on beam-beam compensation held during the workshop on beam-beam effects at Fermilab on 25 to 27 June 2001. The presentations and discussion were focused on two main topics: linear and non-linear compensation with electron lenses in the Tevatron and a compensation scheme for long-range effects in the LHC using a pulsed wire.

## 1 INTRODUCTION

In high luminosity hadron colliders the beam-beam effect eventually limits the bunch intensities. Recently schemes have been proposed to compensate part of the detrimental effects. During this session three presentation were made:

- Correction of the long-range beam-beam effect in LHC using electromagnetic lenses; by J.P. Koutchouk, CERN
- Simulation of the LHC long-range compensation; by F. Zimmermann, CERN
- Study of the Tevatron compensation; by D. Shatilov, BINP

The presentations were discussed and some issues of general interest for beam-beam compensation that were raised during this session are presented here.

## 2 COMPENSATION OF LONG-RANGE EFFECTS

Recently the long-range beam-beam effects have been more and more recognized as important factors for the stability of the beams in lepton and hadron colliders. Both, active or passive compensation of at least part of these effects may be essential for machines with many bunches.

### 2.1 Pulsed wire for compensation of long range effects

The proposal to compensate the long-range beam-beam effects (LRE) was made after initial tracking studies have shown the importance of long-range effects on the dynamic aperture. It was realized that for large enough beam separation the long range forces decrease with  $\frac{1}{r}$ , where  $r$  is the distance between the beams. Such a field can also be

produced by a thin wire. For the bulk of the long-range encounters this assumption is valid and the separation is typically between 7 and 10  $\sigma$ . Furthermore, most of these encounters happen where the beams are still approximately round and at a phase advance of  $\frac{\pi}{2}$  from the collision point. It can therefore be justified to lump all interactions into a single one. The linear part of the long range forces is largely compensated by the alternating crossings in the LHC interaction points. The size of the beam-beam tune-spread (footprint) can be strongly decreased [1] by a wire running along the beam. The current times length of such a wire requires approximately 80A · 1m. The size of the footprint can be decreased by a factor 10. Effects on the closed orbit are corrected simultaneously.

The bunch filling scheme of the LHC causes a difficulty, producing so-called PACMAN bunches which experience only part of the beam-beam effect and therefore need only part of the correction. To account for this it is proposed to pulse the current in the wire at the beginning and end of a batch, i.e. produce smaller compensating fields for the PACMAN bunches.

Preliminary considerations have shown that such a scheme is technically possible, using commercially available equipment.

The wire is operated in the vacuum of the machine and therefore needs a cooling system. Such a cooling is technically difficult for a wire of 1 mm diameter and alternatives have been proposed where a much thicker wire with cooling inside is used and the surface of the wire is shaped to obtain the correct  $\frac{1}{r}$  dependence.

### 2.2 Simulation of long range compensation with pulsed wire

To evaluate the above compensation scheme, a study was launched to simulate the effect on the beam. A second aim was to work out the tolerances and the sensitivity of the proposed setup to imperfections. For that purpose a weak-strong simulation was developed, assuming a linear transport in the arcs and at the interaction point a head-on collision and on both sides long-range collisions together with a wire. The wire was assumed at a distance of 9.5  $\sigma$  and producing a  $\frac{1}{r}$  force. The tests were made on possible betatron phase errors, as well as on wire positioning and strength errors. For the evaluation the footprints and the diffusion rate was used. Without errors the footprints were reduced almost to the size of the head-on footprints alone since the compensation in the program is almost perfect. Already in earlier studies it was shown that the dif-

fusion rate increases steeply for particle amplitudes above  $6\sigma$  (without wire). With a wire the increase of the diffusion sets in about  $1.5$  to  $2\sigma$  later, i.e. a significant increase of the available stable region. With phase errors of  $2^\circ$  to the wire, the improvement is still  $1$  to  $1.5\sigma$ . Only for errors larger than  $10^\circ$  the original steep increase is observed again. However such phase errors are not expected for a reasonably well behaved insertion optics. Studying the effect of static wire strength errors it was found that errors in the range  $[-40\%, +20\%]$  still give a good correction.

The positioning of the wire with respect to the beam is an important issue that may need some further thoughts, a consensus reached during the discussion. The simulation of positioning errors in the range  $[-40\%, +60\%]$  showed a dependence with acceptable compensation in the interval  $[-5\%, +40\%]$ . I.e. in case of positioning errors, an error away from the beam is preferable. While studying a scheme with a single wire compensating the long-range effects from both sides of the interaction point, it was shown that a scheme with two separate wires has advantages.

During the discussion it was agreed that no obstacle was identified up to now and the participants of the workshop strongly recommend to continue with this scheme.

### 3 STUDY OF TEVATRON COMPENSATION

Another simulation study aimed to evaluate the linear and non-linear compensation with electron lenses in the Tevatron, and possibly to define some strategies for the operation. For that purpose a weak-strong beam-beam code was developed (LIFETRAC) for the Tevatron that is fully symplectic in 6D and can use various noise sources, such as tune modulation or beam separation at the collision point.

The main purpose of the linear beam-beam compensation is to suppress the bunch-to-bunch tune spread in the Tevatron. In a first step, good and bad working points are determined with the program. In the second step all bunches at bad working points are moved to the good working points with linear electron lenses. Varying the parameters of the lenses and including perturbations this strategy can be tested. After the application of the linear lenses, the distributions of antiprotons at originally bad working points are practically the same as on good working points. Different electron lens profiles were investigated, studying the antiproton tune-shift and the luminosity. The difference was found to be rather small. Injecting noise on the electron beam led to exponential emittance growth.

The purpose of the non-linear compensation is to reduce the intrabunch tune spread, i.e. the tune footprint. The footprint of long range beam-beam interactions show a characteristic 'folding' for particles at amplitudes close to the beam separation. If this appears close to low order resonances it is considered dangerous since there we have  $\frac{dQ}{dA} \approx 0$ . Bad lifetime of tails must be expected. The effect of the non-linear lens is to scale down the footprint, thus moving the folding over area to smaller particle am-

plitudes. This may now lead to a blowing up of the core of the bunches that must be avoided. The recommended procedure now used in the simulation is to reduce the footprint moderately, i.e. by a factor of two in the first step. A linear lens should then be used to shift the bunch to a better working point where the reduced footprint is in an area free of dangerous resonances. Therefore the non-linear and linear compensation must be applied simultaneously.

In the discussion it was acknowledged that the study helped to understand better the requirements and to define the parameters for the compensation. However more experimental data is desirable. While the linear compensation looks very promising, it is recommended to further study the non-linear compensation. A consensus was reached that a small tune footprint (i.e. tune spread) alone does not guarantee a safe running. It must be considered a necessity but it is not sufficient.

## 4 CONCLUSIONS

Compensation schemes for head-on as well as for long range beam-beam effects have been discussed. Both approaches were found promising and well under way and the workshop strongly recommends to continue.

## 5 REFERENCES

- [1] J.P. Koutchouk; *Correction of the Long-Range Beam-Beam Effect in LHC using Electromagnetic Lenses*; Proc. workshop on beam-beam effects 2001, (FNAL, 2001).
- [2] F. Zimmermann; *Simulation of the LHC Long-Range Compensation*; Proc. workshop on beam-beam effects 2001, (FNAL, 2001).
- [3] D. Shatilov; *Study of the Tevatron Compensation*; Proc. workshop on beam-beam effects 2001, (FNAL, 2001).

## **SECTION III: Weak-strong phenomena**

# Weak–Strong Beam–Beam Tracking for LHC V6.0

Y. Luo and F. Schmidt, CERN, Geneva, Switzerland

## Abstract

Simulations have been performed for the LHC for a complete model of the LHC with the multipole errors of all dipoles and quadrupoles and the triplet errors, at injection and collision energy respectively. For the two energies the weak–strong beam–beam forces are included in the simulations for both the head–on and the long–range collisions by using a realistic beam separation scheme. The transverse amplitudes have been densely varied and several phase space angles have been treated. It has been found that the typical tracking periods of  $10^5$  turns are not sufficient but that the tracking has to be extended to at least  $10^6$  turns. We will demonstrate that early indicators can help to find not too pessimistic bounds for long–term stability.

## 1 INTRODUCTION

The LHC model studied in this note is based on LHC version 6.0, with ATLAS, CMS, LHCb head–on collisions and ALICE halo collisions. The lattice is anti–symmetric about all four IPs. At injection energy the errors of the main dipole’s of error table 9901 (see for instance Ref. [1]) are considered together with the b3 and b5 spool piece correction system. At top energy the errors of low–beta triplet quadrupoles (details see below) are introduced counteracted by two types of correction packages with  $b_3$ ,  $b_6$  and  $b_4$ ,  $a_3$ ,  $a_4$  correctors respectively. The beam–beam interaction was simulated in the weak–strong approximation. The dynamic aperture (DA) is defined as the maximum radius for which the particles are stable for  $10^5$  or  $10^6$  turns. A series of tracking studies are performed for five different radial angles in the phase space. The phase space angle is defined as  $\phi = \arctan \sqrt{\epsilon_y/\epsilon_x}$ , in this paper the angles  $\phi = 15^\circ, 30^\circ, 45^\circ, 60^\circ$  and  $75^\circ$  have been used. To determine the minimum dynamic aperture to a confidence level of 95% the simulations have been performed for 60 different representations of the random components of the multipole errors (seeds). All tracking runs has been performed with the SixTrack code [2].

## 2 TRIPLET ERRORS AND THEIR CORRECTION

At top energy the field errors in the low–beta triplets play an important role in the reduction of the dynamic aperture. The largest components of the latest triplet errors are given in Table 1. The body and end effects have been combined into one single number for the thin–lens approach

used here: each triplet quadrupole is split into four thin–lens quadrupoles at each of IP1, IP2, IP5, IP8.

Component	systematic	uncertainty	random
b3	0	0.72	0.36
b4	-0.175	0.83	0.36
b6	0.34	0.91	0.21
a3	0	0.69	0.34
a4	0	0.33	0.34
Component	systematic	uncertainty	random
b3	0	0.63	0.34
b4	0	0.22	0.34
b6	0.21	0.41	0.18
a3	0	0.32	0.34
a4	0	0.26	0.34

Table 1: Low-beta quadrupole field errors for KEK version 4.x(upper) and FNAL version 3.1 (lower). Values are relative to the main field at  $x = 17\text{mm}$  in units of  $10^{-4}$ .

On either side of IP1, IP2, IP5, and IP8 two corrector groups are placed as proposed by J. Strait at a CERN–KEK–US meeting, April 2000. Each corrector group contains several correction spools such that on either side of each IP one corrector exists for b3, b4, b6, a3 and a4. The correction formalism follows the one outlined by A. Verdier and A. Faus–Golfo [3]. The principle is rather simple: with one corrector for each multipole component on either side of each IP, we compensate the total kick for purely horizontal and purely vertical motion simultaneously.

## 3 BEAM SEPARATION SCHEME

There are 15 parasitic crossing points on either side of each IP. The total crossing angle at collision is fixed throughout to  $300\mu\text{rad}$ . The crossing is horizontal in IP5 and IP8, while at IP1 and IP2 it is vertical [4]. The bunch sizes in the opposite beam appearing in the beam–beam element were calculated under the assumption of full anti–symmetry at all four IPs; the beam separation was taken as the distance of the orbits in ring 1 and ring 2. The beam–beam separation in injection and collision mode are shown in

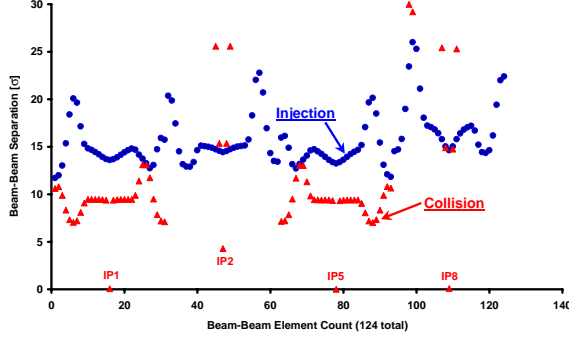


Figure 1: LHC 6.0 beam-beam separations at the four IPs, (blue) circles for the injection and (red) triangles for the collision case respectively.

Figure 1, where the separations at injection and collision are given in the units of beam size in the corresponding crossing plane, the horizontal axis is the count number of the beam-beam encounters, 124 in total, around the four IPs. At collision energy the separation is about  $9.5 \sigma$  while at injection energy it varies between 12 and  $15 \sigma$ .

#### 4 DYNAMIC APERTURE IN COLLISION WITHOUT BEAM-BEAM

First the correction scheme of the low-beta triplet errors has been investigated with the LHC collision mode without beam-beam interaction. Figure 2 shows the dynamic apertures of  $10^5$  turn tracking before and after triplet error corrections.

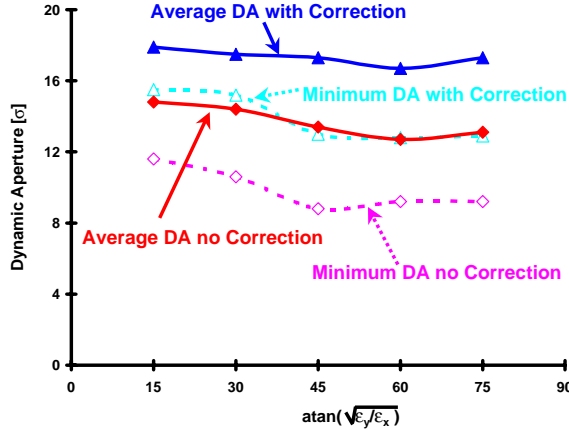


Figure 2: Dynamic aperture without and with low-beta triplet field error correction. The beam-beam kicks are not included and the tracking has been performed for  $10^5$  turns.

The triplet errors reduce the average and minimum dy-

namic aperture to about  $13 \sigma$  and  $9 \sigma$  respectively for  $10^5$  turns. This is mainly due to the large  $b_6$  component of the quadrupoles. After correction, as described above, the average and minimum dynamic apertures increase to some  $17 \sigma$  and  $13 \sigma$  respectively, i.e. a gain of about  $4 \sigma$ . So we conclude that the proposed triplet error correction scheme is indeed very effective. It has to be mentioned that only part of this improvement of the DA remains in the presence of the parasitic beam-beam kicks (see Ref. [5]).

#### 5 DYNAMIC APERTURE AT COLLISION INCLUDING BEAM-BEAM

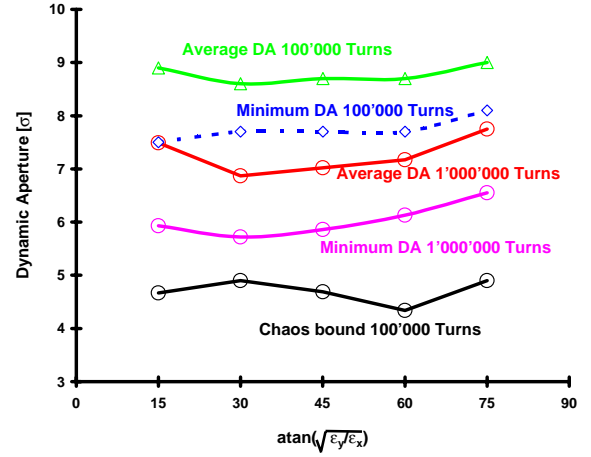


Figure 3: Dynamic aperture at collision including beam-beam kicks. Tracking is performed for  $10^5$  and  $10^6$  turns.

Figure 3 shows the results for  $10^5$  and  $10^6$  turns when the beam-beam interaction is included. Tracking for  $10^5$  turns shows the average DA to go down to about  $9 \sigma$ , while the minimum DA is  $7.5 \sigma$ . As found earlier [6, 7] this reduction is due to the many parasitic beam-beam crossings. We know from numerous tests that the DA for plain nonlinearities is not decreasing very much for tracking runs in excess of  $10^5$  turns (see Ref. [8]). It was therefore surprising that there is a dramatic decrease of the DA when the tracking is extended to  $10^6$  turns. The average and minimum DA becomes about 7 and below  $6 \sigma$  respectively. Our conjecture for this large reduction of the DA is the following: the above mentioned parasitic crossings make the motion very slightly chaotic at small amplitudes. As a result it takes considerable time until a particle is driven to large enough amplitudes such that the nonlinearities are strong enough to cause the loss of the particle. In fact, the chaotic bound (see below) goes down to about  $4 \sigma$  and it has to be feared that particle loss may take place down to that level when the tracking is extended beyond  $10^6$  turns. Presently, our computer power is insufficient to allow systematic studies with those large turn numbers.



## 6 DYNAMIC APERTURE AT INJECTION WITHOUT AND INCLUDING BEAM-BEAM

Tracking including beam-beam over  $10^5$  turns at injection energy (Figure 4) gives about  $10\sigma$  for the minimum DA which is more than  $1\sigma$  smaller than without the beam-beam kicks. Also in this case there is a sizable reduction of the DA when the tracking is extended to  $10^6$  turns, in particular at the phase space angle of  $45^\circ$ . In fact, the DA at that phase space angle agrees well with the chaotic bound which is found to have its minimum at about  $7\sigma$ .

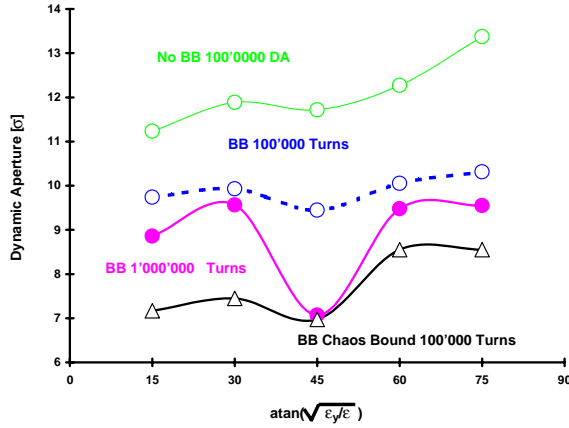


Figure 4: Minimum dynamic aperture at injection without and including beam-beam kicks. Tracking is performed for  $10^5$  and  $10^6$  turns.

## 7 TUNE FOOTPRINTS FOR COLLISION AND INJECTION

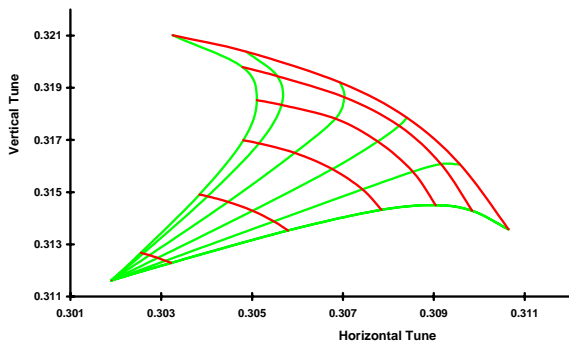


Figure 5: Tune footprint at collision energy

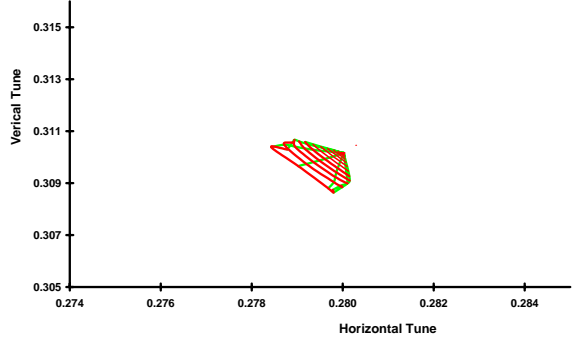


Figure 6: Tune footprint at injection energy

The tune footprints at collision and at injection are shown in Figure 5 and Figure 6 respectively. At injection energy one would naively expect that the beam-beam force will not deteriorate the DA by much since the tune footprint is so much smaller at that energy (the beams do not suffer from head-on collisions). Furthermore, this was to be expected since the beam separation is so much larger at injection. However, as we have seen in the last section, the DA has been reduced by a considerable amount and at one phase space angle by as much as  $4\sigma$ . From this we have to conclude that the parasitic beam-beam kicks are relevant with respect to the DA even for separation in excess of  $12\sigma$ .

## 8 EARLY INDICATOR OF PARTICLE LOSS

Since many years the onset of chaos was used as an early indicator of particle losses (for a more complete review see Ref. [9]). However, due to the fact that the dynamic aperture does not reduce much beyond  $10^5$  turns, the indicator rendered too pessimistic estimates of the DA. However, this is obviously no longer true when beam-beam kicks have been introduced in the simulations. It seems therefore worthwhile to reexamine this technique. The first observation has been that the global onset of chaotic motion is too optimistic. Instead, one has to watch for nests of chaotic motion, which we call “chaotic spikes”, inside the mostly regular regime, i.e. at smaller amplitudes. Of course, by definition, there always exist very thin chaotic regimes deep in the regular domain which will not lead to particle loss after finite times. Our pragmatic approach is to choose a certain width of the chaotic spike as a criterion for very long-term losses. For this report we have chosen a spike width of some  $0.3\sigma$ , but this has to be further optimised to render reliable results.

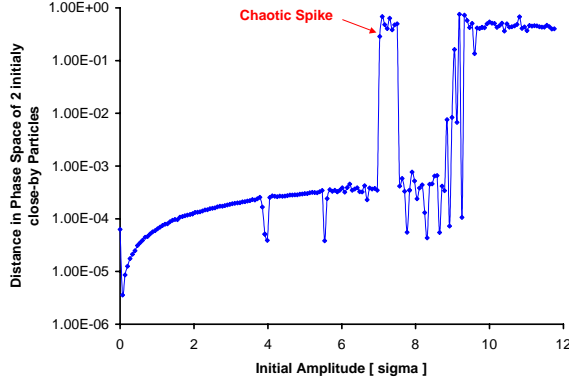


Figure 7: *Example for a chaotic spike. A chaotic spike we consider a limited range of amplitudes with chaotic behaviour. This has to be distinguished from the broad onset of chaos where particle loss sets in rather quickly.*

Chaos is typically being detected by following the evolution of the distance of phase space of two initially close-by particles. Figure 7 shows an example of such a distance after  $10^5$  turns. Whenever this distance rises by many orders of magnitude (the maximum is normalised to 1) the motion exhibits chaotic behaviour. The (red) arrow in the figure indicates what we call a chaotic spike and the probable long-term DA.

In Figure 8 this techniques is shown in action for the 300 individual tracking runs that make a typical study case (60 seeds and 5 phase space angles): the upper curve, (red) squares, shows the  $10^5$  turns DA, the medium curves, (blue) triangles, depicts the  $10^6$  turns DA and lastly the lower curve, (magenta) diamonds, demonstrates that chaotic spikes derived from  $10^5$  turns can serve as a not too pessimistic indicator of long-term losses.

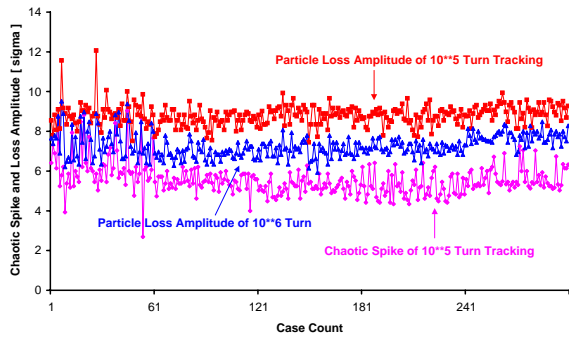


Figure 8: *DA for  $10^5$  turns (upper curve (red) squares) and  $10^6$  turns (medium curve (blue) triangles) in comparison with the chaotic spikes (lower curve (magenta) diamonds)*

## 9 AMPLITUDE BLOW-UP

Another interesting indicator of particle loss is the onset of the amplitude blow-up of a particle. In Figure 9 an example is shown with the maximum and mean amplitudes versus the initial amplitude. (The line “slope=1” represents the condition of mean amplitude equal to the initial one.)

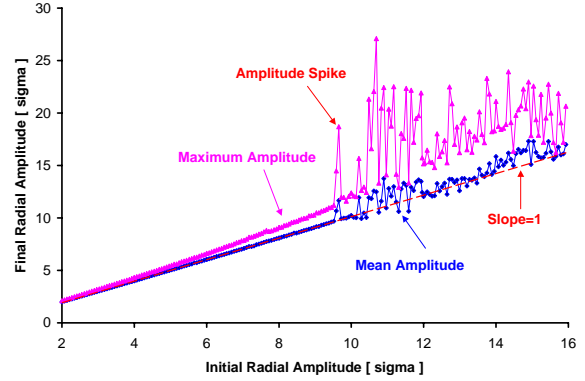


Figure 9: *Example for an amplitude spike.*

As for the case of the global onset of chaos the global amplitude blow-up is too optimistic to predict the long-term DA. As a criterion we define here the “amplitude spike” as that initial amplitude at which the maximum amplitude exceeds by 10% what is expected from previous maximum amplitudes.

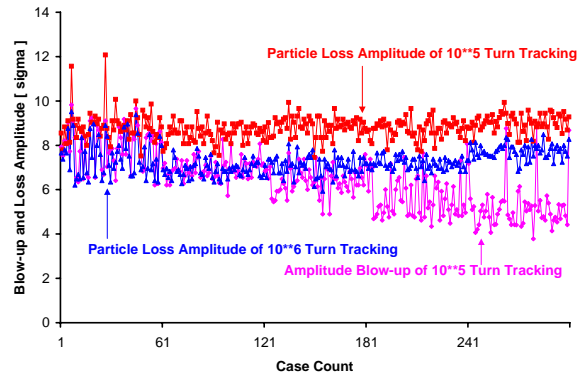


Figure 10: *DA for  $10^5$  turns (upper curve (red) squares) and  $10^6$  turns (medium curve (blue) triangles) in comparison with the amplitude spikes (lower curve (magenta) diamonds); compare with Figure 8.*

Figure 10 shows the same  $10^5$  and  $10^6$  turn DA curves as in Figure 8 but this time together with the amplitude spikes. This type of indicator also seems to have some predictive power but it is probably less reliable than the “chaotic spike” approach.

## 10 CONCLUSIONS

The DA of the LHC including beam–beam kicks has been studied for both injection and collision energy. In both cases the parasitic beam–beam kicks lead to sizable reductions of the DA. In particular, we observe that there are very slow but considerable losses at small amplitudes, such that our usual  $10^5$  turn tracking is by far too optimistic. By the same token early indicator become again important, since they allow to find only slightly pessimistic predictions of the DA for  $10^6$  turns and more.

## 11 ACKNOWLEDGEMENT

We would like to thank Hans Grote for providing us with the triplet correction settings and the beam separation at the locations of the beam encounters.

## 12 REFERENCES

- [1] L. Jin and F. Schmidt, “Tune Scan Studies for the LHC at Injection Energy”, LHC Project Report 377, [http://wwwslap.cern.ch/frs/report/tune\\_scan99\\_v6.ps.gz](http://wwwslap.cern.ch/frs/report/tune_scan99_v6.ps.gz).
- [2] F. Schmidt, “SixTrack, Version 1, Single particle tracking code treating transverse motion with synchrotron oscillations in a symplectic manner”, CERN/SL/90–11(AP) (1990).
- [3] A. Verdier and A. Faus–Golfe, *Multipole Compensation in the LHC low- $\beta$  Insertions*, PAC97 Vancouver, Conference Proceedings, and LHC Project Report 116.
- [4] H. Grote, *Self-consistent Orbits for Beam-beam Interactions in the LHC*, LHC Project Note 216.
- [5] L.H.A. Leunissen, H. Grote, F. Schmidt, “LHC Dynamic Aperture including the Beam-Beam Force”, CERN–LHC–Project–Report–405, paper presented at the EPAC Conference in Vienna 2000, <http://wwwslap.cern.ch/frs/report/TUP6B12.ps.gz>.
- [6] Y. Papaphilippou and F. Zimmermann, “Weak–strong beam–beam simulations for the LHC”, Proceedings of the workshop on: “Beam–Beam Effects in Large Hadron Colliders –LHC99–”, pp. 76–80, CERN–SL–99–039 AP, [http://wwwslap.cern.ch/frs/report/workshop2\\_new.ps.gz](http://wwwslap.cern.ch/frs/report/workshop2_new.ps.gz).
- [7] H. Grote, L.H.A. Leunissen and F. Schmidt, “LHC Dynamic Aperture at Collision”, LHC Project Note 197, <http://wwwslap.cern.ch/frs/report/lhcnotexx.ps.gz>.
- [8] M. Böge and F. Schmidt, “Estimates for Long–Term Stability for the LHC”, LHC Project Report 114, presented in part at the Particle Accelerator Conference, Vancouver, 12–16 May, (1997), AIP Conference Proceedings 405 (1996), <http://wwwslap.cern.ch/frs/report/conj97lh.ps.gz>, and contribution to the workshop on “New Ideas for Particle Accelerators”, Santa Barbara, November 1996.
- [9] F. Schmidt, F. Willeke and F. Zimmermann, “Comparison of methods to determine long–term stability in proton storage rings”, CERN SL/91–14 (AP), DESY HERA 91–07, Part. Accel. **35**, pp. 249–256 (1991), <http://wwwslap.cern.ch/frs/report/lyasl.ps.gz>.

# Beam-beam Interactions in Run II at the Tevatron

T. Sen, M. Xiao and N. Gelfand  
Fermilab, MS 220  
Batavia, IL 60510

## Abstract

The Tevatron in Run IIa is operating with three trains of twelve bunches each. The impact of the long-range interactions on beam stability are more significant compared to Run I. We study these beam-beam interactions (head-on and long-range) with particle tracking using two different codes. The model includes machine nonlinearities such as the field errors of the Interaction Region quadrupoles and the chromaticity sextupoles. Tune footprints and dynamic apertures are calculated for different bunches in a train. Initial studies of the impact of a crossing angle (relevant to Run IIb) are also reported. Ideas for beam experiments that could be useful in understanding the beam-beam limits at the Tevatron are discussed.

## 1 INTRODUCTION

The Tevatron is now operating again in collider mode from summer 2001. In the first phase, termed Run IIa, 36  $\bar{p}$  bunches in three trains of twelve bunches collide with 36 proton bunches. This is a six-fold increase in the number of bunches from the last collider operation Run Ib. Design proton intensities are higher so the head-on beam-beam tune shifts experienced by the anti-protons are higher than in Run Ib. The greater number of long-range beam-beam interactions increase the total beam-beam induced tune spread of the anti-protons. Furthermore these effects are different for each  $\bar{p}$  bunch in a train since the sequence of long-range interactions is different for each of them. All of these effects taken together may reduce the dynamic aperture (DA) and/or lifetime of the anti-protons significantly. In this report we calculate the DA of a few bunches including the nonlinear fields in the IR quadrupoles amongst the nonlinearities. In the second stage of Run II, the plan is to increase the luminosity further with more intense bunches, larger number of bunches to decrease the number of interactions per bunch crossing, and also introduce crossing angles at B0 and D0 to avoid parasitic collisions with zero separation.

## 2 BEAM-BEAM INTERACTIONS IN RUN IIa

The design luminosity will increase from Run I to Run II mainly with an increase in the proton intensities and the number of bunches. Table 1 shows the main beam parameters. In Run IIa each bunch will experience two head-on interactions at B0 and D0 and seventy long-range interactions. These long-range interactions will be distributed over the entire ring with differing beam separations and differing

Table 1: Main beam parameters in Run I and Run II

	Run Ib $p/\bar{p}$	Run IIa $p/\bar{p}$
Luminosity [ $\text{cm}^{-2}\text{sec}^{-1}$ ]	$1.6 \times 10^{31}$	$8.6 \times 10^{31}$
Bunch Intensities $\times 10^{11}$	(2.3/0.55)	(2.7/0.3)
Emittances 95% [mm-mrad]	23/13	20/15
Number of bunches	6	36
Bunch separation [m]	1049.3	118.8
Beam size at IP [ $\mu\text{m}$ ]	37/28	33/29
Beam-beam parameter/IP $\times 10^{-3}$	3.4/7.4	1.5/9.9

phase advances from one interaction to the next. This sequence of interactions will also be different for every bunch in the train, e.g. the leading bunch 1 will experience all long-range interactions downstream of the IP, bunch 6 will experience five interactions upstream and six interactions downstream of the IP etc. The tune footprint will therefore differ from bunch to bunch. The nominal working point ( $\nu_x = 0.585$ ,  $\nu_y = 0.575$ ) is chosen to lie between fifth and seventh order resonances. At this working point the Tevatron beam straddles twelfth order sum resonances. Operational experience during Run I showed that these resonances did not cause a significant reduction in lifetime. However the tune footprints and nonlinearities were also smaller in Run I. Figure 1 shows the footprints due to the beam-beam interactions in Run IIa for bunch 1 and bunch 6 superposed on nearby sum resonances up to twelfth order. Footprints of all bunches except for bunch 1 and 12 are clustered around that of bunch 6. The major differences in the tunes between bunch 6 and bunch 1 and 12 are due to the missing parasitic collision closest to the IP, upstream for bunch 1 and downstream for bunch 12. The variation in the tune shift and in the tune spread from bunch to bunch will be greatly enhanced in Run IIb when the number of bunches is increased to more than one hundred. The Tevatron beam-beam compensation project [1] aims to reduce this spread in tunes by colliding anti-proton bunches with a low energy electron beam whose intensity will be varied from bunch to bunch. However even in Run IIa, the stronger beam-beam interactions at the IP ( $\xi \approx 0.01$  compared to  $\xi \approx 0.0074$  in Run Ib) and the larger number of long-range interactions may cause emittance growth and reduced lifetime of the anti-protons.

Figure 2 shows the beam separation (in units of the rms bunch size) at all the seventy two locations of beam-beam interactions for bunch 6. At most locations the beam separation is of the order of  $10\sigma$ . The prominent exceptions are the parasitic collisions nearest to the IPs where the separa-

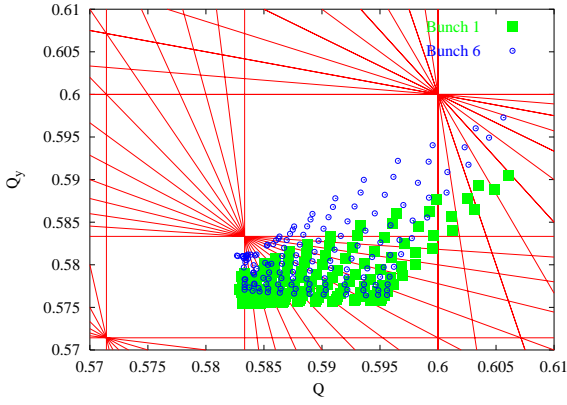


Figure 1: (color) Tune footprint for bunches 1 and 6 in a train.

tion is only about  $6\sigma$ . These nearest interactions in fact also have the dominant contribution to the tune footprint.

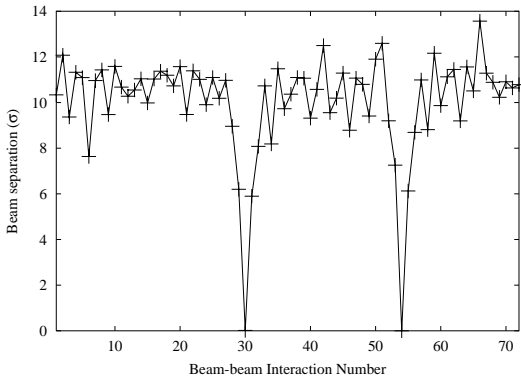


Figure 2: Separation between  $\bar{p}$  bunch 6 and the opposing proton bunch at all 72 beam-beam interactions. The head-on collisions are at locations 30 and 54.

### 3 FOOTPRINTS AND DYNAMIC APERTURE CALCULATIONS

The bunch length in the Tevatron is comparable to the beta function at the IP,  $\sigma_s \approx 37$  cm,  $\beta^* = 35$  cm. Recent theoretical work [2] has shown that bunch length effects which include hour glass effects, longitudinal Gaussian density distribution and phase averaging reduce resonance strengths in the Tevatron by two orders of magnitude compared to strengths calculated with zero length bunches. We include these bunch length effects in the simulations of the head-on interactions described below. The long-range effects are modelled by delta function kicks.

The simulation model includes the beam-beam kicks, the nonlinear fields in the Interaction Region (IR) quadrupoles (the beta functions in these magnets is about an order of magnitude greater than the values in the arcs) and the chromaticity correcting sextupoles. Two simulation programs

MAD and TEVLAT are used to track particles. In most cases the DA calculated by these codes are within  $2\sigma$  (or about 15%) of each other. In this report linear imperfections such as orbit errors and coupling due to misalignments are not included and neither are time-dependent effects such as those due to power supply ripple. Synchrotron oscillations and other momentum dependent effects have yet to be studied in sufficient detail. These effects are important and will be included in further studies.

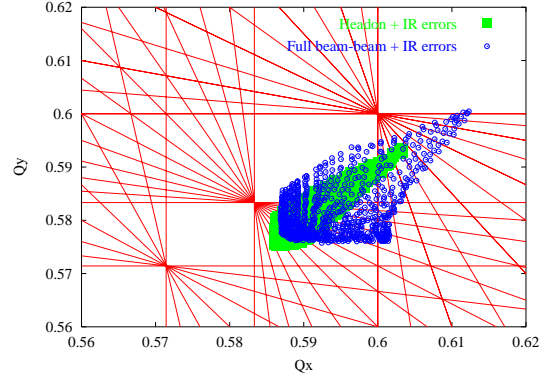


Figure 3: (color) Tune footprint of  $\bar{p}$  bunch 6 with (i) the head-on interactions and (ii) all the beam-beam interactions. IR errors and chromaticity sextupoles are included in each case. The footprint is shown for particles with amplitudes up to  $7\sigma$ . Nearby fifth, seventh, tenth and twelfth order sum resonances are shown. The linear lattice tune is (0.585, 0.575).

Figure 3 shows the tune footprint for  $\bar{p}$  bunch 6 in two cases. The addition of the long-range interactions increases the tune spread significantly and particles at amplitudes up to approximately  $3\sigma$  now straddle the 5th and 10th order resonances. Inclusion of the IR errors does not change the footprint significantly.

Tracking to calculate the DA was done for  $10^5$  and  $10^6$  turns. For  $10^5$  turns, particles were launched at several transverse amplitude ratios. Both the average and the minimum over these values are taken as measures of the DA. Figure 4 shows the DA of bunch 6 with only the beam-beam interactions in one case and with all the beam-beam kicks and machine nonlinearities in the other case. For comparison, the DA with only head-on and IR errors is also shown. It is evident that the long-range interactions cause a sharp drop in the DA. For example, the minimum DA drops from  $13.6\sigma$  to  $8.6\sigma$  when these interactions are included (see Table 2). The IR errors have a smaller relative impact, they reduce the average DA by about  $1.6\sigma$ . The relative importance of these IR errors could change when crossing angles are introduced and particle orbits go significantly off-axis through these magnets.

We have also calculated the DA when the only long-range interactions are the nearest parasitic collisions (PCs) to the IPs. We find that with only these PCs both the aver-

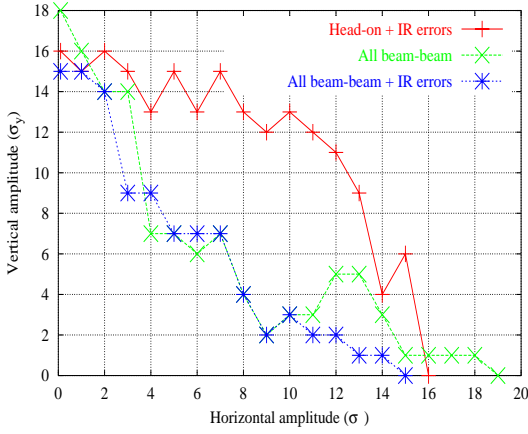


Figure 4: (color) DA for bunch 6 with (i) all beam-beam kicks and (ii) all beam-beam and the IR errors. For comparison, the DA with only head-on interactions and IR errors is also shown.

age and minimum DA are about  $2\sigma$  smaller but not quite as small as when all the PCs are included, see Table 2. It is therefore not obvious that reducing the tune spread alone, for example by choosing a different bunch spacing so that only the nearest PCs are further apart, would necessarily improve the DA.

The DA is sensitive to the machine tune. One might choose the tunes so that only small amplitude particles ( $< 1\sigma$ ) straddle the fifth and tenth order resonances. Calculations with a few tunes chosen to accomplish this do not appear to improve the DA significantly, see Table 2.

Nonlinear effects leading to amplitude growth are often reflected in dramatic tune changes as particles traverse phase space. We have looked at tune changes of particles between two consecutive intervals of 512 turns. A FFT with a Hanning filter is used to improve the accuracy of the tune calculation. This is similar to the technique used in [4] for the LHC. The top figure in Figure 5 shows the change in tune over two consecutive sets of 512 turns with the IR errors and head-on interactions while the bottom figure shows the change in tune when the long-range interactions are added. We find that when the long-range interactions are added, tune diffusion increases by an order of magnitude in regions close to the diagonal ( $x = y$ ) in amplitude space but is relatively unchanged along the  $x$  and  $y$  axes. Figure 4 shows that the DA drops the most close to the diagonal. These figures of tune changes also show that long-range interactions enhance tune diffusion from amplitudes greater than about  $2\sigma$ .

Longer term tracking ( $10^6$  turns) was done only along the diagonal in amplitude space for bunches 1, 6 and 12. Figure 6 shows the survival plot - the number of turns survived as a function of the initial amplitude - for these bunches. Bunch 1 appears to be the least stable and bunch 12 the most stable. The maximum variation in DA from bunch to bunch is  $2\sigma$ . Even after  $10^6$  turns there is no indication that the stable

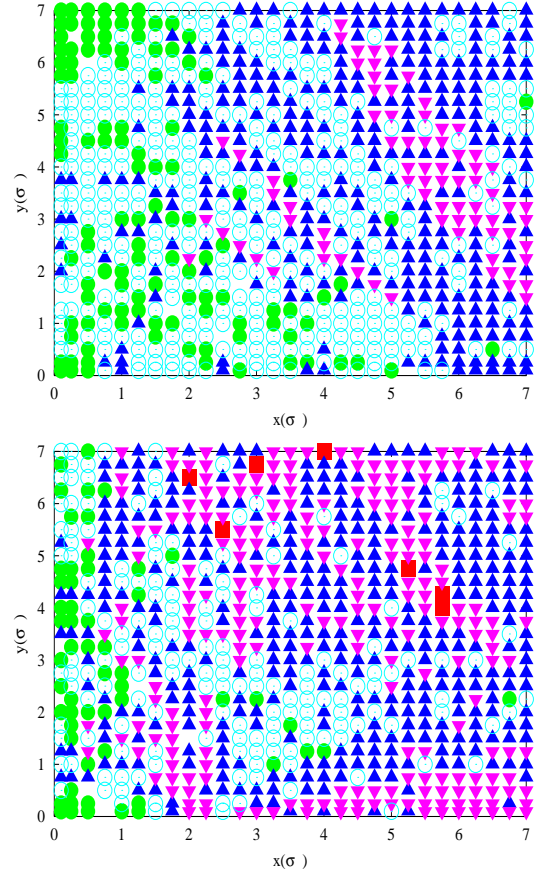


Figure 5: (color) Tune diffusion plot calculated for particles distributed over transverse phase space. The different colored symbols show the change in tune  $\Delta\nu \equiv |\Delta\nu_x| + |\Delta\nu_y|$ ,  $\Delta\nu_x$  for example is the change in horizontal tune from one set of 512 turns to the next set of 512 turns. Green:  $10^{-7} \leq \Delta\nu \leq 10^{-6}$ , Light Blue:  $10^{-6} \leq \Delta\nu \leq 10^{-5}$ , Blue:  $10^{-5} \leq \Delta\nu \leq 10^{-4}$ , Magenta:  $10^{-4} \leq \Delta\nu \leq 10^{-3}$ , Red:  $10^{-3} \leq \Delta\nu \leq 10^{-2}$ . The top figure was obtained in a lattice with IR errors and head-on beam-beam interactions while the bottom figure also had the long-range interactions.

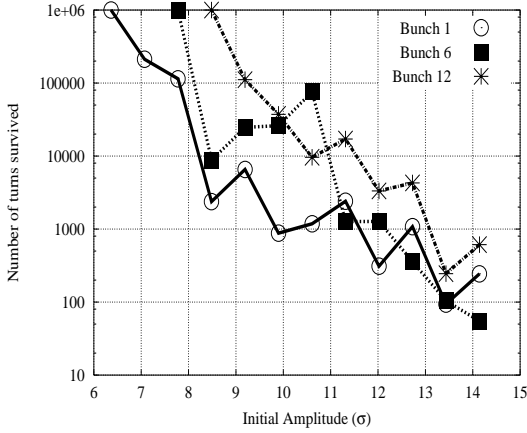
amplitude is levelling off for either of these bunches. Since  $10^6$  turns corresponds to about 21 seconds in the Tevatron, particles at smaller amplitudes than seen in Figure 6 and in Table 2 could be lost over a time scale of minutes. During operation it is only necessary that the real DA exceed the physical aperture which is defined by the primary collimators which are at  $\simeq 8\sigma$  from the beam core.

The tracking results reported so far have been in 4D phase space. Synchrotron oscillations introduce synchrotron resonances which can be driven by a variety of sources. We have begun 6D tracking for the Run IIa scenario - preliminary results and discussion can be found in a companion paper in this workshop [3].



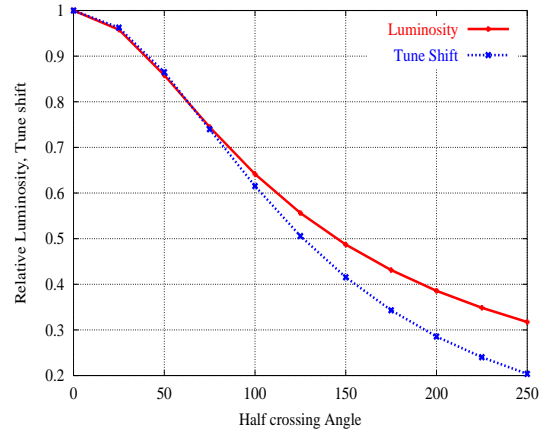
Table 2: DA in  $\sigma$  for bunches 6, 1 and 12

	$\langle DA \rangle$	$DA_{min}$
Bunch 6: $\nu_x = 0.585, \nu_y = 0.575$		
DA after $10^5$ turns		
IR errors	18.7	17.0
Head-on + IR errors	15.5	13.6
Head-on, nearest PCs, IR errors	13.6	11.3
All beam-beam	12.9	8.1
All beam-beam + IR errors	11.3	8.6
All beam-beam + IR errors		
$\nu_x = 0.572, \nu_y = 0.574$	11.0	10.0
$\nu_x = 0.591, \nu_y = 0.580$	8.5	7.6
$\nu_x = 0.575, \nu_y = 0.585$	9.5	8.3
DA after $10^6$ turns		
Bunch 1		6.4
Bunch 6		7.8
Bunch 12		8.5

Figure 6: Survival plot for bunches 1, 6 and 12 up to  $10^6$  turns. All beam-beam kicks and machine nonlinearities are included.

#### 4 IMPACT OF A CROSSING ANGLE

Increasing the luminosity beyond that obtained in Run IIa will require that the bunch spacing decrease to 132 nsecs from the present 396 nsecs and the number of bunches increase from the present 36 per beam to more than a hundred in each beam. This is necessary in order to limit the number of pp inelastic events per bunch crossing to less than three. The shorter bunch spacing introduces a number of beam dynamics issues that have to be considered. One of these is that the parasitic collisions nearest to the IPs now occur before the electrostatic separators. A crossing angle at the IP is needed to separate the beams at these locations. A half crossing angle of about  $200 \mu\text{radians}$  in the  $45^\circ$  plane separates the beams by about  $4\sigma$  at these nearest parasitic collisions. The crossing angle in turn has several other consequences, chief among them is the loss of luminosity at the main IPs. Figure 7 shows the loss of luminosity and the re-

Figure 7: (color) The impact of a crossing angle (in the  $45^\circ$  plane) on the luminosity and the beam-beam parameter. All values are normalized to the value at zero crossing angle. At a half crossing angle of  $200 \mu$  radians, the luminosity is reduced to 40% of its value without a crossing angle.

duced beam-beam parameter as a function of the crossing angle.

The beam-beam parameter is also reduced as seen in this figure. Figure 8 shows the beam-beam tune footprints due to the main collisions at B0 and D0 for two cases: (1) without a crossing angle and (2) with a half crossing angle of  $200 \mu\text{radians}$ . With this crossing angle, there is a sharp reduction in the footprint and the number of resonances spanned by the beam distribution is also reduced. However as is well known, the crossing angle couples the longitudinal dynamics to the transverse and excites synchro-betatron resonances. In addition, particle orbits with crossing angles go through the IR quadrupoles at larger amplitudes and therefore experience more nonlinear fields. These fields can also reduce the dynamic aperture even without coupling from longitudinal fields. Here we will first address the question whether the increased nonlinearities in the presence of the crossing angles have an impact on the dynamic aperture with 4D tracking. We will consider 36 bunches in each beam so this scenario is only likely during a period of machine studies during Run IIa. Then using a separate code we will consider only the impact of synchro-betatron resonances generated by the crossing angles in a perfectly linear machine and without long-range interactions.

Crossing angles at B0 and D0 are generated using the separators in the ring. While almost all separators are changed to some extent, the primary separators used are B17H, B11H, D48H in the horizontal plane and B11V, C17V, A17V in the vertical plane. The maximum crossing angles that are possible are determined by the maximum separator strength which is about 4.5 MV/m. With a crossing angle, large changes in orbit are within the IR but the orbit in the arcs also changes. This changes the separations between the beams at the locations of the long-range interactions. Figure 9 shows the difference in radial separation

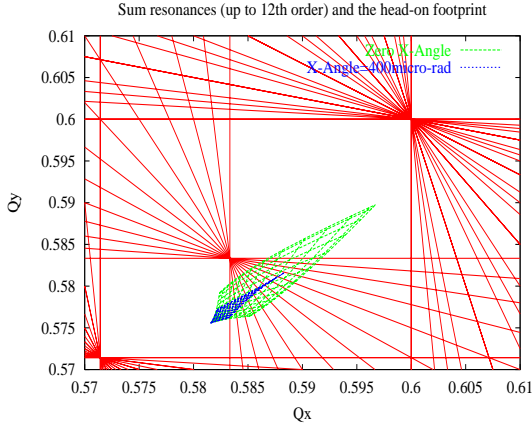


Figure 8: (color) The beam-beam tune footprint for amplitudes to  $6\sigma$  shown with only the main collisions at B0 and D0 for two cases: without a crossing angle and with a total crossing angle of  $400\mu\text{radians}$ . The footprints are superposed on the sum resonances up to twelfth order.

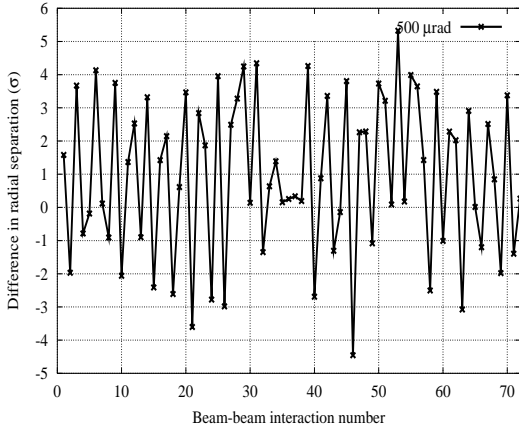


Figure 9: Difference in radial separation between the beams at the locations of the long-range interactions for bunch 6. The differences are taken between separations without a crossing angle and with a  $500\mu\text{radian}$  crossing angle. A positive value implies that the separation with the crossing angle is greater.

at each beam-beam encounter when the crossing angle is increased to  $500\mu\text{radian}$ . While the change in separation fluctuates, on average the separation at this crossing angle increases by about  $1\sigma$ . Figure 10 shows the DA with total crossing angles from  $300\mu\text{rad}$  to  $500\mu\text{rad}$ . For comparison, the DA without a crossing angle is also shown. Without the effects due to synchro-betatron resonances, these 4D tracking results show that at a crossing angle of  $300\mu\text{radian}$ , the DA increases slightly but at  $400$  and  $500\mu\text{radians}$ , the DA decreases to below that without a crossing angle. We conclude that the impact of the IR errors is significant at crossing angles beyond  $300\mu\text{radians}$ . We emphasize though that these results are preliminary and a determination of the optimum

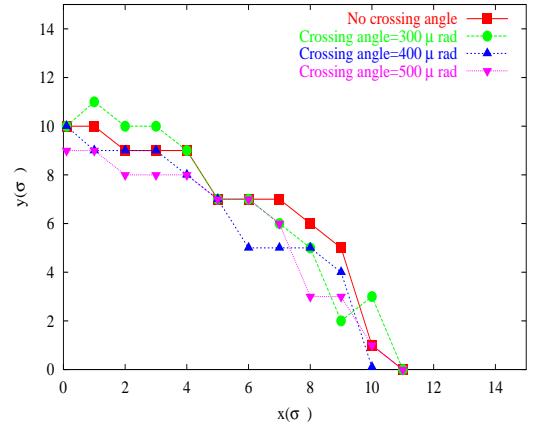


Figure 10: (color) Dynamic aperture of bunch 6 at different total crossing angles. Particles were tracked in 4D for 100,000 turns.

crossing angles will require 6D tracking.

The beam-beam interactions at a crossing angle require careful modelling to include all bunch length related effects. As mentioned earlier, bunch lengths in the Tevatron are comparable to  $\beta^*$ . The beam-beam lens in MAD was modelled to include bunch length effects but the beam-beam kick in MAD is in 4D. A separate code was written to include all bunch length effects (historically, this preceded our tracking with MAD) and the longitudinal kicks from the beam-beam interaction. In the present version of this code, long-range interactions are not included and the lattice is treated as a transverse linear map. Synchrotron oscillations are included. 1000 particles with an initial Gaussian distribution were tracked for a million turns - the amplitude of each particle as well as the amplitudes averaged over the distribution were recorded at each turn. Figure 11 shows the maximum of the averaged transverse sum amplitudes as a function of crossing angle. The opposing bunch was divided into 9 slices and was modelled in two ways: (i) only the hourglass effect is included, (ii) all bunch length effects included. There is a significant difference between the two - the amplitude growth is much smaller in the second case. Tune scans with this code (all bunch length effects included) show that particle dynamics with crossing angles is much more sensitive to the choice of tune but at well chosen tunes the synchrobetatron resonances do not cause significant amplitude growth [2]. Future studies with crossing angles will feature 6D tracking, inclusion of all bunch length effects, long-range interactions and lattice nonlinearities.

## 5 BEAM EXPERIMENTS

### 5.1 Beam-beam tune footprint studies

Measurement of the footprint is the most basic test of the nonlinearity of the beam-beam force and the machine lattice. A comparison with the theoretical footprint will reveal if all important effects have been included in the theoretical



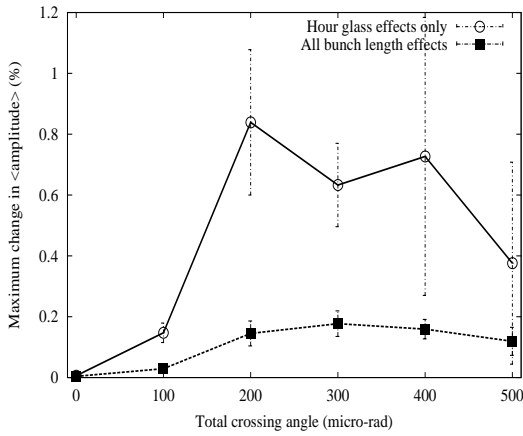


Figure 11: Change in the average transverse amplitude of a bunch as a function of the total crossing angle. The only nonlinearities were the beam-beam kicks at the two main IPs and synchrotron oscillations. The maximum % change recorded over 1 million turns is plotted on the ordinate. The bunch is represented by 1000 particles with three seeds used for the initial 6D Gaussian distribution. The opposing bunch at the collision points was divided into 9 slices but the slices were modelled in two separate ways. In one case only hour glass effects were taken into account, in the other a longitudinal Gaussian density distribution and the phase advance between the slices were also included.

model. The tune as a function of amplitude could be measured with a pencil anti-proton bunch which can be kicked to different amplitudes in both transverse planes. If this pencil bunch is sufficiently narrow, it will probe the force within a small region of phase space where the tune is nearly constant. Following the kick, this probe bunch will decohere due to the nonlinear beam-beam force and its emittance will grow as it fills out phase space by shearing. In order to plan for well-prepared studies, a number of issues have to be understood. These include:

- The decoherence time as a function of the kick amplitude. This will determine how quickly the tune has to be measured.
- The transverse size of the pbar bunch in order to get a well defined tune as a function of amplitude.
- If a single pbar bunch can only be used for tune measurement at one amplitude due to emittance growth, then it would be necessary to have many pencil pbar bunches in the beam and then cog each bunch to bring it into collision. Otherwise, the time to dump a pbar bunch, inject and accelerate another bunch before another tune measurement would prohibit measurements at several amplitudes.
- An alternative possibility could be to use the Tevatron electron lens to adiabatically kick a pbar bunch by gradually increasing the electron beam current. This

might work similar to the AC dipole suggested for other measurements at RHIC. If emittance growth can be avoided by this technique, then each pencil bunch could be used to measure the tune at more than one amplitude.

- For a cleaner comparison with the theoretical model, it might be useful to reduce the energy spread in the beam. This could be done by scraping at high dispersion locations. The momentum spread could be measured after scraping. For any kind of scraping, it will take time to learn how to scrape efficiently without losing the beam.

## 5.2 Crossing angle studies

One could start with a single anti-proton bunch and two proton bunches so the anti-protons collide with a bunch at B0 and D0. Measure the lifetime, and background losses at different crossing angles. Orbit effects due to the crossing angles will need to be eliminated, thus it would be useful to first measure the single beam lifetime without and with crossing angles. Limitations due to physical aperture can be determined this way. These measurements may reveal that there is a crossing angle beyond which the effects due to the nonlinear fields of the IR quadrupoles and the synchro-betatron resonances lead to unacceptably large losses. Some of the issues in these studies are:

- The lower limit on the anti-proton single bunch intensity in order to see a change in say anti-proton background losses on the loss monitors and anti-proton lifetime on the current monitors.
- It would be useful to do these studies with different combinations of signs of crossing angles at B0 and D0. Out of the 16 possibilities (two in each plane at each IP), only a few will yield the required beam separation with  $\sim 100 \times 100$  bunches.
- The bunch length could be increased by shaking it with RF noise or by an injection mismatch. Lifetime and/or background losses could be measured as a function of the bunch length. It would be useful to shorten the bunch length as well but this may not be practical given the limitations on the RF voltage and the transverse focusing. In addition IBS increases the bunch length.
- Tune scan of the pbar bunch to cross several resonances. This would require that the differential sextupole circuits be well controlled so that only the  $\bar{p}$  tune is changed while keeping the proton tune constant.

## 5.3 Long-range interactions

- The limit with  $36 \times 36$  bunches.

A study of the lifetime and losses with 36 bunches per beam with different separations at the locations of the

parasitic collisions. The parasitics nearest to the IPs are the ones with smallest separations so these would be varied first. This might reveal which parasitics need to be controlled the best.

- Are parasitic collisions just equivalent to scraping large amplitude particles?

One way to answer this is to measure lifetimes and losses caused by a scraper moved in closer to the beam with only head-on collisions. Measurements could be repeated with parasitic collisions at different separations and scrapers move out.

If the parasitic crossings only remove all particles beyond a certain amplitude, the results would be similar. If instead the parasitics also cause emittance growth, the results would presumably be different.

- Benchmarking simulations

One could start with a few bunches in the proton beam and spaced so that each anti-proton bunch experiences only the nearest neighbour interactions in each IR but not the head-on interactions. The lifetime could be measured as a function of the proton intensity and also as a function of the beam separation at these nearest neighbour points.

With the bunch spacing at 396 nanoseconds, perhaps the most useful experiment to determine the feasibility of shortening the spacing to 132 nanoseconds would be to collide an anti-proton bunch with 36 proton bunches with crossing angles at B0 and D0. This can be accomplished with the present set of separators. In this experiment the impact of both the synchrobetatron resonances and the long-range interactions will be felt.

## 6 REFERENCES

- [1] V. Shiltsev et al., this workshop
- [2] T. Sen, Fermilab preprint, to be published
- [3] Y. Alexahin, T. Sen, M. Xiao, this workshop
- [4] Y. Papaphilippou & F. Zimmerman, CERN-SL-99-039 AP (1999)

# BEAM-BEAM EXCITED SYNCHRO-BETATRON RESONANCES IN THE TEVATRON RUN II LATTICE

Y.Alexahin<sup>1</sup>, T.Sen, M.Xiao, FNAL, Batavia, IL 60510

## Abstract

Under certain circumstances - such as large chromatic tune modulation, bunch length comparable with the beta-function, crossing at an angle or finite dispersion at the interaction points - the beam-beam interaction can be a source of the synchro-betatron coupling.

In the present report the effect of these factors on the  $\bar{p}$ -bar stability in the Tevatron Run II configuration is considered.

It is found that the long-range interactions in the presence of large dispersion produce large contribution ( $\sim 10$ ) to the chromaticity of the betatron tunes. This chromaticity, in its turn, can give rise to multiple synchrotron satellites of the betatron resonances increasing their effective width.

At the standard Tevatron working point the synchro-betatron resonances are found to be strong enough to affect not only large amplitude particles but even the core particles.

## 1 INTRODUCTION

In Run II [1] beam-beam driven resonances (the synchro-betatron ones in particular) may present a greater danger than in the previous runs: besides an increase in the beam-beam tunes shift due to a larger number of protons per bunch and a smaller proton emittance (see Table 1), there will be a factor of seven increase in the number of parasitic long-range interactions. These numerous parasitic encounters will strongly enhance excitation of the odd-order resonances.

	Run Ib	Run IIa	Run IIb
$N_p/\text{bunch}$ , $10^{11}$	2.32	2.7	2.7
$\epsilon_{pn}$ (95% norm.), $\pi \cdot \mu\text{m}\cdot\text{rad}$	23	20	20
$\xi/\text{nominal IP}$	0.0074	0.01	0.01
$N$ parasitic IPs	10	70	278
$\xi$ , total	$\sim 0.015$	$\sim 0.025$	$\sim 0.025$
$\sigma_s$ , cm	63	37	37/14
$\sigma_E$ , $10^{-4}$	1.5	0.9	3.1
$v_s$ , $10^{-3}$	0.7	0.7	6.4

Table 1. Proton beam parameters for different Tevatron runs.

Another important effect which the long-range interactions give rise to is the beam-beam induced chromaticity (observed experimentally at LEP [2]). It depends on the particle transverse amplitudes and the bunch collision schedule and therefore can not be eliminated with the help of sextupoles. The large chromatic tune modulation of the off-momentum particles

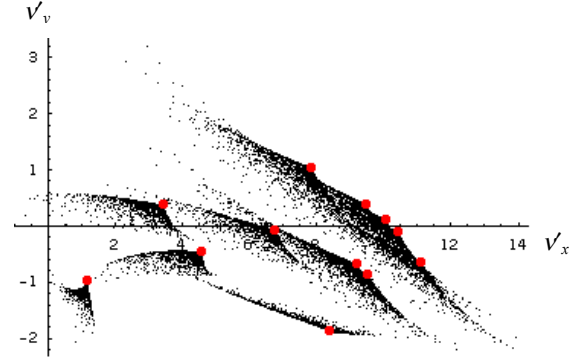


Figure 1: (color) Total  $\bar{p}$  distribution in the chromaticity plane, particles with zero betatron amplitudes in each of the 12 bunches in a train are shown with red circles.

will produce synchrotron satellites increasing the effective width of the betatron resonances.

The effect of the head-on interactions can be more pronounced in the Run II configuration if the bunch length is decreased in the second stage with the use of superconducting RF. One option that was explored was to provide  $V_{RF} = 20\text{MV}$  at  $212\text{MHz}$  compared to  $V_{RF} = 1\text{MV}$  at  $53\text{MHz}$  with the existing RF system. The reduction in the bunch length is large enough to weaken the beneficial phase averaging effect [3, 4, 5] but may be insufficient to avoid exciting the synchrotron satellites by the betatron phase modulation of the beam-beam kicks at the low-beta interaction points (IPs). Another major source of synchro-betatron coupling which will appear in Run IIb is a crossing angle at the low-beta IPs.

This report presents some results on the beam-beam driven synchro-betatron resonances in the Run II configuration obtained by analytical [5, 6] and numerical methods.

## 2 BEAM-BEAM CHROMATICITY

Due to the finite dispersion at parasitic IPs there can be significant variation of the instantaneous values of the tunes shifts in the course of the synchrotron oscillations. We will treat this variation in terms of the beam-beam contribution to chromaticity. To estimate the order of the effect let us consider a single long-range interaction point at horizontal separation  $d_x$ . The tunes shift for a particle with constant momentum deviation  $\delta_p$  is

$$\Delta v_x^{(bb)} = -\frac{r_p N \beta_x}{4\pi\gamma(d_x + D_x \delta_p)^2} \quad (1)$$

Correspondingly, we have for the beam-beam contribution to chromaticity (which we will call just “the beam-beam chromaticity” for brevity)

<sup>1</sup> Permanent address: LPP JINR, Dubna 141980 Russia

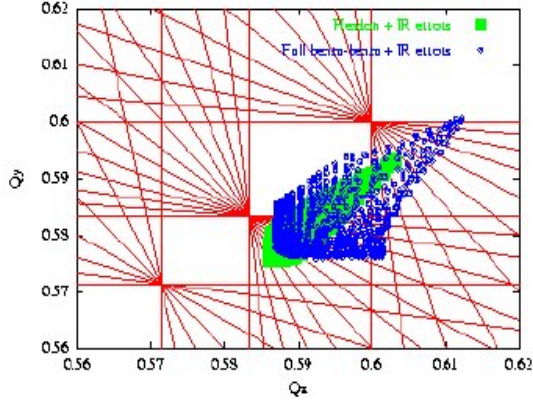


Figure 2: (color) Tune footprint of pbar bunch 6 for two cases: (1) IR quad errors and head-on interactions and (2) IR quad errors and all beam-beam interactions.

$$\Delta v_x^{(bb)} \equiv \frac{\partial}{\partial \delta_p} \Delta v_x^{(bb)} = D_x \frac{\partial}{\partial d_x} \Delta v_x^{(bb)} = -\frac{2D_x}{d_x} \Delta v_x^{(bb)} \quad (2)$$

The ratio  $|D_x/d_x|$  can be as large as  $10^3$ , so that for tuneshifts of the order of  $10^{-3}$ , the shift in chromaticity may reach  $\sim 1$ .

To calculate analytically the beam-beam chromaticity as a function of the betatron amplitudes  $a_{x,y}$

$$\Delta v_{x,y}^{(bb)}(a_x, a_y) = D_x \frac{\partial}{\partial d_x} \Delta v_{x,y}^{(bb)} + D_y \frac{\partial}{\partial d_y} \Delta v_{x,y}^{(bb)} \quad (3)$$

we use the formulas of Ref.[6] for the beam-beam tuneshift taking into account the vertical dispersion which can be quite large on the helical orbit.

Since the set of parasitic IPs is specific for each bunch in the train, there is also significant bunch-to-bunch variation. Fig.1 shows the total distribution of antiprotons (represented by 1500 points/bunch) in the plane of shifts in chromaticities due to 70 parasitic IPs.

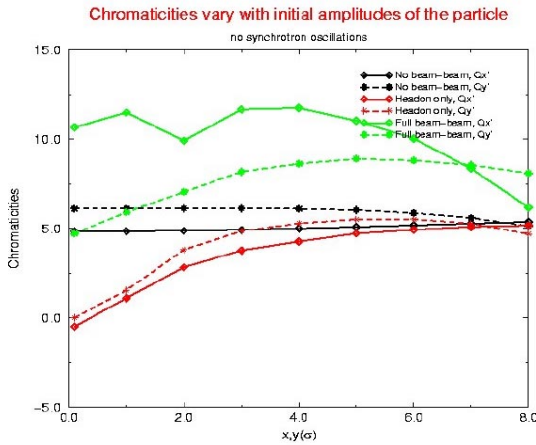


Figure 3: (color) Variation of chromaticities with particle amplitude in pbar bunch 6.

The analytical predictions were checked with tracking.

Figure 3 shows the amplitude dependent chromaticities for three cases: (1) single beam only, (2) machine errors and the head-on beam-beam interactions and (3) machine errors and all beam-beam interactions. Without the beam-beam interactions, the chromaticities stay nearly constant at the desired values. The head-on interactions cause the chromaticities to vary from about  $-5$  units in both planes at small amplitudes to zero at

$$a_{\perp} = \sqrt{a_x^2 + a_y^2} \sim 4, \quad (4)$$

$a_{x,y}$  being taken in the beam r.m.s. sizes. This contribution can be understood as a consequence of the dynamic  $\beta$  effect. The head-on interactions change the maximum beta functions in the IR quadrupoles for example from (1116, 1099) m to (1340, 1347) m. This changes the chromaticity contribution of all the IR quadrupoles by about  $-10$  units. The addition of the long-range interactions first reduces the dynamic beta effect so the beta functions around the ring are almost the same as with the single beam. They also cause, as predicted by the analysis, the horizontal chromaticity to vary from 6 to 12 units and the vertical chromaticity to vary from 5 to 8 units.

We see that the chromaticities cannot be made small simultaneously for all particles in all bunches with the help of correction sextupoles.

### 3 BEAM-BEAM RESONANCES

Fig.2 shows the footprint of the antiproton bunch #6 in the tune diagram obtained with the standard optics and the bare lattice tunes  $v_{x0}=20.585$ ,  $v_{y0}=20.575$ . The 5<sup>th</sup>, 7<sup>th</sup> and 12<sup>th</sup> order sum resonance lines<sup>2</sup> are also shown.

In this report we limit ourselves to a single resonance approximation considering one resonance

$$\underline{m} \cdot \underline{v} \equiv m_x v_x + m_y v_y + m_s v_s \approx n \quad (5)$$

at a time and then applying the Chirikov criterion to assess the cooperative effect of multiple resonances. We calculate analytically the resonance strength and beatings of the betatron amplitudes using the formulae of Ref.[6].

The synchrotron motion affects the resonance behavior in a number of ways. First, it somewhat weakens the principal resonance,  $m_s = 0$ , by the virtue of: i) dephasing the successive beam-beam kicks due to chromatic betatron tune modulation; ii) phase averaging of every kick due to a finite bunch length. On the other hand, these very same mechanisms give rise to synchrotron satellites,  $m_s \neq 0$ , which can effectively widen the resonance if the Chirikov overlap condition is met. In addition to these mechanisms, the crossing angle and finite dispersion can contribute to excitation of the synchrotron satellites.

If there are no offsets, no crossing angle nor dispersion at the IPs and  $\beta_x = \beta_y = \beta^*$ , the effect of the longitudinal motion on the resonance excitation can be described by the factor [6]

<sup>2</sup> Analysis shows that the difference resonances are less important at the working point considered.

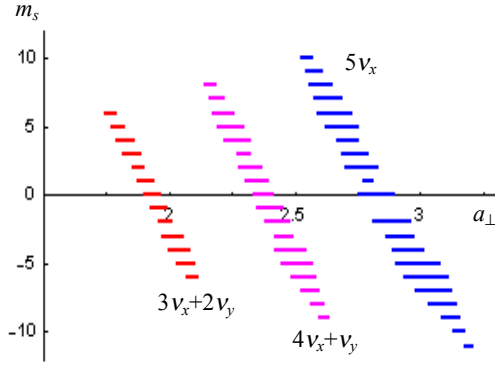


Figure 4: (color) Each horizontal line represents the swing of the transverse amplitude due to the 5<sup>th</sup> order resonances and their synchrotron satellites at  $a_s = \sqrt{2}$ .

$$L_m(J_s) = \frac{1}{(2\pi)^2} \iiint e^{-im_s\psi_s - i(m_x+m_y)\phi - i(m_x\eta_x+m_y\eta_y)\sigma} \times$$

$$F_L(J'_s) dJ'_s d\psi'_s d\psi'_s$$

where  $F_L = \exp(-J_s)$  is the normalized distribution function in the longitudinal action variable  $J_s$  (normalized to  $\mathcal{E}_s = \sigma_s \sigma_E$ ),  $\sigma = \sigma_s \sqrt{2J_s} \sin \psi_s$ ,

$$\eta_x = \frac{1}{\alpha_M R} \frac{dv_x}{d\delta_p} \quad (7)$$

with  $\alpha_M$  and  $R$  being the momentum compaction factor and the mean radius of the orbit,

$$\phi = -\arctan \frac{\sigma - \sigma'}{2\beta^*}. \quad (8)$$

It is obvious that  $|L_m(J_s)| \leq 1$  always.

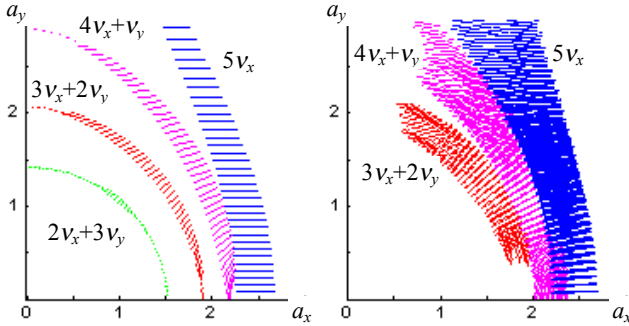


Figure 5: (color) Swing of the transverse amplitudes due to the 5<sup>th</sup> order resonances and their synchrotron satellites at  $a_s = 0$  (left) and  $a_s = \sqrt{2}$  (right).

### 3.1 Betatron tune modulation

Let us first consider odd-order resonances due to parasitic interactions. Since the betatron functions at these points are large in comparison with the bunch length we may put  $\phi \rightarrow 0$  in eq.(7) and obtain the classical formula for the synchrotron satellites excitation:

$$L_m(J_s) = J_m \left[ \frac{(m_x v'_x + m_y v'_y) \sigma_E}{v_s} \sqrt{2J_s} \right] \quad (9)$$

where  $J_m(x)$  is the Bessel function, the relation  $\sigma_s = R \alpha_M \sigma_E / v_s$  has been used.

As discussed in Section 2 the total chromaticity can not be made small by the conventional use of sextupoles. As a result synchrotron satellites up to a high order,

$$m_s \approx \left| \frac{m_x v'_x + m_y v'_y}{v_s} \right| \sigma_E a_s, \quad (10)$$

( $a_s = \sqrt{2J_s}$ ), can be excited leading to an appreciable increase in the effective resonance width.

Fig. 4 shows the swing of the transverse amplitude,  $a_\perp$ , due to the 5<sup>th</sup> order resonances and their satellites excited by 70 parasitic interactions for particles in the 6<sup>th</sup> antiproton bunch with initially  $a_x = a_y$  and  $J_s = 1$  ( $a_s = \sqrt{2}$ ) in the absence of the bare lattice chromaticity ( $\eta_{x0} = \eta_{y0} = 0$ ). The sidebands of different resonances overlap which means the possibility of fast particle transport over the entire set of resonances almost doubling the particle amplitude (from  $a_\perp \approx 1.75$  to  $a_\perp \approx 3.25$ ). This can affect not only the particle lifetime but the luminosity as well.

A 2D picture of the resonance satellites overlap is presented in Fig.5. The left plot shows the width of the betatron resonances for on-momentum particles ( $J_s = 0$ ) when no satellite is excited. At large synchrotron amplitudes ( $J_s = 1$ ) these resonances are, in accordance with Eq. (10), noticeably suppressed (e.g. the  $2v_x + 3v_y$  resonance width falls below the chosen threshold). However, due to excitation of numerous satellites the effective resonance width is substantially increased.

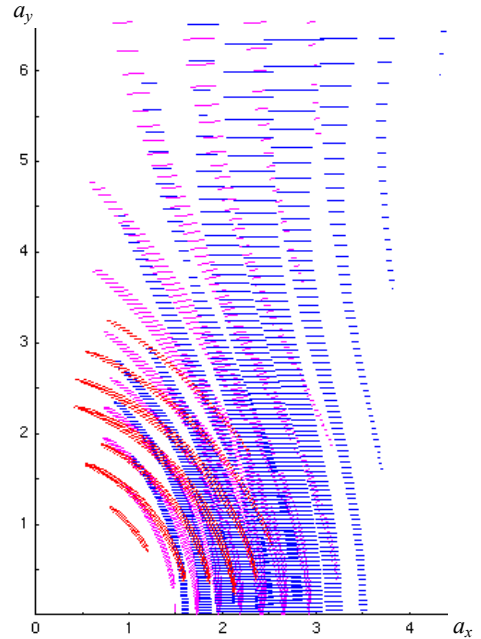


Figure 6: (color) The same as in Fig.4 (right) but with the superconducting RF.

With shorter bunches  $\sigma_s = 14$  cm, the distance between the satellites of each of the 5<sup>th</sup> order resonances becomes larger than the resonance width (Fig. 6) but now the satellites of different resonances overlap so that the amplitude range over which the fast diffusion can occur increases.

It is obvious that the working point should be pulled away from these resonances, e.g. down along the main diagonal. However, the beam distribution in that case will span all the 12<sup>th</sup> order resonances.

### 3.2 Finite bunch length effect

In the case of a large bunch length ( $\sigma_s \sim \beta^*$ ) the synchrotron satellites can be excited also via modulation of the betatron phase of the beam-beam kicks in the course of the synchrotron oscillations. This mechanism is important for low-beta interaction points where (in the absence of misalignments) only even-order resonances (and their satellites) can be excited:

$$m_x + m_y = 2m. \quad (11)$$

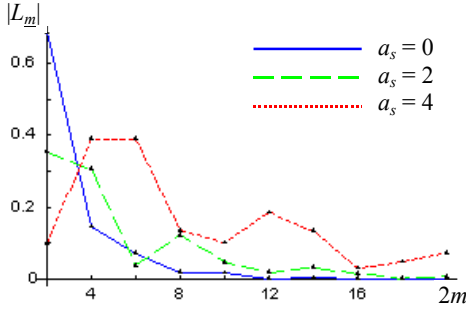


Figure 7: Longitudinal factor vs. resonance order.

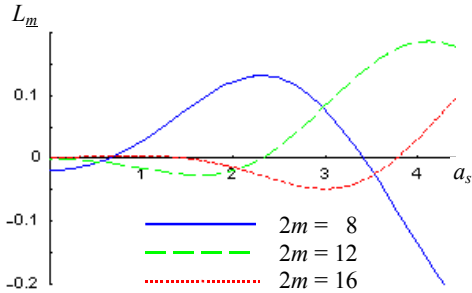


Figure 8: Longitudinal factor vs. synchrotron amplitude.

For numerical calculations we use the representation [6]

$$L_m(J_s) = (-1)^m \{ (-1)^{m_s} J_{m_s} (4m\beta^* \eta \lambda \sqrt{J_s}) + \int_0^\infty dt e^{-t-\lambda^2 t^2/4} J_{m_s} [\lambda(t-4m\beta^* \eta) \sqrt{J_s}] \sum_{k=1}^m \frac{(-2)^k m! t^{k-1}}{(m-k)!(k-1)!k!} \} \quad (12)$$

where  $\lambda = \sigma_s / \beta^* \sqrt{2}$ . Fig. 7 shows the dependence of the absolute value of the longitudinal factor defined in Eq. (12) for the principal resonance,  $m_s = 0$ , on the resonance order,  $2m$ , at several values of the normalized synchrotron amplitude,  $a_s$ ,  $\sigma_s = \beta^*$ , and zero chromaticity,  $\eta = 0$ . For an on-momentum particle,  $a_s = 0$ , the longitudinal factor rapidly falls off with the resonance order due to the phase averaging, reaching as small value as  $10^{-3}$  at  $2m = 12$ . However, with increasing  $a_s$  the phase averaging is less effective, as found in Ref.[5]. It may not be sufficient to suppress the head-on contribution to excitation of high order resonances. Fig. 8 shows the longitudinal factor as a function of  $a_s$  for the resonances of the order  $2m = 8, 12, 16$ .

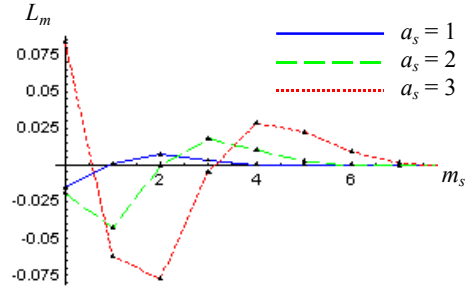


Figure 9: Longitudinal factor of 12<sup>th</sup> order resonances vs. synchrotron satellite number.

Now let us turn to the synchrotron sidebands,  $m_s \neq 0$ . Fig. 9 shows the dependence of the longitudinal factor of the  $2m = 12$  resonances on the sideband number for several values of  $a_s$  at  $\sigma_s / \beta^* = 1$ ,  $\eta = 0$ . We see that the strength of the synchrotron satellites can be comparable with that of the principal resonance effectively increasing its width. Fig. 10 shows beatings in the transverse amplitudes due to the 12<sup>th</sup> order betatron resonances and their synchrotron satellites excited by the beam-beam interaction at two Tevatron low-beta IPs at  $J_s = 1$ ,  $\eta = 0$ ,  $\sigma_s / \beta^* = 37/35$ ,  $v_s = 7 \cdot 10^{-4}$  (left) and  $\sigma_s / \beta^* = 14/35$ ,  $v_s = 6.4 \cdot 10^{-3}$  (right). In the first case the effect, although quite pronounced, should not pose significant problems in the Tevatron operation since the resonance groups are well separated. Let us note that the lines representing effect of a particular resonance are not shown if their length does not exceed a certain threshold value ( $\sim$  the line width) or if they lie outside the circle  $a_\perp = 11$ .

In the second case, which corresponds to the 20 MV, 212 MHz SC RF, i) the width of the resonances becomes larger due decrease in the phase averaging, ii) satellites are farther apart due to a larger synchrotron tune. As a result the 12<sup>th</sup> order resonances and their satellites form a maze through which particles, with some assistance from external noise and higher order resonances, can escape starting from amplitudes possibly as low as  $a_\perp \sim 4$ .



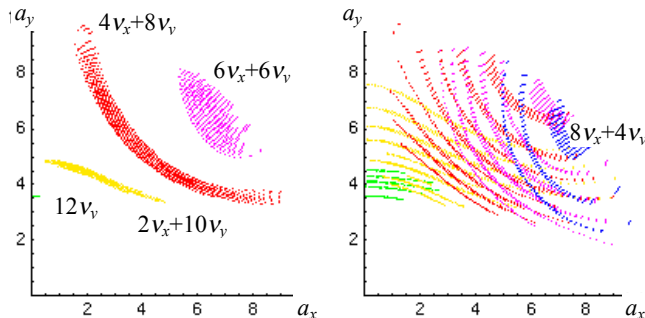


Figure 10: (color) Swing of the transverse amplitudes due to the 12<sup>th</sup> order resonances and their synchrotron satellites excited by the head-on interactions in the case of the existing (left) and SC (right) RF systems.

## 4 DYNAMIC APERTURE

Extensive tracking calculations of the dynamic aperture in 4D are reported in [7]. We have begun 6D dynamic aperture calculations for the optics configuration of Run IIa. Here we report some results of these calculations as a check of the analysis above.

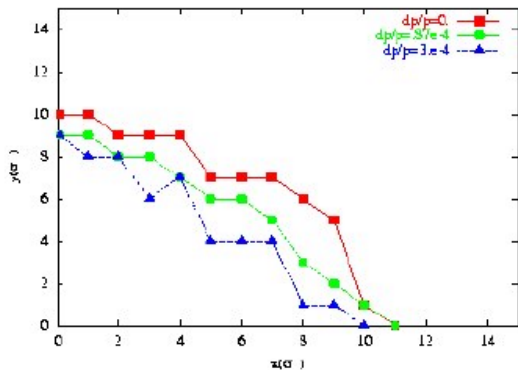


Figure 11: (color) 6D dynamic aperture of pbar bunch 6 after 100,000 turns (about 72 synchrotron periods). The dynamic aperture for the off-momentum cases correspond to  $1\delta_p$  and  $3.45\delta_p$ .

	Average DA ( $\sigma$ )	Minimum DA( $\sigma$ )
dp/p = 0	9.8	8.6
dp/p=8.7E-5	8.9	7.8
dp/p=3.E-4	8.1	6.4

Table 2 : The average and minimum 6D dynamic aperture for the three cases shown in Figure 11.

Figure 11 shows the 6D dynamic aperture calculated for three values of momentum deviation. The average and

minimum DA (shown in Table 2) decrease by about  $1\sigma$  as the momentum deviation is increased. While the reduction in DA is expected, it is not significantly large. This implies that at least at this time scale, the synchro-betatron resonances are not very strong. It is possible that the drop in DA with momentum deviation is more significant at longer time scales. This will be checked with longer term tracking.

## 5 SUMMARY

- Beam-beam resonances may prevent the desired luminosity goals in Run II from being achieved. These resonances will be particularly strong in Run IIb, and more so if shorter bunches are used.
- The chromatic tune modulation is a major driving mechanism of synchro-betatron resonances, it can not be avoided due to large beam-beam chromaticity. Another important mechanism is the betatron phase modulation at low-beta IPs.
- The beam-beam contribution to chromaticity strongly depends on the particle transverse amplitudes and the bunch collision schedule and therefore can not be eliminated with the help of sextupoles. The total (intrabunch + bunch-to-bunch) spread in chromaticity reaches  $\sim 12$  units horizontally and  $\sim 5$  units vertically.
- With the bare lattice tunes around the values,  $\nu_{x0}=20.585$ ,  $\nu_{y0}=20.575$ , it is difficult to avoid exciting low-odd-order (either 5<sup>th</sup> or 7<sup>th</sup> order) resonances, the 12<sup>th</sup> order resonances also lie within the beam-beam footprint. Therefore it may be helpful to choose another working point (e.g. the one at  $\nu_{x0}=20.685$ ,  $\nu_{y0}=20.675$ ).
- Tracking calculations of the 6D dynamic aperture, with all effects mentioned here included, indicate that synchro-betatron resonances do not dramatically reduce the dynamic aperture on relatively short time scales.
- The present analysis should be extended to the RunIIb configuration with  $140 \times 105$  bunches where the effect of the odd-order resonances will be much stronger.
- During optimization of the operating conditions in the Tevatron, it may be helpful to have an on-line program for computation of the beam-beam footprints and resonance widths for the particular bunch fill and tune settings.

## 6 REFERENCES

- [1] "Tevatron run II Handbook", <http://www-bd.fnal.gov/runII/index.html>
- [2] B.Goddard, W.Herr, E.Keil *et al.*, "Bunch Trains for LEP", CERN/SL/97-02 (AP), 1997; *Particle Accelerators*, v.57, p.237 (1998)
- [3] S.Krishnagopal, R.Siemann, *Phys. Rev. D*, v.41, p.2312 (1990).



- [4] D.Pestrikov, "Synchrobetatron Resonances in Long Bunches due to Horizontal Crossing", *in*: Proc. VII Advanced ICFA Beam Dynamics Workshop, Dubna, 1995, pp. 77-90.
- [5] T.Sen, "The Beam-Beam Interaction of Finite Length Bunches in Hadron Colliders", FERMILAB-Pub-00/093-T (2000).
- [6] Y.Alexahin, FERMILAB-TM-2148 (2001).
- [7] T.Sen, M.Xiao and N.Gelfand, "Beam-beam interactions in Run II at the Tevatron", these proceedings

# Beam Rounders for Circular Colliders

A. Burov\*, S. Nagaitsev, FNAL, Batavia, IL  
Ya. Derbenev, Jefferson Laboratory, Newport News, VA

## Abstract

By means of linear optics, an arbitrary uncoupled beam can be locally transformed into a round (rotation-invariant) state and then back. This provides an efficient way to round beams in the interaction region of circular colliders.

## 1 ROUND BEAMS AND ROTATION-INVARIANT MAPS

Round beams in the interaction region of a circular collider are widely believed to be an effective way to increase the luminosity (see e. g. [1] and the references therein).

Canonical angular momentum (CAM) preservation by the IP revolution mapping might play a crucial role in the luminosity upgrade of circular colliders. The CAM is preserved when 2 conditions are satisfied:

- The lattice IP revolution map is CAM-preserving;
- The beams are round in the IR.

General form of the CAM-preserving matrices was found by E. Pozdeev and E. Perevedentsev [2]:

$$\mathcal{T} = \begin{pmatrix} \mathcal{T} \cdot \cos \theta & \mathcal{T} \cdot \sin \theta \\ -\mathcal{T} \cdot \sin \theta & \mathcal{T} \cdot \cos \theta \end{pmatrix} \equiv \mathcal{R}(\theta) \begin{pmatrix} \mathcal{T} & 0 \\ 0 & \mathcal{T} \end{pmatrix} \quad (1)$$

The CAM-preserving group is identical to the symplectic rotation-invariant transformations.

Parameterization of the  $2 \times 2$  unimodular matrix  $\mathcal{T}$  can be taken in the conventional Courant-Snyder form, in terms of its input  $\alpha_1, \beta_1$  and output  $\alpha_2, \beta_2$  parameters and a phase advance  $\mu$ : (see e. g. [3]):

$$\mathcal{T} = \begin{pmatrix} \sqrt{\frac{\beta_2}{\beta_1}}(c + \alpha_1 s) & \sqrt{\beta_1 \beta_2} s \\ -\frac{1 + \alpha_1 \alpha_2}{\sqrt{\beta_1 \beta_2}} s + \frac{\alpha_1 - \alpha_2}{\sqrt{\beta_1 \beta_2}} c & \sqrt{\frac{\beta_1}{\beta_2}}(c - \alpha_2 s) \end{pmatrix}. \quad (2)$$

where  $s = \sin \mu$ ,  $c = \cos \mu$ , the subscript 1 of the Courant-Snyder parameters relates to an initial and 2 to a final states.

## 2 CIRCULAR BASIS

The symplectic basis which form is preserved by the rotation-invariant transformations:

$$U = \frac{1}{\sqrt{2}} \begin{pmatrix} \sqrt{\beta} c_+ & \sqrt{\beta} s_+ & -\sqrt{\beta} c_- & -\sqrt{\beta} s_- \\ \frac{-s_+ - \alpha c_+}{\sqrt{\beta}} & \frac{c_+ - \alpha s_+}{\sqrt{\beta}} & \frac{s_- + \alpha c_-}{\sqrt{\beta}} & \frac{-c_- + \alpha s_-}{\sqrt{\beta}} \\ \sqrt{\beta} s_+ & -\sqrt{\beta} c_+ & \sqrt{\beta} s_- & -\sqrt{\beta} c_- \\ \frac{c_+ - \alpha s_+}{\sqrt{\beta}} & \frac{s_+ + \alpha c_+}{\sqrt{\beta}} & \frac{c_- - \alpha s_-}{\sqrt{\beta}} & \frac{s_- + \alpha c_-}{\sqrt{\beta}} \end{pmatrix}. \quad (3)$$

where  $c_{\pm} = \cos \phi_{\pm}$ ,  $s_{\pm} = \sin \phi_{\pm}$  with arbitrary phases  $\phi_{\pm}$ . Similar, but not exactly same presentation of the circular modes was used by V. Lebedev and S. Bogacz [4]. A great feature of this parameterization:

Under the rotation-invariant transformations (1) the circular set (3) is transformed similar to how the linear basis does under the uncoupled mappings:

$$\tilde{U} \equiv \mathcal{T} \cdot U(\alpha, \beta, \phi_+, \phi_-) = U(\alpha_2, \beta_2, \phi_+ + \mu - \theta, \phi_- + \mu + \theta). \quad (4)$$

Any phase space vector  $x$  can be expanded over this rotating basis:

$$x = U \cdot a. \quad (5)$$

$$a = (\sqrt{2J_+} \sin \chi_+, \sqrt{2J_+} \cos \chi_+, \sqrt{2J_-} \sin \chi_-, \sqrt{2J_-} \cos \chi_-) \quad (6)$$

Taking the amplitudes from their definition (5), the actions can be expressed in terms of 2D vectors of the offset and transverse momentum  $\vec{r} = (x, y)$ ,  $\vec{p} = (p_x, p_y)$ :

$$J_{\pm} = \gamma \vec{r}^2 / 4 + \alpha \vec{r} \vec{p} / 2 + \beta \vec{p}^2 / 4 \pm M / 2 \quad (7)$$

where  $\gamma \equiv (1 + \alpha^2) / \beta$  and  $M = xp_y - yp_x$  is the CAM. Note a similarity of this expression to the corresponding formula in the uncoupled case.

Preservation of the circular actions  $J_{\pm}$  under the invariant mappings means that both their sum and difference are preserved as well:

$$J_+ - J_- = M = \text{const};$$

$$J_+ + J_- = \gamma \vec{r}^2 / 2 + \alpha \vec{r} \vec{p} + \beta \vec{p}^2 / 2 = \text{const}. \quad (8)$$

Inverse expressions are found as

$$\begin{aligned} \vec{r}^2 / \beta &= J_+ + J_- + 2\sqrt{J_+ J_-} \cos \psi \\ \vec{p}^2 \beta &= (J_+ + J_-)(1 + \alpha^2) + \\ &\quad 2\sqrt{J_+ J_-}(-1 + \alpha^2) \cos \psi + 4\sqrt{J_+ J_-} \alpha \sin \psi \\ \vec{r} \vec{p} &= -\alpha(J_+ + J_-) - 2\sqrt{J_+ J_-} \alpha \cos \psi - 2\sqrt{J_+ J_-} \sin \psi \end{aligned} \quad (9)$$

where  $\psi = \phi_+ + \chi_+ + \phi_- + \chi_-$ . When only one of the two circular modes is excited (either  $J_+$  or  $J_-$  is zero), then

$$\vec{r}^2 = \beta J, \quad \vec{p}^2 = \gamma J, \quad \vec{r} \vec{p} = -\alpha J, \quad M = \pm J. \quad (10)$$

## 3 ADAPTERS

Both uncoupled  $V$  and circular  $U$  (3) basic sets are symplectic; therefore, they can be mapped on each other. Symplectic transformations

$$\mathcal{C} = U \cdot V^{-1} \quad \text{and} \quad \tilde{\mathcal{C}} = V \cdot U^{-1} \quad (11)$$

\*burov@fnal.gov

map the uncoupled basis  $V$  on the circular basis  $U$ , and back, respectfully. Note that the uncoupled-to-circular transformation  $\mathcal{C}$  maps the horizontal and vertical phase spaces on the modes of opposite helicities. So the corresponding uncoupled and circular Courant-Snyder invariants are equal:

$$J_x = J_+; J_y = J_- . \quad (12)$$

Adaptive transformations are illustrated schematically by Fig. 1.

#### 4 IMPLEMENTATION OF ADAPTERS

A particular solution for the adaptive transformation [Ya. Derbenev]:

$$\mathcal{C} = \mathcal{R}(\pi/4) \langle M, N \rangle \mathcal{R}(-\pi/4) \quad (13)$$

where  $\langle M, N \rangle$  stands for a block-diagonal  $4 \times 4$  matrix with  $M$  and  $N$  as its  $2 \times 2$  diagonal blocks:

$$M = \begin{pmatrix} \sqrt{\frac{\beta}{\beta_0}}(\cos \phi_0 - \alpha_0 \sin \phi_0) & -\sqrt{\beta\beta_0} \sin \phi_0 \\ \frac{\alpha_0 \cos \phi_0 + \sin \phi_0}{\sqrt{\beta\beta_0}} & \sqrt{\frac{\beta_0}{\beta}} \cos \phi_0 \end{pmatrix} \quad (14)$$

and

$$N = \begin{pmatrix} -\sqrt{\frac{\beta}{\beta_0}}(\alpha_0 \cos \phi_0 + \sin \phi_0) & -\sqrt{\beta\beta_0} \cos \phi_0 \\ \frac{\cos \phi_0 - \alpha_0 \sin \phi_0}{\sqrt{\beta\beta_0}} & -\sqrt{\frac{\beta_0}{\beta}} \sin \phi_0 \end{pmatrix} \quad (15)$$

The matrices  $M, N$  are related as

$$N = F \cdot M \quad F = \begin{pmatrix} 0 & -\beta \\ 1/\beta & 0 \end{pmatrix}. \quad (16)$$

this particular adapter transforms initial uncoupled basis (subscript 0) into a circular basis at its waist point ( $\alpha = 0$ ).

#### 5 CIRCULAR EIGENMODES FOR A SOLENOID

Circular eigenmodes of an extended solenoid: CS parameters remain constant, and only the phases run. The solenoidal transformation:

$$\mathcal{T}_s = \mathcal{R}(-\theta_s) \cdot \langle T_s, T_s \rangle \quad (17)$$

with

$$T_s = \begin{pmatrix} \cos \theta_s & \beta_s \sin \theta_s \\ -\beta_s^{-1} \sin \theta_s & \cos \theta_s \end{pmatrix}. \quad (18)$$

Here  $\theta_s = eBz/(2p_0c) \equiv z/(2\rho)$  is the Larmor phase advance and

$$\beta_s = 2c/(eB) \quad (19)$$

can be referred to as the Larmor  $\beta$ -function. The Courant-Snyder parameters of the circular basis with  $\beta = \beta_s$  and  $\alpha = 0$  are preserved inside the solenoid: the first pair of the basis vectors turns by an angle  $\Delta\phi_+ = \theta_s + \theta_s = 2\theta_s$  and the second pair by  $\Delta\phi_- = -\theta_s + \theta_s = 0$ , i. e. remains constant.

The canonical variables  $\tilde{a}$  associated with these circular modes describe the kinetic momenta

$$k_y = p_y + x/\beta_s \quad k_x = p_x - y/\beta_s \quad (20)$$

and coordinates of the Larmor center

$$d_x = x/2 - \beta_s p_y/2 \quad d_y = y/2 + \beta_s p_x/2; \quad (21)$$

namely,

$$\begin{pmatrix} \tilde{a}_1 \\ \tilde{a}_2 \end{pmatrix} = \sqrt{\frac{\beta_s}{2}} \begin{pmatrix} k_y \\ k_x \end{pmatrix}, \quad \begin{pmatrix} \tilde{a}_3 \\ \tilde{a}_4 \end{pmatrix} = -\sqrt{\frac{2}{\beta_s}} \begin{pmatrix} d_x \\ d_y \end{pmatrix}. \quad (22)$$

When the adapter  $\mathcal{C}$  is matched with an adjacent downstream solenoid, i. e.  $\alpha = 0, \beta = \beta_s$ , the horizontal degree of freedom of the incoming uncoupled beam transforms into the cyclotron mode inside the solenoid, while the vertical one transforms into the drift mode, and the emittances are preserved:

$$\begin{aligned} \varepsilon_x^2 &\equiv \langle x^2 \rangle \langle p_x^2 \rangle - \langle x p_x \rangle^2 = \varepsilon_c^2 \equiv \langle \tilde{a}_1^2 \rangle \langle \tilde{a}_2^2 \rangle - \langle \tilde{a}_1 \tilde{a}_2 \rangle^2 = \\ &= (4/\beta^2) (\langle k_x^2 \rangle \langle k_y^2 \rangle - \langle k_x k_y \rangle^2) \\ \varepsilon_y^2 &\equiv \langle y^2 \rangle \langle p_y^2 \rangle - \langle y p_y \rangle^2 = \varepsilon_d^2 \equiv \langle \tilde{a}_3^2 \rangle \langle \tilde{a}_4^2 \rangle - \langle \tilde{a}_3 \tilde{a}_4 \rangle^2 = \\ &= (\beta^2/4) (\langle d_x^2 \rangle \langle d_y^2 \rangle - \langle d_x d_y \rangle^2) \end{aligned} \quad (23)$$

with the brackets  $\langle \dots \rangle$  standing for an ensemble averaging. For a particular case of the round beam inside the solenoid, when  $\langle d_x^2 \rangle = \langle d_y^2 \rangle \equiv d^2$ ,  $\langle d_x d_y \rangle = 0$  and similar momentum relations, it yields

$$\varepsilon_x = \beta k^2/2, \quad \varepsilon_y = 2d^2/\beta. \quad (24)$$

The solenoid with an opposite field switches mapping: the horizontal degree of freedom is mapped onto the drift mode and the vertical plane is mapped onto the cyclotron mode.

Similar relations take place for the reverse, circular-to-uncoupled transformations  $\tilde{\mathcal{C}}$ .

#### 6 LOCAL ROTATION INVARIANCE

When the rotation invariance is local (continuous):

$$\frac{d\beta}{ds} = -\frac{2\alpha}{p_0}, \quad \frac{d\phi_{\pm}}{ds} = \frac{1}{p_0} \left( \frac{1}{\beta} \pm \frac{1}{\beta_s} \right). \quad (25)$$

and

$$\beta'' - \frac{\beta'^2}{2\beta} + \frac{(\gamma'_0 \beta)' }{\beta_0^2 \gamma_0} + \frac{2\beta}{p_0^2} \left( \frac{1}{\beta_s^2} - \frac{1}{\beta^2} \right) - \frac{2K}{|M_m|} = 0. \quad (26)$$

Here  $\beta_0$  and  $\gamma_0$  are the relativistic factors,  $p_0 = mc\beta_0\gamma_0$  is the total (longitudinal) momentum,  $M_m$  is the CAM of the boundary particle with the offset  $r_m$  and  $K = \frac{2Ie}{mc^3\beta_0^3\gamma_0^3}$  is the so-called generalized perveance, which takes into account the space charge.

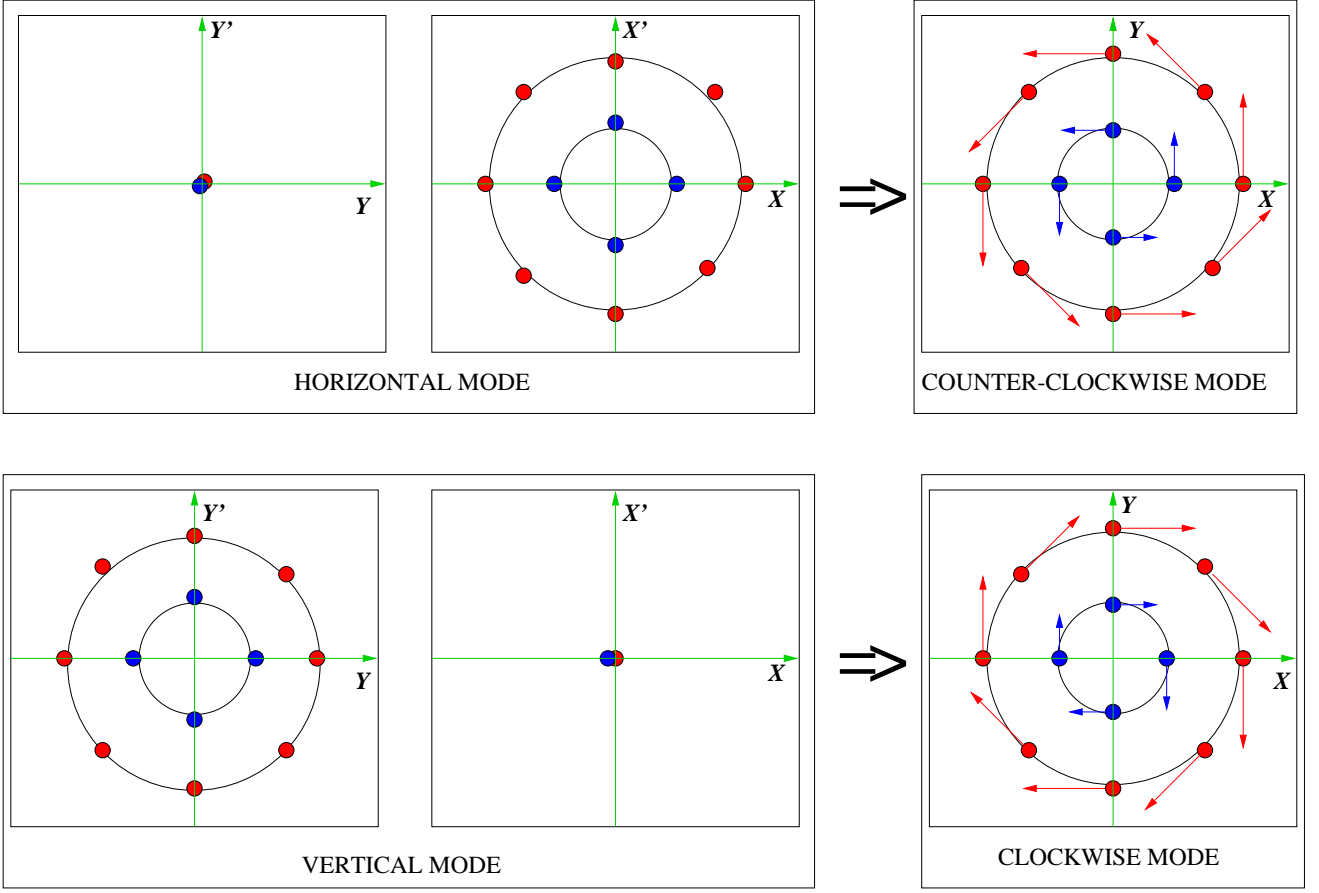


Figure 1: Schematic illustration of the uncoupled-to-circular beam adapter: horizontally and vertically polarized modes are transformed into circular modes of opposite helicities. Blue and red dots represent particles with smaller or  $r$  actions. Arrows on the circular mode portraits show particle momenta, proportional to the offsets. For simplicity, all the phase portraits are depicted as circles; generally, tilted ellipses are mapped onto each other. Direction of external arrows  $\Rightarrow$  specify the direction of transformation. Reverse direction of both upper and lower arrows ( $\Leftarrow$ ) would correspond to the reverse, circular-to-uncoupled adapter.

## 7 DIAGONALIZATION OF BEAM MATRIX

The beam matrix

$$\Sigma_{i,j} = \langle x_i x_j \rangle$$

describes the beam distribution. If  $\mathcal{M}$  is a transfer matrix, then the new  $\Sigma$ -matrix is  $\mathcal{M}\Sigma\mathcal{M}^T$ . The uncoupled state is described by the block-diagonal  $\Sigma$ -matrix in the original Cartesian coordinates; its 4D emittance is a product of the 2D emittances. Normally the phase distributions are homogeneous, in this case the  $\Sigma$ -matrix is diagonal in the matched uncoupled basis (the transfer matrix in this case  $\mathcal{M} = V^{-1}$ ):

$$\Sigma = \text{Diag}(\varepsilon_x, \varepsilon_x, \varepsilon_y, \varepsilon_y), \quad (27)$$

where  $\text{Diag}(\dots)$  is a diagonal matrix with elements listed as the arguments. In the same way, the  $\Sigma$ -matrix of a round beam is diagonal in the matched circular basis.

The  $\Sigma$ -matrix of a round beam can be expressed in rotation-invariant terms:

$$\Sigma = \frac{1}{2} \begin{pmatrix} \Sigma & \langle M \rangle J \\ -\langle M \rangle J & \Sigma \end{pmatrix}; \quad \Sigma = \begin{pmatrix} \langle r^2 \rangle & \langle \vec{r} \vec{p} \rangle \\ \langle \vec{r} \vec{p} \rangle & \langle p^2 \rangle \end{pmatrix}; \quad (28)$$

$$J = \begin{pmatrix} 0 & 1 \\ -1 & 0 \end{pmatrix}.$$

This beam matrix is diagonalized by the circular basis with

$$\beta = \frac{\langle r^2 \rangle}{\sqrt{\langle r^2 \rangle \langle p^2 \rangle - \langle \vec{r} \vec{p} \rangle^2}}, \quad \alpha = -\frac{\langle \vec{r} \vec{p} \rangle}{\sqrt{\langle r^2 \rangle \langle p^2 \rangle - \langle \vec{r} \vec{p} \rangle^2}} \quad (29)$$

leading to

$$\Sigma = \text{Diag}(\varepsilon_1, \varepsilon_1, \varepsilon_2, \varepsilon_2) \quad (30)$$

with the emittances

$$2\varepsilon_{1,2} = \pm \langle M \rangle + \sqrt{\langle r^2 \rangle \langle p^2 \rangle - \langle \vec{r} \vec{p} \rangle^2} \geq 0. \quad (31)$$

These partial emittances are preserved by any symplectic transformation.

The total 4D emittance is a product of these partial emittances :

$$4\epsilon \equiv 4\epsilon_1\epsilon_2 = \langle r^2 \rangle \langle p^2 \rangle - \langle \vec{r}\vec{p} \rangle^2 - \langle M \rangle^2 \quad (32)$$

[S. Nagaitsev, A Shemyakin]. The 4D emittance in terms of the canonical and kinetic momenta are absolutely identical: a transfer from one to another is equivalent to rotation imposed on the beam as a whole, which does not change the total emittance.

## 8 ROUND BEAMS FOR CIRCULAR COLLIDERS

For circular colliders, round beams in the interaction region (IR) are known to be beneficial: angular momentum preservation allows to increase the beam-beam tune shift and so the luminosity. Conventional round-beams schemes require  $\epsilon_x = \epsilon_y$  and  $\nu_x = \nu_y$ . Another approach to get the beams round, the Möbius accelerator [5], based on beam rotator optics [6], is studied experimentally at CESR [7]. This scheme also leads to emittance identity and effective tune degeneration: the resulting normal tunes are inevitably separated by 1/2.

Matched adapters bounding the IR opens a way that is free from all these limitations.



Figure 2: Beam Rounder

This beam rounder allows to have:

- round beam inside it;
- the same uncoupled beam outside it, as it was without the rounder;
- rotation-invariant revolution matrix;
- all these features are kept for any tunes, emittances and the solenoidal field inside.

## 9 REFERENCES

- [1] V. Danilov and V. Shiltsev, FNAL, FERMILAB-FN-655 (1997).
- [2] E. Pozdeev and Perevedentsev, BINP, private communications (1995).
- [3] A. Chao and M. Tigner, "Handbook of Accelerator Physics and Engineering", World Scientific, pp.49-52 (1998).
- [4] V. A. Lebedev and S. A. Bogacz, e-print JLAB-ACC-99-19.
- [5] R. Talman, Phys. Rev. Lett. 74, p. 1590 (1995).
- [6] S. K. Kowalski and H. Enge, in Proc. Int. Conf. on Magnet Tech., Brookhaven, 1972, p. 181.

- [7] S. Henderson et al. in Proc. Part. Acc. Conf., New York, 1999, p. 410.

# EXCERPTS FROM THE VLHC DESIGN STUDY – ACCELERATOR PHYSICS ISSUES

M. Syphers, FNAL, Batavia, IL 60510, USA

## Abstract

A six-month design study for a future high energy hadron collider was initiated by the Fermilab director in October 2000. The request was to study a staged approach where a large circumference tunnel is built that initially would house a low field ( $\sim 2$  Tesla) collider with center-of-mass energy greater than 30 TeV and a peak (initial) luminosity of  $10^{34} \text{ cm}^{-2} \text{ sec}^{-1}$ . The tunnel was to be scoped, however, to support a future upgrade to a center-of-mass energy greater than 150 TeV with a peak luminosity of  $2 \times 10^{34} \text{ cm}^{-2} \text{ sec}^{-1}$  using high field ( $\sim 10$  Tesla) superconducting magnet technology. In a collaboration with Brookhaven National Laboratory and Lawrence Berkeley National Laboratory, a report of the Design Study was produced by Fermilab in June 2001.[1] The Design Study focused on a Stage 1, 20x20 TeV collider using a 2-in-1 transmission line magnet and leads to a Stage 2, 87.5 x 87.5 TeV collider using 10 Tesla  $\text{Nb}_3\text{Sn}$  magnet technology.

The article that follows contains excerpts from the design study work that discuss accelerator physics designs and computational results from the Study. The author is indebted to the other members of the Design Study who contributed to this work, in particular to Steve Peggs. A complete list of contributors can be found in [1] and [2].

## 1 TWO COLLIDERS IN ONE TUNNEL

For the design study it has been envisioned that the Low Field (LF) ring will be comprised of long, combined function magnets -- the bending of the central trajectory and the focusing of the particle beam will be performed using gradient magnets with central field strength on the order of 2 T. The High Field (HF) ring will use separated function magnets -- dipole magnets for bending the central trajectory and quadrupole magnets for focusing. Since the LF and HF designs have different focusing characteristics, the dispersion suppressors must also be designed simultaneously to ensure that the LF and HF orbits line up appropriately when entering the long straight sections for the Interaction Regions and Utility Regions.

The size of the arcs is determined primarily by the low magnetic field of the first stage collider, while the lengths of the major straight sections are determined by the high magnetic rigidity of the beam in the second stage collider. The interaction regions must be made long enough to accommodate trajectory and optics manipulations of high energy proton beams using reasonable guesses for sizes of future high energy, high luminosity detectors. The utility

straight section regions must be made long enough to provide space for extracting a very high energy proton beam toward a beam dump and for beam scraping and beam instrumentation at high energy. All of these functions will be required for the LF collider as well, of course, but the technologies used for injection, extraction, acceleration, and so forth will be similar for the two rings. Thus, the requirements of the HF design will set the scale for the straight sections.

As indicated in Figure 1.1 each collider is made up of two major arcs that connect two clusters of straight sections. At the outset, only one cluster region -- located at or near the Fermilab site -- will be equipped with full interaction region and utility region optics. The opposite cluster will have the same straight section lengths, but optically will consist of simpler, FODO-type modules where applicable, with the exception of a special straight section designs to accommodate beam scraping and future beam transfers between the LF and HF accelerators.

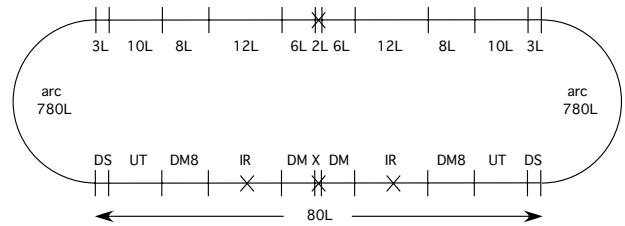


**Figure 1.1: Schematic layout of collider modules. The figure is not to scale, emphasizing the straight section functions.**

Dispersion suppressor modules are adopted following the SSC design, which was also later used in the Fermilab Main Injector. A cell phase advance of 90 degrees has been chosen for which a dispersion suppressor can be made using two special cells, each  $3/4$  the length of a standard cell and each containing  $2/3$  the bending of a standard cell. These modules reduce the periodic arc dispersion function to zero at the output of two such cells. The short bending regions between Interaction Regions and Utility Regions will be composed of back-to-back dispersion suppressor modules. Any additional bending required in these regions is generated by inserting standard half-cells between the DS modules.

Table 1.1 lists the fundamental parameters of the footprint. In the transition from Stage 1 to Stage 2 operation, the experiments will remain centered on the same interaction points. At the same time it is envisaged

that they will be upgraded to take up more space along the beam line, increasing the distance from the IP to the first magnet,  $L^*$ , from 20 to 30 m. It is therefore necessary to allow for a bypass to keep the low field ring beams well clear of the experiments. This must be done without changing the total low field ring circumference.

One advantage of modular construction is that low and high field lattices are guaranteed to have almost identical footprints, and therefore to fit in the same tunnel, so long as corresponding low and high field modules are placed on top of each other. The maximum deviation is only a few millimeters, easily allowing one ring to be placed on top of the other at a tunnel.

**Table 1.1: Fundamental lattice parameters common to both low and high field rings.**

Circumference, $C$	233.037	km
Average arc radius, $R$	35.0	km
Number of interaction points	2	
Half cell length, $L_{hc}$	135.486	m
Half cell bend angle, $\theta_{hc}$	3.875	mrad
Half cell count	1720	
Half cell harmonic, $n_\lambda$	24	
Bunch spacing (53.1 MHz), $S_B$	5.645	m
Time between bunches	18.8	ns
Number of buckets	41280	
Number of bunches, $M$	37152	
Phase advance per cell	90.0	deg
Revolution frequency	1.286	kHz
Revolution period, $T$	0.778	ms
Harmonic number, $h$	371520	
RF frequency ( $9 \times 53.1$ )	478.0	MHz

## 2 STAGE 1 – THE LOW FIELD RING

The first stage low-field collider will have a top energy of 20 TeV and peak (initial) luminosity of  $10^{34} \text{ cm}^{-2}\text{sec}^{-1}$ . The collider will use the Tevatron as its injector operating at a transfer energy of 900 GeV. For this study a transverse emittance of  $1.5 \pi \text{ mm-mrad}$  (rms, normalized) is used, which is typical for the Fermilab Booster, though about half the value at the Tevatron under recent normal operations. It is anticipated that with further Run II experience, the efficiency of emittance preservation will increase. Using the present acceleration systems of the Tevatron injector chain, the collider has a bunch spacing of 5.645 m (53.1 MHz), which sets the number of available RF buckets. With a 90% filling fraction to allow for gaps in the beam for various kicker rise times, the number of protons per bunch required in the Stage 1 collider is approximately  $2.6 \times 10^{10}$ , similar to Tevatron bunch intensities during previous Fixed Target operations. Using an interaction region design with a  $\beta^* = 0.3 \text{ m}$ , we arrive at the desired initial luminosity. Table 2.1 lists the general parameters of the Stage 1 collider.

**Table 2.1: Nominal store parameters for the low field collider.**

Storage energy	20	TeV
Peak luminosity	$10^{34}$	$\text{cm}^{-2}\text{sec}^{-1}$
Packing fraction	89	%
Injection energy	0.9	TeV
Transverse normalized emittance, rms (H&V, inject)	$1.5 \pi$	$\mu\text{m}$
Initial bunch intensity	$2.6 \times 10^{10}$	
Average beam current	195	mA
Stored energy per beam at collision	3.0	GJ
Bend field at storage	2.0	T
Bend magnet gradient	9.0	T/m
Phase advance per cell	90.0	deg
Max RMS arc beam size (inject)	1.2	mm
Bunch spacing (53.1 MHz)	5.645	m
Time between bunches	18.8	nsec
Bunch length	30	mm
Longitudinal emittance, rms (inject)	0.4	eV-s
RF voltage at storage	50	MV
Fill time	60	min
Acceleration time	1000	sec
Beam size (rms) at IP (storage)	4.6	$\mu\text{m}$
Total crossing angle ( $10\sigma$ separation in drift space)	153	$\mu\text{rad}$
Distance from IP to first magnet	21	m
$\beta^*$ at IP (H & V)	0.3	m
Maximum interactions per crossing	20	
Debris power at IP (each direction)	3	kW
SYNCHROTRON RADIATION AT STORE		
Energy loss per turn per particle	38	keV
Radiation damping time, $\tau_0$ ( <i>anti-damping in H plane</i> )	100	hr

Typical store parameter evolution is depicted in Figure 2.1. The figure shows the proton bunch intensity and luminosity decreasing due to collisions. The vertical emittance also decreases slightly due to synchrotron radiation damping which occurs with a damping time of about 100 hr. Due to the use of gradient magnets in the Stage 1 collider the horizontal emittance actually will be *anti-damped*, and will increase at approximately the same rate. This should not be a problem since store times will be much less than 100 hours.



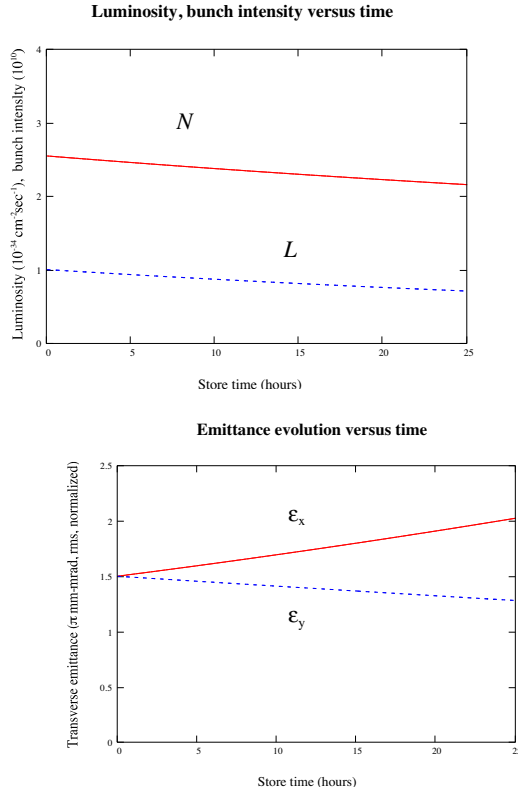


**Figure 2.1: Evolution of collider parameters during a typical store.**

### Interaction Regions

The final foci in the IR's are anti-symmetric triplets, formed from single-bore, 300 T/m magnets. Four additional quadrupole circuits, comprising double-bore, 70 T/m magnets, are also used in optical matching. With a total of 6 independently-tunable quadrupole circuits available it is possible to match the four  $\beta$ 's and  $\alpha$ 's from the IP to regular FODO cells, and hold the phase advance  $\Delta\mu$  constant across the IR through the squeeze from  $\beta^* = 6.00 \text{ m} \rightarrow 0.30 \text{ m}$ . Fixing  $\Delta\mu$  eliminates the necessity of a special phase trombone to maintain the nominal operating point. Figure 2.2 shows the lattice functions through the IR during collisions.

The circulating beams are separated horizontally by 15 cm throughout the arcs and 70 T/m straight-section quads. Four dipoles, 13.6 m each at 1.97 T, situated between the Q3 and Q4 quadrupoles bring the beams together at the entrance to the triplet for collisions at the IP. Dipoles downstream of the IP separate the beams again and channel them back into the inner and outer rings. A half-crossing angle of  $77 \mu\text{r}$  at the IP gives  $10\sigma$  separation between the beams at the first parasitic crossing.

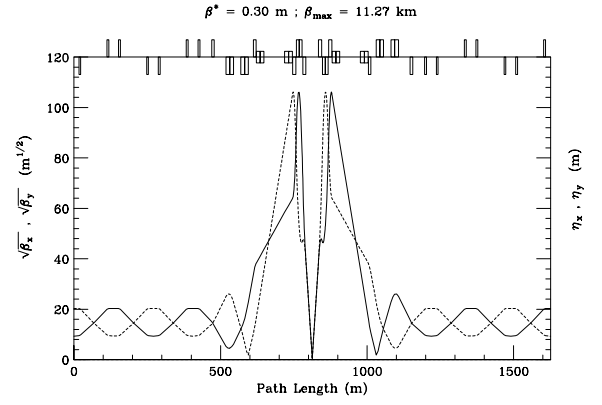


**Figure 2.2: IR lattice functions in the collision configuration.**

## 3 STAGE 2 – THE HIGH FIELD RING

The High Field VLHC ring will be the first cryogenic collider to operate in the synchrotron radiation dominated regime, in which the radiation damping time is shorter than the storage time. In this regime there are practical and economic limits to the cryogenic system that can be installed. There is a maximum value  $P_{cryo}$  for the synchrotron radiation, which can be absorbed in each ring. It is necessary to adjust the beam parameters to stay within the installed power limit, resulting in an average luminosity that depends on the beam energy  $E$  according to a “maximum power law,”

$$L_{ave} < \frac{P_{cryo}}{E} \left( \frac{1}{N_{IP} \sigma_{tot}} \right) \left( \frac{T_0}{T_{store}} \right) \quad \text{Eq. 3.15}$$

Although there is a clear advantage in reducing the storage time,  $T_{store}$  must remain significantly larger than the damping time  $T_0$  in order to take advantage of radiatively damped beam sizes. Other factors (such as the refill time) will also play a role in determining the optimum value of  $T_{store}$ , but it is safe to estimate that

$$\frac{T_0}{T_{store}} \approx 0.2 \quad \text{Eq. 3.1}$$

Except for some uncertainty in this factor, the maximum power law clearly states that the installed capacity to absorb synchrotron radiation at cryogenic temperatures directly limits the attainable product of average luminosity and energy.

Similarly, if the beam stored energy per ring  $U = NME$  must be kept below a maximum value -- for example if the beam dump has a limited capacity -- then

$$L_{ave} < \frac{U_{max}}{E} \left( \frac{1}{N_{IP} \sigma_{tot}} \right) \left( \frac{1}{T_{store}} \right) \quad \text{Eq. 3.2}$$

Insofar as the stored energy is a practical limit to high field performance -- to the product  $L_{ave}E$  -- then there is pressure to reduce  $T_{store}$ , and hence to increase the dipole field, to reduce the circumference, and to reduce the refill time.

## Operational Performance

For the Design Study, the most straightforward approach is to use as a baseline standard triplet optics and round beams, as in previous hadron colliders. It should be noted, however, that the High Field ring will be the first hadron collider with the potential to take advantage of naturally flat beams. While still under discussion, flat beams are sufficiently new and interesting for hadron colliders that most of the Stage 2 Design Study effort was devoted to analyzing this case up to now. The parameters described below have assumed that the beam emittances evolve into an asymmetric state characterized by  $\kappa = \epsilon_y/\epsilon_x$ . The high field ring should be able to achieve  $\kappa \ll 0.1$  during a store, consistent with conventional electron storage rings.

**Table 3.1: Nominal parameters for stores in the high field ring, using flat beams and doublet IR optics.**

Storage energy, $E$	87.5	TeV
Peak luminosity, $L_{max}$	$2 \times 10^{34}$	$\text{cm}^{-2}\text{sec}^{-1}$
Collision debris power, per IP	73	kW
Dipole field at storage	9.765	T
Distance from IP to first magnet	30	M
Injection energy	10	TeV
Fill time	30	sec
Acceleration time	2000	sec
Synchrotron radiation damping time, $T_0$	2.48	hours
Energy loss per turn, $U_0$	15.3	MeV
Natural transverse emittance (H)	0.0397	$\mu\text{m}$
Natural RMS momentum width	5.5	$10^{-6}$
Collision beta horz, $\beta_x^*$	3.7	m
Collision beta vert, $\beta_y^*$	0.37	m
Equilibrium emittance ratio, $\kappa$	0.1	
Initial bunch intensity, $N$	7.5	$10^9$
Beam current	57.4	mA
Synch. rad. power, per beam, $P$	.88	MW
Dipole linear heat load	4.7	W/m
Stored energy, per beam, $U$	3.9	GJ

The instantaneous luminosity is

$$L = \frac{M}{4\pi T} \frac{N^2 \gamma}{\sqrt{\epsilon_x \epsilon_y \beta_x^* \beta_y^*}} \quad \text{Eq. 3.3}$$

where  $T$  is the revolution period. The total number of protons in the ring,  $MN$ , is approximately set by the need to provide enough for “luminosity burn-off.” Since the number of bunches  $M$  is fixed, the need for a given peak luminosity then sets the single bunch population  $N$ . Nominal values for these and other parameters, including a conservative value of  $\kappa = 0.1$ , are given in Table 3.1.

It is the head on beam-beam interaction that sets the minimum horizontal emittance, whether the beams are flat or round. Figure 3.1 shows the horizontal and vertical emittances decreasing to plateau values of  $\epsilon_x$  and  $\epsilon_y$  that are consistent with the beam-beam limit, and which are maintained by transverse beam heating. Figure 3.2 shows the corresponding evolution of instantaneous luminosity, and its average, during the store.

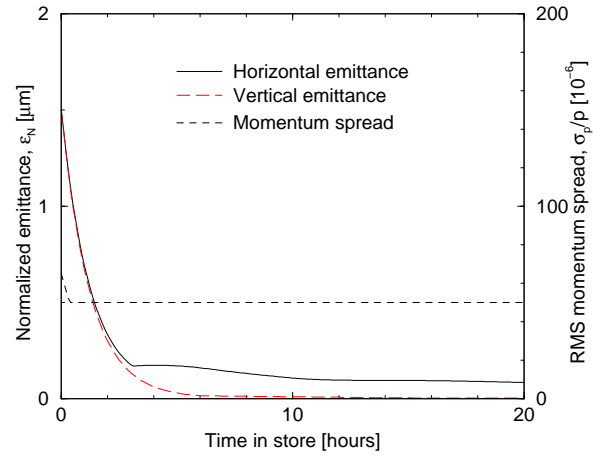


**Figure 3.1: Evolution of the transverse emittances and the rms momentum spread during a store.**

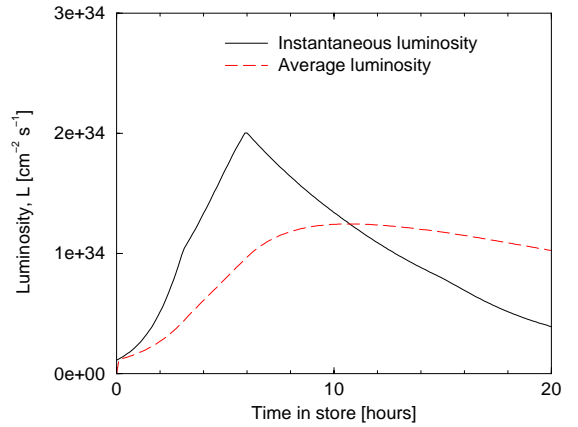


**Figure 3.2: Evolution of the instantaneous and average luminosities, during a store.**

## The Head-on Beam-beam Interaction

The horizontal and vertical tune shift parameters for bi-Gaussian round beams ( $\beta_x^* = \beta_y^*$ ,  $\varepsilon_x = \varepsilon_y$ ) are

$$\xi_x = \xi_y = \frac{r}{4\pi} \frac{N}{\varepsilon_x} \quad \text{Eq. 3.4}$$

By comparison, if the beams are very flat,  $\kappa \ll 1$ , then

$$\xi_x = \xi_y = \frac{r}{2\pi} \frac{N}{\varepsilon_x} \quad \text{Eq. 3.5}$$

In this last expression, the horizontal and vertical beam-beam parameters are made equal for the flat beam case by asserting that the  $\beta^*$  ratio is also  $\kappa$ :

$$\kappa = \frac{\varepsilon_y}{\varepsilon_x} = \frac{\beta_y^*}{\beta_x^*} = \frac{\sigma_y^*}{\sigma_x^*} \quad \text{Eq. 3.6}$$

Equations 3.4 and 3.5 show that, whether the beam is round or flat, the beam-beam parameter depends only on the horizontal emittance  $\varepsilon_x$ . Since the collision beta functions  $\beta_x$  and  $\beta_y$  do not influence the beam-beam parameters, they are adjusted (with a fixed ratio  $\kappa$ , and for given values of  $M$ ,  $N$ , and  $\varepsilon_x$ ) in order to achieve the required peak luminosity.

The beam-beam limit is expected to be approximately the same for round or flat beams, given by

$$\xi \leq 0.008.$$

This value is justified by practical experience at the SPS and at the Tevatron. The SPS operated at  $\xi \approx 0.004$  (or slightly higher) with 6 collisions per turn. More recently, in Run Ib the Tevatron operated with  $\xi \approx 0.0075$  with only 2 head on collisions per turn (as in the VLHC). Simulations predict that radiation damping might give the high field ring a slight additional advantage, which is by no means as strong as that commonly observed in electron storage rings. The numerical value of 0.008 is illustrated in Figure 3.3, which displays empirical data compiled by Keil and Talman for electron storage rings [3]. The “damping decrement” for the high field VLHC -- the fraction of a damping period per head on collision -- is approximately  $10^{-7}$ .

Then, re-writing Eqn. 3.3 as

$$L = \frac{M}{4\pi T} \frac{N^2 \gamma}{\kappa \varepsilon_x \beta_x^*} \quad \text{Eq. 3.7}$$

it is explicitly clear that with flat beams the value of  $\beta_x^*$  can be increased by a factor of about  $1/\kappa$ , significantly simplifying the optics. Equation 3.6 then shows that the value of  $\beta_y^*$  is about the same for flat or round beams.

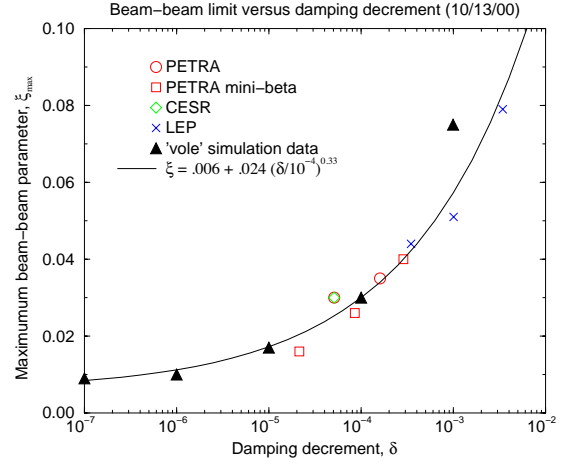


**Figure 3.3: Maximum beam-beam parameter vs. damping decrement.**

## Crossing Angles and Parasitic Beam-beam Collisions

The horizontal and vertical tune shifts due to a single parasitic collision are

$$\Delta q_{x,y} \approx \pm \frac{rN}{2\pi\gamma} \frac{\beta_{x,y}}{\Delta^2} \quad \text{Eq. 3.8}$$

where the approximation is valid if the full beam separation  $\Delta$  is much greater than both horizontal and vertical beam sizes, so that the beam acts like a moving line charge.

If the beams are thoroughly separated (into separate beam pipes, or with very large separations) at a distance  $L_{sep}$  from the IP, then there are  $4L_{sep}/S_B$  parasitic collisions around each IP, where  $S_B$  is the longitudinal bunch separation. The total tune shifts from all parasitic collisions with crossing angle  $\alpha$  in one interaction region are

$$\Delta Q_{x,y} \approx \pm \frac{rN}{2\pi\gamma} \frac{4}{S_B} \frac{L_{sep}}{\beta_{x,y}^* \alpha^2} \quad \text{Eq. 3.9}$$

where the approximation is most valid if the beams are fully separated before the first IR quadrupole.

Again, assuming one exercises the flat beam option, the horizontal beta function at each collision is much less than the vertical

$$\frac{\beta_x}{\beta_y} \approx \frac{\beta_y^*}{\beta_x^*} = \kappa \quad \text{Eq. 3.10}$$

so that, taking Eqns 3.9 and 3.10 together gives

$$\Delta Q_x \approx -\kappa \Delta Q_y \quad \text{Eq. 3.11}$$

The horizontal tune shift is greatly suppressed with flat beams, to be much smaller than it is with round beams -- if the values of  $L_{sep}$  and  $\alpha$  compare favorably between the two cases.

### Advantages and Disadvantages of Flat Beams

All electron colliders, whether circular or straight, take advantage of flat beams and use doublet optics. However, it has never before been possible to use flat beams in a hadron collider. Flat beams have the advantages and disadvantages discussed below, which continue to be investigated.

Flat beams require the first quadrupole on both sides of the IP to be vertically focusing to both counter-rotating beams (whether the crossing angle is vertical or horizontal). Thus, the optics must be symmetric across the IP, and the first quadrupole must be a 2-in-1 magnet. As seen in the next Section, both optical solutions have been developed.

Table 3.2 compares the performance of flat and round beam in the high field ring. In both cases the beam-beam limit of  $\xi = 0.008$  is reached 5 or 6 hours into the store, when the luminosity is at its peak. The horizontal and vertical emittances values recorded in Table 3.2 are those that are initially maintained (preventing further emittance shrinkage) when the horizontal and vertical beam-beam parameters first saturate. The same peak luminosity is achieved in both flat and round beam cases by adjusting the horizontal and vertical  $\beta^*$  values.

**Table 3.2: Flat and round beam performance parameters after about 6 hours into the store, just after peak luminosity, when both horizontal and vertical beam-beam parameters are saturated.**

	FLAT	ROUND
Flatness parameter	0.1	1
Beam-beam parameter	0.008	0.008
$\xi_x = \xi_y$		
Peak luminosity ( $10^{34} \text{ cm}^{-2} \text{ sec}^{-1}$ )	2.0	2.0
Initial protons/bunch ( $10^9$ )	7.5	7.5
Collision beta horz $\beta$ (m)	3.7	0.71
Collision beta vert $\beta$ (m)	0.37	0.71
Max beta horz $\beta$ (km)	7.84	14.58
Max beta vert $\beta$ (km)	10.75	14.58
Horizontal emittance ( $\mu\text{m}$ )	0.161	0.082
Vertical emittance ( $\mu\text{m}$ )	0.016	0.082
Collision beam size horz	2.53	0.79
$\sigma_x^*$ ( $\mu\text{m}$ )		
Collision beam size vert	0.25	0.79
$\sigma_y^*$ ( $\mu\text{m}$ )		
Max beam size horz $\sigma_{x-max}^*$	116	113
( $\mu\text{m}$ )		
Max beam size vert $\sigma_{y-max}^*$	43	113
( $\mu\text{m}$ )		
Total crossing angle ( $\mu\text{rad}$ )	10.0	10.0
Separation distance (m)	30	120
Long range collisions per	20	84
IR		
Long range tune shift (H)	0.0008	0.0166
Long range tune shift (V)	0.0081	0.0166

The value of the total crossing angle  $\alpha$  is set to be identical with flat or round beams -- and is independent of the plane of the crossing angle. The major advantages and disadvantages of flat beams are outlined in the list below:

### Flat Beam Advantages

Order of magnitude increase of  $\beta_x^*$ , and subsequent reduction of horizontal  $\beta_{max}$  in the doublet quadrupoles. While early separation pushes the first quadrupole further from the IP, the values of  $\beta_{max}$ , both horizontal and vertical, are still reduced, as indicated in Table 3.2.

There are far fewer parasitic collisions per interaction region with flat beams than with round beams, greatly reducing the long-range (especially horizontal) tune shift.

### Flat Beam Disadvantages

The design of the first quadrupole and splitting dipole are difficult. A 2-in-1 quadrupole with relatively close separation will not have as good field quality a single bore element. But, with lower  $\beta_{max}$  in the doublet design, the tolerable field errors are likely to be larger.

Neutral particles generated at the IP will aim head-on for the conductor located at the center of the first 2-in-1 quadrupole.

Lack of energy flexibility may be a disadvantage to flat beams. At lower energies, damping times are longer and thus flat beams are no longer viable. (However, a lattice has been demonstrated in which 4 IR quadrupoles can act as a doublet or as a triplet [4].)

An operational disadvantage is the need for careful tuning to keep the vertical emittance small. Electron rings, however, routinely achieve beam flatness in the range  $0.001 < \kappa < 0.01$  by controlling dispersion and global betatron coupling. Flatness values of  $\kappa \approx 0.01$  should be achievable.

A round beam solution for the VLHC is in hand, including IR magnet designs and optical layouts. Because of the difficult design of a 2-in-1 quadrupole magnet for the doublet optics, the flat beam scenario is at this time a promising upgrade path. The flat beam case with its possible advantages merits further work and discussion and will continue to be studied over the upcoming months.

### Triplet IR Optics Approach

Using interaction region optics standard in modern hardron colliders, collisions are created using anti-symmetric triplets for the final focusing. The "round beam" model discussed here is qualitatively similar to the low-field IR design. The triplet quadrupoles are 400 T/m single-bore magnets. Four additional circuits, comprising double-bore 400 T/m magnets are also used for optical

matching. With a total of 6 independently-tunable quadrupole circuits available it is possible to match the four  $\beta$ 's and  $\alpha$ 's from the IP into the regular FODO cells, plus hold the phase advance  $\Delta\mu$  constant across the IR through the squeeze from  $\beta^* = 12.0 \rightarrow 0.50$  m. Fixing  $\Delta\mu$  eliminates the need for a special phase trombone somewhere in the ring to maintain the nominal operating point. Figure 3.4 shows the lattice functions through the insertion region at collision.

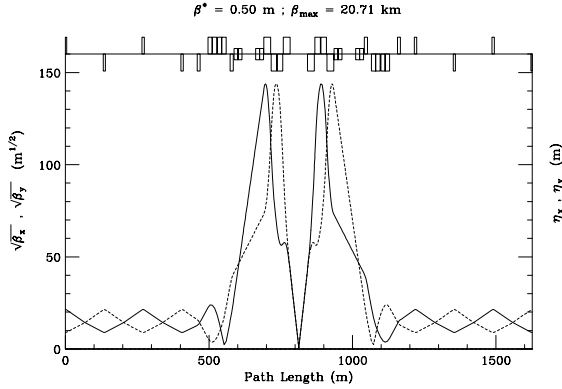


**Figure 3.4: Lattice functions near the IP in collision optics, using triplet focusing.**

The circulating beams are separated vertically everywhere in the ring, except in the triplet quadrupoles. Four 10 T dipoles between the Q3 and Q4 quadrupoles bring the beams together at the entrance to the triplet for collisions at the IP. Dipoles downstream of the IP separate the beams again vertically and channel them back into the upper and lower rings. A half-crossing angle of  $28.8 \mu\text{r}$  gives  $10\sigma$  separation between the beams at the first parasitic crossing 2.823 m downstream of the IP ( $\epsilon_N = 1.5 \pi \mu\text{m}$  at 87.5 TeV/c).

### Doublet IR Optics Approach

Doublet optics are more naturally suited to the flat beams of the high-field ring. The IR gives 30 m free space from the interaction point to the first magnetic element. For the doublet optics, the first magnet encountered is a high field small bore magnet of 16 T field. This can handle the beams until they total separation becomes 8 mm. Then the beams enter a lower field, 12 T, magnet with a larger bore. These beam separation dipoles bend the beam vertically. This crossing region requires that the beam separation at the first quadrupole be 30 mm. With these dimensions the first quadrupole is limited to 400 T/m gradient. As the beams separate, a higher quadrupole field can be attained with a limit of 600 T/m.

With this design of the crossing region, two interaction regions can fit in the on-site cluster region. The  $\beta^*$  can be varied from 0.37 m to 7.12 m (vertically,  $\beta^*$  horizontally is 10 times larger). The maximum beta is 10.6 km with the

collision optics and only about 760 m at injection. Figure 3.5 shows the collision optics of the interaction region.

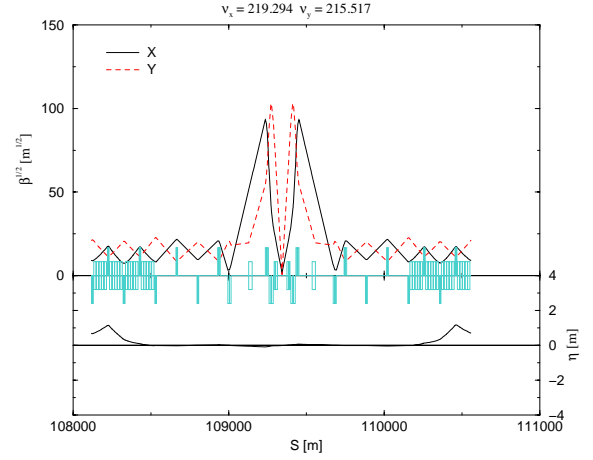


**Figure 3.5: Lattice functions near the IP in collision optics, using doublet focusing.**

## REFERENCES

- [1] G. Ambrosio, et al., "Design Study for a Staged Very Large Hadron Collider," Fermilab Report TM-2149 (2001).
- [2] M. Blaskiewicz, et al., "VLHC Accelerator Physics," Fermilab Report TM-2158 (2001).
- [3] E. Keil, R. Talman, *Scaling of Luminosity Data Between  $e^+e^-$  Storage Rings*, Particle Accelerators Vol. 14 pp. 109-118, 1983.
- [4] S. Peggs, M. Harrison, F. Pilat, M. Syphers, *Flat beams in a 50 TeV hadron collider*, Vancouver PAC 97, 1997.

# Summary of the Session on Weak-Strong Phenomena

J.P. Koutchouk, CERN, Geneva, Switzerland

## Abstract

This session took place June 26th in the afternoon, with the participation of (by memory) Y. Alexahin, M. Boscolo, A. Burov, J.P. Koutchouk, F. Schmidt, Y. Shatunov, V. Shiltsev, M. Syphers, T. Sen, M. Xiao, F. Zimmermann. The charge to this session as foreseen by the organizers was

- to review the present understanding of the weak-strong phenomena in general
- and more specifically the performance limitations of the Run II of the Tevatron,
- review, propose and prioritize experiments crucial to Run II, LHC, CESR and VLHC.

## 1 INTRODUCTION

This summary is organized as follows:

- The talks given in the session are briefly summarized together with the discussions which arose,
- An attempt is made at comparing the evolution of the understanding and of the outstanding questions over the last few beam-beam workshops,
- A list of proposed actions is submitted.

## 2 SUMMARY OF THE TALKS AND DISCUSSIONS

### 2.1 VLHC Proposal, by M. Syphers/FNAL

This proposal is now an official Fermilab document Fermilab TM2149, June 4th 2001 and can be consulted on the Web. The main feature of this proposal is a big tunnel to house initially a 40 TeV machine and later a 200 TeV machine. Two experimental points are foreseen. A selection of parameters relevant to the beam-beam effect is given in Table 1. The beam aspect ratio at the IP's (round or flat) is

Energy	TeV	40	200
Luminosity		$10^{34}$	$2 \cdot 10^{34}$
$\beta^*$	m	.3	.71
$\sigma_s$	m	.03	.08
$\xi/\text{IP}$		$\approx .003$	.008
# LR interactions	comparable to Run II and LHC		
LR separation	$\sigma$	10	
Rad damping	hour	many	1

Table 1: A selection of VLHC Parameters

not yet decided. As commented by the author, the parameters of the beam-beam interactions in the VLHC proposal are comparable to those of Run II and LHC and actually less demanding.

The recent findings on Run II and LHC show however that a long-range beam-beam separation of  $10 \sigma$  is insufficient. This machines will have to leave with this limitation. It is recommended to increase this separation in a new design. The target value is presently not clear, perhaps as large as  $15 \sigma$ .

### 2.2 Tracking for LHC, by F. Schmidt/CERN

The issues in tracking with the beam-beam effect is an accurate model of the physical phenomena and tracking over long times. For LHC, the tracking is carried out in 6D except for the b-b lens which is 4D. The tracking time has been increased from  $10^5$  to  $10^6$  turns (89 s in accelerator time). The average beam separation at the LR interaction points is  $14 \sigma$  at injection and  $9.5 \sigma$  in collision. The main results are summarized in table 2. The conclusions that can

	Injection	Collision
no beam-beam	$\geq 12$	$\geq 12$
with beam-beam, $10^5$ turns	$\geq 9$	$\geq 6$
with beam-beam, $10^6$ turns	$\geq 7$	$\geq 5$
onset of chaos	7	4.5

Table 2: Dynamic aperture in LHC in  $\sigma$

be drawn from this study are:

- As already observed in former studies, the long range beam-beam effect is indeed the limiting phenomenon. It is significantly stronger than the machine non-linearities.
- The few places where the beam separation is only  $7 \sigma$  in collision do play a significant role.
- The phenomenology resembles that of a tune modulation. Particles may be lost after  $10^5$  turns, i.e. on a long time scale. What happens after  $10^6$  turns?
- With the nominal machine parameters, the LHC dynamic aperture in presence of the beam-beam interaction might be too small.
- The tune spread at  $12 \sigma$  at injection due to the LR interactions is only 0.001. It is clearly uncorrelated with the dynamic aperture. The onset of chaos, though not always easy to identify, seems well correlated.

### 2.3 Tracking for Run IIa, by M. Xiao/FNAL

In Run IIa, the numbers of bunches is significantly increased to increase the luminosity while reducing the number of events per collision. Each beam is made of 3 trains of 12 bunches, i.e. 36 bunches instead of 6 in Run I. The tracking scenario includes two head-on collision and 70 long-range interactions. The beam separation is  $10\sigma$  except at 4 places where it is only  $6\sigma$ .

After discussion it appears that the tracking is 4D only. This is OK for the footprints. For the dynamic aperture however, without the synchrotron modulation, its results should be interpreted as optimistic. Yet, the tracking results show a drastic effect of the long-range interactions:

- The footprint of the PACMAN bunches is shifted by 0.01.
- The LR interactions increase the footprint by 60% (comparable to LHC).
- The dynamic aperture decreases from 12 to  $6\sigma$  at  $10^6$  turns (again comparable to LHC).
- A tune diffusion is noticeable for amplitude from 2 *sigma* onwards.

A crossing angle (4D, with beam slicing) improves the dynamic aperture by 1 to  $2\sigma$ , with some reduction of the luminosity.

Altogether, although the physics is not exactly the same (the long-range interactions are spread in betatron phase all around the Tevatron), the LHC and Run IIa tracking results show significant similarities. In both cases, the beam separation of  $10\sigma$  appears too small. The footprint criterion which revealed to be the significant non-linear parameter for the head-on collisions does not hold in presence of long-range interactions. The 4D on-momentum tracking does not incorporate dispersion-related phenomena analysed in the next talk.

### 2.4 Synchro-betatron Coupling, by Y. Alexahin/FNAL

This study is analytic and the quantitative results based on perturbation theory. Three families of phenomena are studied:

- The beam-beam *chromaticity*: due to the non-vanishing dispersion at the long-range interaction points, the chromaticity is perturbed by the residual sextupolar field of the exciting beam. The chromaticity spread induced by the PACMAN effect is as large as 14 units. This seems to be probably just acceptable at the Tevatron.
- Odd-order resonances close to the nominal working point are excited. calculations show that the 5th order family together with its synchrotron satellites overlap, creating the condition of a diffusion of the particles in the core of the beam.

- The finite bunch length causes synchrotron satellites of even order resonances (12th order) to be broadened. The resonance lines remain separated with the Cu RF system. The stronger Sc RF system causes the high Qs resonances to overlap.

Yuri advocates to change the nominal working point to .685/.675 to minimize the excitation of the 5th order resonances. The other effects seem rather drastic and likely to limit the performance in Run II. Experimental data will be very useful.

### 2.5 Beam Rounder, by A. Burov/FNAL

This theoretical study provides a convenient formalism using circular modes to describe the beam motion. It can be used to express and enforce the conservation of the angular momentum. In this way, round beams may be provided at an interaction point from any emittance ratio. With this new invariant, the motion is essentially 2D where the diffusion in amplitude is minimized.

To support this approach, Y. Shatunov/Novosibirsk showed tracking results for the future VEPP 2000 in the case of beams rounded by betatron coupling. The blow-up of the core occurs at a significantly larger beam-beam parameter.

## 3 EVOLUTION OF THE UNDERSTANDING

### 3.1 Issues in Novosibirsk/1989

At this time, only the head-on beam-beam effect was an issue.

- Is  $\xi = 0.02$  possible in only one IP?: Not an issue anymore. The ultimate limit seems on the side of the coherent effects (see J. Shi in the Session on coherent effects).
- The diffusion in the tails need to be studied and measured: still true.
- The correction of the leading beam-beam effect (detuning) by octupoles should be studied. S. Temnykh/CESR mentions that this was done with some success in electron machines. For protons, the new ideas of an electron lens or a wire compensator are clearly superior.

### 3.2 Issues in Montreux/1995

- Matching the beam sizes is more important than a residual beam separation: this statement (from experience) seems not consistent with observations reported in Geneva/1999. Clear experimental evidences of the consequence of a residual separation are needed (PACMAN bunches).
- Strong diffusion observed in HERA for amplitudes above  $2\sigma$ : That was not beam-beam.



- Long-range at LHC: the SPS footprint criterion was consistent with a beam separation by only  $1\sigma$ .

### 3.3 *Issues in Geneva/1999*

- The LR interactions are identified to be the major performance limit.
- Standardization of the simulation code: It is noted that it is impossible to compare tracking results with many codes and as many input conventions. It is still the case with no prospect in this direction.

### 3.4 *Issues for this Workshop*

It is quite clear that the hadron colliders entered the long-range interaction era which appears much more significant than anticipated.

In electron machines, the main issue is the trade-off between flat and round beams.

## 4 PROPOSED ACTIONS

We propose here a list of actions related to the main issues of this workshop.

- Footprint due to the long-range interactions: a simple start to compare calculations and measurements and gain confidence.
- Phenomenology associated to the long-range interactions: Gathering of data: (lifetime, background, diffusion) versus (LR separation, number of LR's, tunes)
- Pacman Effect: bunch-by-bunch measurements of orbits, tunes, coupling, chromaticity, luminosity: is the effect as expected? how to handle all these data? usefulness.
- measurement of synchro-betatron coupling versus Xing angle with and without LR's.

This series of experiments is particularly suitable to Run II.

- Effect of a residual separation at the IP: what is tolerable? This experiment could be carried out at RHIC.
- Compensation of the LR effect. The progress at Fermilab with the electron lens is significant and further experiments are of large interest for the community. The 'pulsed wire' method is under study at Cern. V. Shiltsev/FNAL proposes to test the idea (as much as possible) at the Tevatron. This is very much encouraged.
- Flat versus round beams (for electrons but as well hadrons): The studies on the Moebius machine are planned to be resumed. S. Temnykh challenges the community to help in finding a chromaticity correction scheme which works in this machine. When VEPP2000 will be ready, it will be an excellent place to study this issue.

- The report on the progress in understanding Daphne was very interesting and the community is looking forward to hear about the developments.

- Beam rounder: the concept is very interesting. Tracking and resonance calculations are necessary to evaluate the robustness of the scheme versus the imperfections which cannot be avoided in a real machine. These numerical studies are encouraged.

## 5 CONCLUSION

The beam-beam experiments are generally not very popular. They require long study sessions. Given the complexity of the problem, their conclusions may be ambiguous. Nevertheless, the performance of new colliders are limited by new issues (hadrons or electrons) with hardware consequences (Xing angle, Corrections schemes, focusing doublets versus triplets). It becomes therefore necessary to launch a significant experimental study programme to improve the understanding and exploit the new ideas which are emerging.

## 6 ACKNOWLEDGEMENTS

Thanks to the organisers and the participants for a very interesting session. This report is based on on-the-fly workshop notes. Please be indulgent in case of minor mistakes. Otherwise, let me know.

## **SECTION IV: Strong-strong phenomena**

# SELF-CONSISTENT ORBITS WITH BEAM-BEAM EFFECT IN THE LHC

H. Grote and W. Herr, CERN, Geneva, Switzerland

## Abstract

In part of the straight sections of the LHC the two beams share a common beam tube. Therefore the bunches cross each other not only at the interaction point, but as well at many places on either side, with a typical transverse separation of 10 times the transverse beam size. These "parasitic" encounters lead to orbit distortions and tune shifts, in addition to higher order effects. Since the string of bunches from the injection machine contains gaps, not all possible 3564 "buckets" around the machine are filled, but only about 3000. This in turn causes some bunches to not always encounter bunches in the opposite beam at one or several parasitic collision points (so-called "pacman" bunches), or even at the head-on interaction point ("super-pacman" bunches). With a special program self-consistent orbits in the LHC have been calculated for the first time with the full beam-beam collision scheme resulting from various injection scenarios [1]. The offsets at the interaction points, and the tune shifts are shown to be small enough to be easily controlled.

## 1 INTRODUCTION

In the LHC [2] the two opposite beams share a common beam tube for roughly 50 m on either side of the four interaction points. Since the bunch spacing is only 7.5 m, in order to avoid unwanted head-on collisions the beams cross with an angle. Even so, in addition to the one head-on encounter at each interaction point there remain 15 positions on either side of it where the closed orbits at nominal energy are only about  $10\sigma$  apart, and even less in the focusing quadrupoles at either side of each interaction point. Various effects (alignment errors, field errors, momentum errors, imperfect injection, beam-beam kicks) may lead to significant orbit distortions and further distance reduction. Because of "holes" in the filling scheme the situation differs from bunch to bunch. The principal effects on the bunches caused by the beam-beam encounters are tune shifts and orbit offsets at the interaction points. The former are potentially dangerous because they may shift the tune of a bunch onto a resonance which may lead to its loss; the latter reduce the luminosity, and the offset at the head-on collision creates an extra orbit kick that adds to the distortions already present. Further possible causes for worry are changes in the chromaticity, non-zero dispersion at the interaction point, odd order resonances, and possibly higher order effects. The aim of the current study was therefore to see whether acceptable closed orbits exist for all bunches in both beams, whether the coherent tune shifts remain small enough to be of no concern, and the other effects mentioned can be corrected if necessary. The study provides as well

input for the layout of the correction system in that it gives typical values for orbit errors caused by beam-beam effects.

The results are presented in graphical form because of the large number of bunches. The bucket number for ring-1 is constructed as follows: bucket number zero is at IP5, bucket number one to the left of it (seen from top), number two further to the left and so on backwards through IP4, IP3, IP2, IP1, IP8 etc. until to the right of IP5. The beam rotates clockwise. For ring-2 the numbering is done from IP5 to the right, the beam rotates anti-clockwise.

## 2 BUNCH FILLING SCHEME

$72 \times 1 \ 8 \times 0 \ 72 \times 1 \ 8 \times 0 \ 72 \times 1 \ 38 \times 0$   
 $72 \times 1 \ 8 \times 0 \ 72 \times 1 \ 8 \times 0 \ 72 \times 1 \ 38 \times 0$   
 $72 \times 1 \ 8 \times 0 \ 72 \times 1 \ 8 \times 0 \ 72 \times 1 \ 8 \times 0 \ 72 \times 1 \ 39 \times 0$   
 $72 \times 1 \ 8 \times 0 \ 72 \times 1 \ 8 \times 0 \ 72 \times 1 \ 38 \times 0$   
 $72 \times 1 \ 8 \times 0 \ 72 \times 1 \ 8 \times 0 \ 72 \times 1 \ 38 \times 0$   
 $72 \times 1 \ 8 \times 0 \ 72 \times 1 \ 8 \times 0 \ 72 \times 1 \ 8 \times 0 \ 72 \times 1 \ 39 \times 0$   
 $72 \times 1 \ 8 \times 0 \ 72 \times 1 \ 8 \times 0 \ 72 \times 1 \ 38 \times 0$   
 $72 \times 1 \ 8 \times 0 \ 72 \times 1 \ 8 \times 0 \ 72 \times 1 \ 38 \times 0$   
 $72 \times 1 \ 8 \times 0 \ 72 \times 1 \ 8 \times 0 \ 72 \times 1 \ 8 \times 0 \ 72 \times 1 \ 39 \times 0$   
 $72 \times 1 \ 8 \times 0 \ 72 \times 1 \ 8 \times 0 \ 72 \times 1 \ 38 \times 0$   
 $72 \times 1 \ 8 \times 0 \ 72 \times 1 \ 8 \times 0 \ 72 \times 1 \ 38 \times 0$   
 $72 \times 1 \ 8 \times 0 \ 72 \times 1 \ 8 \times 0 \ 72 \times 1 \ 119 \times 0$

Whatever the bunch filling scheme, as long as it is the same for both rings, and the injection is symmetric to IP1 and IP5, every bunch in ring-1 will collide with a bunch in ring-2 (and vice versa) at IP1 and IP5. For this to be true as well at IP2 and IP8, the following condition has to be fulfilled:

The distance from IP to IP is 891 half-buckets (bunches collide every half-bucket since both beams move) except for IP8 which is 888 from IP7 and 894 from IP1. The reason is the longitudinal displacement of IP8 with respect to the symmetry point. If the injection scheme repeats itself every 891 buckets, then at all IPs a bunch will always meet a bunch. Therefore super-pacman bunches are created at IP8 due to this displacement. The filling scheme shown here respects this symmetry almost fully, only at the end a batch of 72 bunches is missing to allow for the risetime of the beam dump kickers, creating super-pacman bunches at IP2 and IP8. In symbolic form it can be written as above (1 means bunch present, 0 absent).

## 3 ALGORITHM

The calculations are performed with two programs, MAD [3] and TRAIN, the latter being a heavily modified version

of the program TRAIN [4] developed for LEP. Both programs communicate via a database DOOM.

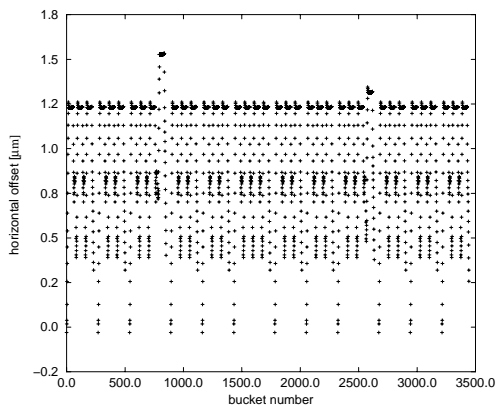


Figure 1: Horizontal offset at IP1 for all ring-1 bunches. The offset is caused exclusively by beam-beam interactions. The spread is about 1/10 of the beam size.

For the results presented here, a thin-lens model of the LHC version 6.0 was used, containing the latest separation and crossing schemes of version 6.1 [5], [6]. In the first step, the two LHC lattice and optics files are prepared for the TRAIN program: the lattice file for LHC ring-1 is read, the crossing and separation bumps are matched, tunes and chromaticities are adjusted, the places of head-on and parasitic encounters are marked, and the second order maps between all these beam-beam interaction points are lumped. This is justified since the optics under study contains only dipoles, quadrupoles, and sextupoles; field and alignment errors are not present. The Twiss parameters, element, lattice, force, and map tables are then stored in DOOM. The same procedure is followed using a matched thin-lens version for ring-2. At the end of this step, then, the database contains the necessary information for both rings to perform the self-consistent orbit finding.

This second step is performed by the program TRAIN. It first reads the description of the two rings from the database, and in particular the number and position of all beam-beam encounters. It then reads the injection schedule from an independent file and establishes the "encounter list" for all bunches in both beams. Next the program finds an initial closed orbit from the linear one-turn matrices with beam-beam encounters switched off. The program then iterates in a double loop over all bunches in both rings, with beam-beam encounters switched on. Where which bunch meets which bunch in the other ring is known from the bunch filling scheme. The inner loop is iterated with fixed distances between bunches at the beam-beam encounters, i.e. fixed beam-beam kicks. When it has converged to closed orbits for all ring-1 and ring-2 bunches, then the bunch positions at the beam-beam encounters are updated, and the outer loop is iterated until these positions do not change anymore. The bunch sizes are kept fixed as calcu-

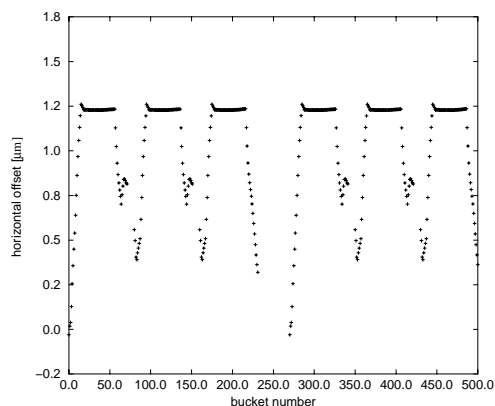


Figure 2: Detail of Figure 1. The 15 pacman bunches at either end of each bunch packet of 72 bunches can clearly be seen. The small irregularities are caused at IP2 and IP8.

lated from the undisturbed beta-functions, their change in size is negligible. Once all orbits (i.e. their six-dimensional initial coordinate vectors) are known, each bunch pair is tracked with the second order maps to get the tunes, chromaticity, and dispersion. The total CPU time for 2808 bunches in each beam is of the order of a few minutes on a fast workstation (e.g. Pentium III).

#### 4 COHERENT TUNES, CHROMATICITY, LUMINOSITY, AND DISPERSION

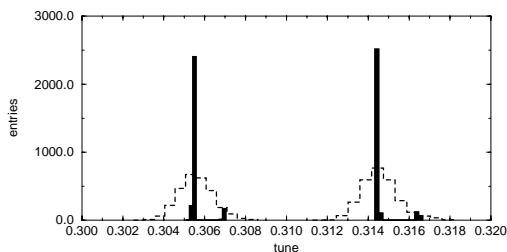


Figure 3: Solid: horizontal (left) and vertical tunes for all 2808 bunches in ring-1. The two offset bumps belong together. They represent the 186 super-pacman bunches occurring at IP8. Dashed: tune spread resulting from a Gaussian beam current distribution.

The coherent horizontal and vertical tunes for all bunches are shown in Figure 3. The offset batch stems from the super-pacman bunches at IP8; IP2 has practically no effect since there the beams are separated by about  $4\sigma$ . The offset of the normal bunches is as expected, i.e. roughly  $-3 \times 0.00342/2 = -0.0051$  (the undisturbed fractional tunes are 0.31 and 0.32, respectively). When the bunch currents in both rings have a Gaussian distribution rather than being equal as in the results presented up to now, this has very little effect on the orbit offsets, since they are

caused by over one hundred parasitic encounters and are thus averaged; however, there is a visible effect on the coherent tune shift which is caused by the head-on collisions only, of which there are up to three (the separation of  $4\sigma$  at IP2 makes this head-on collision insignificant for the tune shift). Figure 3 shows the coherent horizontal tune shift resulting from a Gaussian bunch current distribution with  $\sigma = 0.2 c_{nom}$  ( $c_{nom} = 0.189$  [mA] is the nominal bunch current). The spread doubles with respect to the case with fixed beam current, but is still within  $\pm 2 \times 10^{-3}$  which is not dramatic. Bunch current variations of this order can therefore be tolerated, provided there are no other effects not studied here that give reasons for concern.

The change in the dispersion is below 1 mm for all bunches. The luminosity resulting from the offset at the collision points lies between 0.98 and 1 without correction. When the average offset (see Figure 2) is corrected, the overall luminosity drops by less than 0.001.

The horizontal and vertical chromaticity without beam-beam effect were adjusted to 1.6 and 1.8, respectively. The chromaticities with beam-beam effect are given in Figure 4. This effect can be tolerated since the range of acceptable chromaticities is between one and two.

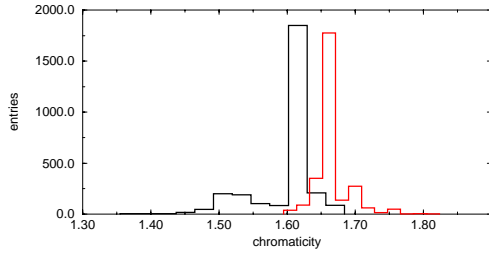


Figure 4: Horizontal (black) and vertical chromaticities for bunches in ring-1.

## 5 OTHER APPLICATIONS

The program TRAIN has some very important applications in the definition of LHC parameters. Various different filling schemes have been proposed, mainly to optimize the number of bunches and therefore the luminosity. However, possible implications of the filling scheme on the beam dynamics, in particular on the beam-beam induced orbits have been ignored or estimated on an averaged basis. This program now allows to test the different proposals and chose the most suitable one.

### 5.1 Test of alternative filling schemes

72 × 1 8 × 0 72 × 1 8 × 0 72 × 1 8 × 0 72 × 1 38 × 0  
72 × 1 8 × 0 72 × 1 8 × 0 72 × 1 8 × 0 72 × 1 38 × 0  
72 × 1 8 × 0 72 × 1 8 × 0 72 × 1 8 × 0 72 × 1 38 × 0  
72 × 1 8 × 0 72 × 1 8 × 0 72 × 1 8 × 0 72 × 1 38 × 0  
72 × 1 8 × 0 72 × 1 8 × 0 72 × 1 8 × 0 72 × 1 38 × 0  
72 × 1 8 × 0 72 × 1 8 × 0 72 × 1 8 × 0 72 × 1 38 × 0

72 × 1 8 × 0 72 × 1 8 × 0 72 × 1 8 × 0 72 × 1 38 × 0  
72 × 1 8 × 0 72 × 1 8 × 0 72 × 1 8 × 0 72 × 1 38 × 0  
72 × 1 8 × 0 72 × 1 8 × 0 72 × 1 8 × 0 72 × 1 38 × 0  
72 × 1 8 × 0 72 × 1 8 × 0 72 × 1 8 × 0 48 × 1 126 × 0

The bunch filling scheme defined above can provide the largest number of bunches (2856), but does not any more exhibit a fourfold symmetry, but rather a ten fold symmetry. That does not match the periodicity of the LHC layout and, although the luminosity is highest in the interaction points 1 and 5, the symmetry is strongly broken by interactions points 2 and 8, leading to a much more irregular structure. In particular the number of bunches missing head-on collisions is largely increased. This is

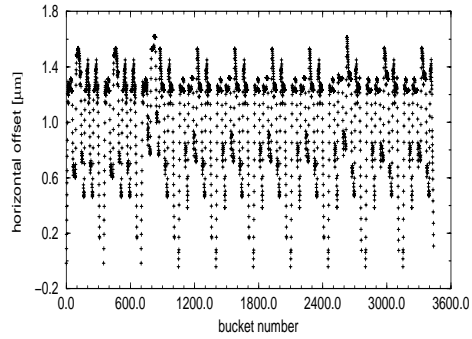


Figure 5: Closed orbit along bunch structure in the LHC. No fourfold symmetry.

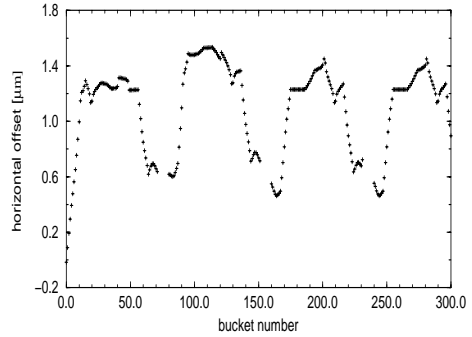


Figure 6: Closed orbit along bunch structure in the LHC, zoomed into 3 batches. No fourfold symmetry.

shown in Figs.5 and 6. Most important, it is difficult to identify nominal bunches (see Fig.6). This bunch filling scheme was discarded following these studies.

### 5.2 Effect of bunch to bunch intensity variations

Another effect can easily be studied using the TRAIN program. It allows to assign individual bunch intensities to all bunches of the train. The presently assumed bunch to

bunch variation is about 20%. The result of the calcula-

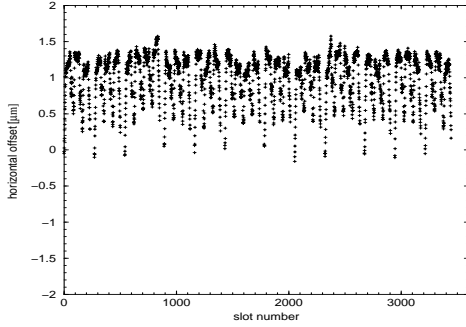


Figure 7: *Closed orbit along bunch structure in the LHC. 20% intensity variation between bunches.*

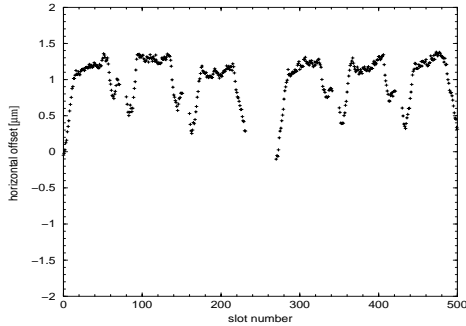


Figure 8: *Closed orbit along bunch structure in the LHC, zoomed into 3 batches. 20% intensity variation between bunches.*

tion is shown in Figs.7 and 8. Although the orbits are now all different for the originally nominal bunches, the variation is small (1 - 2% of the beam size).

## 6 CONCLUSIONS

The self-consistent bunch orbits presented here for the latest bunch filling scheme allow the following conclusions which of course concern only the closed orbits for zero phase-space amplitude, and not any other parameter such as long-term stability, lifetime, emittance blow-up, dynamic aperture etc.:

- The bunch offsets lie within  $\pm 0.1\sigma$  at the physics collision points
- The effects on other parameters (tune, chromaticity, dispersion) are small, and their shifts can easily be corrected (not their spread)
- The algorithm allows to evaluate and decide on filling schemes

- The effect of bunch to bunch intensity variations can be studied

## 7 REFERENCES

- [1] H. Grote, "Self-Consistent Orbits with beam-beam effect in the LHC", Proc. of Europ. Part. Acc. Conf. 2000 (Vienna, 2000), 1202.
- [2] The LHC Study Group, "The Large Hadron Collider - Conceptual Design", CERN/AC/95-05
- [3] H. Grote and F.C. Iselin, "The MAD Program", CERN/SL/90-13 (AP) (Revision 3) (1992).
- [4] E. Keil, "Truly Self-Consistent Treatment of the Side Effects with Bunch Trains", CERN SL/95-75
- [5] O. Brüning, W. Herr, R. Ostojic, "A beam separation and collision scheme for IP1 and IP5 at the LHC for optics version 6.1", CERN LHC Project Report 315
- [6] O. Brüning, W. Herr, R. Ostojic, "A beam separation and collision scheme for IP2 and IP8 at the LHC for optics version 6.1", CERN LHC Project Report 367

# Beam Sizes in Collision and Flip-Flop States at KEKB

F. Zimmermann, CERN, Geneva, Switzerland

## Abstract

Evaluating a simplified linear model of the beam-beam interaction, self-consistent horizontal beta functions, emittances and beam sizes are computed for the two unequal colliding beams in KEKB. For head-on collisions only one equilibrium solution exists at the nominal tunes. However, if for off-center collisions the quadrupolar component of the beam-beam force becomes defocusing, we obtain two solutions, one of which describes a flip-flop state with increased size of the positron beam. This result may explain observations of sudden luminosity drops.

## 1 INTRODUCTION

During KEKB operation drops in the luminosity are observed, which are associated with step changes in the horizontal and/or vertical beam sizes at the interaction point (IP) [1]. Often the LER horizontal beam size increases. Changes in the beam size appear to be correlated with small orbit variations. In particular, a hysteresis is observed when the beam-beam separation at the collision point is varied. In this report, we study a simple linear model of the self-consistent horizontal optics and emittances for the two unequal colliding beams, evaluate their dependence on the betatron tune and the beam-beam tune shift, and demonstrate the existence of flip-flop solutions for off-center collisions.

## 2 SELF-CONSISTENT OPTICS AND BEAM SIZES

In collision, the beam emittance and beta functions are changed by the focusing force of the opposing beam. Neglecting the change in the other beam (weak-strong approximation), the horizontal dynamic beta function,  $\beta_{x,1(2)}$ , at the collision point is usually obtained as [2]

$$b_{x,1(2)} \equiv \frac{\beta_{x0,1(2)}}{\beta_{x,1(2)}} = \frac{\sin 2\pi(Q_{1(2)} + \Delta Q_{1(2)})}{\sin 2\pi Q_{1(2)}} \quad (1)$$

where

$$Q_{1(2)} + \Delta Q_{1(2)} = \frac{1}{2\pi} \arccos \left( \cos 2\pi Q_{1(2)} - 2\pi \xi_{0,1(2)} \sin 2\pi Q_{1(2)} \right) \quad (2)$$

and  $Q_{1(2)}$  denotes the unperturbed horizontal betatron tune of beam 1 (or beam 2). The subindices 1 and 2 refer to the electron (HER) and positron beam (LER), respectively; the subindex '0' signifies the values of beta function and emittance without the focusing effect of the opposing beam.

Table 1: Parameters relevant to the flip-flop analysis.

variable	HER	LER
hor. beam-beam tune shift $\xi_x$	0.049	0.055
vert. beam-beam tune shift $\xi_y$	0.025	0.037
hor. tune	44.520	45.505
vert. tune	41.587	43.575
hor. beta function $\beta_{x0}$	63 cm	59 cm
vert. beta function $\beta_{y0}$	0.7 cm	0.7 cm
vert. beam-beam tune shift $\xi_y$	0.025	0.037
single-bunch current	0.48 mA	0.63 mA

The parameter  $\xi_{0,1(2)}$  is the horizontal beam-beam tune shift, calculated from the unperturbed beta functions and emittances,

$$\xi_{0,1(2)} \equiv \frac{N_{2(1)} r_0}{2\pi \gamma \epsilon_{x0,2(1)}} \frac{\beta_{x0,1(2)}}{\beta_{x0,2(1)}}, \quad (3)$$

where  $r_0$  denotes the classical electron radius. For the parameter values of KEKB, summarized in Table 1, the (inverse) normalized dynamic beta functions evaluate to  $b_{x,1} = 2.40$  and  $b_{x,2} = 4.78$ .

Since the actual beam-beam tune shift,  $\xi_{1,2}$ , depends on the dynamic beta function, Eq. (1) does not describe a self-consistent solution of the problem. Neither can it account for flip-flop phenomena or for the simultaneous existence of more than one equilibrium state. The flip-flop effect with linearized beam-beam force for round beams was recently analyzed by A. Otboev and E. Perevedentsev [3], who computed self-consistent beta functions and equilibrium emittances. We here follow and extend their formalism, and then apply it to the KEKB case of flat beams with unequal parameters. For simplicity, we limit the discussion to the horizontal plane, in which flip-flop effects are frequently observed.

The basic equations governing the evolution of the beta functions are [3]

$$b_1^2 = 1 + 2c_1 x_1 \frac{b_2}{e_2} - x_1^2 \frac{b_2^2}{e_2^2} \quad (4)$$

$$b_2^2 = 1 + 2c_2 x_2 \frac{b_1}{e_1} - x_2^2 \frac{b_1^2}{e_1^2} \quad (5)$$

where  $c_{1(2)} \equiv \cot(2\pi Q_{1(2)})$ ,  $b_{1(2)} \equiv \beta_{x0,1(2)}/\beta_{x,1(2)}$ ,  $x_{1(2)} \equiv 2\pi \xi_{0,1(2)}$ , and  $e_{1(2)} \equiv \epsilon_{x,1(2)}/\epsilon_{x0,1(2)}$ .

Figure 1 displays the graphical method [4] of solving Eqs. (4) and (5). Plotting the two curves  $b_1(b_2)$  and  $b_2(b_1)$ ,



solutions to (4) and (5) are given by their intersections. As can be seen, for the parameters considered and for constant emittances,  $e_1 = e_2 = 1$ , there is only one intersection and, hence, no flip flop is expected. Figure 2 shows an equivalent picture obtained by neglecting the quadratic terms in (4) and (5). The difference to Fig. 1 is insignificant.

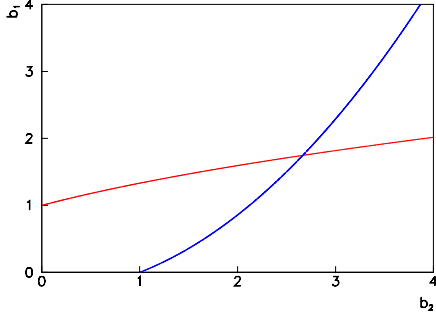


Figure 1: Graphical solution of the complete Eqs. (4)–(5) for constant emittances,  $e_{1(2)} \equiv \epsilon_{x,1(2)}/\epsilon_{x0,1(2)} = 1$ . Plotted is the variation of the inverse electron beta function,  $b_1 = \beta_{x0,1}/\beta_{x,1}$ , as a function of the inverse positron beta function,  $b_2 = \beta_{x0,2}/\beta_{x,2}$ , for the parameters of Table 1.

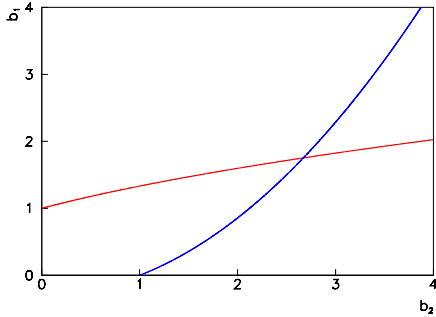


Figure 2: Graphical solution of Eqs. (4)–(5), considering only the terms proportional to  $c_{1(2)}x_{1(2)}$ , for constant emittances,  $e_{1,2} \equiv \epsilon_{x,1(2)}/\epsilon_{x0,1(2)} = 1$ . Plotted is the variation of the inverse electron beta function,  $b_1 = \beta_{x0,1}/\beta_{x,1}$ , as a function of the inverse positron beta function,  $b_2 = \beta_{x0,2}/\beta_{x,2}$ , for the parameters of Table 1.

If the beams collide with a horizontal offset, the quadrupolar component of the beam-beam force may change sign. Figure 3 shows the graphical solution for an unperturbed beam-beam tune shift parameter  $\xi_0$  equal to  $-1/4$  times the nominal value. Still there is only one intersection.

Next we include the variation in emittance. Following Ref. [5], or ignoring the oscillatory term in the solution

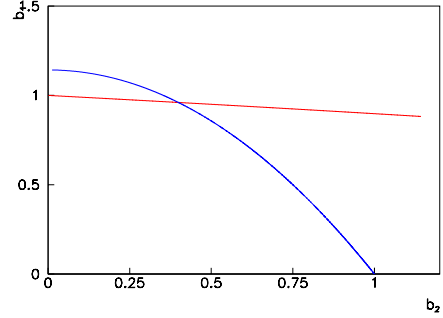


Figure 3: Graphical solution of Eqs. (4)–(5) for constant emittances,  $e_{1,2} \equiv \epsilon_{x,1(2)}/\epsilon_{x0,1(2)} = 1$ , assuming a negative beam-beam tune shift  $\xi_{0,1(2)} = -0.25\xi_{0,1(2)}^{\text{nom}}$ , where  $\xi_{0,1(2)}^{\text{nom}}$  represents the nominal value listed in Table 1. Plotted is the variation of the inverse electron beta function,  $b_1 = \beta_{x0,1}/\beta_{x,1}$ , as a function of the inverse positron beta function,  $b_2 = \beta_{x0,2}/\beta_{x,2}$ .

of Ref. [3], the emittance changes with the strength of the beam-beam focusing according to

$$e_{1(2)} = \frac{1 + p_{1(2)} \cot 2\pi Q_{x,1(2)}}{\sqrt{1 + 2p_{1(2)} \cot 2\pi Q_{x,1(2)} - p_{1(2)}^2}}, \quad (6)$$

where  $e_{1(2)} \equiv \epsilon_{x,1(2)}/\epsilon_{x0,1(2)}$  and  $p_{1,2} \equiv x_{1,2}b_{2,1}/e_{2,1}/b_{1,2}$ . This equation is illustrated in Fig. 4.

Figures 5 and 6 shows a more precise SAD computation of the dynamic emittances and beta functions as a function of the beam-beam tune shift, provided by H. Koiso, which accounts for the exact ring optics. The emittance variation in Fig. 5 agrees within 10% with the simplified estimate of Eq. (6) and Fig. 4.

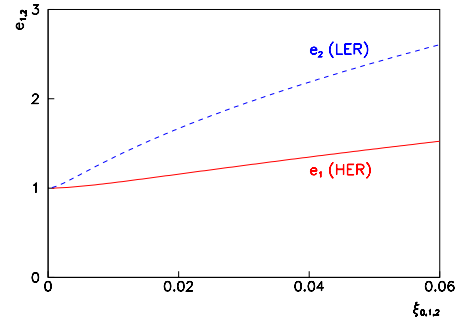


Figure 4: Horizontal emittance  $e_{1,2}$  in the high energy and low energy ring as a function of beam-beam parameter  $\xi_{1,2}$ , for constant values of  $b_{2,1} = e_{2,1} = 1$ , according to Eq. (6).

From Figs. 4 and 5, we approximate the dependence of the horizontal emittances on the beam-beam lens by the

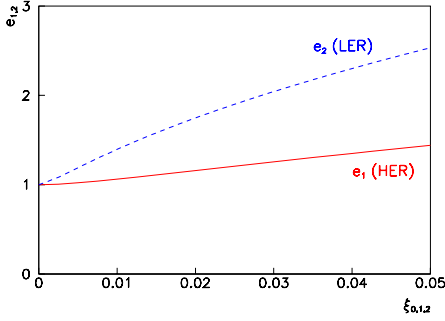


Figure 5: Dynamic emittance in units of the unperturbed emittance,  $e_{1,2}$ , as a function of beam-beam tune shift for the low and high-energy rings of KEKB, computed by SAD. (Courtesy H. Koiso)

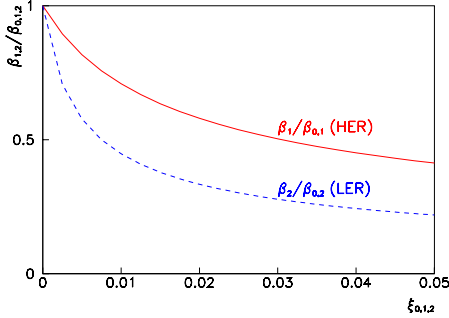


Figure 6: Horizontal beta functions  $\beta_{1,2}/\beta_{0,1,2} \equiv 1/b_{1,2}$  as a function of beam-beam tune shift for the low and high-energy rings of KEKB, computed by SAD. (Courtesy H. Koiso)

linear relations

$$e_1 \approx 1 + k_1 x_1 \frac{b_2}{b_1 e_2}, \quad (7)$$

$$e_2 \approx 1 + k_2 x_2 \frac{b_1}{b_2 e_1}, \quad (8)$$

where, for the nominal tunes (subindex 0),  $k_1 = k_{0,1} \approx 1.3$ , and  $k_2 = k_{0,2} \approx 4.6$ . The reason why the values of  $k_{0,1}$  and  $k_{0,2}$  are so different is that in the LER the horizontal tune is much closer to the half integer resonance (see Eq. (6) and Table 1). Note that the equation for  $e_{1(2)}$  also contains the beta function  $b_{1(2)}$ , which is an extension of the formulae in Ref. [3] that naturally follows from Eq. (6) inserting the definitions of  $p_{1,2}$  and  $x_{1,2}$ . Equations (7) and (8) are approximations, which could be refined in future studies.

We can solve the two equations (7) and (8) for  $e_{1,2}$ :

$$e_1 = \frac{1}{2} \left( 1 + k_1 x_1 \frac{b_2}{b_1} - k_2 x_2 \frac{b_1}{b_2} \right) + \sqrt{\frac{1}{4} \left( 1 + k_1 x_1 \frac{b_2}{b_1} - k_2 x_2 \frac{b_1}{b_2} \right)^2 + k_2 x_2 \frac{b_1}{b_2}},$$

$$e_2 = \frac{1}{2} \left( 1 + k_2 x_2 \frac{b_1}{b_2} - k_1 x_1 \frac{b_2}{b_1} \right) + \sqrt{\frac{1}{4} \left( 1 + k_2 x_2 \frac{b_1}{b_2} - k_1 x_1 \frac{b_2}{b_1} \right)^2 + k_1 x_1 \frac{b_2}{b_1}}.$$

Inserting these expressions into Eqs. (4) and (5), we may once again use the graphical method to determine the remaining two unknowns  $b_1$  and  $b_2$ .

Figure 7 shows the solution for the nominal parameters of Table 1. There is only one intersection, which indicates a unique equilibrium. The curves look similar to those in Fig. 1, which were computed for constant emittances.

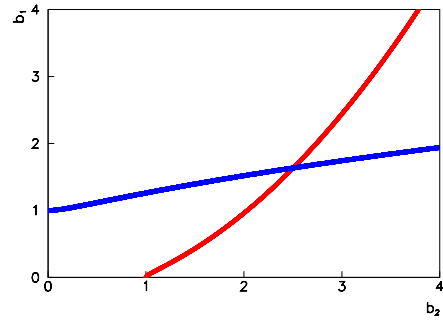


Figure 7: Graphical solution of Eqs. (4)–(5) for emittances that vary linearly with the strength of the beam-beam force as in Eqs. (7) and (8). Plotted is the electron beta function,  $b_1 = \beta_{x0,e}/\beta_{x,e}$ , as a function of the positron beta function,  $b_2 = \beta_{x0,p}/\beta_{x,p}$ , for the nominal parameters of Table 1.

The situation changes dramatically, if we invert the sign of the beam-beam tune shift, in order to model a situation with off-center collisions. Figure 8 illustrates a typical example, where we consider an unperturbed tune shift equal to  $-0.25 \xi_{0,1(2)}^{\text{nom}}$ . In this case there are two intersections, *i.e.*, two solutions. This is quite different from the result for constant emittances in Fig. 3. One of the two solutions represents a large increase of the positron beta function (small value of  $b_2$ ), possibly consistent with the observed flip-flop state.

The self-consistent beta functions and emittances depend on the tunes of both beams. Figures 9 and 10 illustrate the dependence of the normalized beam sizes  $\sigma_{x,1(2)}/\sigma_{x0,1(2)} = \sqrt{e_{1(2)}/b_{1(2)}}$  on the tunes in either ring, respectively, for the nominal beam-beam tune shift. In this calculation, we have approximated the variation of the coefficients  $k_1$  and  $k_2$  in Eqs. (7) and (8) with the tunes  $Q_{1,2}$

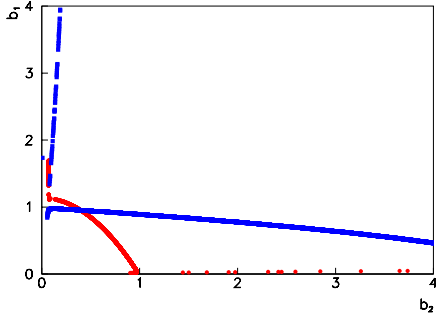


Figure 8: Graphical solution of Eqs. (4)–(5) assuming a negative beam-beam tune shift  $\xi_{0,1(2)} = -0.25\xi_{0,1(2)}^{\text{nom}}$ , for emittances that vary linearly with the strength of the beam-beam force as in Eqs. (7) and (8). Plotted is the electron beta function,  $b_1 = \beta_{x0,e}/\beta_{x,e}$ , as a function of the positron beta function,  $b_2 = \beta_{x0,p}/\beta_{x,p}$ .

as

$$k_{1(2)} \approx k_{0,1(2)} \cot(2\pi Q_{1(2)}) / \cot(2\pi Q_{0,1(2)}). \quad (9)$$

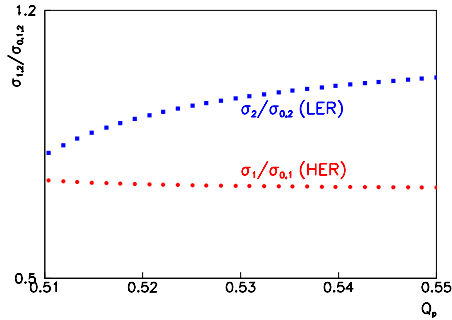


Figure 9: Self-consistent horizontal beam sizes  $\sigma_x/\sigma_{x0}$  as a function of the positron tune (right). The positron tune is set to 0.505.

An offset between the two beams at the collision point distorts the closed orbit, introduces a change in the linear focusing, and excites additional higher-order resonances. As indicated earlier in this paper, we only consider the variation in the quadrupolar focusing force, and approximate the change in the focusing due to a varying beam-beam separation by a common multiplication factor  $M_\xi$  for the two beam-beam tune shift parameters. This is based on the assumption that a small beam-beam offset reduces the strength of linear focusing experienced at the collision point by a similar factor for either beam, provided the sizes of the two beams are equal (note that they will not remain equal once a flip-flop state is established). For larger off-

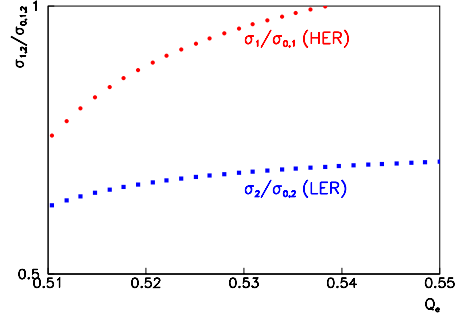


Figure 10: Self-consistent horizontal beam sizes  $\sigma_x/\sigma_{x0}$  as a function of the positron tune. The electron tune is set to 0.520.

sets, the beam-beam focusing force changes sign, which we model by a negative value for  $M_\xi$ .

Figures 11–13 illustrate the dynamic variation of beta function, emittances and beam sizes as a function of a positive multiplication factor  $M_\xi$ . The beta functions decrease more strongly than the emittances increase as a function of the beam-beam tune shift, such that the IP beam sizes shrink for higher current. Equivalent results for a negative multiplication factor  $M_\xi$  are shown in Figs. 14–16. Consistent with Fig. 3, in the latter case two solutions coexist. The additional solution appears to be of the flip-flop type. It is characterized by a large increase in the LER IP beta function (Fig. 14), a decrease in the emittance (Fig. 15) and a resulting net growth of the IP beam size (Fig. 16).

A tentative explanation of the observed hysteresis may then be the following. For a sufficiently large beam-beam offset of about  $2\sigma_x$ , the ‘quadrupolar’ component of the horizontal beam-beam force changes sign, *i.e.*, the force becomes defocusing instead of focusing, and there emerges a new equilibrium, which represents a flip-flop state. Therefore, repeated changes in the sign of  $\xi$  — due to varying beam-beam separation —, might induce transitions between the different solutions that exist for  $\xi < 0$ .

### 3 CONCLUSIONS

Calculations of horizontal equilibrium sizes for head-on colliding beams at KEKB suggest the existence of a unique equilibrium solution. If the beams are horizontally separated sufficiently far that the ‘quadrupolar’ component of the beam-beam force is defocusing, two self-consistent solutions coexist, one of which describes a flip-flop state, in which the positron beam is blown up. This appears consistent with some of the observations.

Our analysis was based on a simplified model, which considers only the horizontal plane, a linearized beam-beam force, a linear dependence of the emittance on the beam-beam tune shift, and a common scale factor for both beam-beam parameters representing the effect of a trans-

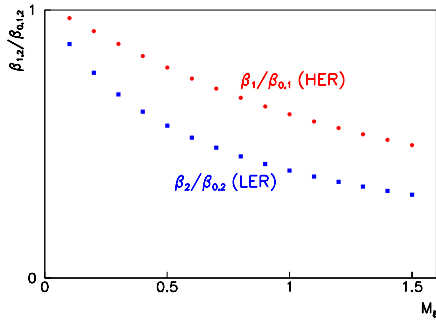


Figure 11: Self-consistent dynamic beta functions  $\beta_{1,2}/\beta_{0,1,2} \equiv 1/b_{1,2}$ , as a function of a common positive multiplication factor  $M_\xi$  for both tune shift parameters. This multiplication factor is intended to model a change in linear focusing arising from a beam-beam offset. The tunes are set to 0.520 (HER,  $e^-$ ) and 0.505 (LER,  $e^+$ ), respectively.

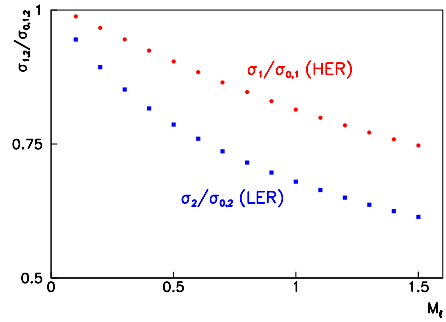


Figure 13: Self-consistent dynamic beam sizes  $\sigma_{1,2}/\sigma_{0,1,2} \equiv \sqrt{e_{1,2}/b_{1,2}}$ , as a function of a common positive multiplication factor  $M_\xi$  for both tune shift parameters. This multiplication factor is intended to model a change in linear focusing arising from a beam-beam offset. The tunes are set to 0.520 (HER,  $e^-$ ) and 0.505 (LER,  $e^+$ ), respectively.

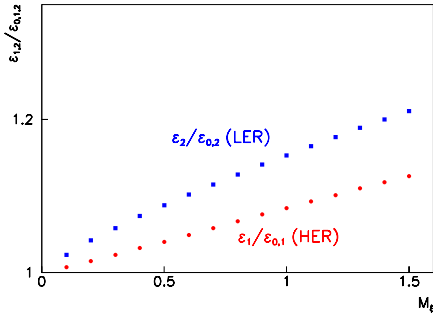


Figure 12: Self-consistent dynamic emittances  $e_{1,2} \equiv \epsilon_{1,2}/\epsilon_{0,1,2}$ , as a function of a common positive multiplication factor  $M_\xi$  for both tune shift parameters. This multiplication factor is intended to model a change in linear focusing arising from a beam-beam offset. The tunes are set to 0.520 (HER,  $e^-$ ) and 0.505 (LER,  $e^+$ ), respectively.

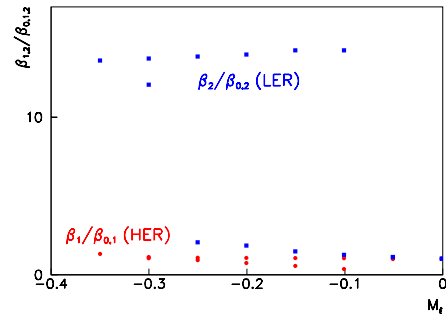


Figure 14: Self-consistent dynamic beta functions  $\beta_{1,2}/\beta_{0,1,2} \equiv 1/b_{1,2}$ , as a function of a common negative multiplication factor  $M_\xi$  for both tune shift parameters. This multiplication factor is intended to model a change in linear focusing arising from a beam-beam offset. The tunes are set to 0.520 (HER,  $e^-$ ) and 0.505 (LER,  $e^+$ ), respectively.

verse offset. All of these approximations could be improved. Future extensions might also include the vertical plane, bunch length and crossing angle, as well as the non-linear components of the force including an arbitrary beam-beam separation.

#### 4 ACKNOWLEDGEMENTS

I thank K. Oide for suggesting this study, H. Fukuma, Y. Funakoshi, H. Koiso, K. Ohmi, K. Oide, and J. Urakawa for the hospitality at KEK and for helpful discussions, W. Herr and F. Ruggiero for their support, and the organizers and participants of the FNAL 2001 beam-beam workshop, especially T. Sen and M. Xiao, for their interest in

this work.

#### 5 REFERENCES

- [1] K. Oide, private communication; and M. Tawada, this workshop (2001).
- [2] M. A. Furman, “Beam-beam tune shift and dynamical beta function in PEP-II,” LBL-34957, EPAC 94, London (1994).
- [3] A.V. Otboev and E.A. Perevedentsev, “Self-Consistent Beta Functions and Emittances of Round Colliding Beams,” PRST-AB 2, 104401 (1999).
- [4] A.B. Temnykh, INP Report No. INP 82-148 (1982).

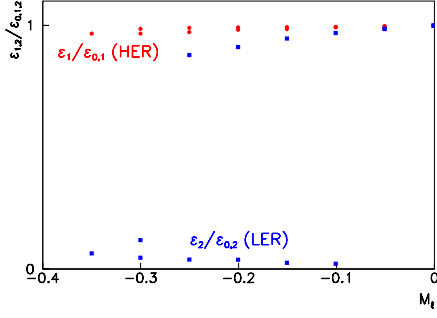


Figure 15: Self-consistent dynamic emittances  $e_{1,2} \equiv \epsilon_{1,2}/\epsilon_{0,1,2}$ , as a function of a common negative multiplication factor  $M_\xi$  for both tune shift parameters. This multiplication factor is intended to model a change in linear focusing arising from a beam-beam offset. The tunes are set to 0.520 (HER,  $e^-$ ) and 0.505 (LER,  $e^+$ ), respectively.

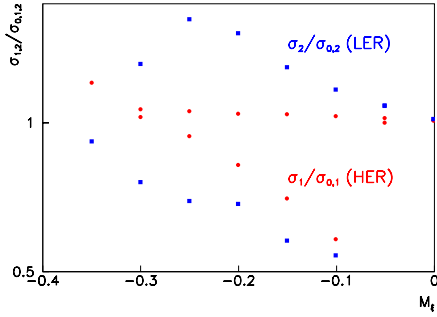


Figure 16: Self-consistent dynamic beam sizes  $\sigma_{1,2}/\sigma_{0,1,2} \equiv \sqrt{e_{1,2}/b_{1,2}}$ , as a function of a common negative multiplication factor  $M_\xi$  for both tune shift parameters. This multiplication factor is intended to model a change in linear focusing arising from a beam-beam offset. The tunes are set to 0.520 (HER,  $e^-$ ) and 0.505 (LER,  $e^+$ ), respectively.

- [5] K. Hirata and F. Ruggiero, LEP Note 611 (1988).
- [6] K. Yokoya, Y. Funakoshi, E. Kikutani, H. Koiso, and J. Urakawa, KEK Preprint 89-14 (1989).
- [7] Y. Alexahin, "A Study of the Coherent Beam-Beam Effect in the Framework of the Vlasov Perturbation Theory," CERN-LHC-Project-Report-461, submitted to NIM A (2001).

# SPECTRA OF COHERENT TRANSVERSE OSCILLATIONS IN COLLIDING BUNCHES OF FINITE LENGTH

Y.Alexahin<sup>1</sup>, FNAL, Batavia, IL 60510

## Abstract

The effect of various factors on the spectra of coherent transverse oscillations in colliding beams is considered, including the synchro-betatron coupling due to chromaticity and finite bunch length; several interaction points, compensation of the incoherent beam-beam tunespread with electron lenses. Possible consequences for the coherent beam stability are discussed.

## 1 INTRODUCTION

As a rule when the beams are put into collision the coherent transverse oscillations get damped by large incoherent beam-beam tunespread. However, it may be not so in the strong-strong case when there exist discrete spectral lines of coherent oscillations [1] well separated from the incoherent tunespread. Moreover, if other sources of betatron tunespread are weak, the beam-beam interaction can switch off their stabilizing effect rendering the coherent oscillations unstable. Probably such a situation was observed at ISR [2].

There are various factors which can influence coherent beam-beam oscillations [3], coupling to the longitudinal motion being especially important in the case of large bunch length. The overlapping synchrotron sidebands of the incoherent tunes can provide Landau damping of the coherent oscillations if the ratio of the synchrotron tune to the beam-beam parameter lies within certain limits.

Understanding of the beam-beam spectra is also important for correct interpretation of the measurement data which may be not an easy task in the case of many bunches colliding at several interaction points.

In the present report we address the above-mentioned problems developing the formalism of the Vlasov perturbation theory of Ref.[3] for the case of large bunch length. The analysis is limited to the first order in the beam-beam parameter leaving aside such phenomena as the dynamic  $\beta$ -effect which may be important in  $e^+e^-$  machines.

## 2 WEAK-STRONG CASE

Let us first consider horizontal oscillations in the weak beam in the presence of chromaticity and nonlinear betatron tunespread due to interaction with the strong beam. Some efficient formulas for analytical computation of the beam-beam tuneshift and chromaticity (which may be quite large in the case of numerous long-range interactions in the arcs) are given in Ref.[4].

A rigorous way to deal with chromatic tune modulation is to apply a Lie-transform to eliminate the Hamiltonian dependence on the longitudinal angle variable,  $\varphi_s$  (see e.g. Ref.[3]). The Lie-transform gives

new action-angle variables,  $J_i, \psi_i, i=x, y, s$ , related to the original ones in the following way:

$$J_i = I_i, \quad \psi_{x,y} = \varphi_{x,y} + \frac{v'_{x,y}}{\alpha_M R} \sigma, \quad \psi_s = \varphi_s, \quad (1)$$

where  $\alpha_M$  is the momentum compaction factor,  $R$  is the average machine radius,  $\sigma$  is the longitudinal coordinate, the prime denotes the tune derivative w.r.t. the momentum deviation,  $\delta_p$ .

In the absence of external perturbation the particle motion is described by equations

$$J_i = \text{const}, \quad \psi_i = v_i^{(k)}(J) \theta, \quad (2)$$

where the generalized azimuth  $\theta = s/R$  plays the role of the independent variable, the superscript  $k$  refers to the beam number. In the following we will ignore the betatron tune dependence on the synchrotron amplitude which may still remain after the transformation (e.g. due to crossing angle at the interaction point); also, we assume the synchrotron tune to be independent of the betatron and synchrotron amplitudes.

Let us now apply an initial perturbation (a horizontal dipole kick of unitary magnitude in the beam  $\sigma$ ) to the weak beam (let it be the first one). Assuming  $J_i$  to be normalized by the corresponding r.m.s. emittances we can write for the initial perturbation of the distribution function

$$F_1^{(1)}|_{\theta=0} = -\sqrt{J_x/2} \frac{\partial F_0}{\partial J_x} e^{i\varphi_x} + \text{c.c.} = -\sqrt{J_x/2} \frac{\partial F_0}{\partial J_x} e^{i\psi_x} \sum_{m=-\infty}^{\infty} e^{im(\psi_s+\pi)} J_m(\chi\sqrt{2J_s}) + \text{c.c.} \quad (3)$$

where  $J_m$  is the Bessel function,

$$\chi = \frac{v'_x \sigma_s}{\alpha_M R} = \frac{v'_x \sigma_E}{|v_s|}, \quad (4)$$

$F_0$  is the equilibrium distribution function assumed to be Gaussian for both beams:

$$F_0(J, \psi) = \frac{1}{(2\pi)^3} \exp\left(-\sum_{i=x,y,s} J_i\right). \quad (5)$$

Evolution of the perturbed distribution function is described by the Liouville equation

$$\frac{\partial}{\partial \theta} F_1^{(1)} + \underline{v}^{(1)} \cdot \frac{\partial}{\partial \underline{\psi}} F_1^{(1)} = 0, \quad (6)$$

with the obvious solution

$$F_1^{(1)}(J, \underline{\psi}, \theta) = -\sqrt{J_x/2} \frac{\partial F_0}{\partial J_x} e^{i\psi_x} \times \sum_{m=-\infty}^{\infty} e^{im(\psi_s+\pi)-i(v_x+m v_s)\theta} J_m(\chi\sqrt{2J_s}) + \text{c.c.} \quad (7)$$

Let us introduce the complex Courant-Snyder variable,  $\eta$ , and express it via the new action-angle variables:

<sup>1</sup> Permanent address: LPP JINR, Dubna 141980 Russia

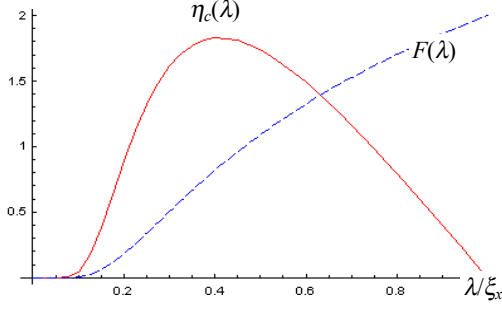


Figure 1: Spectral density of horizontal center-of-mass oscillations at  $\chi = 0$  and distribution in the incoherent tune in the case of flat beams.

$$\eta = \frac{x - i(\beta_x p_x + \alpha_x x)}{\sigma_x} = \sqrt{2J_x} \exp(i\psi_x - i\chi\sigma/\sigma_s) \quad (8)$$

Averaging it with the distribution function (7) and performing the Fourier transformation over  $\theta$  we obtain for the spectral density of the center-of-mass motion

$$\begin{aligned} \eta_c^{(1)}(\lambda) &= i \int d^2 J_x J_x \frac{\partial F_{\perp 0}}{\partial J_x} \sum_{m=-\infty}^{\infty} \delta(\lambda - v_x^{(1)} - m v_s) I_m(\chi^2) e^{-\chi^2} \\ &= i \int dJ_y \sum_{m=-\infty}^{\infty} J_x \frac{\partial F_{\perp 0} / \partial J_x}{\partial v_x^{(1)} / \partial J_x} \Big|_{J_x = J_m} I_m(\chi^2) e^{-\chi^2} \times \end{aligned} \quad (9)$$

$$\Theta[\lambda - m v_s - v_x^{(1)}(J_y)] \Theta[v_x^{(1)}(J_y) - \lambda + m v_s]$$

where  $F_{\perp 0}$  is the distribution function in the transverse action variables,  $I_m(x)$  and  $\Theta(x)$  are the modified Bessel and Heaviside functions,  $J_m(\lambda, J_y)$  is the solution of the equation

$$v_x^{(1)}(J_m, J_y) = \lambda - m v_s. \quad (10)$$

It is worthwhile to compare the spectral density (9) in the limit of zero chromaticity,  $\chi \rightarrow 0$ , with the distribution function in the incoherent tune:

$$F(\lambda) = \int dJ_y \frac{F_{\perp 0}}{\partial v_x^{(1)} / \partial J_x} \Big|_{J_x = J_0} \times \quad (11)$$

$$\Theta[\lambda - v_x^{(1)}(J_y)] \Theta[v_x^{(1)}(J_y) - \lambda]$$

where  $J_0$  is the solution of eq.(10) at  $m = 0$ .

The major difference is that the spectral density (9) has the additional factor  $J_x$  in the integrand which diminishes contribution of the core particles. In the case of beam-beam oscillations these particles have the largest tunes, hence the spectrum is peaked at smaller tunes than the maximum of distribution (11).

Fig.1 shows these functions in the case of flat beams when  $v_x$  does not depend on  $J_y$ : for Gaussian beams ( $F_{\perp 0} = \exp(-J_x - J_y)$ )

$$v_x^{(1)} = \xi_x \frac{1 - \exp(-J_x)}{J_x}. \quad (12)$$

Let us now return to the case of finite chromaticity. If the tunespread (equal to  $\xi_x$  in our example) is small compared to the synchrotron tune then the satellites are well resolved as shown with red lines in Fig.2 for  $\chi=0.75$  which corresponds to chromaticity  $\nu'_x = 5.9$  in Tevatron.

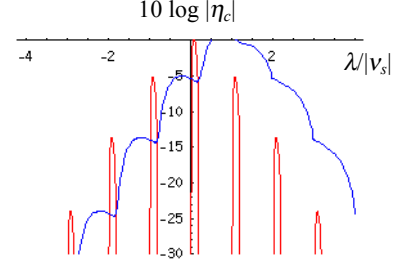


Figure 2: Spectral density of horizontal oscillations in flat beams at  $\chi = 0.75$  and  $\xi_x/|v_s| = 0.2$  (red line) and  $\xi_x/|v_s| = 2$  (blue line).

In the opposite limit the satellites merge (blue line).

### 3 STRONG-STRONG CASE

In the case of comparable numbers of particles per bunch in the two beams,  $N_1 \sim N_2$ , the small-amplitude oscillations are described by the system of the Vlasov equations ( $k = 1, 2$ ):

$$\frac{\partial}{\partial \theta} F_1^{(k)} + \underline{v}^{(k)} \cdot \frac{\partial}{\partial \underline{\psi}} F_1^{(k)} = \quad (13)$$

$$\frac{r_p N_{3-k}}{\gamma} \sum_{IP} \delta_p(\theta - \theta_{IP}) F_0 \underline{\epsilon}^{-1} \cdot \frac{\partial}{\partial \underline{\psi}} \int G^{(k)} F_1^{(3-k)} d^3 J' d^3 \psi'$$

where the incoherent tunes  $\underline{v}^{(k)}$  include the beam-beam tunes,  $r_p = -e_1 e_2 / mc^2$  is the classical radius of particles ( $r_p > 0$  for the  $p-p$  case),  $\delta_p(\theta)$  is the periodic  $\delta$ -function,  $\underline{\epsilon}^{-1}$  is vector of inverse emittances (assumed equal in both beams).

In long bunches the actual collision point may be significantly displaced w.r.t.  $\theta_{IP}$ , but the interaction can be formally ascribed to the nominal IP with the help of a similarity transformation [5]. In the result the Green function explicitly depends on the momenta [6]

$$\begin{aligned} G = -\ln \Big\{ & \left[ x - x' + \frac{p_x + p'_x}{2} (\sigma - \sigma') \right]^2 + \\ & + \left[ y - y' + \frac{p_y + p'_y}{2} (\sigma - \sigma') \right]^2 \Big\} \end{aligned} \quad (14)$$

Performing Fourier expansion in the angle variables

$$F_1^{(k)} = \sqrt{N_2 / N_k} \exp(-\sum_i J_i / 2) \sum_{\underline{m}} \exp(i \underline{m} \cdot \underline{\psi}) f_{\underline{m}}^{(k)}(J, \theta) \quad (15)$$

in the non-resonance case we may retain only one transverse harmonic ( $m_x = 1, m_y = 0$  for the horizontal dipole oscillations). However, the coupling between longitudinal harmonics can not be ignored in the case of large bunch length and low synchrotron tune (as in Tevatron), so the dimensionality of the problem is four (three action variables and the longitudinal phase angle).

In many practical cases some simplifications are possible. For horizontal oscillations in flat and round beams in absence of crossing angle and dispersion at the IP the Green function can be factorized into a product of the transverse function  $G_{\perp}(\underline{J}_{\perp}, \underline{J}'_{\perp})$  (see [3] and references



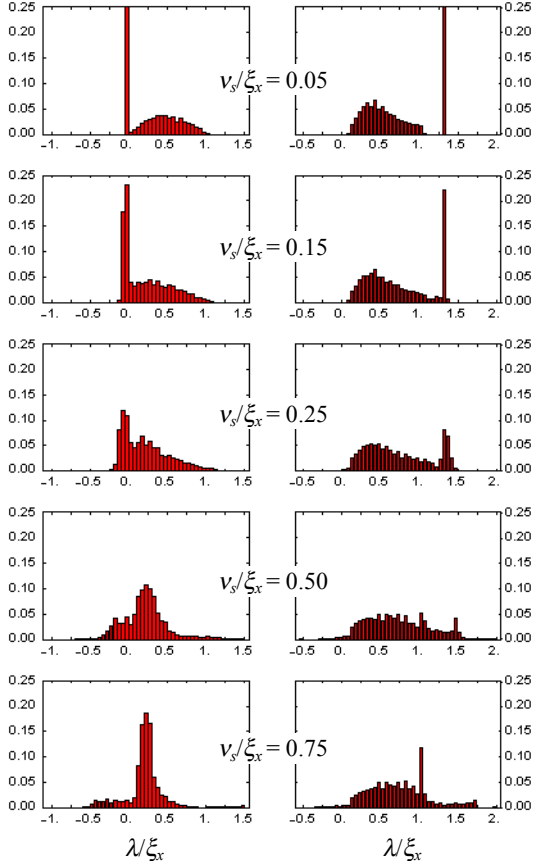


Figure 3: Spectral density of  $\Sigma$  (left) and  $\pi$  (right) modes in long bunches ( $\sigma_s = \beta_x^*$ ) excited by a dipole kick at different values of the synchrotron tune and  $\chi = 0$ .

therein for various representations) and the longitudinal factor

$$G_L = \exp(2i \arctan \frac{\sigma - \sigma'}{2\beta_x^*} - i\chi \frac{\sigma - \sigma'}{\sigma_s}). \quad (16)$$

As discussed in [7], series expansion of the perturbed distribution function in the Laguerre polynomials (or other smooth functions) of the transverse action variables fails to converge due to a singularity associated with the resonance particles. However, this does not refer to the longitudinal action variable, so that the solution of the Vlasov equation (13) can be sought for as the expansion

$$f_{m_s}^{(k)}(\underline{J}) = \sum_{\mu=0}^{\infty} a_{m_s\mu}^{(k)}(\underline{J}_{\perp}) \Lambda_{m_s\mu}(J_s) \quad (17)$$

in the basis functions

$$\Lambda_{m_s\mu}(J_s) = \sqrt{\frac{\mu!}{(m_s + \mu)!}} e^{-J_s/2} J_s^{m_s/2} L_{\mu}^{m_s}(J_s) \quad (18)$$

where  $L_{\mu}^m(x)$  is the associated Laguerre polynomial.

The matrix element of the Green function (16) can be presented in the form

$$G_L^{m\mu, n\nu} = \{ 2 \int_0^{\infty} \exp[-t - (\frac{\sigma_s}{2\beta_x^*} t - \chi)^2] (\frac{\sigma_s}{2\beta_x^*} t - \chi)^{2\mu+2\nu+m+n} dt - (-1)^{m+n} e^{-\chi^2} \chi^{2\mu+2\nu+m+n} \} / \sqrt{2^{\mu+2\nu+m+n} \mu! (m+\mu)! \nu! (n+\nu)!} \quad (19)$$

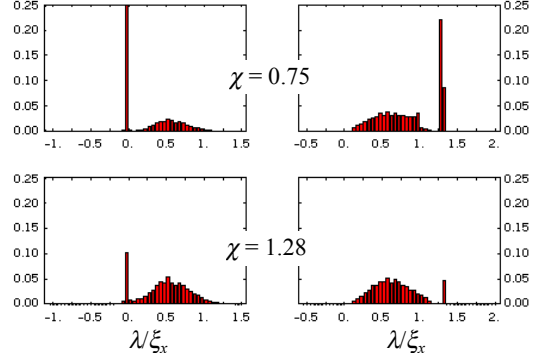


Figure 4: Spectral density of  $\Sigma$  and  $\pi$  modes at  $v_s/\xi_x = 0.15$ ,  $\sigma_s/\beta_x^* = 1$  and different values of chromaticity.

To achieve precision in eigenfrequencies of better than  $10^{-4}$  for the bunch length as large as  $\sigma_s = \beta_x^*$  it is sufficient to take into account the longitudinal harmonics  $m_s = -3, \dots, 3$  and the Laguerre polynomials with  $\mu = 0, \dots, 3 - |m_s|$ . Fig. 3 shows spectra of oscillations in flat beams obtained by solving the Vlasov equation with 60 points in the  $J_x/(1+J_x)$  variable.

The discrete  $\pi$ -mode has the eigenvalue 1.33, so that at  $v_s/\xi_x = 0.15$  it can be overlapped only by sidebands  $m_s \geq 3$  of the incoherent tunes. One can see a noticeable, though small, damping effect of the third sideband. With increasing synchrotron tune the second and then the first sideband overlap the discrete modes leading to their practically complete suppression. With further increase the discrete lines reappear but at shifted positions by coupling to the sidebands.

As noted earlier in Refs.[3,4] and can be easily seen in eq.(16), there is interference between finite bunch length and chromaticity at  $\chi \sim \sigma_s/\beta_x^*$ . Fig.4 presents beam-beam spectra at  $v_s/\xi_x = 0.15$  and two values of parameter  $\chi$  corresponding to  $v'_x = 5.9$  and 10 in Tevatron. Comparison with the plots for the same synchrotron tune and  $\chi = 0$  in Fig.3 shows that the relative weight of the discrete lines (given by the covered area) first increases with  $\chi$  but then rapidly falls off.

Another interesting observation is absence of the synchrotron satellites of the discrete spectral lines.

## 4 MULTI-BUNCH MODES

The beam-beam spectra look even more complicated for multiple bunches colliding at several interaction points. In the case of  $K$  identical and equidistant bunches in each beam the individual distribution functions are related to the multi-bunch normal modes [1, 3] as follows:

$$f^{\{k, \beta\}} = \sum_{n=0}^{K-1} e^{2\pi i n \beta / K} g_n^{(k)}, \quad k = 1, 2, \quad \beta = 1, \dots, K \quad (20)$$

where functions  $g_n^{(k)}$  satisfy the Vlasov equation (13) with the additional factor  $\exp[-2i(-1)^k n \theta]$  under the sum sign in the right hand side.

In Tevatron the bunches experience two head-on collisions at the IPs situated  $2\pi/3$  apart in  $\theta$  and a number of parasitic long-range interactions which we neglect in

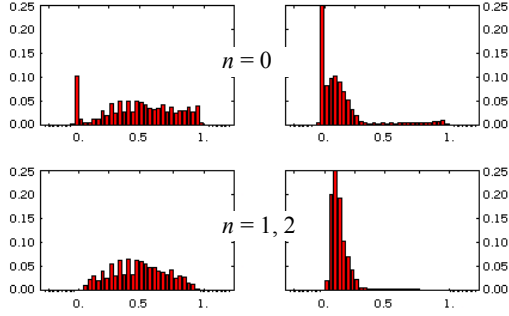


Figure 5: Spectra of the normal multi-bunch modes in the weak (left) and strong (right) flat beams with  $r_\xi = 0.3$  and  $v_s/\xi_x = 0.05$ ,  $\sigma_s/\beta_x^* = 1$ ,  $\chi = 0$ .

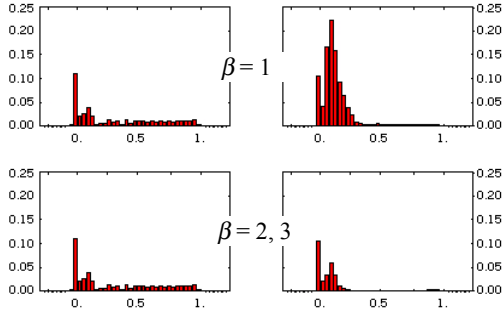


Figure 6: Spectra of oscillations in the bunches of the weak (left) and strong (right) beams after a dipole kick at the first bunch of the strong beam.

the present report. It is easy to see that in this case the beams are split into independent groups of 3 on 3 bunches. Correspondingly, there are three families of the multi-bunch modes: fundamental ( $n = 0$ ) and two intermediate ( $n = 1, 2$ ) with coinciding spectra.

Fig.5 shows the normal modes spectra in flat beams (excited by a proper combination of the dipole kicks) with the intensity ratio  $r_\xi = N_1/N_2 = 0.3$ . The fundamental mode spectra is dominated by the  $\Sigma$ -oscillations at the bare lattice tune ( $\lambda = 0$ ). A remarkable feature of the intermediate modes is a pronounced peak at  $\sim 0.1\xi_x$ ;  $\xi_x$  being the tuneshift in the weak beam. With lower  $r_\xi$  it gets closer to the bare lattice tune.

Fig.6 shows spectra of oscillations in the individual bunches (which are superposition of the normal modes) excited by a dipole kick at the first bunch of the strong beam. The characteristic double-peak structure of the spectrum can be employed in the beam diagnostics.

## 5 BEAM-BEAM COMPENSATION

As can be seen in Fig.5, at the intensity ratio  $r_\xi = 0.3$  there is no trace left of the discrete  $\pi$ -mode; the  $\Sigma$ -mode at  $\sigma_s/\beta_x^* = 1$  is noticeably damped by the synchrotron sidebands of the incoherent tunes.

It is planned, however, to reduce with the help of electron lenses [8] the incoherent tunespread of the antiprotons in Tevatron. Since the electron lenses do not affect the coherent part of the beam-beam interaction

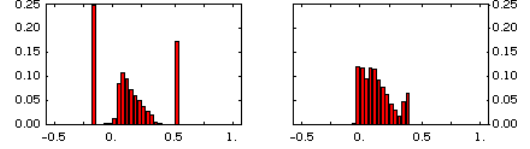


Figure 7: Spectra of the fundamental (left) and intermediate (right) multi-bunch modes with 70% reduction in the weak beam incoherent tunespread.

described by the right hand side of eq.(13), the question arises whether the residual tunespread will be sufficient to damp the coherent modes. Another important issue is how to use the beam-beam spectra for adjustment of the electron lenses.

To get an insight the incoherent tunespread in the weak beam was reduced by 70% to match that in the strong beam. Otherwise the conditions were as those of the previous section. With identical tunespreads the spectra of oscillations in the two beams look the same.

As can be seen in Fig.7, there appear discrete lines in the spectrum of the fundamental multi-bunch mode, well separated from the incoherent tunespread ( $0, r_\xi\xi_x$ ,  $\xi_x$  being the tuneshift without compensation. To insure stability of the discrete modes in the presence of external impedances a large chromaticity may be necessary.

On the other hand, the discrete  $\pi$ -mode can be used for adjustment of the electron lenses by maximizing its intensity.

## 6 SUMMARY

- There is strong damping effect on the coherent beam-beam modes by the overlapping synchrotron sidebands of the incoherent tunes; in long bunches ( $\sigma_s \sim \beta_x^*$ ) of equal intensity it already takes place at  $v_s/\xi_x = 0.15$ .
- In the case of small intensity ratio and two IPs  $2\pi/3$  apart the strong beam spectrum has two peaks: the  $\Sigma$ -mode at the bare lattice tune and the intermediate mode with tune shifted by  $\sim 0.1\xi_x$  at  $r_\xi = 0.3$ .
- Due to compensation of the antiproton incoherent tunespread with the electron lenses the discrete spectral lines can appear even at small intensity ratio.
- To interpret the observations and extract useful information it may be helpful to have an on-line running program computing the beam-beam spectra for the particular collider settings.

## 7 REFERENCES

- [1] K.Yokoya et al., *Particle Accelerators*, 27, 181 (1990)
- [2] J.-P. Kouchouk, private communication.
- [3] Y. Alexahin, LHC Project Report 461 (2001).
- [4] Y. Alexahin, Fermilab-TM-2148 (2001).
- [5] K.Hirata, H.Moshhammer and F.Ruggiero, *Particle Accelerators*, 40, 205 (1993).
- [6] Y.Alexahin, Frascati Physics Series, X, 255 (1998).
- [7] Y.Alexahin, *Particle Accelerators*, 59, 43 (1998).
- [8] V.Shiltsev et al., Phys. Rev. ST-AB 2, 071001 (1999).

# SUMMARY OF THE COHERENT PHENOMENA WORKING GROUP

Joseph T. Rogers, Laboratory of Nuclear Studies, Cornell University, Ithaca, NY 14853, USA  
Mathias Vogt, Department of Mathematics, University of New Mexico, Albuquerque, NM 78131, USA

## Abstract

The coherent phenomena working group considered beam-beam phenomena in which the particles in both beams display collective dynamics. Both direct beam-beam collisions and the long-range beam-beam interaction were considered. Attention was given to the coherent modes and spectra of the beams, particularly because the coherent spectra are accessible to observation and give information about the beam-beam interaction that is otherwise inaccessible. Static equilibrium states of the beam were also considered: closed orbit perturbations due to the long-range beam-beam interaction and the flip-flop effect. Excellent progress is evident in theory, numerical methods, and observations. Recommendations for future for future experimental, simulation, and theoretical work are made.

## 1 OBSERVATIONS AND ISSUES

Coherent beam-beam phenomena include:

- collective modes of oscillations of the colliding beams;
- an associated frequency spectrum of coherent oscillations distinct from the spectrum of incoherent motion of beam particles, leading to a possible loss of Landau damping;
- a self-consistent static equilibrium state, including orbit shifts (in the case of the long-range beam-beam interaction) or flip-flop (for direct collisions).

Each of these phenomena was considered in this working group. Each is an example of a strong-strong phenomenon, in which the dynamics of both beams must be taken into account together.

We attempted to address the points in the workshop charge:

1. Review the present understanding of weak-strong and strong-strong beam-beam phenomena.
2. Critique and future prospects of beam-beam compensation methods.
3. Review the performance limitations due to weak-strong phenomena in Run II of the Tevatron, LHC.
4. Review and critique proposals for experiments at present colliders.
5. Review and critique theoretical strong-strong studies.

The topics considered in the coherent phenomena working group are relevant for points 1, 4, and 5 of the charge.

The theory and observation of the spectrum of coherent oscillations of colliding beams were presented in papers by Y. Alexahin and A. Temnykh. A calculation of the self-consistent closed orbit in the LHC was presented by

W. Herr, and an explanation of the *egure* (flip-flop) effect seen in KEKB was presented by F. Zimmermann.

## 2 SPECTRUM OF COHERENT OSCILLATIONS

### 2.1 Spectrum of coherent oscillations for finite bunch length

Y. Alexahin presented a calculation of the spectrum of coherent transverse oscillations in colliding bunches of finite length [1] with emphasis on Run II of the Tevatron. The Tevatron has specific characteristics that must be accounted for in the coherent beam-beam effect:

- different intensities for  $p$  and  $\bar{p}$ ;
- a split in the lattice tunes for  $p$  and  $\bar{p}$ , due to the helical separation in the sextupoles;
- multibunch modes (from multiple interaction points);
- bunch length;
- large chromaticity; and
- the effect of the electron lens used for beam-beam compensation.

An important point was made: the transverse spectrum of a beam subjected to a single kick is *not* given simply by the distribution in single-particle tunes. In fact, there is the possibility that the Landau damping arising from the spread in single-particle tunes may be completely lost under some conditions.

Alexahin found that Landau damping is indeed lost for equal tunes when the ratio of intensities  $r > 0.6$ . Also, he found that both beams were involved in the coupled oscillation even for  $r = 0.3$ . That is, one must model the beam-beam interaction as strong-strong even if the two beams have quite different intensities. As the lattice tune split is varied with  $r = 0.3$ , Landau damping can be made to disappear.

The conclusion is that the ability to interpret the experimental coherent beam-beam spectrum depends on a model which includes the lattice tune split, the intensity ratio, the synchrotron tune, and chromaticity.

### 2.2 Coherent spectrum and particle density in tune space

A. Temnykh presented a calculation of the particle density distribution in transverse tune space  $N(Q_x, Q_y)$  which was then used to determine the spectrum of coherent transverse oscillations [2]. The goal of this study is to use the coherent spectrum as seen in the control room to gain information about  $N(Q_x, Q_y)$ . Features in  $N(Q_x, Q_y)$  (e.g., tails) can then be used to diagnose effects such as a displacement of the minimum

in beta from the interaction point or the effect of the long-range beam-beam interaction.

For beams which are longer than  $\beta^*$ , the longitudinal tails of the bunch see stronger focusing than the longitudinal core, since they interact with the other beam at locations with (on the average) a higher  $\beta$ . For flat beams in electron machines,  $\beta_x^* \gg \beta_y^* \approx \sigma_z$ , so  $N(Q_x, Q_y)$  has much larger tails in  $Q_y$  than in  $Q_x$ . The sharp edge in the horizontal tune distribution gives a spike in the spectrum of horizontal coherent oscillations, but the smoother vertical tune distribution does not produce a spike in the vertical coherent spectrum. This behavior is confirmed by spectrum analyzer measurements. A spike is observed only in the horizontal spectrum.

A practical outcome from this study was a set of recommendations for the CESR operators:

- Use the  $x$ - $y$  coupling “knob” to increase the coherent signal seen on the spectrum analyzer at the high end of the spectrum (to increase the beam-beam parameter).
- Use the  $\beta^*$  and  $\beta^*$ -location knobs to decrease the high frequency tails seen on the spectrum analyzer (to decrease the excessive focusing of longitudinal tails).

These recommendations have been a practical aid in luminosity tuning.

### 2.3 Phase-amplitude beam-beam transfer function

A. Temnykh also presented a simple model and observations from CESR of the complex (phase-amplitude) transfer function for colliding beams [3]. In the model and the observations, one beam is shaken, and the phase and amplitude of both the shaken beam and the counter-rotating beam are measured.

The model is of two rigid bunches interacting via a linear beam-beam force. The difference in transfer function phase in going from low to high frequency is  $\pi$  when measuring the shaken beam and  $2\pi$ , when measuring the counter-rotating beam.

In measurements of the vertical transfer function in CESR, the phase shifts of  $\pi$  and  $2\pi$  were observed, in accordance with the rigid-bunch model.

## 3 CLOSED ORBIT WITH LONG RANGE BEAM-BEAM INTERACTION

W. Herr presented a calculation of the closed orbits of individual bunches in the LHC [4]. The orbits are perturbed by the long-range beam-beam interaction near each interaction point. Because the LHC bunch pattern is unsymmetrical (due to gaps for the injection, extraction, and dump kickers), each bunch experiences a different perturbation. Each bunch interacts with approximately 120 counter-rotating bunches, and the size of the orbit perturbation can become large—of the order of the bunch width. All 2808 bunches are coupled together.

Because the orbit perturbation is so large, the source of the perturbation cannot be considered fixed. It is necessary to find the self-consistent closed orbits in which both beams are perturbed. The self-consistent orbit was found using an iterative procedure. A significant result is that this procedure always converges, which was not known *a priori*. This procedure was also used to find tunes and chromaticities, and was valuable in preparing input for weak-strong particle tracking. This technique was used to evaluate the LHC filling pattern and to determine the sensitivity to bunch-to-bunch intensity variations.

## 4 FLIP-FLOP INSTABILITY

F. Zimmermann presented a description of the *egure* (flip-flop) instability of the colliding beams in KEKB, and a theoretical analysis that explains this effect [5]. A sudden step-like change in the horizontal beam sizes in KEKB is sometimes observed during “aggressive” tuning of the horizontal beam offset. The low energy ring (LER)  $\sigma_x^*$  (beam size at the interaction point) increases as the high energy ring (HER)  $\sigma_x^*$  decreases.

A simple weak-strong calculation of the dynamic beta effect shows that the horizontal beta at the interaction point  $\beta_x^*$  is decreased by a factor of 2.40 in the HER and 4.78 in the LER relative to the lattice  $\beta_x^*$ . This strong dynamic beta effect occurs because the horizontal tune is so close to a half-integer value:  $Q_x = 44.520$  (HER) and 45.505 (LER), but does not explain the observed flip-flop. A self-consistent (strong-strong) calculation of the dynamic beta effect, assuming unperturbed emittances, was found to have only one solution. Multiple solutions are required to explain the existence of the normal and flip-flop states.

The emittance is, however, perturbed by the dynamic beta effect, because  $\beta$  is perturbed in the arcs of the machine as well as at the interaction point. For head-on collisions, there is still only one self-consistent solution for the dynamic beta effect including emittance perturbations. When the beams are given a relative horizontal offset so that the horizontal beam-beam force is defocusing, three solutions appear: one with nearly equal beam sizes and two flip-flop states. This result is consistent with the observation in KEKB that the flip-flop state occurs when the beams get a large relative horizontal offset.

## 5 FUTURE WORK

### 5.1 Experiments

There is very little experimental work to date on the strong-strong aspects of the long-range beam-beam interaction. To verify the self-consistent closed orbit calculations, one might deliberately vary the bunch filling pattern and create nonuniformities in bunch intensities at RHIC or at the Tevatron. One would then monitor the bunch position, tunes, and chromaticities.

Observations of the coherent spectrum of transverse oscillations in hadron machines are needed to examine the conditions for loss of Landau damping. These would be useful for understanding the coherent beam-beam interaction in general, but particular attention should be paid to the characteristics of the Run II Tevatron. In the Tevatron the constraint of using a single beam chamber leads to a difference in beam intensities (due to the use of  $p$  and  $\bar{p}$ ) and bare tunes (due to the helical separation in the sextupoles). Both RHIC and the Tevatron would be suitable for these studies. One would excite coherent modes by single kick and:

- vary the split in the bare tunes;
- vary the beam intensities independently; and
- vary the chromaticity, crossing angles, and strength of non-linearities (*e.g.*, IR sextupoles).

The mechanism proposed by F. Zimmermann to explain the flip-flop effect in KEKB should apply to other radiation-damped machines as well. Experiments could be performed in PEP-II, DAFNE, CESR, or other  $e^+e^-$  colliders in which the beams are intentionally horizontally mis-steered to verify the conditions for flip-flop.

## 5.2 Simulations

The theory and observations presented in this working group indicates that the coherent beam-beam interaction and the spectrum of coherent oscillations many machine parameters. Thus, particle-tracking simulations should:

- have the best possible resolution of the phase space densities or their projections or higher order moments;
- track for a large number of turns, and must be optimized for speed;
- include six-dimensional dynamics;
- include impedances;
- include non-linearities;
- include closed orbit perturbations;
- include feedback; and
- be carefully benchmarked against experiment.

Calculations of the coherent beam-beam spectrum and transfer function based on macroparticle models, and observations of the spectrum and transfer function, should be compared with particle-tracking simulations.

## 5.3 Theory

Theoretical models beyond the linearized Vlasov equation might be developed to help deepen our understanding of the beam-beam interaction.

The model used by F. Zimmermann to explain the existence of flip-flop states in KEKB is linearized and considers only horizontal displacements at the IP, but might be extended to include vertical displacements, crossing angles, bunch length effects, and a nonlinear beam-beam force.

## 6 REFERENCES

- [1] Y. Alexahin, “(Notes on the) Spectra of Coherent Transverse Oscillations in Colliding Bunches of Finite Length”, these proceedings.
- [2] A. Temnykh, “Modeling of the 2D particle density distribution function in tune space resulted from beam-beam interaction”, these proceedings.
- [3] A. Temnykh, “Study of phase - amplitude characteristics of colliding beams spectrum”, these proceedings.
- [4] H. Grote and W. Herr, “Self-consistent closed orbit caused by beam-beam effects in the LHC”, [http://wwwslap.cern.ch/collective/zwe/lhcbb/talks\\_beambeam.html](http://wwwslap.cern.ch/collective/zwe/lhcbb/talks_beambeam.html).
- [5] F. Zimmermann, “Beam sizes in collision and flip-flop states for KEKB”, these proceedings.

## **SECTION V: Theory and simulations of Strong-strong interactions**

# Integral Equation for the Equilibrium State of Colliding Electron Beams \*

R.L. Warnock, SLAC, Stanford, CA 94309  
J.A. Ellison, University of New Mexico, Albuquerque, NM 87131

## Abstract

We study a nonlinear integral equation for the equilibrium phase distribution of stored colliding electron beams. It is analogous to the Haissinski equation, being derived from Vlasov-Fokker-Planck theory, but is quite different in form. We prove existence of a unique solution, thus the existence of a unique equilibrium state, for sufficiently small current. This is done for the Chao-Ruth model of the beam-beam interaction in one degree of freedom. We expect no difficulty in generalizing the argument to more realistic models.

## 1 INTRODUCTION

In the theory of stability of stored beams a primary step should be the study of equilibrium states, expected at low current. An equilibrium state should become unstable at some threshold in current, but in order to compute the threshold we must linearize the kinetic equation (Vlasov or Vlasov-Fokker-Planck) about the equilibrium phase space distribution. Historically, investigators have often been lazy about this point, linearizing the Vlasov equation about some state that might be at best a rough approximation to an equilibrium. This may be excused by the fact that determination of the equilibrium is a nonlinear problem, in general rather difficult.

There is one case in which there is a widely known theory of equilibrium that makes some contact with experiment; namely, the case of longitudinal motion of a single stored electron beam subject to a wake field [1, 2]. The theory is based on a model in which the exact longitudinal wake field is replaced by its average over one turn. The averaged wake of course depends only on the distance between source and test particles, not on the position in the ring. With such a wake one may seek a time-independent, factorized solution of the Vlasov-Fokker-Planck (VFP) equation; namely, a product of a Gaussian in the canonical momentum  $p$  (proportional to the energy deviation) and the charge density  $\rho(q)$ , where  $q$  is the canonical coordinate (proportional to the distance from the synchronous particle). The equation is satisfied by such a factorized form, provided that the charge density satisfies the Haissinski equation [1], a nonlinear integral equation. If the wake field satisfies a mild restriction, it is not difficult to prove that the equation has a unique solution in a large function space  $\mathcal{S}$ , at sufficiently small current. The corresponding solution of the VFP equation is the unique, small-

current solution satisfying the principle of detailed balance (with  $\rho \in \mathcal{S}$ ).

There are many ways in which this prototype theory of equilibrium might be extended. For instance, one might include multi-bunch beams, long-range wakes from cavity resonators or resistive walls, nonlinear r.f., proton beams with non-Gaussian distribution in  $p$ , localized wakes not averaged over azimuth. Here we are interested in two counter-rotating beams in collision. In mathematical aspects the problem has similarities to the case of a single beam with localized wake contributions.

The beam-beam collision gives a large transverse force that substantially modifies the beams at every collision. Consequently, the equilibrium state, if any, cannot be time-independent. Rather, it must be defined as a phase space distribution that is periodic in azimuthal position  $s$ . As a zeroth approximation, one could smear out the localized beam-beam kick, distributing it over a full turn. This has been done in linear stability studies [3]. Here we wish to avoid such a step, accounting fully for the localization. It then follows that we cannot deal with a factorized distribution. We must expect the equilibrium equation to be an integral equation for functions on phase space, not just on coordinate space as in the Haissinski case. We derive and analyze the simplest instance of such an equation, retaining the full nonlinearity of the beam-beam force.

Some background to the present study is found in a recent paper [4]. There we made an analytic study of equilibria by linearizing the beam-beam force, but retaining the quadratic nonlinearity of the Vlasov equation. We also carried out a numerical integration of the nonlinear VFP system. Here we adopt the notation and equations of motion as given in Ref. [4].

## 2 FORMULATION OF THE PROBLEM

We treat vertical transverse motion with normalized phase-space variables  $(q, p)$  defined in terms of the lattice function  $\beta(s)$  and emittance  $\epsilon$  as

$$q = y(\beta\epsilon)^{-1/2}, \quad p = (\beta y' - \beta' y/2)(\beta\epsilon)^{-1/2}, \quad (1)$$

where  $y$  is the vertical displacement and the prime denotes  $d/ds$ . The Hamiltonian of motion unperturbed by the beam-beam interaction is  $H = (p^2 + q^2)/2$  and the independent “time” variable of Hamilton’s equations is the phase advance  $\theta = \int_0^s du/\beta(u)$ . We distinguish the two beams by superscripts (1), (2).

The Chao-Ruth model [5] is intended to represent flat beams, with large  $x : y$  aspect ratio. The force on a particle

\* Work supported in part by Department of Energy contracts DE-FG03-99ER41104 and DE-AC03-76SF00515.



in beam (1) is approximated as though it came from infinite uniform planes of charge perpendicular to the  $y$ -axis, distributed with a density  $\rho^{(2)}(y)$ . This force is concentrated in time, however, at the instant of collision. The resulting kernel function for the beam-beam force is proportional to  $\text{sgn}(q - q')$ , where  $\text{sgn}(x)$  is the signum function, equal to 1 for  $x > 0$  and  $-1$  for  $x < 0$ . For simplicity in notation we take the two beams to have equal properties (tune, energy, bunch height and width,  $\beta^*$ , damping time). The mathematical argument would be the essentially the same with unequal beam properties. The formal Vlasov-Fokker-Planck system is

$$\begin{aligned} & \frac{\partial f^{(1)}}{\partial \theta} + p \frac{\partial f^{(1)}}{\partial q} - \left[ q + (2\pi)^{3/2} \xi \sum_n \delta(\theta - 2\pi n) \right. \\ & \cdot \left. \int_{-\infty}^{\infty} \text{sgn}(q - q') \int_{-\infty}^{\infty} f^{(2)}(q', p', \theta) dq' dp' \right] \frac{\partial f^{(1)}}{\partial p} \\ & = 2\alpha \frac{\partial}{\partial p} \left[ p f^{(1)} + \frac{\partial f^{(1)}}{\partial p} \right], \quad (\text{and } 1 \leftrightarrow 2), \end{aligned} \quad (2)$$

where the distribution function for beam ( $i$ ) is  $f^{(i)}(q, p, \theta)$ , the vertical betatron tune is  $\nu$ , and the beam-beam parameter is  $\xi = N\beta^* r_e / ((2\pi)^{1/2} \gamma \sigma_y L_x)$ . Here  $\beta^*$  is the beta function at the IP,  $r_e = e^2 / (4\pi\epsilon_0 mc^2)$  is the classical electron radius,  $\gamma$  is the Lorentz factor,  $L_x$  is the bunch width, and  $\sigma_y = (\beta^* \epsilon)^{1/2}$  is the bunch height. The right hand side of (2) is the Fokker-Planck contribution, with damping constant  $\alpha = 1/(2\pi\nu n_d)$ , where  $n_d$  is the number of turns in a damping time. Our phase space coordinates have been defined so that the damping and diffusion constants are equal.

Equation (2) has only a formal significance, since the  $\theta$ -dependent factors multiplying the delta function actually change discontinuously at the IP where the delta function acts. Consequently, we cannot say how to evaluate those factors without further analysis. Actually, the correct change of the distribution function at the IP is easy to see. Let  $f^{(1)}(q, p, 0-)$  and  $f^{(1)}(q, p, 0+)$  represent the distributions just before and just after  $\theta = 0 \pmod{2\pi\nu}$ . Then by the usual argument from probability conservation [2] the distribution is changed by the inverse of the kick map; i.e., by the Perron-Frobenius operator for that map:

$$f^{(1)}(q, p, 0+) = f^{(1)}(q, p - F(q, 0-), 0-), \quad (3)$$

where

$$F(q, 0-) = -(2\pi)^{3/2} \xi \int \text{sgn}(q - q') f^{(2)}(q', p', 0-) dq' dp'. \quad (4)$$

For propagation of the distribution function between IP kicks, we have in (2) a linear Fokker-Planck equation with harmonic force. The propagator or fundamental solution of that equation is known [6], namely a function  $\Phi(z, z', \theta)$ ,  $z = (z_1, z_2) = (q, p)$  such that for any initial distribution  $f(z, 0)$  the solution at time  $\theta$  is

$$f(z, \theta) = \int \Phi(z, z', \theta) f(z', 0) dz'. \quad (5)$$

There are several equivalent representations of  $\Phi$ . The following form, which was derived from a probabilistic argument, is especially convenient for our work:

$$\begin{aligned} \Phi(z, z', \theta) &= \frac{1}{2\pi(\det \Sigma)^{1/2}} \exp \left[ - (z - e^{A\theta} z')^T \Sigma^{-1} (z - e^{A\theta} z') / 2 \right], \\ \Sigma &= I - e^{A\theta} e^{A^T \theta}. \end{aligned} \quad (6)$$

Here  $T$  denotes transposition and  $e^{A\theta}$  is the transfer matrix for the single-particle harmonic motion with damping. With damping constant  $\alpha$  we have

$$\begin{aligned} e^{A\theta} &= e^{-\alpha\theta} \begin{pmatrix} a_+ & b \\ -b & a_- \end{pmatrix}, \\ a_{\pm} &= \cos \Omega\theta \pm (\alpha/\Omega) \sin \Omega\theta, \quad b = (1/\Omega) \sin \Omega\theta \\ \Omega &= (1 - \alpha^2)^{1/2}, \quad \det(e^{A\theta}) = e^{-2\alpha\theta}. \end{aligned} \quad (7)$$

Let  $\Phi$  denote the operator corresponding to the kernel  $\Phi(z, z', \theta)$  in (5). The action of  $\Phi$  has a simple expression in Fourier space. Writing  $\hat{h}$  for the Fourier transform of  $h$ , we have

$$\widehat{\Phi h}(v) = \exp[-v^T e^{A\theta} \Sigma e^{A^T \theta} v / 2] \hat{h}(e^{A^T \theta} v). \quad (8)$$

We can now set down a system of integral equations for the equilibrium distribution. The equations are for the distributions evaluated just *after* the IP,  $f^{(i)}(z, 0+)$ . Henceforth we suppress the time specification  $0+$ . Starting with  $f = (f^{(1)}, f^{(2)})$ , we propagate one turn by (5) with  $\theta = 2\pi\nu$ , and then apply the beam-beam kicks according to (3). For equilibrium (periodicity), the result must be the starting  $f$ . To state this in equations we first define the linear operator  $\mathbf{L}$  by

$$\mathbf{L}f(q) = (2\pi)^{3/2} \int \int \text{sgn}(q - q') K(z'|z'') f(z'') dz' dz'', \quad (9)$$

where  $K$  is the Fokker-Planck propagator for one turn,

$$K(z|z') = \Phi(z, z', 2\pi\nu). \quad (10)$$

The integral equations take the form

$$f^{(i)}(z) = \int K(q, p + \xi \mathbf{L}f^{(j)}(q) | z') f^{(i)}(z') dz', \quad i \neq j, \quad i, j = 1, 2, \quad (11)$$

with

$$\int f^{(i)}(z) dz = 1. \quad (12)$$

It is essential that the normalization constraint (12) be regarded as part of the definition of the mathematical system; otherwise in Eqs.(11) there is nothing to set the scale of the beam-beam force. We choose to build in the constraint by redefining the integral equations, dividing the right hand side of (11) by  $\int f^{(i)}(z) dz$ . Then, since  $\int K(z|z') dz = 1$ ,

any solution of the modified equation will automatically satisfy (12). Finally we multiply by  $\int f^{(i)}(z)dz$  and rearrange to state the pair of equations as

$$G(f, \xi) = 0, \quad (13)$$

where  $G = (G^{(1)}, G^{(2)})$  with

$$\begin{aligned} G^{(i)}(f, \xi)(z) &= f^{(i)}(z) \int f^{(i)}(z') dz' \\ &- \int K(q, p + \xi \mathbf{L} f^{(j)}(q) | z') f^{(i)}(z') dz', \quad i \neq j. \end{aligned} \quad (14)$$

We know the solution of (13) at  $\xi = 0$ ; it is the Gaussian equilibrium in the absence of beam-beam force,

$$\begin{aligned} G(f_0, 0) &= 0, \quad f_0 = (f_0^{(1)}, f_0^{(2)}), \\ f_0^{(i)} &= \frac{1}{2\pi} \exp\left(-\frac{1}{2}(q^2 + p^2)\right). \end{aligned} \quad (15)$$

We apply the implicit function theorem to prove that this solution can be continued in a unique way to a solution  $f(\xi)$  of (13) for small  $\xi \neq 0$ . This requires an implicit function theorem in an infinite-dimensional function space. Let us first recall the intuitive basis of the theorem in finitely many dimensions, so that (13) represents  $n$  real (generally nonlinear) equations in  $n$  unknowns  $f_j$ ,  $j = 1, \dots, n$ . We wish to solve for the  $f_j$  as a function of the parameter  $\xi$ , supposing that a solution  $f_{0j}$  for  $\xi = 0$  is known. Supposing that  $G$  is smooth, we can expand it by Taylor's formula with remainder  $R$  about the point  $(f_0, 0)$ :

$$G(f, \xi) = G_f(f_0, 0)(f - f_0) + G_\xi(f_0, 0)\xi + R(f, \xi) = 0. \quad (16)$$

If the Jacobian matrix  $G_f = \{\partial G_i / \partial f_j\}$  is non-singular at the expansion point, and the nonlinear remainder  $R$  is small, an approximate solution of our problem is

$$f(\xi) \approx f_0 - G_f(f_0, 0)^{-1} G_\xi(f_0, 0)\xi. \quad (17)$$

The implicit function theorem takes into account the nonlinear term, and assures us that for sufficiently small  $\xi$  there will be a unique exact solution of (13) close to the approximation (17). The Jacobian is required to be nonsingular *only* at the single point  $(f_0, 0)$ .

In the infinite-dimensional case we must first decide on the arena of the discussion: in what space of functions do we seek a solution of (13)? Physicists are usually familiar with Hilbert space, but here we can get by with a simpler notion, a Banach space. Like the Hilbert space, it is a complete linear space with a norm, but is not required to have a scalar product. For instance, the set of all continuous functions  $f(x)$  on the unit interval  $[0, 1]$  is a Banach space if the norm is defined as  $\|f\| = \max_{[0,1]} |f(x)|$ . Secondly, we must give a meaning to the Jacobian  $G_f$  when  $f$  is a function rather than a finite-dimensional vector. A simple possibility is the Fréchet derivative, which for a function

$G(f)$  on a Banach space is defined at  $f_0$  as a linear operator  $G_f(f_0)$  such that

$$\lim_{\|h\| \rightarrow 0} \frac{1}{\|h\|} \|G(f_0 + h) - G(f_0) - G_f(f_0)h\| = 0. \quad (18)$$

We are now ready to state the implicit function theorem in Banach space, in a form sufficiently general for our purposes (but hardly the most general).

**Theorem:** Let  $B$  be a Banach space, and suppose that  $G$  is a continuously differentiable mapping (operator) of  $B \times I$  into  $B$ , where  $I = (-\Delta\xi, \Delta\xi)$  is an open interval, the domain of  $\xi$ . The continuous differentiability implies that the partial (Fréchet) derivatives  $G_f(f, \xi)$ ,  $G_\xi(f, \xi)$  exist and are continuous in  $B \times I$ . Let  $f_0 \in B$  be a solution of  $G(f_0, 0) = 0$ , and suppose that  $G_f(f_0, 0)$  is a continuous linear map of  $B$  onto  $B$  with a continuous inverse. Then there exists a unique solution  $f(\xi)$  of  $G(f, \xi) = 0$  such that  $f(0) = f_0$ , for  $\xi$  in some interval  $I_0 = (-\delta\xi, \delta\xi) \subset I$ ,  $\delta\xi \neq 0$ . Moreover, for  $\xi \in I_0$  this solution has a continuous derivative with respect to  $\xi$  and  $(G_f(f(\xi), \xi))^{-1}$  exists. The derivative is given by  $f'(\xi) = -(G_f(f(\xi), \xi))^{-1} G_\xi(f(\xi), \xi)$ .

The theorem alone does not give us an estimate of the size of the interval  $I_0$  in which the solution exists. In specific cases analytic estimates can be made, but they may be pessimistic. In our problem, we mainly seek assurance that an equilibrium exists for sufficiently small current. We shall have to rely on numerical calculations to determine a maximum interval of existence. Calling on experience with the Haïssinski equilibrium, we expect that as the current is increased the equilibrium will become unstable long before it ceases to exist.

To apply the implicit function theorem to (13), a crucial matter is to find a suitable space  $B$ . As is usual in applications of functional analysis, this requires some experimentation. The space has to be tailored to fit the properties of the operator. A primary requirement is that  $B \times I$  be mapped into  $B$ , and that is relatively easy to check for some candidates for  $B$ . Further requirements such as invertibility of  $G_f(f_0, 0)$  may be harder to verify, and lead us to refine the choice, perhaps taking a subspace of an initial candidate for  $B$ .

After various estimates of integrals we find that a suitable  $B$  consists of all pairs  $f = (f^{(1)}, f^{(2)})$  of continuous functions on the phase space  $\mathbb{R}^2$  such that the following expression, identified as the norm, is finite:

$$\|f\| = \max_i \sup_{z \in \mathbb{R}^2} |(1 + \|z\|^{2a}) f^{(i)}(z)|, \quad a > 2, \quad (19)$$

where  $\|z\| = (z_1^2 + z_2^2)^{1/2}$  and  $\sup$  (supremum) denotes the least upper bound. This is a "big" space, in the sense that it contains functions with slow, polynomial decrease at

infinity, whereas intuition and the results of Ref.[4] indicate that the actual decrease of the solution is close to Gaussian. The advantage of a big space is that our assertion of uniqueness of the solution means uniqueness in a bigger universe. The disadvantage is that our resulting theorem will give no close information on the actual fall-off of the solution, since it merely asserts that the solution is in  $B$ . We did not succeed in finding a space with Gaussian fall-off, mapped into itself by  $G$ .

### 3 SOME HIGHLIGHTS OF THE PROOF

Here we give a few main points of the proof, deferring full details to a future report. We have to verify the three main hypotheses of the implicit function theorem, namely

1.  $G : B \times I \rightarrow B$
2.  $G_f, G_\xi$  exist and are continuous in  $B \times I$
3.  $G_f(f_0, 0)^{-1}$  exists and is continuous

Suppose that  $f \in B$ . Then its Fourier transform  $\hat{f}$  exists and is bounded. By (8) one then sees that every derivative of  $\mathbf{K}f(z) = \int K(z|y)f(y)dy$  exists and is bounded, being the Fourier transform of an absolutely integrable function. For estimates of the action of  $\mathbf{K}$  on  $f$  we can prove the lemma

$$\left| \frac{\partial^{m+n}}{\partial z_1^m \partial z_2^n} \int \frac{K(z|y)dy}{1 + \|y\|^{2a}} \right| \leq \frac{M_{mn}}{1 + \|z\|^{2a}}, \quad (20)$$

for any  $m \geq 0, n \geq 0$ , where the constant  $M_{mn}$  depends on  $a$  and the parameters defining  $K$ . Using these results one verifies that hypothesis (1) holds.

To check (2) for  $G_f$ , we compute the formal variational derivative of  $G$ , applied to a variation  $h \in B$ . That is a linear integral operator  $\mathcal{L}$  applied to  $h$ . Then some work with the lemma and the mean-value theorem shows that  $\mathcal{L}$  is indeed the Fréchet derivative. In fact, the numerator under the limit in (18) is  $\mathcal{O}(\|h\|^2)$  if  $G_f = \mathcal{L}$ .

The hardest part of the proof is verifying item (3). In textbook examples it is usual to suppose that  $G_f - 1$  is a compact operator, in which case one can apply Fredholm theory to discuss existence of  $G_f^{-1}$ . In the present case this operator appears to be non-compact, and we have to resort to a more subtle method. We get the inverse by proving uniform convergence of an operator power series development, and the convergence is at a slow rate determined by the damping constant. Thus, the proof fails for a proton system with no damping, and it does not seem at all likely that one could get a proof for zero damping by somehow taking a limit.

Since the power series method is interesting and novel, we give a few details. We have to show that the equation

$$G_f(f_0, 0)x = y \quad (21)$$

has a unique solution  $x \in B$  for any  $y \in B$ . At zero current  $G_f$  breaks into two identical and independent blocks for the

two beams. Then (21) for one block takes the form

$$x(z) + f_0(z) \int x(z')dz' - \mathbf{K}x(z) = y(z), \quad (22)$$

where now  $x$  and  $y$  are single functions, not pairs. We discuss (22) in the space  $B_1$ , which is defined in the same way as  $B$ , except that it consists of single functions; i.e.,  $B = B_1 \times B_1$ . For any  $x \in B_1$ ,

$$\int \mathbf{K}x(z)dz = \int x(z)dz, \quad (23)$$

from which it follows that any solution of (22) must satisfy

$$\int x(z)dz = \int y(z)dz. \quad (24)$$

Consequently, any solution of (22) must also be a solution of

$$x(z) - \mathbf{K}x(z) = p(z), \quad (25)$$

$$p(z) = y(z) - f_0(z) \int y(z')dz', \quad \int p(z)dz = 0.$$

We look for solutions of (22) among the solutions of (25). Iterating (25)  $n - 1$  times we find

$$x = \mathbf{K}^n x + \sum_{m=1}^{n-1} \mathbf{K}^m p + p. \quad (26)$$

Here the story is different from the familiar case of the Neumann series, since the term  $\mathbf{K}^n x$  does not vanish in the limit of large  $n$ . By the semigroup property of the linear Fokker-Planck evolution, the kernel of  $\mathbf{K}^n$  is given by (6) with  $\theta = 2\pi n\nu$ . If  $x \in B_1$  the integral defining  $\mathbf{K}^n x$  converges uniformly in  $n$ , since the integrand is majorized by  $|x(z')|$  and  $\int |x(z)|dz < \infty$ . We may then take the limit under the integral to obtain

$$\lim_{n \rightarrow \infty} \mathbf{K}^n x(z) = f_0(z) \int x(z)dz. \quad (27)$$

Thus, from (26) a solution of (25) in  $B_1$  is expected to have the form

$$x = f_0 \int x(z')dz' + \sum_{m=1}^{\infty} \mathbf{K}^m p + y - f_0 \int y(z')dz'. \quad (28)$$

A candidate for a solution of (22) must satisfy (24), so that from (28) the unique candidate is

$$x(z) = \sum_{m=1}^{\infty} \mathbf{K}^m p(z) + y(z). \quad (29)$$

We are now faced with a delicate step of the proof, to show that for any  $y \in B_1$  the series in (29) converges and represents an element of  $B_1$ . Once that it is done, it is easy to check that (29) represents a solution of (22), unique in  $B_1$ .

To estimate the  $\mathbf{K}^n p$  we formally subtract  $\exp(-z^T z/2) \int p(z')dz'$ , which is zero, and then do

some analysis with the mean value theorem to get the following bound:

$$\begin{aligned}
I_n &= \left| 2\pi(\det \Sigma_n)^{1/2} \mathbf{K}^n p(z) \right| \\
&= \left| \int \left[ \exp[-(z - e^{n\theta A} z')^T (z - e^{n\theta A} z')/2] \right. \right. \\
&\quad \left. \left. - \exp[-z^T z/2] \right] p(z') dz' \right| \\
&\leq \frac{M(1 - \exp(-z^T z/2))}{z^T z} (1 + \|z\|) e^{-n\theta\alpha}, \\
&\quad \theta = 2\pi\nu, \tag{30}
\end{aligned}$$

where  $\alpha$  is the damping constant. (We write  $M$  for a generic constant in majorizations. In any statement  $M$  may have a value larger than in any previous statement.) Now (30) is enough to show uniform convergence (in the maximum norm) of the series in (29) over any finite ball  $\|z\| < r$ , but not enough to show that the sum of the series belongs to  $B_1$ . To complete the job we get a bound by a different method which fails at small  $\|z\|$  but works for  $\|z\| > r$ . For that we break the integral in (30) into two parts, one for  $\|\exp(n\theta A)z'\| < b\|z\|$  and the other for  $\|\exp(n\theta A)z'\| > b\|z\|$ , with  $0 < b < 1$ . In the second region the coefficient of  $p(z')$  is not small, and we have to rely wholly on the fall-off of  $p(z')$ . Using appropriate estimates for the two regions (and supposing  $\alpha < 1/2$ , which is more than safe for real machines) we find

$$I_n \leq \frac{M}{1 + \|z\|^{2a}} e^{-n\theta\alpha}, \quad \|z\| > r. \tag{31}$$

Combining (30) and (31) we have for all  $z$  that

$$|\mathbf{K}^n p(z)| \leq \frac{M}{1 + \|z\|^{2a}} e^{-n\theta\alpha}, \tag{32}$$

from which it follows that  $x$  as given in (29) exists and belongs to  $B_1$ . Furthermore, this function satisfies the original equation (22):

$$\begin{aligned}
&\sum_{m=1}^{\infty} \mathbf{K}^m p + y + f_0 \int \left[ \sum_{m=1}^{\infty} \mathbf{K}^m p(z') + y(z') \right] dz' \\
&- \sum_{m=2}^{\infty} \mathbf{K}^m p - \mathbf{K}y = y \tag{33}
\end{aligned}$$

since we know that  $\mathbf{K}f_0 = f_0$  and  $\int \sum_{m=1}^{\infty} \mathbf{K}^m p(z) dz = \sum_{m=1}^{\infty} \int \mathbf{K}^m p(z) dz = \sum_{m=1}^{\infty} \int p(z) dz = 0$ , the reversal of sum and integral in the latter being justified by (32).

To prove that the solution is unique, suppose that there were two solutions  $x_1, x_2$  in  $B_1$ . Then  $x = x_1 - x_2$  satisfies (22) with  $y = 0$ , from which it follows that  $\int x(z) dz = 0$ , hence  $x - \mathbf{K}x = 0$ . Iterating the latter equation, we have  $x = \mathbf{K}^n x = \lim_{n \rightarrow \infty} \mathbf{K}^n x = f_0 \int x(z) dz = 0$ . Finally, the continuity of  $G_f(f_0, 0)^{-1}$  is clear, since a small change in  $y$  evidently produces a small change in  $x$ .

## 4 CONCLUSION

We have sketched the proof that there is a unique solution to the Vlasov-Fokker-Planck system for the Chao-Ruth model of colliding electron beams at sufficiently small current. The details of the various estimates involved will be given in a longer report. We are fairly confident that the proof will go through in almost the same way for other models in one degree of freedom [3] and for the model in two degrees of freedom in which the force is obtained from the two-dimensional Poisson equation. The case of protons, without radiation damping, is an entirely different story. One expects infinitely many approximate equilibria [4, 7], but the question of exact equilibria is open.

## 5 REFERENCES

- [1] J. Haïssinski, *Nuovo Cimento* **18 B**, 72 (1973)
- [2] R. L. Warnock and J. A. Ellison, *Proc. 2nd ICFA Advanced Accelerator Workshop on the Physics of High Brightness Beams, UCLA, November 9-12, 1999* (World Scientific, Singapore, 2001); also available as SLAC-PUB-8494.
- [3] K. Yokoya and H. Koiso, *Particle Accelerators* **27**, 181-186 (1990); P. Zenkevich and K. Yokoya, *ibid.* **40**, 229-241 (1997)
- [4] J. A. Ellison and R. L. Warnock, *Proc. 18th Advanced ICFA Beam Dynamics Workshop on Quantum Aspects of Beam Physics, Capri, Italy, October 15-20, 2000*, to be published by World Scientific, Singapore; also available as SLAC-PUB-8778.
- [5] A. Chao and R. D. Ruth, *Particle Accelerators* **16** 201-216 (1985).
- [6] S. Chandrasekhar, *Rev. Mod. Phys* **15**, 1-91 (1943), reprinted in *Selected Papers on Noise and Stochastic Processes*, N. Wax, Ed. (Dover, New York, 1954).
- [7] J. A. Ellison and M. Vogt, *An Averaged Vlasov Equation for the Strong-Strong Beam-Beam*, these proceedings.

# An Averaged Vlasov Equation for the Strong–Strong Beam–Beam

J. A. Ellison, M. Vogt, UNM, Albuquerque, NM 87131, USA

## Abstract

The Strong–Strong Beam–Beam is studied in the framework of maps with a “Kick–Rotate” model. The classical method of averaging is applied to derive an approximate map which is equivalent to a flow within the averaging approximation. This flow leads to an averaged Vlasov equation (AVE); the basic model of this paper. The power of this approach is evidenced by the fact that the AVE has exact equilibria and the associated linearized equations have uncoupled azimuthal Fourier modes. In the usual way, the Fourier mode equations lead to a Fredholm integral equation of the third kind. We have solved this numerically in a special case, found the  $\sigma$  and  $\pi$  mode frequencies and they are in excellent agreement with simulation.

## 1 INTRODUCTION

In this paper we introduce a new approximate model for the strong–strong beam–beam interaction. This both generalizes and simplifies the work of [1, 2, 3] on the strong–strong beam–beam interaction in high energy colliders. Our model is based on the classical method of averaging generalized to maps and collective forces and leads to an averaged Vlasov equation (AVE). The previous pioneering works make several assumptions and approximations which are difficult to assess mathematically. Here we make only one assumption, we assume that the classical method of averaging is valid for this problem. We do not introduce a delta function into the Vlasov equations of motion, which is ambiguous because the density is discontinuous at the point of the delta function. Thus we have no need to smooth the delta function, an approximation, the nature of which is hard to assess. The technique we introduce should be of general interest to studies of the Vlasov equation with a perturbative collective force.

To motivate the method of averaging for maps with a collective force we review our approach to rigorous averaging theory in Section 2. In Section 3, we discuss our basic model, the kick-rotate model. We transform the basic equations to slowly varying coordinates so that the equations are in the standard form for the method of averaging. In Section 4, we present our averaging procedure for the model of Section 3 in the off resonance case. Our averaged equations are a pair of coupled Vlasov equations. We do not yet have error bounds and so we must rely on our experience with simpler problems as in Section 2 and comparison with simulation. The averaged equations, as usual, have special structures not shared by the exact equations.

For example, they have equilibrium solutions, and this is discussed in Section 5. This suggests the exact model has quasi–equilibria. We have compared one of the equilibria with the simulation for that initial density and we obtain excellent agreement over 130,000 turns. Because we have equilibria, we can linearize about these equilibria and study the linearized equations. This is done in Section 6, where we introduce the equations for the  $\sigma$  and  $\pi$  modes. Unlike previous approaches, these equations have uncoupled Fourier modes in the azimuthal variable. Using the usual ansatz, we derive an integral equation of the third kind for the  $\sigma$  and  $\pi$  mode frequencies. We have solved the equations for the dipole Fourier mode, and obtain excellent agreement with simulation for both the  $\sigma$  and  $\pi$  mode frequencies. Section 7 discusses our plans for the future. The appendix contains three topics which are germane to our discussions. The Gronwall inequality which is a basic inequality of the elementary theory of ODEs, the Besjes Lemma which is the basic tool in our approach to obtaining rigorous error bounds in our averaging procedures and finally a statement of the Birkhoff Ergodic Theorem which we need for the existence of our averaged problem.

## 2 AVERAGING PROCEDURE AND ERROR BOUNDS

Here we show how the method of averaging can be applied to a perturbed autonomous linear system defined by a matrix  $\underline{A}$ . We use  $t$  as the independent variable, but of course it could refer to distance  $s$  or azimuthal variable  $\theta$  for example.

Consider the IVP

$$\frac{d}{dt}\vec{x} = \underline{A}\vec{x} + \epsilon \vec{f}(\vec{x}, t) + O(\epsilon^2) ; \quad \vec{x}(0) = \vec{x}_0 , \quad (1)$$

where  $f(x, \cdot)$  is quasiperiodic. The first step is to transform it to slowly varying coordinates. It is natural to use the “variation of parameters” transformation given by

$$\vec{x} =: e^{\underline{A}t} \vec{z} . \quad (2)$$

This leads to

$$\frac{d}{dt}\vec{z} = \epsilon e^{-\underline{A}t} \vec{f}(e^{\underline{A}t} \vec{z}, t) + O(\epsilon^2) := \epsilon \vec{g}(\vec{z}, t) + O(\epsilon^2) , \quad (3)$$

which is in a standard form for averaging. The averaged IVP is given by

$$\frac{d}{dt}\vec{v} = \epsilon \vec{g}(\vec{v}) ; \quad \vec{v}(0) = \vec{x}_0 , \quad (4)$$

where

$$\bar{g}(\vec{v}) := \lim_{T \rightarrow \infty} \frac{1}{T} \int_0^T \vec{g}(\vec{v}, t) dt. \quad (5)$$

The averaging formalism is now complete and we turn our attention to the error analysis. We subtract (4) from (3) and integrate to obtain

$$\begin{aligned} \vec{z}(t) - \vec{v}(t) &= \epsilon \int_0^t [\vec{g}(\vec{z}(t'), t') - \vec{g}(\vec{v}(t'), t')] dt' \\ &+ \epsilon \int_0^t [\vec{g}(\vec{v}(t'), t') - \bar{\vec{g}}(\vec{v}(t'))] dt' \\ &+ O(\epsilon^2 t). \end{aligned} \quad (6)$$

The second integral on the r.h.s. has zero mean and by the Besjes Lemma (see appendix) it can be bounded by a constant, say  $C_1$  on  $O(1/\epsilon)$   $t$ -intervals, in the case where, for example,  $g$  is quasiperiodic. Thus we obtain

$$|\vec{z}(t) - \vec{v}(t)| \leq \epsilon L \int_0^t |\vec{z}(t') - \vec{v}(t')| dt' + \epsilon (C_1 + C_2), \quad (7)$$

for  $0 \leq t \leq T/\epsilon$ , where  $L$  is the Lipschitz constant for  $g$ .

The Gronwall inequality (see appendix) then gives

$$|\vec{z}(t) - \vec{v}(t)| \leq \epsilon C e^{LT} ; \quad 0 \leq t \leq T/\epsilon, \quad (8)$$

where  $C = C_1 + C_2$  and  $C_2$  came from the  $O(\epsilon^2)$  term in (1). Thus we say that the solution of (4) gives an  $O(\epsilon)$  approximation to the solution of (3) on  $O(1/\epsilon)$   $t$ -intervals. We call this a formal error analysis because solution domains and associated constants must be carefully defined and resonance considerations addressed. Reference [4] discusses this in detail and an improved approach for maps is given in [5].

### 3 THE KICK-ROTATE MODEL IN 2-D PHASE SPACE

Here we consider head on collisions of two counter rotating bunches with one IP and with the betatron motion modeled by a rotation with tune  $Q_0 =: \mu/2\pi$ . Our viewpoint is directly before the IP and  $\psi_n(\vec{x})$  and  $\psi_n^*(\vec{x})$  denote the phase space densities of the two bunches just before the  $n$ -th passage bunch crossing at the IP. All densities are normalized to 1. In general, any symbol *without* a star will refer to one (the “unstarred”) beam and any symbol *with* a star will refer to the other (the “starred”) beam.

The beam-beam kick is written

$$\vec{x}_n \equiv \begin{pmatrix} q \\ p \end{pmatrix}_n \mapsto \begin{pmatrix} q_n \\ p_n - \zeta (g \star \psi_n^*)(\vec{x}_n) \end{pmatrix} := \vec{x}_n^*, \quad (9)$$

where

$$(g \star \psi)(\vec{x}) := \int_{\mathbb{R}^2} g(q - q') \psi(\vec{x}') d^2x', \quad (10)$$

and  $g(q)$  is the derivative of the Green’s function of the appropriate Poisson problem. For example,

$$\text{CR: } g(q) \propto \text{sgn}(q), \quad , \quad \text{YKZ: } g(q) \propto \text{P.V.} \frac{1}{q}, \quad . \quad (11)$$

where CR refers to the case discussed in [1] and YKZ refers to the case discussed in [2]. Equation (9) is the kick on the unstarred beam due to the starred beam. The perturbation parameter  $\zeta$  is proportional to the linear beam-beam tune shift parameter as will be seen in Eq. (43). For the propagation through a linear lattice we assume linear normal form coordinates, thus

$$\vec{x}_n' \mapsto \underline{R} \vec{x}_n' := \vec{x}_{n+1}, \quad \underline{R} = \begin{pmatrix} \cos \mu & \sin \mu \\ -\sin \mu & \cos \mu \end{pmatrix} = e^{\underline{J}\mu} \quad (12)$$

where  $\mu = 2\pi Q$  is the phase advance per turn and  $\underline{J}$  is the symplectic unit matrix.

Thus the OTM becomes

$$\vec{x}_{n+1} = \underline{R} \left[ \vec{x}_n - \zeta \begin{pmatrix} 0 \\ 1 \end{pmatrix} (g \star \psi_n^*)(\vec{x}_n) \right], \quad (13)$$

and the turn-by-turn evolution of the densities is given by

$$\psi_{n+1}(\vec{x}_{n+1}) = \psi_n(\vec{x}_n) \quad \& \quad \psi_{n+1}^*(\vec{x}_{n+1}) = \psi_n^*(\vec{x}_n^*). \quad (14)$$

We assume in the following that  $Q_0 = Q_0^*$  and  $\zeta = \zeta^*$ .

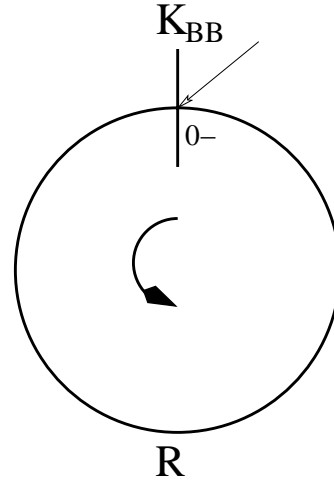


Figure 1: The kick rotate model

We now go to slowly varying coordinates by the action–“angle” transformation

$$\vec{x} =: \sqrt{2J} \begin{pmatrix} \sin(n\mu + \Theta) \\ \cos(n\mu + \Theta) \end{pmatrix}. \quad (15)$$

Note that the transformation is symplectic and has an explicit time dependence through  $n$ . The OTM in the  $(\Theta, J)$  coordinates is

$$\Theta_{n+1} = \Theta_n + \zeta \frac{1}{\sqrt{2J_n}} \sin(n\mu + \Theta_n) \times$$

$$(g \star \psi_n^*)(\vec{x}(\Theta_n, J_n)) + O(\zeta^2) \quad (16)$$

$$J_{n+1} = J_n - \zeta \sqrt{2J_n} \cos(n\mu + \Theta_n) \times \\ (g \star \psi_n^*)(\vec{x}(\Theta_n, J_n)) + O(\zeta^2). \quad (17)$$

We note that for small  $\zeta$  the angle  $\Theta$  and action  $J$  are slowly varying. Introducing the slowly varying density by

$$\Psi_n(\Theta, J) := \psi_n(\sqrt{2J} \sin(n\mu + \Theta), \sqrt{2J} \cos(n\mu + \Theta)), \quad (18)$$

we can rewrite the convolution  $g \star \psi_n$  as an integral over the slow variables as

$$(g \star \psi_n^*)(\vec{x}(\Theta_n, J_n)) = \int_{\mathcal{C}} g(\sqrt{2J_n} \sin(n\mu + \Theta_n) - \sqrt{2J'} \sin(n\mu + \Theta')) dP_n, \quad (19)$$

where  $\mathcal{C} := [0, 2\pi) \times \mathbb{R}^+$  is the product of the one-torus and the positive real axis and  $dP_n$  is shorthand for  $\Psi_n(\Theta', J') d\Theta' dJ'$ . Furthermore, introducing the Green's function  $G(q)$  via  $\frac{d}{dq} G = g$  we can rewrite the OTM defined by (16 – 17) compactly in terms of a map generator  $F$  as

$$\Theta_{n+1} = \Theta_n + \zeta \partial_J F(\Theta_n, J_n, n\mu; \Psi_n^*) + O(\zeta^2), \quad (20)$$

$$J_{n+1} = J_n - \zeta \partial_\Theta F(\Theta_n, J_n, n\mu; \Psi_n^*) + O(\zeta^2), \quad (21)$$

where

$$F(\Theta, J, \kappa; \Psi) := \int_{\mathcal{C}} G(\sqrt{2J} \sin(\kappa + \Theta) - \sqrt{2J'} \sin(\kappa + \Theta')) dP, \quad (22)$$

and

$$\Psi_{n+1}(\Theta_{n+1}, J_{n+1}) = \Psi_n(\Theta_n, J_n). \quad (23)$$

## 4 MAP-AVERAGING

The OTM (16), (17) (and (20), (21) of course) contain the slow variables  $(\Theta, J)$ , the slow density  $\Psi$  and have an explicit time dependence through the term  $n\mu$ . The averaged equations could be obtained by simply averaging  $F$  in (20), (21), but in order to avoid the issue of the commutation of partial derivative and average we proceed with the explicit form of the OTM (16), (17). Thus the averaged equations are obtained by dropping the  $O(\zeta^2)$  term in (16), (17) and averaging over  $n$  holding  $\Theta_n, J_n$  and  $\Psi_n^*$  fixed, in complete analogy with Section 2.

First we note that the argument of  $g$  in (19) can be written

$$\sqrt{2J} \sin(n\mu + \Theta) - \sqrt{2J'} \sin(n\mu + \Theta') = \cos(n\mu + \theta(\Theta, J, \Theta', J')) D(J, J', \Theta - \Theta') \quad (24)$$

where

$$D(J, J', \vartheta) := \sqrt{2J + 2J' - 4\sqrt{JJ'} \cos \vartheta}, \quad (25)$$

where  $\theta$  is defined by (24) and both  $\theta$  and  $D$  do not explicitly depend on  $n$ . We rewrite (16), (17) as

$$\Theta_{n+1} = \Theta_n + \zeta \frac{1}{\sqrt{2J_n}} \sin(n\mu + \Theta_n) \times f(\Theta_n, J_n, n\mu; \Psi_n^*), \quad (26)$$

$$J_{n+1} = J_n - \zeta \sqrt{2J_n} \cos(n\mu + \Theta_n) \times f(\Theta_n, J_n, n\mu; \Psi_n^*), \quad (27)$$

$$f(\Theta, J, \kappa; \Psi) := \int_{\mathcal{C}} g(D(J, J', \Theta - \Theta') \times \cos(\kappa + \theta(\Theta, J, \Theta', J'))) dP. \quad (28)$$

Clearly,

$$e^{i(n\mu + \Theta)} f = \int_{\mathcal{C}} e^{i(\Theta - \theta)} e^{i(n\mu + \theta)} g(D \cos(n\mu + \theta)) dP, \quad (29)$$

and for  $g$  bounded the dominated convergence theorem gives

$$\overline{e^{i(n\mu + \Theta)} f}^n = \int_{\mathcal{C}} e^{i(\Theta - \theta)} \overline{e^{i(n\mu + \theta)} g(D \cos(n\mu + \theta))}^n dP, \quad (30)$$

that is, we can interchange the order of taking the average and integrating. If  $\mu/2\pi$  is irrational then Birkhoff's ergodic theorem, [6, p. 30] (see appendix also), gives

$$\begin{aligned} & \overline{e^{i(n\mu + \theta)} g(D \cos(n\mu + \theta))}^n := \\ & \lim_{N \rightarrow \infty} \frac{1}{N} \sum_{n=0}^{N-1} e^{i(n\mu + \theta)} g(D \cos(n\mu + \theta)) = \\ & \frac{1}{2\pi} \int_0^{2\pi} g(D \cos t) e^{it} dt = \\ & \frac{1}{2\pi} \int_0^{2\pi} g(D \cos t) \cos t dt =: \bar{g}(D). \end{aligned} \quad (31)$$

Thus we obtain the averaged OTM

$$\Theta_{n+1} = \Theta_n + \zeta \frac{1}{\sqrt{2J_n}} \times \int_{\mathcal{C}} \sin(\Theta_n - \theta) \bar{g}(D) dP_n^*, \quad (32)$$

$$J_{n+1} = J_n - \zeta \sqrt{2J_n} \times \int_{\mathcal{C}} \cos(\Theta_n - \theta) \bar{g}(D) dP_n^*. \quad (33)$$

These can be written

$$\Theta_{n+1} = \Theta_n + \zeta \partial_J \bar{F}(\Theta, J; \Psi_n^*), \quad (34)$$

$$J_{n+1} = J_n - \zeta \partial_\Theta \bar{F}(\Theta, J; \Psi_n^*), \quad (35)$$

where

$$\bar{F}(\Theta, J; \Psi) = \int_{\mathcal{C}} \bar{G}(D(J, J', \Theta - \Theta')) dP, \quad (36)$$

$$\bar{G}(D) = \frac{1}{2\pi} \int_0^{2\pi} G(D \cos \vartheta) d\vartheta. \quad (37)$$

It can be shown that  $\bar{F}$  is actually the average of  $F$ , justifying the comment in the first paragraph of this section. Note the convolution structure w.r.t  $\Theta$  in (36), which will be important in what follows. In the CR case  $\bar{G}(D) = \frac{\pi}{2}D$ .

The OTMs of (32), (33) and (34), (35) are only symplectic to  $O(\zeta^2)$  as is easily checked. However, we can interpret (34), (35) as an Euler-step with step length 1 of a strictly Hamiltonian system with the time independent Hamiltonian  $\zeta \bar{F}(\Theta, J, \Psi^*)$ , that is,

$$\frac{d}{dt}\Theta = \zeta \partial_J \bar{F}(\Theta, J, \Psi^*) , \quad (38)$$

$$\frac{d}{dt}J = -\zeta \partial_\Theta \bar{F}(\Theta, J, \Psi^*) . \quad (39)$$

To see this, integrate these Hamiltonian equations from  $t = n$  to  $t = n + 1$  and apply Taylor's theorem to obtain (32) and (33) to  $O(\zeta^2)$ . (Note that this does not work for the non-averaged OTM because the associated Hamiltonian flow is explicitly time dependent and the Euler step does not give back the OTM to  $O(\zeta^2)$ .) Comparing these maps and applying a Gronwall inequality for maps such as in Section 2, shows that these two systems are  $O(\zeta)$  close on  $O(1/\zeta)$   $n$ -intervals, which is what we expect for the relation between the exact model and the averaged model of (32) and (33). Thus we take the Hamiltonian flow and the associated Vlasov equations as our averaged model.

Scaling the independent variable by  $\tau := \zeta t$  we obtain coupled system of AVEs for  $\Psi$  and  $\Psi^*$

$$0 = \partial_\tau \Psi + \partial_J \bar{F}(\Theta, J; \Psi^*) \partial_\Theta \Psi - \partial_\Theta \bar{F}(\Theta, J; \Psi^*) \partial_J \Psi , \quad (40)$$

$$0 = \partial_\tau \Psi^* + \partial_J \bar{F}(\Theta, J; \Psi) \partial_\Theta \Psi^* - \partial_\Theta \bar{F}(\Theta, J; \Psi) \partial_J \Psi^* . \quad (41)$$

These scaled AVEs allow an increase of the step size for numerical integration by a factor of  $O(1/\zeta)$  in comparison with the non-averaged OTM.

## 5 QUASI-EQUILIBRIA

Now let  $\Psi = \Psi^* = \Psi_e(J)$ , then

$$\begin{aligned} \bar{F}_e(J; \Psi_e) &:= \bar{F}(\Theta, J; \Psi_e) \\ &= \int_0^\infty \left[ \int_0^{2\pi} \bar{G}(D(J, J', \Theta - \Theta')) d\Theta' \right] \times \\ &\quad \Psi_e(J') dJ' \end{aligned} \quad (42)$$

is independent of  $\Theta$  because of the convolution structure and because  $D(\cdot, \cdot, \vartheta)$  is periodic in  $\vartheta$ .

Thus  $\Psi_e(J)$  is an exact equilibrium of the averaged kick-rotate system and thus we expect it to be a quasi-equilibrium of the exact system for large times.

Figure 2 shows the evolution of the action density of one of the bunches for two different initial phase space densities. The densities are plotted at a hundred out of 130,000 turns. In the case of the red crosses, the initial densities

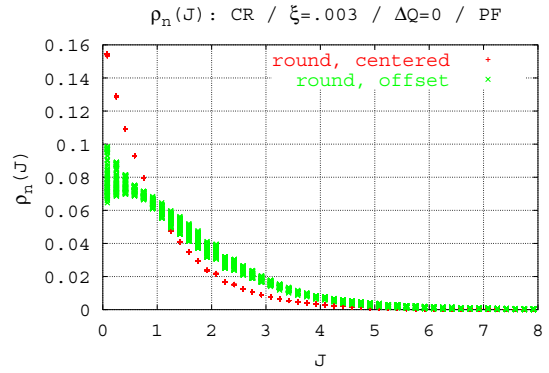


Figure 2: The action density

of both beams were the centered Gaussians  $\Psi_0^*(\Theta, J) = \Psi_0(\Theta, J) = \frac{1}{2\pi}e^{-J}$ . To the eye there is no evolution, consistent with the averaging approximation. In the case of the green  $\times$ -es, both initial densities had been given a  $\Theta$  dependence by shifting the Gaussians by  $\pm 1\sigma$ . Here one observes an oscillating action density, again consistent with the averaging approximation.

For future reference we note that the "weak-strong" amplitude dependent tune shift

$$\Delta Q(J) := \frac{\zeta}{2\pi}\omega(J) := \frac{\zeta}{2\pi}\partial_J \bar{F}_e(J; \Psi_e) \quad (43)$$

depends on the choice of the equilibrium. The linear beam-beam tune shift parameter is then  $\xi := \frac{\zeta}{2\pi}\omega(0)$ .

## 6 THE LINEARIZED EQUATIONS

To determine the linearized equations we write

$$\Psi(\Theta, J, \tau) = \Psi_e(J) + \Psi_1(\Theta, J, \tau) , \quad (44)$$

$$\Psi^*(\Theta, J, \tau) = \Psi_e(J) + \Psi_1^*(\Theta, J, \tau) . \quad (45)$$

Plugging into the AVEs and dropping the nonlinear terms gives

$$\partial_\tau \Psi_1 + \omega(J) \partial_\Theta \Psi_1 - \Psi_e'(J) \partial_\Theta \bar{F}(\Theta, J; \Psi_1^*) = 0 \quad (46)$$

and a corresponding equation with  $\Psi_1$  and  $\Psi_1^*$  interchanged. The two equations can be decoupled by introducing

$$\Psi^\pm := \Psi_1 \pm \Psi_1^* , \quad (47)$$

which yields

$$\partial_\tau \Psi^\pm + \omega(J) \partial_\Theta \Psi^\pm \mp \Psi_e'(J) \partial_\Theta \bar{F}(\Theta, J; \Psi_1^\pm) = 0 . \quad (48)$$

The function  $\bar{G}(D(J, J', \Theta))$  is periodic in  $\Theta$  and can be expanded as

$$\bar{G}(D(J, J', \Theta)) = \sum_{k \in \mathbb{Z}} G_k(J, J') e^{ik\Theta} . \quad (49)$$



Here the  $G_k$  are real, symmetric in  $k$  ( $G_k = G_{-k}$ ) and symmetric under interchange of  $J$  and  $J'$  ( $G_k(J, J') = G_k(J', J)$ ). Let

$$\Psi^\pm(\Theta, J, \tau) = \sum_{k \in \mathbb{Z}} \Psi_k^\pm(J, \tau) e^{ik\Theta}, \quad (50)$$

then the convolution structure of  $\bar{F}$  w.r.t.  $\Theta$  gives

$$\begin{aligned} \bar{F}(\Theta, J; \Psi^\pm) = \\ 2\pi \sum_{k \in \mathbb{Z}} \int_{\mathbb{R}^+} G_k(J, J') \Psi_k^\pm(J, \tau) dJ' e^{ik\Theta}. \end{aligned} \quad (51)$$

Therefore the Fourier modes of  $\Psi^\pm$  are automatically decoupled in first order averaging and satisfy

$$\begin{aligned} 0 = & \partial_\tau \Psi_k^\pm + ik\omega(J) \Psi_k^\pm \\ & \mp ik \Psi_e'(J) 2\pi \int_{\mathbb{R}^+} G_k(J, J') \Psi_k^\pm(J', \tau) dJ'. \end{aligned} \quad (52)$$

The ansatz

$$\Psi_k^\pm(J, \tau) = e^{i\Omega\tau} \sqrt{|\Psi_e'(J)|} \Phi_k^\pm(J) \quad (53)$$

leads to the Fredholm integral equation of the third kind

$$\begin{aligned} 0 = & (\Omega + k\omega(J)) \Phi_k^\pm(J) \\ & \mp 2\pi k \int_{\mathbb{R}^+} G_k(J, J') \sqrt{\Psi_e'(J) \Psi_e'(J')} \times \\ & \Phi_k^\pm(J') dJ'. \end{aligned} \quad (54)$$

with a symmetric kernel. Thus it is easy to show that for non-trivial solutions  $\Omega$  is real. Also for  $\Omega \notin$  the range of  $-k\omega(J)$  it can be transformed to a Fredholm IE of the second kind. We have computed the solution of (54) for the dipole modes ( $k = 1$ ) using the equilibrium density  $\Psi_e(J) = \frac{1}{2\pi} e^{-J}$  and the behavior of  $\omega$  defined in (43) is shown in Fig. 3.

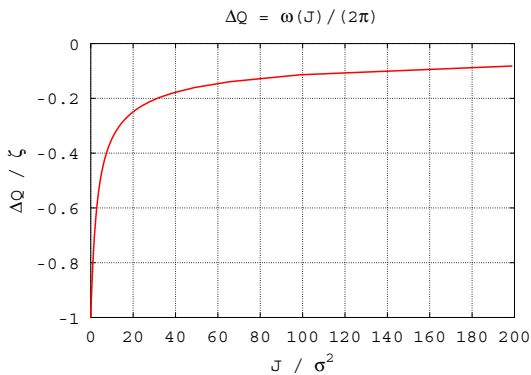


Figure 3: The weak strong amplitude dependent tune shift

Figures 4 and 5 show the numerically computed eigenvalues  $\Omega_i$  for the  $\sigma$  and the  $\pi$  mode. We used Alexahin's [7] trick of transforming the interval  $[0, \infty)$  to  $[0, 1]$  by the substitution  $J = I/(1 - I)$ . The kernel of (54) is

then re-symmetrized by introducing  $\chi_k^\pm(I) := \Phi_k^\pm(I)/(1 - I)|1 - I|^{-1}$  and then discretized in 50 equidistant nodes in  $I$  ( $1 \leq i \leq 50$ ). In Fig. 4 one clearly sees the continuum and the discrete eigenvalue  $\Omega_{50} = 0$  for the  $\sigma$  mode. The  $\pi$  mode spectrum in Fig. 5 shows the same type of continuum and the discrete mode  $\Omega_0 = -1.513$  for the  $\pi$  mode. This is in excellent agreement with our WMPT [8] and PF [9] simulations where the Yokoya factor was found to be 1.51.

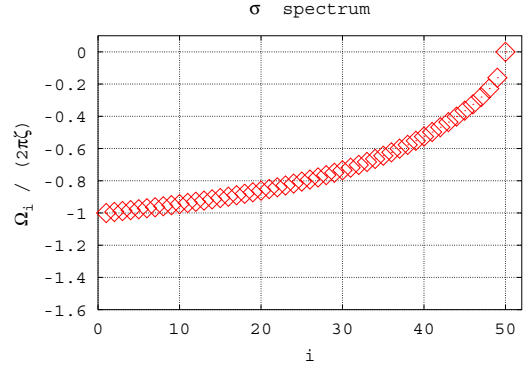


Figure 4: The eigen-spectrum of the  $\sigma$  mode

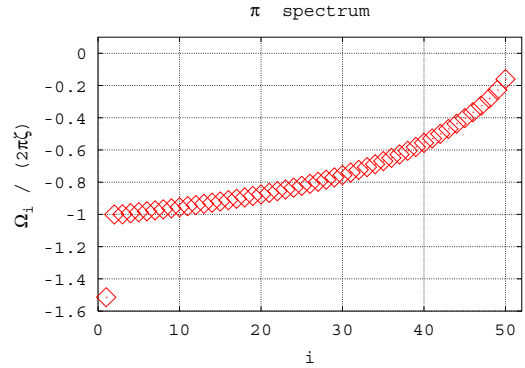


Figure 5: The eigen-spectrum of the  $\pi$  mode

## 7 SUMMARY AND OUTLOOK

We have derived an averaged Vlasov equation, which both simplifies and clarifies previous pioneering work. The AVE has exact equilibria which are quasi-equilibria of the exact model. This is in excellent agreement with simulation as discussed in Fig. 2. Linearization leads to  $\sigma$  and  $\pi$  modes in excellent agreement with simulation as shown in Figs. 4 and 5, giving further confidence in the AVE.

The next steps in this one-degree-of-freedom model are: (1) do a more refined analysis of the integral equation of the third kind using the work of Warnock and Bart [10], (2) study the near resonance case by generalizing the near resonance formalism in [5] and [4], (3) include a tune split in the off resonance case, (4) work out the error analysis

as presented in Section 2 and (5) investigate numerics for the AVE to see if the increased step size of  $O(1/\zeta)$  which is now possible can be used to advantage. We have already extended the formalism to two degrees of freedom [11] and plan to consider some form of the three degree of freedom case.

## 8 ACKNOWLEDGMENTS

Work supported by DOE contract DE-FG03-99ER41104.

Discussions with R. L. Warnock and Y. Alexahin are gratefully acknowledged.

## 9 REFERENCES

- [1] A. W. Chao and R. D. Ruth, *Part.Acc.* **16**, pp. 201–216 (1985)
- [2] K. Yokoya and H. Koiso, *Part.Acc.* **27**, pp. 181–186 (1990) ;  
K. Yokoya and P. Zenkevich, *Part.Acc.* **40**, pp. 229–241 (1993)
- [3] Y. Alexahin, *Part.Acc.* **59**, pp. 43–71 (1998)
- [4] J. A. Ellison and H.-J. Shih, The Method of Averaging in Beam Dynamics, proceedings of the workshop on Accelerator Physics at the Superconducting Super Collider, Dallas, TX, 1992–1993, Ed.: Y. T. Yan, J. P. Naples and M. J. Syphers, AIP conference proceedings **326** (1995)
- [5] H. S. Dumas, J. A. Ellison and M. Vogt, First-Order Averaging Principles for Maps with Applications to Beam Dynamics in Particle Accelerators, Preprint, 2001
- [6] K. Petersen, Ergodic theory, Cambridge University Press (1983)
- [7] Y. Alexahin, private communication
- [8] M. Vogt, T. Sen, J. A. Ellison, FNAL Pub-01/096-T, submitted to Phys. Rev. S.T.–AB (2001)
- [9] M. Vogt, J. A. Ellison, T. Sen and R. L. Warnock, in these proceedings
- [10] G. R. Bart and R. L. Warnock, *SIAM J. Math. Anal.* **4**, 4, pp. 609–622 (1973) ;  
G. R. Bart, *J. of Math. Anal. and Appl.* **79**, 1, pp. 48–57 (1981)
- [11] J. A. Ellison and M. Vogt, to be submitted

## 10 APPENDIX

In this appendix we state the basic theorems used in the text.

**Gronwall Inequality** If  $\alpha$  is a real constant,  $\beta(t) \geq 0$  and  $\phi(t)$  are continuous real functions for  $a \leq t \leq b$  which satisfy

$$\phi(t) \leq \alpha + \int_a^t \beta(s) \phi(s) ds, \quad a \leq t \leq b, \quad (55)$$

then

$$\phi(t) \leq \alpha e^{\int_a^t \beta(s) ds}, \quad a \leq t \leq b. \quad (56)$$

**Besjes Inequality** Let  $f(x, t)$  be quasiperiodic in  $t$  with frequencies that satisfy a Diophantine condition and let  $f$  have zero  $t$ -mean for fixed  $x$ , then there exist  $T > 0$  and  $C(T) > 0$  such that

$$\left| \int_0^t f(x(\epsilon s), s) ds \right| \leq C, \quad 0 \leq t \leq \frac{T}{\epsilon}. \quad (57)$$

**Birkhoff's Ergodic Theorem** Let  $(X, \mathcal{B}, P)$  a probability space,  $T : X \rightarrow X$  a measure preserving map and  $f \in L^1(X, \mathcal{B}, P)$ . Then

1.  $\lim_{n \rightarrow \infty} \frac{1}{n} \sum_{k=0}^{n-1} f(T^k x) =: \bar{f}(x)$  exists almost surely for  $x \in X$  ;
2.  $\bar{f}(Tx) = \bar{f}(x)$  almost surely ;
3.  $\bar{f} \in L^1(X, \mathcal{B}, P)$  and  $\|\bar{f}\|_{L^1} \leq \|f\|_{L^1}$  ;
4. if  $A \in \mathcal{B}$  with  $T^{-1}A = A$ , then  $\int_A f dP = \int_A \bar{f} dP$  (this says that if  $\mathcal{I}$  is the sub- $\sigma$ -algebra of  $\mathcal{B}$  consisting of all the  $T$ -invariant sets, then  $\bar{f} = E(f|\mathcal{I})$  almost surely)
5.  $\frac{1}{n} \sum_{k=0}^{n-1} f \circ T^k \xrightarrow{L^1} \bar{f}$ .

Note that in the case when  $T$  is ergodic, like in the case of  $T : \mathcal{T}^1 \rightarrow \mathcal{T}^1, x \mapsto (x + \mu) \bmod 2\pi, \mu$  irrational, then  $\mathcal{I}$  is the trivial  $\sigma$ -algebra and  $\bar{f}$  is constant almost surely, in particular  $\bar{f} = \int_X f dP$ .

# ODYSSEUS: AN ADAPTIVE 3D STRONG-STRONG BEAM-BEAM SIMULATION CODE

Edwin B. Anderson\* and Joseph T. Rogers, Laboratory of Nuclear Studies, Cornell University, Ithaca, NY 14853, USA

## Abstract

ODYSSEUS is a 3D simulation code for the beam-beam interaction in storage ring colliders. It is a true strong-strong simulation in which no constraints are placed on the distribution of particles in the beams. The program achieves its speed by adaptively choosing between alternative electromagnetic field calculation methods. Linear tracking through the ring and wake fields are included. We plan to include nonlinear tracking through the ring in the next version of the code.

## 1 INTRODUCTION

In storage ring colliders the beam-beam force can cause a blowup of the beam emittance, particle loss, or instability. Because the beam-beam force is strongly nonlinear, particle-tracking methods are useful for determining the dynamics of the beams. Strong-strong simulations, in which the force exerted by each beam on the opposing beam is calculated, are capable of modeling coherent instabilities of the beams. These simulations are very time-intensive because of the need to repeatedly calculate the electromagnetic field of each beam. To include longitudinal as well as transverse degrees of freedom, an unconstrained strong-strong code must use special techniques to improve its speed.

ODYSSEUS is an unconstrained 3D strong-strong beam-beam simulation that includes broadband wake fields [1, 2]. It is capable of rapidly calculating the electromagnetic field of a beam divided into many longitudinal slices because it adaptively chooses from a variety of different field computation methods. Different algorithms are used for the core, transverse tails, and longitudinal tails of the beam. The parameters of the program can be changed to model flat or round beams. Inclusion of the longitudinal degree of freedom and wake fields allows the investigation of previously inaccessible physics.

A flowchart for ODYSSEUS is shown in Figure 1. The individual calculations are described in detail in the following sections.

## 2 PARTICLE TRACKING

### 2.1 Storage Ring

On each simulated turn through the storage ring, each macroparticle is propagated through the linear optics of the storage ring, including chromaticity, synchrotron radiation excitation and damping, RF phase focusing, and wake field deflections. macroparticles which have migrated past a transverse aperture are no longer considered in the

simulation. Longitudinal and transverse short-range wake fields are modeled as a sum of broadband resonators.

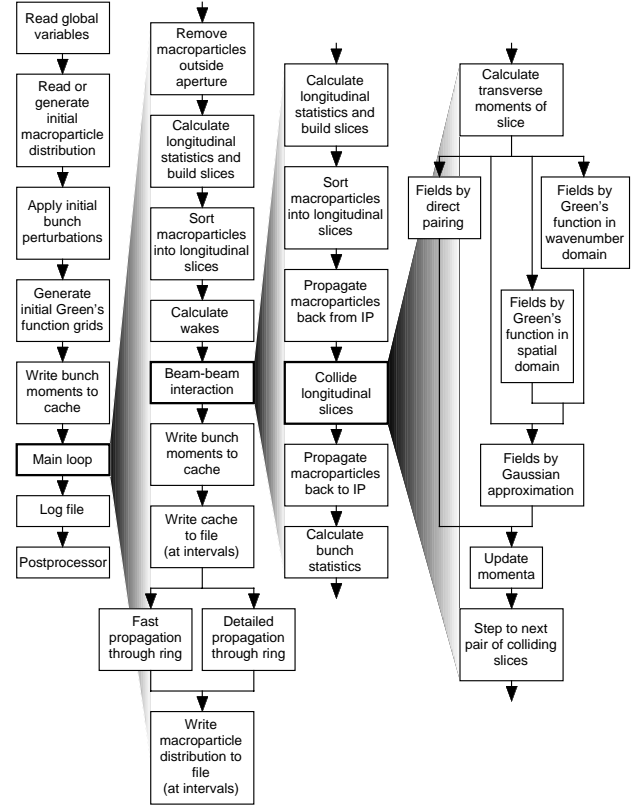


Figure 1: Flowchart for ODYSSEUS.

### 2.2 Collisions

During its passage through the opposing bunch, the transverse position of each macroparticle may change appreciably because the vertical beta function at the interaction point in many colliders is comparable to the bunch length. ODYSSEUS handles the longitudinal variation of the electromagnetic field of the beam by dividing the beam into slices. The simulation collides each pair of slices sequentially, updating the transverse momenta and positions of each macroparticle after each pair-wise collision of slices. For each slice collision the slice electromagnetic field is calculated by one of the methods described below. Macroparticles undergo longitudinal oscillations and migrate from slice to slice, so on each turn the macroparticles are sorted according to their longitudinal position and are reassigned to slices.

\* currently at McKinsey & Co.

### 3 ELECTROMAGNETIC FIELD CALCULATION

#### 3.1 Beam Core

If the number of macroparticles,  $N$ , within a slice is very small, the integrated field at a probe beam macroparticle is calculated from radius vector from each opposing source beam macroparticle. Because it involves a sum over source-probe particle pairs, the number of calculations goes as  $N^2$ , making this method efficient only for  $N < 50$ .

For larger values of  $N$ , the electromagnetic field is calculated on a rectangular grid (Particle-In-Cell method) using pre-calculated Green's functions for charges on the grid points. The macroparticle charge is assigned to the grid points using one of the two area-weighted techniques described below. If the number of grid points  $N_g$  is less than about 200, the convolution of the charge density and Green's function is done as a summation in coordinate space and the number of calculations required goes as  $N_g^2$ . For larger values of  $N_g$ , the convolution of the Green's function and charge density is done as a multiplication in wavenumber space. The speed of this method is limited by the speed of the necessary Fourier transform to wavenumber space and the inverse transform back to coordinate space. Thus the number of calculations goes as  $N_g \log_2 N_g$ . To suppress edge effect problems in the Fourier transforms the size of the wavenumber space can be doubled in both directions and padded with zeros [3], although this is both to be unnecessary for the typical, Gaussian-like, beam charge distribution.

The grid itself is adaptive. The number of cells in each transverse direction and their aspect ratio change as needed to cover the beam, with a constraint on the aspect ratio, described below in Section 4.2.

#### 3.2 Beam Tails

The tails of the beam, typically taken to be particles with a displacement of more than  $(10/3)\sigma$  in any direction, are treated differently than the core particles. The tail particles have very little influence on the beam-beam force. They do respond to the beam-beam force, so a weak-strong calculation is used for them.

Longitudinal tail particles are subject to forces from the core of the opposing beam. A full calculation of the field from the opposing (strong) beam slice is performed, but the tails are assumed to have no effect on the strong beam (see Figure 2). Alternatively, the user may choose a strong-strong calculation for all slices.

The transverse tail particles are subject to a beam-beam force of similar magnitude to that experienced by the core particles. However, the high-wavenumber component of the charge distribution of the core has little influence on the field in the transverse tails, so the field used is that of a Gaussian charge distribution with the same charge and first- and second-order moments as the slice. The field

from this Gaussian charge distribution is calculated from the rational approximation of Talman and Okamoto [4].

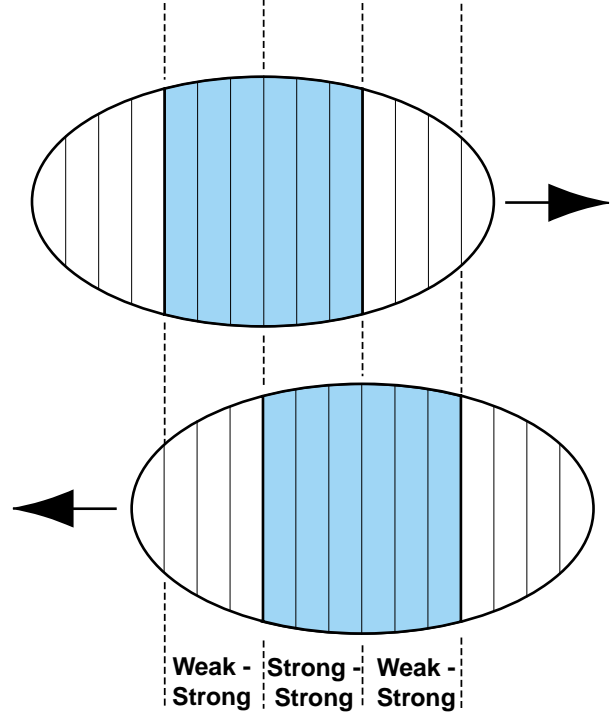


Figure 2: The beam is divided into longitudinal slices and the collision of each pair of slices is simulated in sequence. Slices are marked as either “weak” (white) or “strong” (gray) and the appropriate technique is applied when they interact. No two weak slices ever interact.

#### 3.3 Interpolation Techniques

Whenever a grid-based method is used, it is necessary to interpolate from the fields on a grid to arbitrary probe macroparticle locations and to deposit charge on the grid from arbitrary source macroparticle locations. ODYSSEUS gives the user a choice between three interpolation methods: Nearest-Grid-Point (NGP); four-point Cloud-In-Cell (CIC); and a nine-point extension of the Triangular-Shaped-Cloud (TSC) technique [3]. Lower order interpolation methods tend to introduce noise into the simulation. Higher order interpolation methods reduce this noise but tend to broaden small features in the charge distribution. In ODYSSEUS a “sharpening function” is used during the convolution of the charge density and Green's function in wavenumber space to compensate this broadening.

### 4 SPEED AND ACCURACY CONSIDERATIONS

#### 4.1 Speed

ODYSSEUS is being run on a farm of 500 MHz Alpha based processors that operate under Linux. The fast Fourier transforms typically take about 90% of the computation time. The code is not parallelized, because one typically wishes to run the code with a large set of

varying parameters (*e.g.*, for tune scans). The speed of ODYSSEUS may be compared with that of a non-adaptive Particle-In-Cell (PIC) calculation by setting its options to include only the PIC method. The calculation is found to run 5 times faster with the adaptive options.

#### 4.2 Field Error Due to Transverse Grid

For round beams a field calculation grid can be constructed out of square cells with equal numbers of cells in each dimension. This construction allows for accurate field calculation with a low number of cells. In contrast, the extreme aspect ratios of flat beams force the use of either large numbers of cells or individual cells with large aspect ratios. The Green's function technique fails to provide a good approximation to the electromagnetic field when the cell aspect ratio is far from unity, especially when a scalar Green's function is used. ODYSSEUS uses a two-component Green's function and limits the cell aspect ratio. This limit is typically set to 1.4.

#### 4.3 Field Error Due to Longitudinal Slicing

The electromagnetic field error introduced by dividing the beam into longitudinal slices is a source of noise that tends to increase the emittance of the simulated beam. This is a problem when simulating flat beams with a low natural emittance and large vertical beam-beam parameter  $\xi_y$  when the number of slices is small. The noise produces a maximum possible value of  $\xi_y$  in the simulation. In a particle-tracking simulation using longitudinal slices of uniform length  $\Delta z$ , we find that the maximum  $\xi_y$  is

$$\xi_{y,\max} = \frac{4\sqrt{3}}{\pi} \frac{\beta_y^*}{\Delta z} \sqrt{\delta} \quad (1)$$

where  $\beta_y^*$  is the vertical beta function at the interaction point and  $\delta$  is the transverse damping decrement. Other physical or numerical effects may further reduce  $\xi_y$ . Figure 3 shows the vertical beam-beam parameter as a function of the number of slices. This behavior is consistent with the limit of Eq. (1).

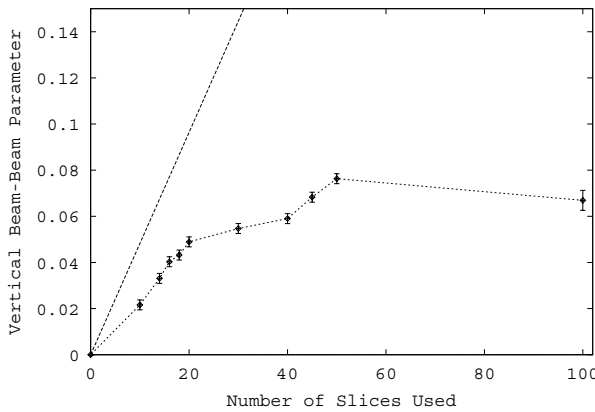


Figure 3: Vertical beam-beam parameter  $\xi_y$  as a function of the number of slices used in the simulation. The straight line is an estimate of the maximum possible equilibrium  $\xi_y$  from Equation 1.

## 5 CONCLUSIONS

The adaptive nature of ODYSSEUS allows it to run several times faster than a code using PIC methods alone. Simulations of several tens of thousands of turns can be completed in a reasonable amount of time, varying from hours to several days, depending on the parameters of the calculation.

ODYSSEUS has been applied to tune-plane scans with CESR parameters to determine the operating point with the best luminosity; to tune-plane scans at lower energy for the proposed CESR-c; to quantifying the effect of damping time on the maximum beam-beam parameter; and to determining the mechanism of the beam-beam limit in CESR. The luminosity tune scans agree very well with observations in CESR [5]. In the next version of ODYSSEUS we plan to include calls to BMAD [6], a particle-tracking code, to realistically model the remainder of the ring.

## ACKNOWLEDGMENTS

This work was supported by the National Science Foundation. The authors extend their thanks to T. Banks, R. Talman, G. Codner, R. Helmke, R. Ng, J. Irwin, R. Siemann, M. Furman, S. Krishnagopal, and R. Ryne.

## REFERENCES

- [1] E.B. Anderson, T.I. Banks, and J.T. Rogers, Proc. 1999 Particle Accelerator Conf., New York (1999) 1686.
- [2] E.B. Anderson, Ph.D. dissertation, Cornell University (1998).
- [3] R.W. Hockney and J.W. Eastwood, *Computer Simulation Using Particles*, Hilger, Bristol, U.K., 1988.
- [4] Y. Okamoto and R. Talman, Cornell Laboratory of Nuclear Studies report CBN 80-13 (1980).
- [5] J.T. Rogers, M.A. Palmer, A.P. Romano, and C.R. Jones, "Beam-Beam Simulation Studies of CESR-c and Observations in CESR", these proceedings.
- [6] D.L. Rubin and D. Sagan, "CESR Lattice Design", to be published in Proc. 2001 Particle Accelerator Conf., Chicago (2001).

# A Hybrid Fast Multipole Method applied to beam-beam collisions in the strong-strong regime.

W. Herr, M.P. Zorzano, CERN, and F. Jones, TRIUMF

## Abstract

The strong-strong interactions of two colliding beams are simulated by tracking the motion of a set of macroparticles. The field generated by each distribution is evaluated using the Fast Multipole Method (FMM) together with some elements of particle-mesh methods. This technique allows us to check the exact frequencies of the coherent modes and the frequencies of oscillations of individual particles in the beam. The agreement between the simulations and analytical calculations is largely improved. Furthermore it is an efficient method to study the coherent modes in the case of separated beams.

## 1 INTRODUCTION

Two colliding beams exert a force on each other which is defocusing for beams of equal polarity as in the case of the LHC. Solutions of the linearized Vlasov equation show that for round beams and in the case of one bunch per beam with equal parameters (intensity, beam size, betatron tune) two coherent dipole modes of oscillations appear: the  $\sigma$  mode, whose frequency is equal to the unperturbed betatron tune, and the  $\pi$ -mode with a tune shift of  $Y = 1.21$ , where  $Y$  is the Yokoya factor [1], times the beam-beam parameter  $\xi$ .

In this paper the transverse coherent motion of two colliding proton beams is studied by multiparticle tracking. In a self-consistent model of the coherent interaction, the distributions of both beams evolve as a consequence of the mutual interaction and are used at the interaction points to calculate the force on the individual particles. A number of studies have been done for LHC using the so-called “soft Gaussian model” [2]. This model assumes the force experienced by a particle when traversing the counter rotating beam as originating from a Gaussian beam distribution with variable barycenters and rms beam sizes. This allows the use of an analytical expression for the forces. This Gaussian model cannot take into account the non-Gaussian deformations of the distribution and as a result underestimates the force and yields a Yokoya factor that is slightly smaller ( $Y = 1.1$  in our case). This symptom has also been recently discussed by Yokoya [3]. In the worst case this simplification can inhibit the appearance of coherent effects. Nonetheless the use of the analytical expression of the force generated by a Gaussian beam allows simulations in a reasonable computing time and it is therefore more convenient for studies with multiple bunches.

It has been predicted [4, 5] that the coherent  $\pi$ -mode may not be Landau damped for certain strong-strong conditions

and therefore an accurate knowledge of the Yokoya factor is highly desirable.

## 2 SIMULATIONS BEYOND THE SOFT GAUSSIAN MODEL

To avoid this problem and to increase the accuracy of the simulations, we have to introduce a field solver for an arbitrary distribution of charges in space. The choice of the solver is constrained by the problems under investigation:

- Large number of particles in simulation ( $10^4$ ).
- Separated beams (separation between zero and 10 times the beam size or more).

A direct integration of forces (particle-particle methods) is ruled out since the necessary time grows with the square of the number of particles ( $O(N_p^2)$ ). For the number of particles used in our simulation this is impossible. Other possible solvers employ so-called particle-mesh methods and have been shown to give good results [6]. Their advantage is speed since the number of computations is smaller and depends on the number of grid points  $N_g$ : ( $O(N_g \ln N_g)$ ). A strong disadvantage is that particle-mesh methods have problems handling non-uniform distributions. For the case of separated beams (as in our case with the important effect of long-range collisions) most of the space is basically empty. Moving or adaptive grids may be used for that purpose, but may lead to a rather complicated structure.

Another possibility is to use Fast Multipole Methods (FMM). In this algorithm the potential or force acting on a particle is divided into two components. The component of close particles is computed directly and between distant particles the potential is approximated by multipole expansion [7, 8]. This method is therefore well adapted to handle problems like separated beams. Problems with FMM are close encounters and “charge-overloading”, i.e. for the LHC bunches  $10^{11}$  particles are represented by  $10^4$  macroparticles.

## 3 BASIC HFMM ALGORITHM

For our problem we studied a modified version of FMM, a Hybrid FMM (HFMM) [9]. It resembles a particle mesh method for the handling of charges and super particles, however the forces on the superparticles are evaluated using the FMM. Smoothing can help to avoid charge-overloading. The HFMM is a robust implementation of a

Fast-Multipole Method (FMM) field solver, which is designed to solve the field for an arbitrary collection of discrete charges. It divides the solution domain into a grid and a halo area. The grid area is subdivided into a hierarchical tree of square regions. In the first step of the calculation, the macroparticles inside the grid are assigned to grid points. All macroparticles outside the grid are treated as discrete, independent superparticles and form the halo. The charge assignment can be done with a 'nearest-grid-point' method, i.e. the charge is assigned to the nearest grid point. This is the simplest method, however the field values are not continuous and the results are more noisy. Alternatively one can use the cloud-in-cell (CIC) charge assignment where the charge is shared between the neighbouring grids points. This method gives continuous field values but requires more book-keeping.

Finally, multipole expansions of the field are computed for every point, i.e. for each grid point as well as for every halo particle, and the program derives the resulting forces on the particles of the counterrotating beam. In the case of a CIC charge assignment, appropriate interpolation between the fields calculated for the grid points have to be applied. The grid size and shape does not have to follow any special geometry and can be chosen freely to achieve the desired speed and precision, depending on the problems under investigation. Unlike other Poisson solvers, the grid points with no charges assigned are left out of the computation and the number of computations scales roughly with the number of particles. More details of the method used in this report are found in [9]. This method is already implemented in the ACCSIM program [10] to study space charge problems.

In this work we have implemented the HFMM in our beam-beam simulation program to evaluate the force on a test particle generated by an arbitrary charge distribution. This will be applied to study the strong-strong collision of two bunches colliding at one interaction point (IP). We will study the coherent modes that are excited in the collision of two equal round bunches similar to those of LHC, when colliding head-on or separated by a constant offset at one interaction point (long-range interactions). This will enable us to obtain the correct Yokoya factor by multiparticle tracking and in a later stage to study in detail the modes excited by long-range interactions. Finally, it should allow us to study the possible emittance growth of collisions of partially overlapping bunches [11].

## 4 TRACKING WITH HFMM.

We simulate the collision of two strong proton beams. Our variables are: horizontal position  $x$ , vertical position  $y$ , horizontal angle  $v_x = x'$ , and vertical angle  $v_y = y'$ . The prime denotes the derivative with respect to longitudinal position  $s$ , e.g.  $x'$  is the slope of the horizontal trajectory.

Each of the beams has one bunch that is represented by a set of  $N_p$  macroparticles, whose trajectories are followed over  $n$  turns, assuming linear betatron motion without cou-

pling and a beam-beam collision at one interaction point (IP). At the IP every particle in the bunch experiences a deflection by the field of the counter-rotating beam that depends on its position.

The deflection applied to a single particle in one of the beams is calculated using the HFMM.

The linear map from one IP to the next is

$$\begin{pmatrix} x(n+1) \\ v_x(n+1) \end{pmatrix} = \begin{pmatrix} \cos(2\pi Q_x) & \sin(2\pi Q_x) \\ -\sin(2\pi Q_x) & \cos(2\pi Q_x) \end{pmatrix} \begin{pmatrix} x(n) \\ v_x(n) + \Delta v_x(n) \end{pmatrix} \quad (1)$$

An equivalent map is applied in the vertical plane,  $(y, v_y)$ .

The horizontal deflection experienced at the interaction point is:

$$\Delta v_x(n) = \frac{r_p N^*}{\gamma} E_x(x, y) \quad (2)$$

where  $E_x(x, y)$  is the horizontal force evaluated with the HFMM technique at the particle position  $(x, y)$ . The number of particles in the opposing beam is  $N^*$ .

For the simulation of parasitic (long-range) collisions, the same model is employed. The two beams collide with a horizontal separation  $L_x$  (in units of  $\sigma_x$ ). For a low  $\beta$  insertion we have about  $90^\circ$  phase advance between the IP and the long-range collision region. Since in the LHC the betatron phase advance between long-range collisions on one side of the interaction region is very small, we can lump all  $n_{par}$  parasitic collisions into a single one, to reduce the computing time. This overestimates the effect slightly because the bunches oscillate with different phases with respect to each other.

Because a static dipole kick would change the closed orbit of the bunch, the static kick from the long-range collision must be subtracted [12]. The beam-beam long-range kick used in our simulation code is then

$$\Delta v_x(n) = n_{par} \frac{2r_p N_p^*}{\gamma} (E_x(x + L_x \sigma_x, y) - D_x(L_x \sigma_x, 0)). \quad (3)$$

where  $D_x(L_x \sigma_x, 0) = -1/L_x \sigma_x (1.0 - \exp(-\frac{L_x^2}{2\sigma_x^2}))$  is the (constant) dipole kick generated by a Gaussian distribution at a distance  $x = L_x \sigma_x$ . This assumes that a closed orbit exists [11] and the bunches oscillate coherently around this orbit. At the LHC, there are about  $n_{par} = 16$  parasitic encounters on each side of an IP, with a minimum transverse separation of  $L_x = 7.5$  (in units of  $\sigma_x$ ). The fractional part of the horizontal and vertical tunes are 0.31 and 0.32, and unlike LEP [13], the results are not strongly affected by dynamic beta effects. In Figs.1 and 2 we show comparisons between the beam-beam kicks calculated with the HFMM and those obtained from an analytical expression, both for the case of round, exactly Gaussian beams.

In the Fig.1 we test the different methods for the charge assignment for a grid spacing of  $0.25\sigma$  with a grid of  $81 \times 81$ , where 81 is the number of grid points in each plane. Thus the grid for the head-on collisions covers the amplitudes between  $-10\sigma$  to  $+10\sigma$ . While the 'nearest-grid-point' assignment gives visibly discontinuous values, the force evaluated with the CIC assignment is continuous and therefore preferable.

In the Fig.2 we have used a different grid spacing of  $0.10\sigma$  with a grid of  $201 \times 201$  to test the obtained accuracy. The effect of the discontinuous values in the 'nearest-grid-point' assignment is now smaller and barely visible as one could expect. The grid size for the simulation is a compromise between precision and computing speed. A grid spacing of  $0.1\sigma$  or below gives good results. For most simulations we have therefore chosen such a spacing and the Cloud-in-Cell (CIC) charge assignment.

## 5 SIMULATION RESULTS

In this section we shall give quantitative results on the coherent modes for head-on as well as some first results with long-range interactions. Since the symmetry of beam parameters plays an important role for the coherent motion, we study the relevance of intensity differences as well as tune and beam size asymmetries. They are expected to make it more difficult to maintain a coherent motion and will eventually help to avoid it.

### 5.1 Head-on collisions with equal betatron tunes and intensity

First let us consider the strong-strong case and head-on collisions of two round bunches, using the previous maps. The statistical variation in the initial distribution of particles is sufficiently large to excite the coherent modes. We start with equally strong beams, i.e. the intensity ratio  $R_I$  between the weaker and stronger beam is 1.0. If we perform a harmonic analysis of the motion of the barycentre of one bunch, we find two coherent modes. One is located at the unperturbed tune  $Q$ , the other has a lower frequency. In Fig. 3 we plot the amplitude frequency spectrum. The horizontal axis gives the tune shift from the unperturbed tune  $Q$  in units of  $\xi$  (i.e.:  $w = \frac{\nu - Q}{\xi}$ , for the round beam case  $\xi_x = \xi_y = \xi = 0.0034$ ,  $Q_x = 0.31$ ,  $Q_y = 0.32$ ). For the other beam and the other plane a similar picture is obtained. Analysing the spectra of the distance between the centroids, i.e. the expressions  $\langle x^{(1)} \rangle - \langle x^{(2)} \rangle$  and  $\langle y^{(1)} \rangle - \langle y^{(2)} \rangle$ , the coherent mode at the unperturbed frequency disappears. On the other hand, when we analyse the sum of the centroids ( $\langle x^{(1)} \rangle + \langle x^{(2)} \rangle$ ,  $\langle y^{(1)} \rangle + \langle y^{(2)} \rangle$ ) the lower mode frequency disappears. We can thus identify the mode at the unperturbed frequency as the so-called  $\sigma$ -mode, for which the centroids of the bunches oscillate in phase with equal frequencies and amplitudes. The lower frequency mode is called  $\pi$ -mode and in this mode the centroids oscillate also with equal fre-

quencies and amplitudes but in opposite phase. The motion of the bunch centroids is a superposition of these two modes.

Between the  $\pi$ - and the  $\sigma$ -mode in Fig. 3 we find the incoherent *continuum*. A single particle crossing the opposing beam at a distance from its axis feels a defocusing force (or focusing force in the case of oppositely charged beams like LEP), which leads to a change in its tune. For particles near the centre of the counter rotating beam this tune shift is equal to  $-\xi$ . For particles further away the defocusing force is smaller (due to the non-linearity of the beam-beam force) and vanishes asymptotically. This creates an incoherent tune spread which extends from 0 to  $-\xi$ .

In our simulations we find the  $\pi$ -mode at a tune shift of exactly  $1.21 \pm 0.005$  in units of  $\xi$  (and  $\xi = 0.0034$ ). The  $\pi$ -mode is thus shifted outside of the continuum. The shift calculated with HFMM is therefore in excellent agreement with the theoretical prediction [1, 4].

### 5.2 Head-on collisions with equal betatron tunes and different intensity

It has been predicted [4] that for intensity ratios of 0.6 or lower, the  $\pi$ -mode merges with the continuum. In the soft Gaussian model this prediction cannot be tested exactly since the  $\pi$ -mode tune shift is underestimated [2, 3]. In this section we can now make a more precise quantitative comparison. Fig. 4 clearly confirms this prediction: the  $\pi$ -mode merges into the incoherent spectrum at Alexahin's ratio of 0.6 and is Landau damped. In the LHC the expected bunch to bunch intensity difference may be as large as  $\pm 20\%$ . Although this alone will not be sufficient to recover Landau damping, together with other uncertainties (see e.g. section 5.4) and suggested remedies (see next section) it should simplify the damping of the modes.

### 5.3 Head-on collisions with different betatron tunes

The first proposed remedy to avoid coherent beam-beam modes was to decouple the two beams by using different fractional tunes for their tunes [14]. This is possible in the LHC since we have two separate rings. Possible unwanted side effects of such a scheme were discussed in [15]. The sensitivity to the expected small tune differences is demonstrated here quantitatively. While the fractional part of beam 1 is kept at 0.310, the tune of the second beam is slightly varied. For a tune difference between the two beams of more than approximately  $\approx 0.7\xi$  the  $\pi$ -mode disappears into the continuum as shown in Fig.5.

### 5.4 Head-on collisions with different beam sizes

Similar to an intensity imbalance, different beam sizes of the two beams can lead to loss of coherence and damped coherent modes. In Fig.6 we show the spectra for beam



size ratios of 0.90 and 0.70. Since the beam size (of the second beam) is now smaller, the tune shift is slightly larger than in the original case. While for a ratio of 0.90 the  $\pi$ -mode is still very visible, it has merged with the incoherent spectrum for 0.70. The mechanism is the same as for a beam intensity imbalance. At this point one can speculate whether the size imbalance can be compensated by an intensity imbalance, adjusted to give the same beam-beam tune shift parameter  $\xi$ . The result of such a simulation is shown in Fig.7 with the beam radius of the second beam reduced to 0.7, but with a smaller beam intensity (50%). The beam-beam parameter is therefore the same. We observe a clear coherent mode again. This observation however is non trivial. When the beams have different sizes and geometrical distributions, the fields seen by the two beams are rather different, although the tune shift parameter for the small amplitude particles is the same. The reason is that the larger beam experiences a very non-linear force for particles at much smaller amplitudes than the smaller beam. Particles at larger amplitudes must therefore behave rather differently. For the single particle behaviour, i.e. population of beam tails and lifetime, this is known to be of extreme importance [16, 17]. For a coherent oscillation it is mainly the oscillation frequency that must be the same and it is known that for the head-on collisions studied in this example, it is mainly the core of the beam contributing to the coherent oscillation and the tune shift. The core particles experience always an almost linear force proportional to the beam-beam parameter and this explains the observation.

Similar observations have been made in simulations of asymmetric colliders such as PEP-II [18] where the energy transparency condition was studied, i.e. where the energy asymmetry was compensated by an asymmetry of the beam currents.

### 5.5 Coherent modes from long-range collisions

Since the transverse distance between two bunches at the parasitic collision is larger than the rms beam size, the effects will be similar to the coherent interaction of rigid, point-like bunches. In that case the contribution of parasitic crossings to the tune shift of coherent oscillation modes would be

$$\begin{aligned}\Delta\nu_\pi &= 2 \times (\text{incoherent long-range tune shift}) \propto 1/L_x^2 \\ \Delta\nu_\sigma &= 0.\end{aligned}$$

Moreover, the incoherent long-range tune shifts for beam separations larger than  $\approx 1.5 \sigma$  have different signs for the two planes. Both, the coherent and incoherent tune shifts depend on the separation and for sufficiently large separation they scale with the inverse of the separation squared.

Most important however, the width of the incoherent spectrum (tune spread) of long-range collisions alone depends on the separation and in the LHC is smaller than the tune spread from head-on collisions [19, 20]. The distance of the  $\pi$ -mode from the edge of the incoherent spectrum

is therefore rather different from the head-on case and one must expect a different behaviour. In particular the necessary measures to merge the coherent modes with the incoherent spectrum must be at least quantitatively different. In this report we have a first look at the dynamics of long-range collisions separately to demonstrate the differences. For an evaluation of the necessary operational parameters, both head-on as well as long-range collisions must be considered together, like it was done with the Gaussian approximation [2]. A more complete study should also include multiple bunches and interaction points and will be treated at a later stage [21].

### 5.6 Simulation of long-range collisions

The simulation of coherent modes from separated beams is a good example where the HFMM can be used to great advantage. In a conventional particle-mesh method, most grid points between and around the beams are empty and with a typical separation around  $10 \sigma$  the necessary computing time becomes unacceptable. With the HFMM we have the option to either treat the opposing beam as a halo or to choose the grid large enough to cover both beams. Although at first sight the second option looks like a conventional grid method, the advantage is clear: the fields are calculated with the FMM field solver only at the grid points with charges and the saving in computing time is large. Treating the opposing beam as a real halo object usually requires more time than covering the whole area. In Fig.8 we show the horizontal spectrum for long-range collisions with a horizontal separation  $L_x = 10.0$  (in units of  $\sigma_x$ ). We plot it again as a function of the distance to the unperturbed tune, normalized to the head-on beam-beam tuneshift  $\xi$ , to allow a quantitative comparison to the head-on modes. For one of the figures (left) the particles in the opposing beam were treated as halo particles, i.e. were not covered by the grid. In the right figure the grid was extended to  $15\sigma$ , i.e. included both beams. Both methods give the same results, however the computing speed is very different. The treatment as real halo is very time consuming. The real difference to a particle-mesh code then comes from the fact that only grid points with particles are treated, thus the number of computations scales like  $O(N_p)$ . The computing speed difference is about a factor 2.5 between the two options, therefore in all simulations we choose the procedure to cover the whole area with a grid, including both beams.

Like in the case of head-on coherent modes we identify the  $\sigma$ - and  $\pi$ -mode easily by analysing the sum and the difference of the barycentres separately. The peaked structure between the two modes represents again the incoherent continuum, this time arising from the long-range interaction. As expected, the coherent shift is two times larger than the shift of the incoherent spectrum.

## 5.7 Long range collisions with equal tunes

Fig. 9 shows the horizontal and vertical spectra of centroid oscillations of a bunch subject to long-range collisions with a horizontal separation of  $L_x = 10.0\sigma_x$ . To obtain realistic tune shifts, we have lumped all 32 long range interactions of a LHC interaction region into a single collision. The optics and geometry of the interaction regions permits this simplification [2, 12]. The horizontal axis gives the tune shift relative to the unperturbed tune  $Q$  in units of the head-on beam-beam parameter  $\xi$ :  $w = \frac{\nu-Q}{\xi}$ . In the horizontal plane, the tune shifts are positive, and the coherent dipole  $\pi$ -mode has twice the incoherent tune shift. In the vertical plane, the tune shifts are negative. The normalized tune shifts of the  $\pi$ -modes are  $(w_x, w_y) = (0.645 \pm 0.005, -0.644 \pm 0.005)$ . In Fig. 10 we show the results for a separation of  $6.0\sigma_x$  and find values of  $(w_x, w_y) = (1.828 \pm 0.005, -1.762 \pm 0.005)$ . Comparing Figs. 9 and 10, the larger tune shift for the smaller separation is clearly visible as well as the increased tune spread of the incoherent spectrum. Both scale with  $1/L_x^2$  as expected.

## 6 CONCLUSIONS.

We have implemented the HFMM technique to describe the beam-beam collision of two beams in the strong-strong regime. This allows us to study, by means of multi-particle tracking and with no approximation in the evaluation of the electromagnetic force, the coherent modes of oscillations of two colliding beams. Future improvements shall extend this work to several bunches per beam and, in particular, will allow us for the first time to study details of the modes excited by long-range interactions.

## 7 ACKNOWLEDGEMENTS

We should like to express our gratitude to M. Craddock (TRIUMF) for supporting this study and to M. D'Yachkov (TRIUMF) who has first suggested the use of the Fast Multipole Method for our problem.

## 8 REFERENCES

- [\*] Present Address: BULL, Paseo Doce Estrellas 2, 28042 Madrid, SPAIN
- [1] K. Yokoya, H. Koiso, *Tune shift of coherent beam-beam oscillations*. Particle Accelerators, Vol. **27**, 181 (1990).
- [2] M.P. Zorzano, F. Zimmermann, *Coherent beam-beam oscillations at the LHC*. CERN, LHC Project Report 314, (1999).
- [3] K. Yokoya, *Limitation of the Gaussian approximation in beam-beam simulations*. Phys.Rev.STAB, Vol. **3**, 124401 (2000).
- [4] Y.I. Alexahin, *On the Landau damping and decoherence of transverse dipole oscillations in colliding beams*. Particle Accelerators, Vol. **59**, 43 (1999).
- [5] Y.I. Alexahin, *A study of the Coherent Beam-beam Effect in the Framework of the Vlasov Perturbation Theory*. CERN, LHC Project Report 467, (2001).
- [6] S. Krishnagopal and R. Siemann, *Coherent beam-beam interactions in electron-positron colliders*. Phys.Rev.Lett., Vol. **67**, 2461 (1991).
- [7] L. Greengard, *The rapid evaluation of potential field in particle systems*. Thesis, Yale (1987), Cambridge, Mass. MIT Press, 1988.
- [8] L. Greengard and V. Rokhlin, *A fast algorithm for particle simulations*. J.Comp.Phys. Vol. **73**, (1987).
- [9] F.W. Jones, *A Hybrid Fast-Multipole Technique for Space-Charge Tracking With Halos*. In Proceedings of the workshop on Space Charge Physics in High Intensity Hadron Rings, Shelter Island NY, May 1998, (AIP Conf. Proc. 1998) 448.
- [10] F.W. Jones, *Development of the ACCSIM tracking and simulation code*. In Proceedings of the 1997 Part. Acc. Conf. Vancouver, May, 1997.
- [11] H. Grote, *Self-consistent orbits with beam-beam effect in the LHC*. CERN, LHC Project Report 404, (2000).
- [12] W. Herr, *Coherent dipole oscillations and orbit effects induced by long-range beam-beam interactions in the LHC*. CERN/SL/91-34 (AP) (1991).
- [13] D. Brandt, W. Herr, M. Meddahi, A. Verdier, *Is LEP beam-beam limited at its highest energy?*. In Proceedings of the 1999 Part. Acc. Conf., New York 1999, (1999).
- [14] A. Hofmann, *Beam-beam modes for two beams with unequal tunes*. In Proceedings of the LHC-99 Beam-beam workshop at CERN, 1999, edited by J. Poole and F. Zimmermann (CERN, Geneva, 1999).
- [15] Y.I. Alexahin and M. P. Zorzano, *Excitation of Coherent Beam-Beam resonances for beams with unequal tunes in the LHC*. CERN LHC Project Note 226, 2000 (unpublished).
- [16] M. Meddahi, *Effets faisceau-faisceau dans le collisionneur protons-antiprotons du SPS*. PhD Thesis, Univ. Paris 7 and CERN SL 91-30 (BI) (1991).
- [17] L. Evans, J. Gareyte, M. Meddahi, R. Schmidt, *Beam-beam effects in the strong-strong regime at the CERN-SPS*. In Proceedings of 1989 Part. Acc. Conf., Chicago 1989, (1989).
- [18] S. Krishnagopal, *Energy transparency and symmetries in the beam-beam interaction*. Phys.Rev.STAB, Vol. **3**, 024401 (2000).
- [19] W. Herr and J. Miles, *A comparative study of beam-beam tune footprints for colliding beams with a crossing angle and offset vertex in LHC V4.1*. CERN LHC Project Note 4, 1995 (unpublished).
- [20] O. Meincke and H. Grote, *Tune footprints for collision optics 5.0*, CERN LHC Project Note 161, 1998 (unpublished).
- [21] W. Herr, M.P. Zorzano and F. Jones, *Analysis of coherent long-range interactions using a Hybrid Fast Multipole Method*. To be published.

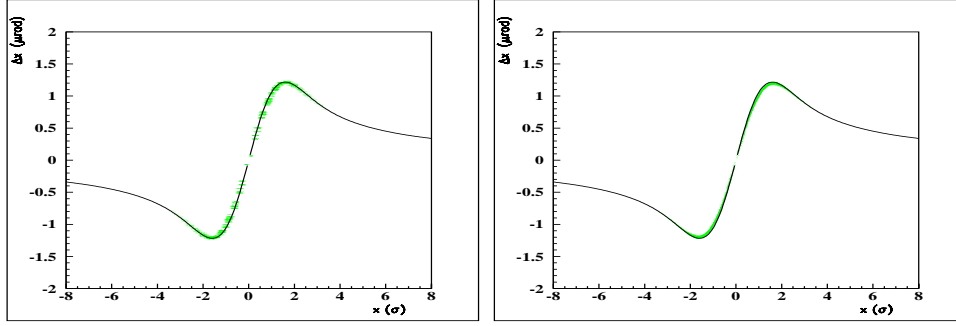


Figure 1: Beam-beam kick as calculated with HFMM (points) and from analytical expression (solid line) for round beams with Gaussian distribution. Left figure with  $0.25\sigma$  grid ( $81 \times 81$ ) and 'nearest-grid-point' assignment. Right figure with 'cloud-in cell' (CIC) assignment.

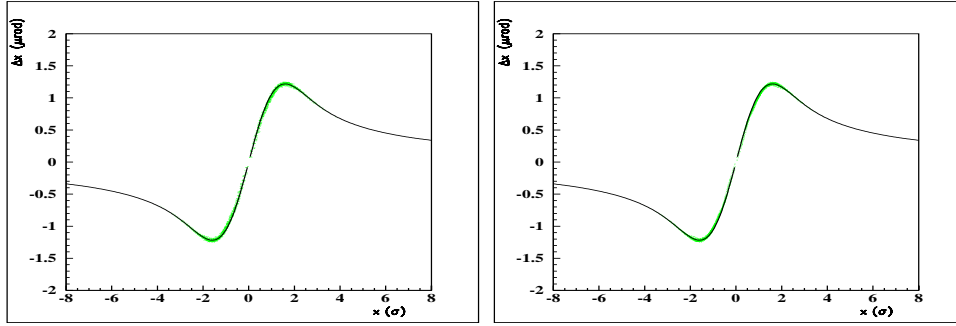


Figure 2: Beam-beam kick as calculated with HFMM (points) and from analytical expression (solid line) for round beams with Gaussian distribution. Left figure with  $0.10\sigma$  grid ( $201 \times 201$ ) and 'nearest-grid-point' assignment. Right figure with 'cloud-in cell' (CIC) assignment.

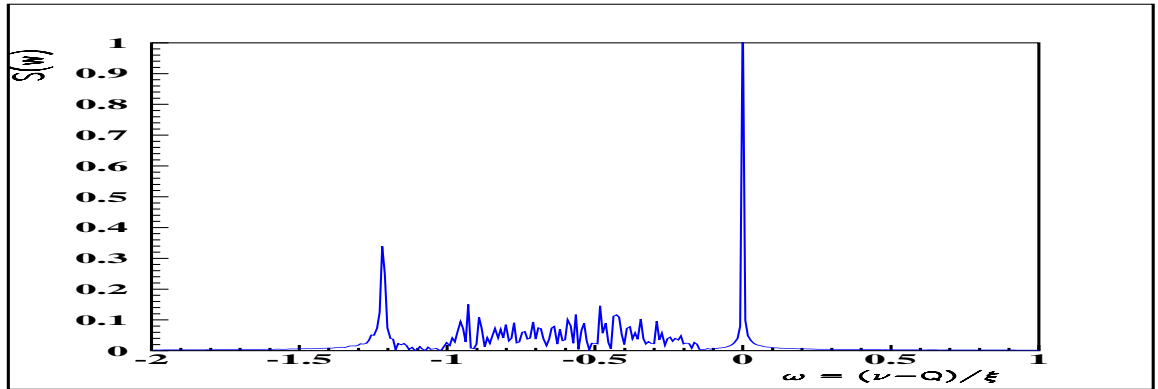


Figure 3: Frequency spectrum of the bunch centroid motion (for  $2^{17}$  turns,  $N = 10^4$  macroparticles) for round beams. The grid covers from  $-10\sigma$  to  $10\sigma$ , the rest of the particles being treated as halo particles. The horizontal axis gives the tune shift from the unperturbed tune  $Q$  in units of  $\xi$ , i.e.  $w = \frac{\nu - Q}{\xi}$ . The vertical axis is the corresponding amplitude. The  $\pi$ - and  $\sigma$ - oscillation modes are clearly visible.

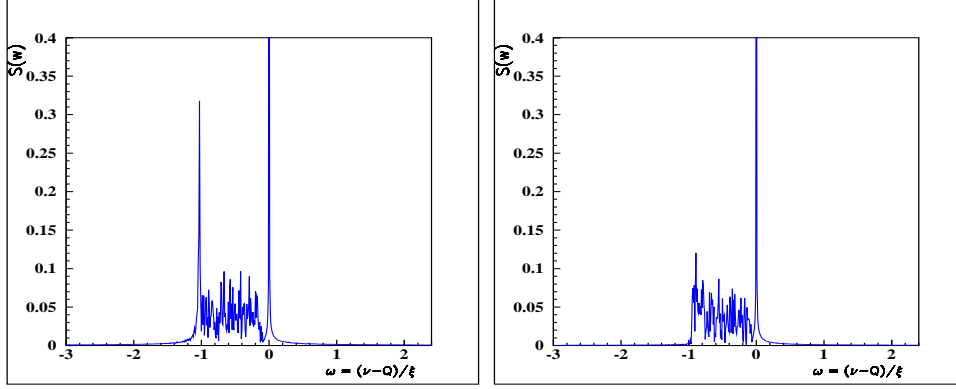


Figure 4: Frequency spectrum of the bunch centroid motion (over  $2^{17}$  turns,  $N = 10^4$  macroparticles) for round beams and intensity ratio  $R_I = 0.65$  (left) and  $0.55$  (right).

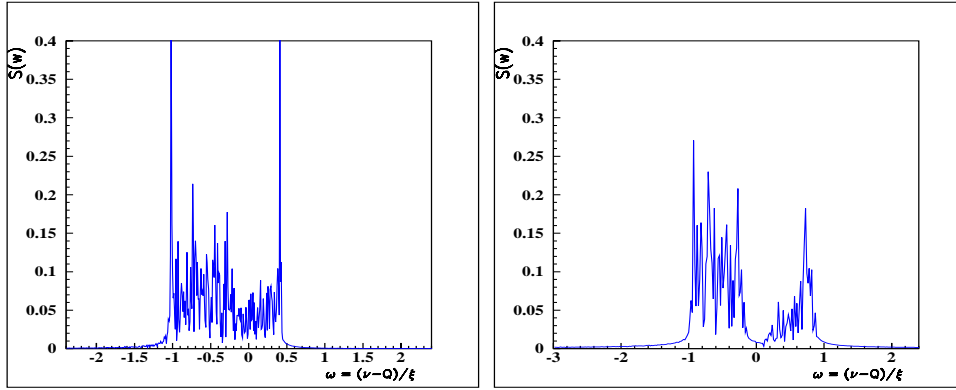


Figure 5: Frequency spectrum of the bunch centroid motion (for  $2^{17}$  turns,  $N = 10^4$  macroparticles) for round beams and different fractional tunes of the second beam:  $0.312$  (left) and  $0.313$  (right). The tune of the first beam is kept at  $0.310$ .

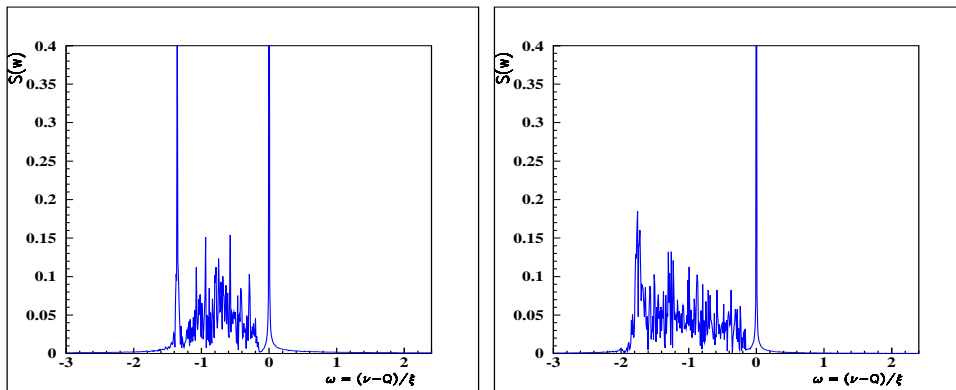


Figure 6: Frequency spectrum of the bunch centroid motion (for  $2^{17}$  turns,  $N = 10^4$  macroparticles) for round beams and size ratios  $\sigma^{(2)}/\sigma^{(1)}$  of  $0.90$  (left) and  $0.70$  (right).

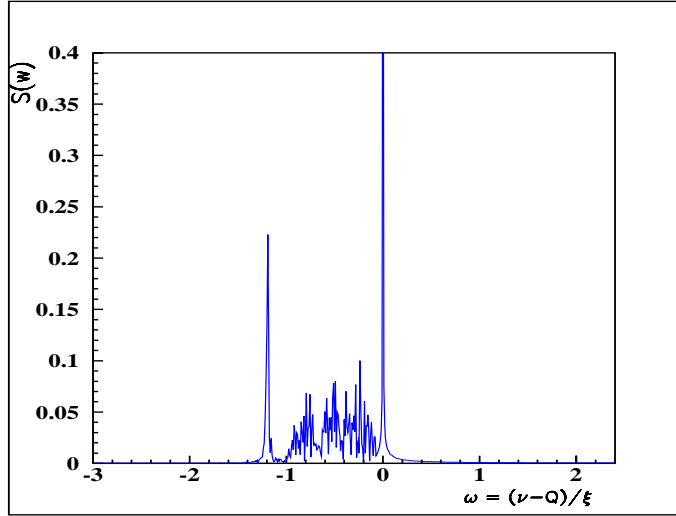


Figure 7: Frequency spectrum of the bunch centroid motion (for  $2^{17}$  turns,  $N = 10^4$  macroparticles) for round beams and size ratios  $\sigma^{(2)}/\sigma^{(1)} = 0.70$  and intensity ratio  $R_I = 0.5$ .

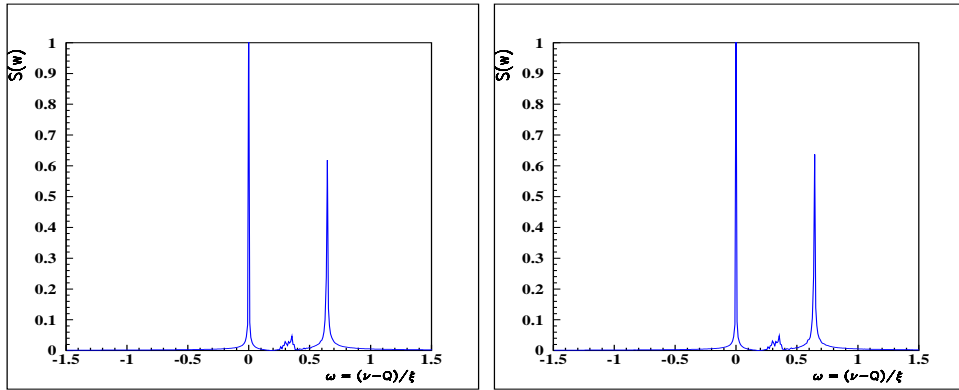


Figure 8: Spectrum of the horizontal centroid motion for long-range collisions with horizontal separation  $L_x = 10.0$  (in units of  $\sigma_x$ ) and no head-on collision ( $2^{15}$  turns,  $N = 10^4$  macroparticles). For the left figure the grid did not cover both separated beams, i.e. the particles in the second beam were treated as halo particles. In the right figure the grid covered both beams.

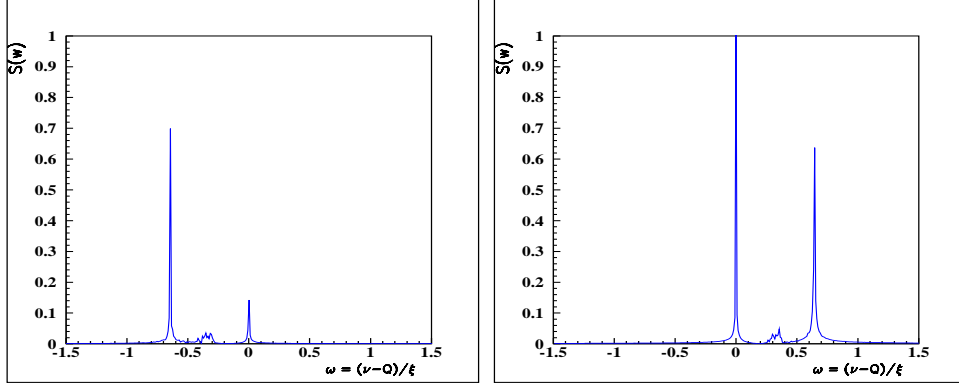


Figure 9: Spectrum of the vertical (left) and horizontal (right) centroid motion for long-range collisions with horizontal separation  $L_x = 10.0$  (in units of  $\sigma_x$ ) and no head-on collision ( $2^{15}$  turns,  $N = 10^4$  macroparticles). The tune shifts due to long-range collisions have opposite sign in the two transverse planes. The coherent  $\pi$ -mode is at twice the incoherent tune shift.

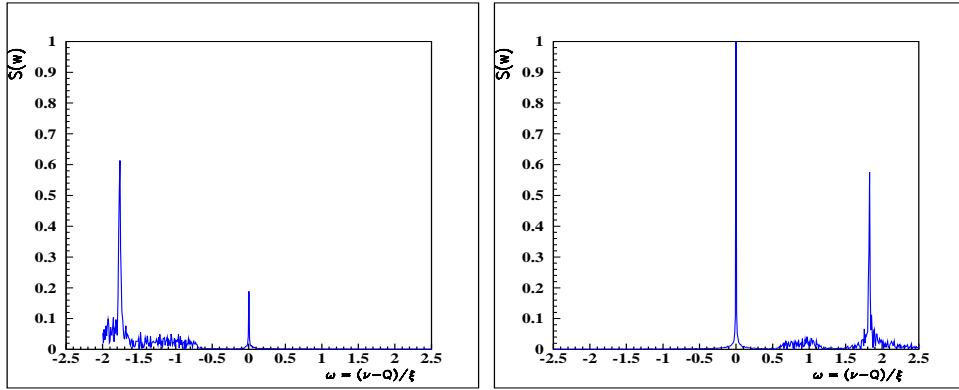


Figure 10: Spectrum of the vertical (left) and horizontal (right) centroid motion for long-range collision with horizontal separation  $L_x = 6.0$  (in units of  $\sigma_x$ ) and no head-on collision ( $2^{15}$  turns,  $N = 10^4$  macroparticles). The tune shifts due to long-range collisions have opposite sign in the two transverse planes.

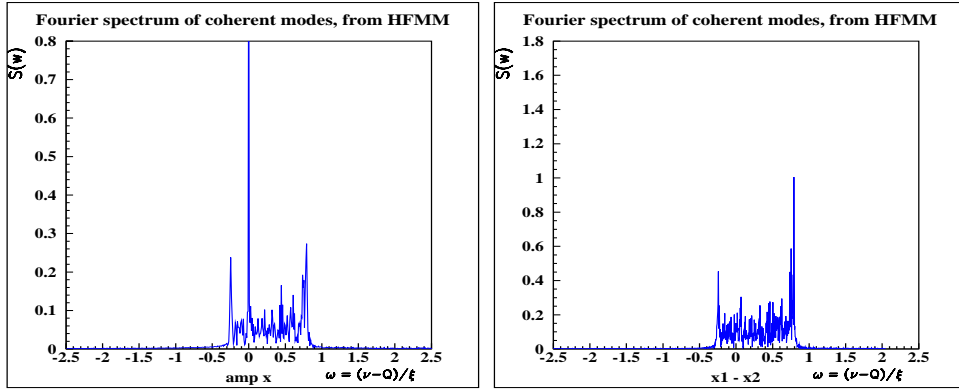


Figure 11: Spectrum of the horizontal centroid motion for head-on together with long-range collision with horizontal separation  $L_x = 6.0$  (in units of  $\sigma_x$ )  $2^{15}$  turns,  $N = 10^4$  macroparticles. planes. In the right figure  $\pi$ -oscillations only.

# Two Methods for Simulating the Strong–Strong Beam–Beam Interaction in Hadron Colliders

Mathias Vogt (UNM), James A. Ellison (UNM),  
Tanaji Sen (FNAL), and Robert L. Warnock (SLAC)

## Abstract

We present and compare the method of weighted macro particle tracking and the Perron–Frobenius operator technique for simulating the time evolution of two beams coupled via the collective beam–beam interaction in 2–D and 4–D (transverse) phase space. The coherent dipole modes, with and without lattice nonlinearities and external excitation, are studied by means of the Vlasov–Poisson system.

## 1 INTRODUCTION

Simulations of coherent effects in many particle systems traditionally employ Particle–in–Cell (PIC) methods with an ensemble of macro–particles generated by the Monte Carlo method. We have developed two alternative approaches, the discretized Perron–Frobenius method (PF) and weighted macro–particle tracking (WMPT). We have written several codes, a PF/Fokker–Planck code in one degree of freedom (including diffusion and dissipation) and the hadron codes BBPF $m$ D (Beam–Beam Perron–Frobenius) and BBDeMomD (Beam–Beam Density and Moments, i.e. WMPT) with  $m = 1, 2$  in  $m$  degrees of freedom. The PF/Fokker–Planck code is described in detail in [1]. Here we will concentrate on the completely symplectic hadron codes.

## 2 MODELS AND METHODS

### 2.1 The Ring Model

We assume a ring with one IP at  $\theta = 0$  and two counter-rotating bunches. We only treat head–on collisions here and our reference point at which the distribution is studied is directly *before* the IP ( $\theta \bmod 2\pi = 0^-$ ). In what follows we will always use the convention that if some parameter, or dynamical variable  $X$  describes one beam, then  $X^*$  describes the other beam.

Let  $\psi_n(\vec{z})$  and  $\psi_n^*(\vec{z})$  ( $\vec{z} := (q, p)^T$ ) denote the normalized phase space densities of the beams at  $\theta = 0^- + 2n\pi$  (Here and in the following we use  $:=$  or  $\equiv$ : if we want to emphasize that the quantity on the left or right respectively is being defined). Then the representations of the one turn map for the unstarred beam from turn  $n$  to  $n + 1$ , implemented in BBPF $m$ D and BBDeMomD so far, are

$$\vec{T}[\psi_n^*] = \vec{A} \circ \vec{K}[\psi_n^*] \quad (1)$$

where

$$\vec{A} = \begin{cases} \vec{R} & : \text{linear} \\ \vec{R}^{\frac{1}{2}} \circ \vec{K}_p \circ \vec{R}^{\frac{1}{2}} & : \text{lin. \& pert.} \\ \vec{R}_{\frac{\pi}{2}}^- \circ \vec{K}_s \circ \vec{R}' \circ \vec{K}_s \circ \vec{R}_{\frac{\pi}{2}}^+ & : \text{lin. \& IR-sxt.} \end{cases} \quad (2)$$

The  $\vec{R}$ 's represent the linear stable symplectic parts of the lattice ( $\vec{R}(\vec{z}) = \underline{R}\vec{z}$ ). At the moment the two degree of freedom versions of our simplified ring models have block diagonal representations of the linear lattice, in other words they do not contain linear coupling. The  $\vec{K}$ 's are symplectic kicks. In particular,  $\vec{K}[\psi_n^*]$  is the collective beam–beam kick on the unstarred beam due to the starred beam,  $\vec{K}_p$  is an RF–dipole and/or a multipole kick (up to dodecapole) and  $\vec{K}_s$  is an IR–sextupole. In the case of a completely linear lattice,  $\underline{R}$  is parameterized by the tune  $Q$  and the unperturbed Courant–Snyder parameters  $\beta_0$  and  $\alpha_0$  at the IP. In the second case, where a perturbation is included in the center of the arc,  $\underline{R}^{\frac{1}{2}}$  each have a phase advance of  $\pi Q$  so that  $\underline{R} = (\underline{R}^{\frac{1}{2}})^2$ . In the third case,  $\underline{R}_{\frac{\pi}{2}}^-$  and  $\underline{R}_{\frac{\pi}{2}}^+$  transform the Courant–Snyder parameters at the IR–sextupoles to those at the IP with a phase advance of  $\pi/2$  and  $\underline{R}'$  is parameterized by the phase advance  $2\pi(Q - 1/2)$  and the Courant–Snyder parameters at the IR sextupoles. Note that all three possible ring layouts are mirror symmetric around the axis through the IP and the center of the arc. The different different ring layouts are shown in Figure 1. The collective kick  $\vec{K}[\psi]$  is given by

$$\vec{K}[\psi](q, p) = \begin{pmatrix} q \\ p + K[\psi](q) \end{pmatrix}, \quad (3)$$

$$K[\psi](q) = \zeta \int_{\mathbb{R}^m} g(q, q') \rho(q') d^m q' \quad (4)$$

with a model dependent kernel function  $g$ , a strength parameter  $\zeta$  and the spatial density  $\rho(q) = \int_{\mathbb{R}^m} \psi(q, p) d^m p$ . The ring models described in Eq. (2) are illustrated in Fig. 1, where S.O.D... refers to sextupole, octupole, decapole, etc. and RFD refers to RF–dipole. For the codes in two degrees of freedom, we plan to implement the MAD–interpreter and the map generators from the spin code SPRINT [2] and the higher order symplectic integrators described in [3].

The particle trajectories are propagated turn by turn via

$$\vec{z}_{n+1} = \vec{T}[\psi_n^*](\vec{z}_n), \quad \vec{z}_{n+1}^* = \vec{T}^*[\psi_n](\vec{z}_n^*) \quad (5)$$

and since the maps are measure preserving, the densities evolve via

$$\psi_{n+1}(\vec{z}_{n+1}) = \psi_n(\vec{z}_n), \quad \psi_{n+1}^*(\vec{z}_{n+1}^*) = \psi_n^*(\vec{z}_n^*) \quad (6)$$



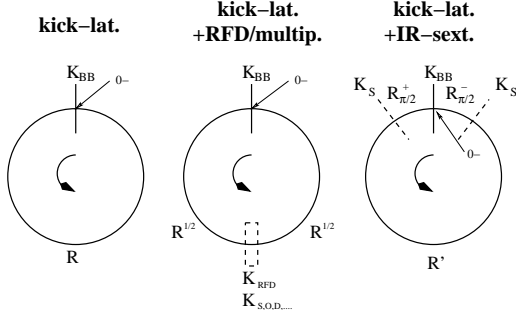


Figure 1: Ring models.

Note that the  $\vec{T}$  and  $\vec{T}^*$  are explicitly distinguished, allowing for different parameter sets describing the starred and the unstarred lattice. Equations (1–6) define a representation of the beam–beam Vlasov–Poisson system using maps.

In highly relativistic beams the beam–beam force for head–on bunch crossings with zero crossing angle is essentially transverse. In this approximation the collective kick is determined by the solution of a 2–D Poisson problem,  $-\Delta u = f$ . The Green function in two dimensions for open boundary conditions is given by

$$G(x, y, x', y') = -\frac{1}{2\pi} \log \left( \sqrt{(x - x')^2 + (y - y')^2} \right). \quad (7)$$

We started our study by analyzing three different limits of the beam–beam interaction giving one degree of freedom. Here we shall discuss only the limit studied by Chao and Ruth (CR) [5], which is meant to model beams with large horizontal-to-vertical aspect ratio, a case often found in electron machines. The force on a particle in one beam from the other beam is computed as though it came from infinite planes of charge, perpendicular to the vertical ( $y$ ) axis, and distributed in  $y$  with some density. This force is concentrated in time, however, at the instant of collision. The motion is in the  $y$ -direction only. Although not quite appropriate for hadron machines, the model is an attractive starting point because it is the only case in one degree of freedom for which a completely self-consistent calculation can be done with an operation count  $\mathcal{O}(N \log N)$  in the WMPT method. Similarly, it is particularly easy to implement in the PF method. The Green function of the corresponding Poisson problem is equal to  $-|y - y'|/2$ , while its gradient  $-\text{sgn}(y - y')/2$  is proportional to the kernel of Eq. (4). See [5, 6, 4] for more information on the three limits giving one degree of freedom.

## 2.2 The Perron–Frobenius Method

The Perron–Frobenius method [1] and weighted macro-particle tracking are both based on the evolution law (6) for the phase space densities given a measure preserving map. We can rewrite Eq. (6) in the form  $\psi_{n+1}(\vec{z}) = \psi_n(\vec{T}^{-1}[\psi_n^*](\vec{z}))$  and an analogous equation for  $\psi_{n+1}^*$ .

This defines the action of the Perron–Frobenius operator associated with (1) on the densities. Now consider a rectangular mesh for  $m = 1$ :  $\{\vec{z}_{ij}\}$ ,  $\vec{z}_{ij} := (i\Delta_q, j\Delta_p)$ , where  $\Delta_q$  and  $\Delta_p$  are the grid spacings in configuration and momentum space respectively and the integers  $i$  and  $j$  satisfy  $-\frac{n_q}{2} \leq i \leq \frac{n_q}{2}$  and  $-\frac{n_p}{2} \leq j \leq \frac{n_p}{2}$ . In the case of a  $2m$  dimensional phase space ( $m > 1$ ),  $i$  and  $j$  are  $m$ -dimensional multi-indices and  $\Delta_q, n_q$ , etc. are  $m$ -dimensional vectors and we have the obvious generalization of the above rectangular grid. Given approximations  $\Psi_{ij}(n)$  and  $\Psi_{ij}^*(n)$  to  $\psi_n(\vec{z}_{ij})$  and  $\psi_n^*(\vec{z}_{ij})$  and an  $l$ -th order local interpolation scheme (“stencil”)  $S_l[f](\vec{z})$  which interpolates values of  $f$  at neighboring mesh points of  $\vec{z}$ , we can update  $\Psi(n)$  to  $\Psi(n+1)$  by

$$\Psi_{ij}(n+1) = S_l[\Psi(n)] \left( \vec{T}^{-1}[\Psi^*(n)](\vec{z}_{ij}) \right). \quad (8)$$

For example in the kick–lattice model of Eq. (1) we have  $\vec{T}[\psi_n^*] = \vec{R} \circ \vec{K}[\psi_n^*]$  and  $\vec{T}^{-1}[\psi_n^*] = \vec{K}^{-1}[\psi_n^*] \circ \vec{R}^{-1}$ . To compute this given the  $\Psi_{ij}^*(n)$  we first sum over  $j$  to get an approximation  $\varrho_i^*(n)$  of the spatial density,  $\rho_n^*(q_i)$ , on the spatial sub-mesh  $\{q_i\}$  and then we use  $\varrho^*(n)$  to determine the kicks at the mesh points  $q_i$ . Spatial interpolation then gives the kicks at all  $q$ . Thus we obtain  $\vec{T}^{-1}[\psi_n^*](\vec{z}_{ij}) \approx \vec{K}^{-1}[\Psi^*(n)](\vec{R}^{-1}\vec{z}_{ij})$  where  $\vec{R}$  is the matrix for the linear lattice. These points are not mesh points so we need the interpolant of  $\Psi(n)$  in (8). Note that this procedure uses two interpolations where in (8) we only emphasize the latter. This is because the intermediate interpolation is relatively cheap, being an interpolation in configuration space rather than in phase space. The lattice–kick model,  $\vec{T}[\Psi^*(n)] = \vec{K}[\Psi^*((n+1)^-)] \circ \vec{R}$  where  $\Psi_{ij}^*((n+1)^-) := S_l[\Psi^*(n)](\vec{R}^{-1}\vec{z}_{ij})$ , would be more expensive because it would require two interpolations in *phase space* and phase space interpolation is the most expensive part of this calculation.

We want to stress that since  $\Psi(n)$  is known, the corresponding spatial density  $\varrho(n)$  on the  $m$ -dimensional spatial sub-mesh is given by simply summing  $\Psi(n)$  over the second, momentum multi-index. If the mesh has  $N =: n_g^{2m}$  mesh points in total, then in the *worst case* the  $\sqrt{N} = n_g^m$  different kicks on the spatial sub-mesh can be computed by multiplying the  $\sqrt{N}$  vector  $\varrho(n)$  with a  $\sqrt{N} \times \sqrt{N}$  matrix, the discretized kernel, giving a worst case operations count of  $\mathcal{O}(N)$  for computation of the collective kick. Actually, even if (e.g. in the CR case) the collective kick can be computed less expensively ( $\mathcal{O}(\sqrt{N} \log N)$ ), the application of the kick to the  $N$  mesh points is, although usually unproblematic, always  $\mathcal{O}(N)$ . In other words a  $N$  particle tracking routine with an operations count of less than  $\mathcal{O}(N)$  is impossible.

We have developed a Vlasov Fokker–Planck code[1] in 2–D phase space for leptons (not restricted to beam–beam interaction) and two hadron codes (without the Fokker–Planck step) in 2–D and 4–D phase space (BBPF1D and BBPF2D). The order of the interpolation scheme can be chosen, but at least in 2–D phase space quadratic or cubic inter-

polarization seems sufficient. In Section 2.5 we will compare PF and WMPT simulations in one degree of freedom and see that with properly chosen mesh parameters the methods are in good agreement, at least in principal aspects.

In 4-D phase space unfortunately the number  $n_g$  of mesh points in *each* dimension required to preserve probability to a decent level has to be so large that the 4-D PF algorithm in its serial (single CPU) version is possibly too slow. In particular since the local 4-D interpolation between neighbors along the 4-D mesh axis is not local in the *linear* memory of the computer, it requires accessing array elements with potentially large stride and thus potentially produces a large amount of cache misses (potentially many more than one per updated mesh point). Note that already in a serial code, domain decomposition of the mesh into blocks smaller but comparable with the cache size of the computer would give some (unfortunately hardware dependent, non-portable) relief.

### 2.3 Weighted Macro Particle Tracking

WMPT [4] is a method for computing time dependent phase space averages of  $f$

$$\langle f \rangle_n := \int_{\mathbb{R}^{2m}} f(\vec{z}) \psi_n(\vec{z}) d^{2m} z \quad (9)$$

$$\langle f \rangle_n^* := \int_{\mathbb{R}^{2m}} f(\vec{z}) \psi_n^*(\vec{z}) d^{2m} z \quad (10)$$

via

$$\begin{aligned} \langle f \rangle_n &= \int_{\mathbb{R}^{2m}} f(\vec{z}) \psi_0(\vec{M}_n^{-1}(\vec{z})) d^{2m} z \\ &= \int_{\mathbb{R}^{2m}} f(\vec{M}_n(\vec{z})) \psi_0(\vec{z}) d^{2m} z \end{aligned} \quad (11)$$

where  $\vec{M}_n := \vec{T}[\psi_{n-1}^*] \circ \dots \circ \vec{T}[\psi_0^*]$  is the symplectic  $n$ -turn map containing successive collective kicks. Note that the beam-beam kick function can be written as such an average over the beam-beam kernel with  $q$  fixed

$$K[\psi_n^*](q) = \zeta \langle g(q, \cdot) \rangle_n^* . \quad (12)$$

Now starting with the initial densities  $\psi_0$  and  $\psi_0^*$  defined on an *initial mesh*  $\{\vec{z}_{ij}\}$ , a quadrature formula with weights  $w_{ij}$ , and trajectories  $\vec{M}_n(\vec{z}_{ij})$ , we can approximate  $\langle f \rangle_n \approx \sum_{ij} f(\vec{M}_n(\vec{z}_{ij})) \psi_0(\vec{z}_{ij}) w_{ij}$ . Of course if we approximate the kicks in Eq. (12) by this method we will only have approximate trajectories  $\vec{\eta}_{ij}(n) \approx \vec{M}_n(\vec{z}_{ij})$ . Thus our final approximation is

$$\langle f \rangle_n \approx \sum_{ij} f(\vec{\eta}_{ij}(n)) \psi_0(\vec{z}_{ij}) w_{ij} . \quad (13)$$

Note that this procedure uses only forward tracking of particles with an additional pre-assigned and a constant “total weight”  $\mathfrak{W}_{ij} := \psi_0(\vec{z}_{ij}) w_{ij}$ . Conservation of probability is guaranteed by construction. Also note that the initial mesh structure is lost after the first turn. Thus, in contrast

to methods with an explicit mesh (like PF), naive computation of the collective kick is an  $O(N^2)$  operation. In the CR case, ordering the trajectories  $\vec{\eta}_{ij}(n)$  and  $\vec{\eta}_{ij}^*(n)$  with respect to the spatial coordinate at the cost of  $O(N \log N)$  makes the remaining part of the computation of the collective kick  $O(N)$  (see [4]). In the two degree of freedom case the hybrid fast multipole method (HFMM) [7] allows efficient computation of the kicks ( $O(N)$  with a *reasonable* order constant !) as long as the distributions of the trajectories in configuration space are sufficiently regular.

### 2.4 An Implementation of HFMM for WMPT

HFMM [7] is a hybrid of the fast multipole method (FMM) developed by Greengard and a PIC based reduction of the number of independent particles developed by Jones for space charge and applied the first time to beam-beam simulations by Herr, Zorzano and Jones. FMM is a tree code that allows the computation of the collective force of an ensemble of  $N$  charges on themselves to a given accuracy  $\delta$  with an operations count  $O(N)$  given that the distribution of the ensemble in configuration space is not too irregular. It employs the fact that the force on a test charge due to a distant localized “clump” of charge is given by a *finite order* multipole expansion up to precision  $\delta$ .

The FMM algorithm successively subdivides an outer rectangle in configuration space occupied by the ensemble until, on the finest level of subdivision, no more than a fixed number (typically 40) of particles are in each box. This leads to a tree structure of boxes containing boxes containing boxes and so on, until the boxes on the finest level finally contain a small number of particles. In the non-adaptive version of the scheme all boxes on the same level have the same number of child boxes (weighted tree). We use the adaptive version, which means that a box only branches into child boxes if the box itself still contains too many particles. Then the algorithm computes the multipole (long distance) expansions for all boxes on the finest level explicitly. The next step is to generate multipole expansions around the center of the parent boxes by translating their children’s expansions to the center and adding them up so that in the end every box, no matter which level of mesh refinement it belongs to, has its own long distance expansion. Then the far fields inside each box due to all sufficiently well separated boxes are converted to Taylor (local) expansions on each level going down from the coarsest possible level to the finest level. Finally, for each box on the *finest* level, the forces due to charges in a close vicinity have to be computed directly. The 2-D adaptive routines (DAPIF2), used in our simulations, were supplied by Greengard. For more details see Greengard in [7].

Unfortunately, FMM needs about 16–18 times  $N$  REAL\*8 words of workspace and in addition the order constant of this  $O(N)$  algorithm is large enough to be prohibitive for the purpose of multi-turn tracking of many millions of particles.

The original HFMM (Jones) divided the configuration

space into core- and halo domains, superimposed a PIC mesh on the core domain, deposited the core charges on the PIC mesh and passed the joint set of the mesh points and halo particles to FMM. The idea is that if the core is populated densely enough, then the approximation of a PIC type charge collection strongly decreases the required computational resources while not strongly affecting the accuracy of the force computation. On the other hand, the halo particles would not be very well represented on a PIC mesh and in addition would need an unreasonably large mesh to cover the halo.

Our implementation of HFMM in BBDeMo2D first determines an outer rectangle in configuration space around the joint starred and unstarred particles. We then divide the rectangle into two parts, a “core” region where the density of particles is high and a “halo” region where the density of particles is small. To do this we divide this rectangle into  $n_g \times n_g$  cells. The idea is (as pointed out above) to represent the core by depositing the weights of the particles on the corners of the cells and to represent the halo particles by themselves. In order to find the core and halo regions dynamically (adaptively) we proceed as follows. The population of each cell is determined. Cells with less than a specified minimum number of particles are put into the halo and the remaining cells are put into the core. This determines the number of corners of the core cells,  $N_c$ , and the number of halo particles,  $N_p$ , and then  $N_c + N_p$  is the number of entries in the charge and coordinate lists for the FMM routine. If  $N_c + N_p$  is deemed too large, we decrease the minimum number of particles required for a cell to be part of the core and evaluate the cells anew. In general this increases  $N_c$  but decreases  $N_p$  significantly. Once we are satisfied with the size of  $N_c + N_p$ , the total weights  $\mathfrak{W}_{ij}^*$  of the trajectories of the starred beam are either assigned to the corners of the finally chosen core cells by some PIC scheme (currently “cloud in cell”) or, if the trajectories are inside halo cells their weights are kept as single entries in the charge list. In this step, the weights  $\mathfrak{W}_{ij}$  of the unstarred beam are not used but the unstarred trajectories inside halo cells are passed to the coordinate list. Then the FMM routine computes the forces due to the starred charges at all the  $N_c + N_p$  coordinates. The kicks are either directly applied to the unstarred trajectories in the halo cells or distributed among the unstarred trajectories in the core cells by an interpolation scheme related to the original PIC deposition scheme. Finally, the process is repeated with the role of the starred and the unstarred trajectories interchanged. Note that only the charge list has to be reassigned. The coordinate lists stay the same for both calls to DAPIF2.

This method performs the most time consuming step, the FMM, in  $O(N_c + N_p)$  operations and only needs 16–18 times  $(N_c + N_p)$  REAL\*8 words of workspace. Thus if  $N_c + N_p \ll N$ , a significant decrease in computation time and workspace is achieved. For example, in a typical BBDeMo2D run with  $45^4 \approx 4 \cdot 10^6$  macro-particles per beam, we use a PIC mesh of size  $150 \times 150 = 22,500$ . If we allow  $N_c + N_p \leq 5 \times 22,500$ , the reduction of entries in the

FMM lists is about 70. For a more extreme example with  $61^4 \approx 14 \cdot 10^6$  particles per beam the reduction is actually close to 250.

## 2.5 Comparison of PF and WMPT

Both the PF and WMPT methods, in their current implementation in BBPFmD and BBDeMoD, use a uniform (in the case of WMPT *initial*) mesh, but, in principle, both methods allow more general non-uniform meshes. The uniform (initial) mesh which covers a finite rectangular domain in phase space, typically  $\pm 5$  initial beam widths ( $\sigma_0$ ) for WMPT or  $\pm 6-7\sigma_0$  for PF, treats its inner (core) and outer (“halo”) regions equally. Thus in contrast to conventional macro-particle methods, where the initial beam distribution is typically represented by a Monte Carlo generated ensemble of particles of equal weight and concentrated around the core, the two methods used here are expected to simulate the evolution of the higher order beam moments more accurately. A round-Gaussian ensemble in 2-D phase space with 40,000 particles has about 39,600 (99%) of its particles contained in the  $\pm 3\sigma_0$  square. A WMPT or PF ensemble with  $200 \times 200$  particles or mesh points on a uniform square mesh of size  $\pm 5\sigma_0$  has only  $120 \times 120 = 14,400$  (36%) of the particles/mesh points in the  $\pm 3\sigma_0$  square and 25,600 particles outside. In the current implementation, the BBPFmD codes use local interpolation in the tensor-product space spanned by the quadratic or cubic polynomials over the mesh axes. All 4 codes use the simplest possible quadrature formula, namely the Gaussian midpoint formula with  $w_{ij} = \prod_{i=1}^{2m} \Delta z_i$  independent of  $i$  and  $j$ .

In several one degree of freedom examples, we have checked agreement between the BBPF1D and BBDeMo1D codes. Here we study the turn by turn evolution of the centroids  $\bar{q}_n^{\sigma,\pi} := \langle q \rangle_n \pm \langle q \rangle_n^*$ , as well as the evolution of the beam emittance  $\epsilon_n := \sqrt{C_n^{2,0} C_n^{0,2} - (C_n^{1,1})^2}$ , where  $C_n^{i,j} := \langle (q - \langle q \rangle_n)^i (p - \langle p \rangle_n)^j \rangle_n$ .

Let us summarize the approximations of the time dependent phase space averages used in the two cases

$$\langle f \rangle_n \approx \begin{cases} \sum_{ij} f(\vec{z}_{ij}) \Psi_{ij}(n) w_{ij} & : \text{PF} \\ \sum_{ij} f(\vec{\eta}_{ij}(n)) \psi_0(\vec{z}_{ij}) w_{ij} & : \text{WMPT} \end{cases} \quad (14)$$

Figure 2 shows excellent agreement between the  $\pi$  mode frequencies and the spectra of the  $\sigma$  modes obtained for  $\xi = 0.003$  and almost identical linear tunes  $Q_0 = \sqrt{5} - 2$  in the CR limit, giving some confidence in the methods. The difference between the two  $\pi$  mode spectra needs further study, but we will comment briefly on this later. Both beams were initially round Gaussians in phase space with the unstarred beam having an initial coherent betatron amplitude of  $0.1\sigma_0$ . The initial density was represented by a  $201 \times 201$  square grid over  $\pm 5\sigma_0$  in both directions for WMPT and the grid for the PF simulation used  $241 \times 241$  points over  $\pm 6\sigma_0$ . Note that the initial mesh used for WMPT only needs to cover the domain in

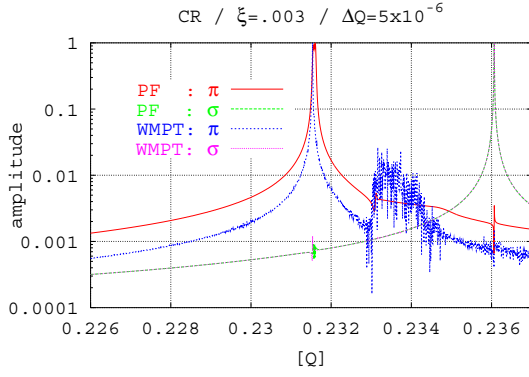


Figure 2: (color) Comparison between PF and WMPT : coherent dipole modes.

phase space where the *initial* density contributes significantly to the phase space averages. If we want to follow up to 4-th order centered moments of an initially round Gaussian ensemble, then  $\pm 5\sigma_0$  around  $\langle z \rangle_0$  is a reasonable choice, as that is the domain where the functions  $(z_k - \langle z_k \rangle_0)^4 e^{-(z_k - \langle z_k \rangle_0)^2 / (2\sigma_0^2)}$ ,  $k = 1, 2m$  are not negligibly small. Thus for example the *computed* initial kurtosis  $C_0^{4,0}$  with the chosen cut off is close enough (typically  $10^{-4}$ ) to its exact value  $3\sigma_0^2$ . PF on the other hand requires a mesh that is large enough to take care of centroid oscillations and emittance blow up *during* the simulation. The FFT was performed over data from  $2^{17}$  turns. The two  $\sigma$  mode spectra (peak on the right) are indistinguishable and the two  $\pi$  mode spectra have nearly the same tune. The Yokoya factor  $(Q_\sigma - Q_\pi)/\xi$  for the Chao–Ruth model comes out higher ( $\approx 1.51$ ), than in the round beam case [4]. In [8] we have introduced an averaged Vlasov equation and linearization around a Gaussian equilibrium of the averaged system yields exactly this value for the Yokoya factor. We don't understand as yet why the agreement is so good. The incoherent continuum due to the single particle motion is more pronounced in the WMPT spectrum, because it keeps track of  $N$  actual trajectories, whereas PF smoothes out the density in each interpolation step. This needs further study. Figure 3 shows the initial emittance growth due to filamentation in an example with a tune split  $\Delta Q_0 = 2\xi = 0.006$ . The unstarred beam had an initial coherent betatron amplitude of  $1\sigma_0$ . All other beam and simulation parameters were the same as in Fig. 2. Both simulations agree up to the 1% level, but the general impression is that the time evolutions obtained with WMPT are a little more noisy (“wiggly”) than those obtained with PF. We conclude here that with properly chosen mesh sizes both methods agree very well qualitatively and also, to a large extent, quantitatively. Nevertheless, in situations where there are neither large amplitude coherent oscillations nor large emittance growths present the PF method in one degree of freedom is slightly more efficient and stable than WMPT.

Simulations in 4–D phase space (2 d.o.f.) are much more

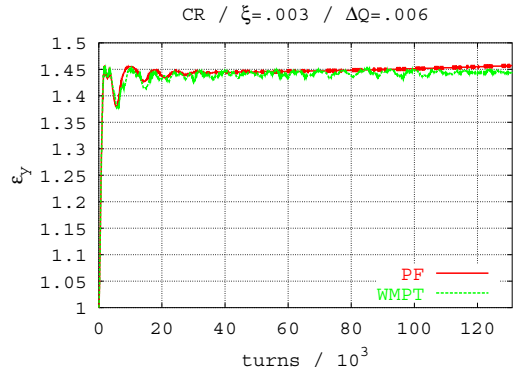


Figure 3: (color) Comparison between PF and WMPT : emittances.

computationally expensive. In conventional macro-particle simulations the phase space ensemble is generated by the Monte Carlo method. There one is tempted to use a relatively small number of macro-particles to gain computational speed, because the actual accuracy of the representation of the density in phase space is somewhat hidden at first sight. But looking at the sampling from the point of a uniform (initial) mesh, suggests that following the evolution of a phase space density over a large number of turns in the presence of a collective force requires a large number of macro-particles or mesh points. Let us assume we want a decent representation of the density on a rectangular domain with  $\pm 5\sigma_0$  in 4–D phase space. Then even with moderate beam–beam parameters around  $3 \cdot 10^{-3}$ , our studies using WMPT with  $N = 11^4$  to  $N = 61^4$  have shown that one should have at least 30–40 particles *per phase space dimension* and per bunch in order avoid instabilities over 16,000 turns. It is clear that with this large number of macro-particles / mesh points any method for the computation of the collective kicks which has an operations count of more than  $O(N)$  is prohibitive, but even with an operations count of  $O(N)$  the restrictions imposed by computation time and memory requirements are hard to meet. In the case of BBDeMo2D, we employ HFMM as explained in Section 2.4, and a typical (serial) run with  $45^4$  macro-particles over  $2^{14}$  turns on a SUN ULTRA–80 dual UltraSparc–II workstation with 450 MHz clock, 3GB RAM and 4MB cache takes about 145h (6 days) CPU time.

In the PF case, the interpolation and not the calculation of the collective force determines the performance. With a local cubic 4–D interpolation, the updating of each mesh point touches 256 neighboring mesh points in phase space. As pointed out in Section 2.2, the 4–D structure of the mesh leads to a large amount of cache misses and thus increases the execution time even more. In addition, even with cubic 4–D interpolation and with  $N = 51^4 \approx 6.8 \cdot 10^6$  mesh points the conservation of probability is relatively poor. As an example, a BBPF2D run with  $N = 51^4$  and using cubic 4–D interpolation took over 300h (12 days) for 5000 turns on our ULTRA–80. During this run the density in

the outer mesh region degraded so badly that the computed kurtosis actually became negative. Note that the code had been completely inlined and pre-optimized *by hand* which increased the performance (with the SUN compiler) by a factor of 2. We are working on improved interpolation schemes and other enhancements to speed up the code.

Last but not least, the memory needed to store the main array (the mesh table (PF) or the particle table (WMPT)) for two bunches in  $m$  degrees of freedom and in REAL\*8 is

$$\text{Memory/bytes} = \begin{cases} 16 \cdot n_g^{2m} \cdot 2 & : \text{PF} \\ 16 \cdot n_g^{2m} \cdot (2m + 1) & : \text{WMPT} \end{cases} \quad (15)$$

Here  $n_g$  is the number of mesh points/particles per dimension, the factor of 16 is 2 bunches times 8 bytes, the factor of 2 for PF is due to the fact that we have to store 2 instantiations of the mesh for the purpose of interpolation (“old/new”) and the factor of  $2m + 1$  for WMPT comes from  $2m$  phase space coordinates plus the total weight  $\mathcal{W}_{ij}$  of the trajectory.

We will discuss some of our first results with WMPT in 4-D phase space in Section 3.2.

### 3 SIMULATIONS

#### 3.1 Some Results in One d.o.f.

We have studied extensively the dependence of the coherent dipole modes ( $\pi/\sigma$  modes) on the split of the bare machine tunes ( $\Delta Q_0$ ) and on the ratio of the beam-beam parameters in one degree of freedom. These studies were reported in [4]. In [8] we report on the existence of quasi-equilibria for the Chao–Ruth limit. Here we only report some new results based on the implementation of RF-dipoles and higher order multipoles in the lattice and their interaction with the beam-beam kick.

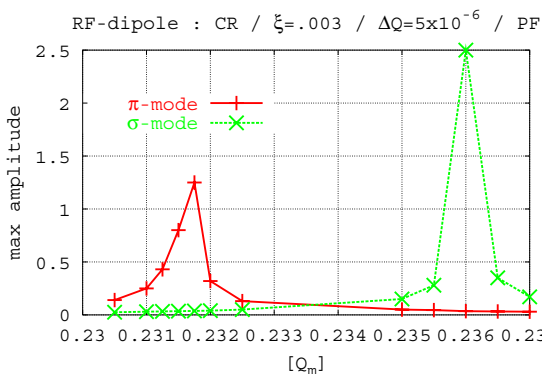


Figure 4: (color) Maximum amplitudes with RF-dipole excitation.

Figure 4 shows the response of the coherent modes to an external excitation with an RF-dipole located at the center of the arc. The simulations were performed with BBPF1D

and with a mesh of  $241 \times 241$  points over  $\pm 6\sigma_0$ . The beam-beam parameter is 0.003 and the tune split is  $5 \cdot 10^{-6}$  with  $Q_0 \approx Q_0^* \approx 0.236$  (as in Fig. 2) and the normalized kick strength of the RF-dipole was  $1 \cdot 10^{-3}$ . Both beams had no initial coherent betatron amplitude and the simulation was performed over  $2^{17}$  turns. When the RF-dipole operates at a constant modulation tune  $Q_m := f_{\text{dip}}/f_0$  both modes are excited and their amplitudes are modulated with a tune comparable to  $|Q_m - Q_{\pi,\sigma}|$ . Figure 4 shows the maximum amplitude of the  $\pi$  mode (red) and the  $\sigma$  mode (green) in the CR limit as a function  $Q_m$ . The maximum amplitude is given in units of  $\sigma_0$ . For both modes we find a resonance excitation peak at the frequency predicted in Fig. 2.

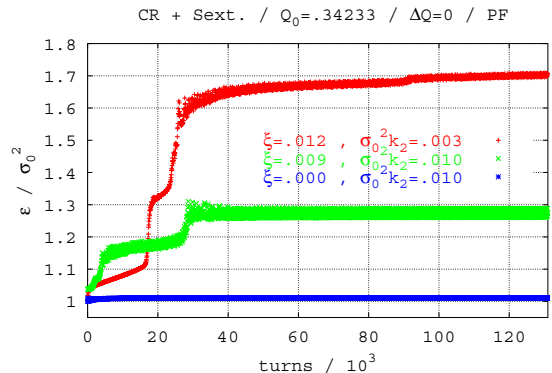


Figure 5: (color) Beam-beam with sextupole: emittance growth.

Figures 5 to 7 show the emittance growth and the instability of the centroid motion induced by the interaction of a strong sextupole kick in the center of the arc and a strong beam-beam interaction in the CR limit close to the third-integer resonance. Both beams were initially round in phase space and one had a  $0.1\sigma_0$  offset. The sextupole alone (blue curve) (or with  $\xi$  up to 0.006) leads to hardly any emittance growth. However, when the incoherent tune spread reaches 1/3 ( $\xi = 0.009$ , green) the emittance is significantly increased. Moreover, in the latter case the  $\pi$  mode amplitude is enhanced from about  $0.1\sigma_0$  to about  $1.5\sigma_0$  whereas the  $\sigma$  mode amplitude stays small (Fig. 6). Finally when the 1/3 resonance is well inside the incoherent tune spread ( $\xi = 0.012$ , red), the emittance grows strongly and the amplitudes of both modes are significantly enhanced (Fig. 7). These observations seem to be consistent with the 4-D PIC simulations presented by Shi and Jin [9] at this workshop.

#### 3.2 First Results in Two d.o.f.

We have simulated the coherent dipole modes in 4-D phase space with BBDeMo2D using the HFMM representation of the collective kick and a linear lattice very close to the difference resonance ( $Q_x = Q_y =: Q_0, Q_x^* = Q_y^* =: Q_0^*$ ) with  $Q_0 = \sqrt{5} - 2$  and  $\Delta Q_0 = 5 \cdot 10^{-6}$  (Fig. 8, 9) and  $\Delta Q_0 = 6 \cdot 10^{-3}$  (Fig. 10, 11). The beam-beam tune shift

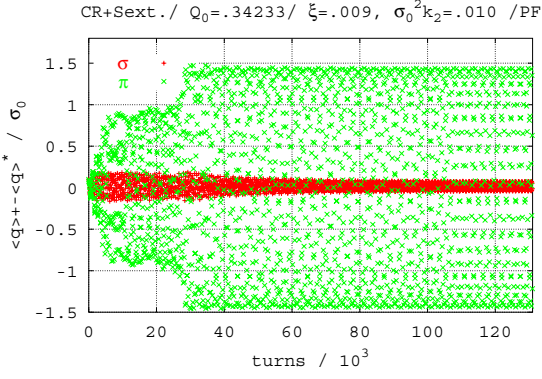


Figure 6: (color) Beam–beam with sextupole: dipole mode oscillations for  $\xi = 0.009$  and  $k_2 = 0.1\sigma_0^{-2}$ .

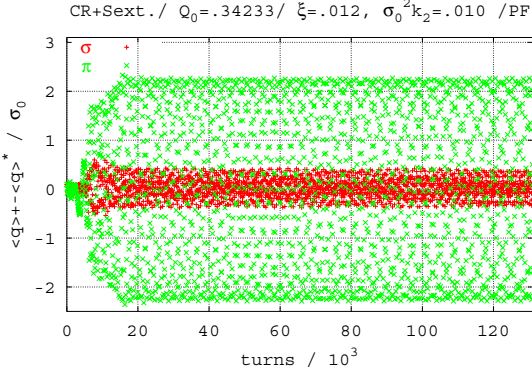


Figure 7: (color) Same as Fig. 6 but with  $\xi = 0.012$ .

in both cases, given by the extent of the incoherent continuum, is  $\xi_x = \xi_y = 0.0036$ . Figure 8 shows the spectra of

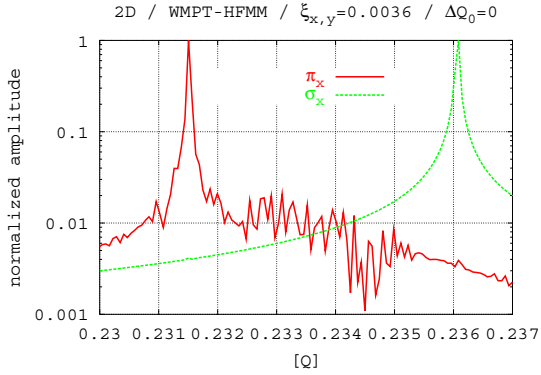


Figure 8: (color) The  $\pi$  and  $\sigma$  mode spectra without tune split.

the  $\pi_x$  and the  $\sigma_x$  mode,  $\langle x \rangle_n \mp \langle x \rangle_n^*$  obtained from an FFT over  $2^{14}$  turns. Both beams were initially round Gaussians in their four dimensional phase space and in each plane one of them had an initial coherent betatron amplitude of  $0.1\sigma_0$  whereas the other was at rest. Both modes can clearly be

resolved. The separation of the  $\pi_x$  mode tune from the  $\sigma_x$  mode tune is  $(1.28 \pm 0.02)\xi_x$  with  $\xi_x$  being the extent of the incoherent continuum. The spectra of the dipole modes for the vertical motion (not shown) are the same. Figure

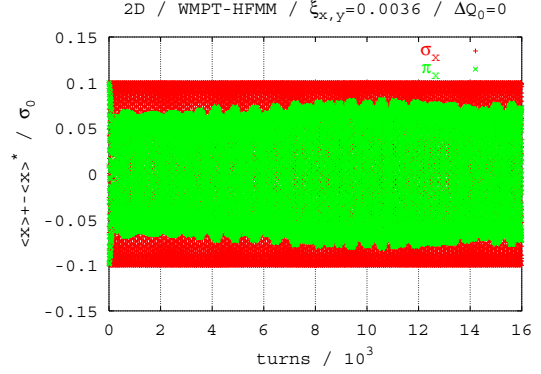


Figure 9: (color) The  $\pi$  and  $\sigma$  modes in time domain without tune split.

9 shows the turn by turn evolution of the dipole modes for the above parameters. The  $\sigma$  mode (red) has a completely stationary amplitude. The  $\pi$  mode (green) amplitude drops slightly to about 80% of its initial value but then stays almost constant. The weak but visible low-frequency modulation of the  $\pi$  mode amplitude seems to be an artifact of the discretization. It is reduced when the number of particles is increased (not shown). The emittances (also not shown) stay constant to the 1% level. This, in combination with our earlier results in one degree of freedom [4, 8], indicates that, for a linear lattice, moderate beam–beam parameters and in the absence of external excitation, the dipole modes are neutrally stable.

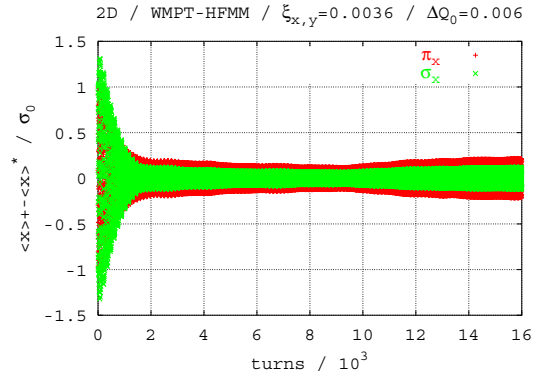


Figure 10: (color) Filamentation of the  $\pi$  and  $\sigma$  modes with large tune split.

Figure 10 and 11 show an example with  $\Delta Q_0 = 0.006$ , i.e. almost twice the beam–beam tune shift parameter so that the coherent dipole modes should be Landau damped. The initial coherent betatron amplitudes of the beams are  $1\sigma_0, 0$  for the horizontal and vertical planes respectively of



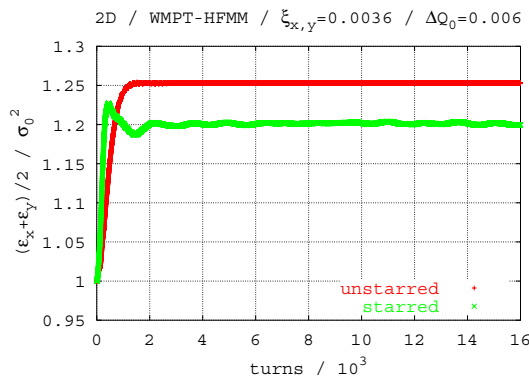


Figure 11: (color)Emittance blow up with large tune split.

the unstarred beam and  $0, 1\sigma_0$  for starred beam. Figure 10 shows the decay of the modes in the horizontal plane. Figure 11 shows the blow up of the emittances because of the filamentation of the dipole modes. The mean  $(\epsilon_x + \epsilon_y)/2$  is printed for the unstarred and the starred beam. Both beams stay round up to the 10% level. The unequal emittance blow up of the two beams can most likely be explained by their different tunes ( $Q_0 \approx 0.236$ ,  $Q_0^* \approx 0.230$ ) and thus different sensitivity to the nonlinear perturbation of the beam–beam force.

## 4 SUMMARY AND OUTLOOK

We have developed two methods, PF and WMPT, for the simulation of nonlinear collective effects in beams described by Vlasov–Poisson systems. Both methods are based on the symplecticity of the one turn map, but PF easily allows extension to Vlasov Fokker–Planck systems by means of operator splitting. We have written codes for simulating the beam–beam interaction in the strong–strong model. WMPT and PF show good agreement in the one degree of freedom limits of the beam–beam and we have extended both methods to the more important two degree of freedom case. At present WMPT is more efficient in higher dimensions. We will try to improve on the efficiency of PF in 4–D phase space and we have already started developing a parallel (distributed memory) version of the WMPT code. Moreover, we will include a MAD–reader, higher order maps for real beam line elements, and interpolated higher order generating functions (see [3]) for composed IP–to–IP maps. We will pursue the idea of speeding up of both methods (PF and WMPT) by incorporating our results on averaging [8].

In one degree of freedom, we have studied the dipole modes and Landau damping [4]. In addition, we have studied the response to external excitations (RF–dipole) and have observed large emittance growth together with a strong increase of the amplitudes of the centroid motion in the presence of lattice nonlinearities (e.g. sextupole) combined with a sufficiently large beam–beam parameter.

We have just begun analyzing the dynamics of the beam–beam in 4–D phase space and have begun determining optimal parameter settings for the codes, e.g.  $n_g$ ,  $N$ , etc. as functions of  $\xi$ ,  $\xi^*$ , the distance of the bare tunes to orbital resonances, the total turn number, etc. First tests clearly resolve the dipole modes and their neutral stability in a linear lattice and with moderate tune shift parameters. They also indicate the possibility of introducing Landau damping via a tune split.

## 5 ACKNOWLEDGEMENTS

We thank L. Greengard for supplying the adaptive FMM routines. Our work was supported by DOE contracts DE-FG03-99ER41104, DE-AC02-76CH03000, DE-AC03-76SF00515 and the US-LHC project.

## 6 REFERENCES

- [1] R. L. Warnock and J. A. Ellison, *Proc. 2nd ICFA Advanced Accelerator Workshop on the Physics of High Brightness Beams, UCLA, November 9-12, 1999*, (World Scientific, Singapore, 2001); *Proc. 2nd ICFA Workshop on Quantum Aspects of Beam Physics, Capri, October, 2000*, to be published by World Scientific.
- [2] G. H. Hoffstaetter and M. Vogt, *The SPRINT Manual*, to appear in 2001.
- [3] R. L. Warnock and J. A. Ellison, *Appl. Num. Math.* **29**, 89-98 (1999); Also published in *Beam Stability and Nonlinear Dynamics*, ed. Z. Parsa, AIP Conf. Proc. **405**, p.41 (Amer. Inst. Phys., Woodbury, NY, 1997).
- [4] M. Vogt, T. Sen, J. A. Ellison, FNAL Pub-01/096-T, submitted to Phys. Rev. ST-AB, (2001).
- [5] A. W. Chao and R. D. Ruth, *Particle Accelerators* **16**, 201–216 (1985).
- [6] K. Yokoya and H. Koiso, *Particle Accelerators* **27**, 181–186 (1990).
- [7] L. Greengard, *Thesis*, The MIT Press, Cambridge, MA (1988); F. W. Jones, *Proc. Workshop on Space Charge Physics in High Intensity Hadron Rings*, Ed. A. U. Luccio and W. T. Weng, AIP Conf. Proc. **448**, (1998); W. Herr, M.–P. Zorzano and F. W. Jones, Phys. Rev. ST-AB **4** 054402, (2001); W. Herr, in these proceedings.
- [8] J. A. Ellison and M. Vogt, in these proceedings.
- [9] J. Shi and L. Jin, in these proceedings.

# EFFECT OF ELECTRON-BEAM COMPENSATION OF BEAM-BEAM TUNE SPREAD ON BEAM-SIZE GROWTH IN TEVATRON

L. Jin and J. Shi

Department of Physics, the University of Kansas, Lawrence, KS 66045, USA

## Abstract

Electron-beam compensation of beam-beam tune spread in Tevatron was studied with a self-consistent beam-beam simulation (particle-in-cell method with a million macro-particles). It was found that the additional beam-beam interactions between the electron and hadron beams could excite the beam-beam instability on the anti-proton beam while the tune-spread of the anti-proton beam is shrunk significantly. This study indicates that the phase-dependent terms in the Hamiltonian for the beam-beam interaction could dominate the beam-beam effects and the reduction of the beam-beam tune-spread by introducing additional nonlinear beam-beam interactions could deteriorate the stability of the anti-proton beam.

## 1 INTRODUCTION

In a storage ring collider, the beam-beam interaction is one of major factors limiting the beam current and luminosity. Recent studies showed that when the beam-beam parameter exceeds a threshold the beam-beam interaction could excite a chaotic coherent beam-beam instability that results in an enhanced growth of beam sizes and significant reduction of luminosity [1, 2]. For the Large Hadron Collider (LHC) being constructed at CERN and Tevatron upgrading (RUN IIB) at Fermi Lab, efforts are being made to reduce beam-beam effects in order to achieve the designed luminosity [3, 4]. The compensation of the beam-beam tune spread with electron beams is one of schemes proposed for the Tevatron RUN IIB [3]. In this scheme, high intensity low-energy electron ( $e$ ) beams will collider with anti-proton ( $\bar{p}$ ) beam at certain locations in the ring other than the nominal interaction points for proton ( $p$ ) and  $\bar{p}$  beams to compensate the tune spread of the  $\bar{p}$  beam due to beam-beam interactions between  $p$  and  $\bar{p}$  beams. To have a better understanding of such electron-beam compensation, let us take a quick look at the Hamiltonian for the transverse motion of the  $\bar{p}$  beam. Neglecting nonlinearities (magnetic field errors) in the lattice, the Hamiltonian can be approximately written as

$$\begin{aligned} H &= \vec{\nu} \cdot \vec{I} + H_{p\bar{p}}(\vec{I}, \vec{\phi}, t) + H_{e\bar{p}}(\vec{I}, \vec{\phi}, t) \\ &= \vec{\nu} \cdot \vec{I} + \langle H_{p\bar{p}} \rangle + \langle H_{e\bar{p}} \rangle + \{H_{p\bar{p}}\} + \{H_{e\bar{p}}\} \end{aligned} \quad (1)$$

where  $\vec{\nu}$  is the betatron tune and  $(\vec{I}, \vec{\phi})$  the action-angle variables for the transverse motion of the  $\bar{p}$  beam.  $H_{p\bar{p}}$  and  $H_{e\bar{p}}$  are the perturbative Hamiltonian for the beam-beam interactions between  $p$  and  $\bar{p}$  beams and between  $\bar{p}$

and  $e$  beams for the electron-beam compensation, respectively.  $\langle H_{p\bar{p}} \rangle$  ( $\langle H_{e\bar{p}} \rangle$ ) is the average of  $H_{p\bar{p}}$  ( $H_{e\bar{p}}$ ) that leads to the lowest-order tune spread due to the beam-beam interactions between  $\bar{p}$  and  $p$  ( $e$ ) beams. Because of the opposite charge of  $p$  and  $e$ ,  $\langle H_{p\bar{p}} \rangle$  and  $\langle H_{e\bar{p}} \rangle$  have an opposite sign and cancel each other if the  $e$  beam has the same intensity and charge distribution as that of the  $p$  beam.  $\{H_{p\bar{p}}\} = H_{p\bar{p}} - \langle H_{p\bar{p}} \rangle$  and  $\{H_{e\bar{p}}\} = H_{e\bar{p}} - \langle H_{e\bar{p}} \rangle$  are the nonlinear phase-dependent (oscillating) parts of the perturbative Hamiltonians that could lead to resonances and beam instabilities. The electron-beam compensation of beam-beam tune spread is based on the assumption that  $\langle H_{p\bar{p}} \rangle$  is the dominant term of  $H_{p\bar{p}}$  and a smaller beam-beam tune spread would always improve beam performance because of less resonance crossings. The minimization of the tune spread of the  $\bar{p}$  beam with the electron-beam compensation, however, unavoidably introduces an additional nonlinear phase-dependent perturbation  $\{H_{e\bar{p}}\}$  to the  $\bar{p}$  beam. The question here is how important the nonlinear phase-dependent terms  $\{H_{p\bar{p}}\}$  and  $\{H_{e\bar{p}}\}$  are when the beam tune spread is reduced as desired by using the electron-beam compensation. To answer this question, a self-consistent beam simulation study was conducted with the lattice model of Tevatron. In this paper, the results of this study are reported. This paper is organized as follows. In Section 2, the simulation models are discussed briefly. The simulation results are presented in Section 3. Section 4 contains a summary.

## 2 SIMULATION AND LATTICE MODELS

The test lattice used in this study is Tevatron lattice V3h15av2 [5]. In this study only linear lattice were used since multipole field errors in the lattice normally do not change the characteristic of the beam-beam instability [1]. In the simulation,  $p$  and  $\bar{p}$  beams are collided only at one interaction point D0 ( $\beta^* = 0.35m$ ) and the electron beam for the compensation is located at F0 where  $\beta$ -function is about 70m in both horizontal and vertical planes. As the intensity of the  $p$  beam is much larger than that of the  $\bar{p}$  beam, the  $\bar{p}$  beam is perturbed more severely than the  $p$  beam due to the collision between the  $p$  and  $\bar{p}$  beams. The electron beam compensation of the beam-beam tune spread was thus only used on the  $\bar{p}$  beam as proposed for the Tevatron RUN IIB [3].

Our self-consistent (strong-strong) beam-beam simulation code has been fully tested and presented in detail in our previous paper [1]. In this code, each beam is represented by a large number of macro-particles with given



initial distributions in transverse phase space. In this study, the initial phase-space distributions of two counter-rotating beams are chosen to be round Gaussian beams in the normalized transverse phase space with standard deviation  $\sigma_0$  and truncated at  $\pm 4\sigma_0$ , where  $\sigma_0 = \sigma/\sqrt{\beta^*}$ .  $\sigma$  and  $\beta^*$  are the nominal transverse beam size and the value of the  $\beta$  at IP, respectively. Different initial emittance for the  $\bar{p}$  and  $p$  beams in the Tevatron was also taken into account in the simulation and the emittance ratio between the  $\bar{p}$  and  $p$  is 3/4. During the tracking, beam-beam kicks in four-dimensional transverse phase space are calculated at each IP by using the particle-in-cell method. The task consists of three major steps [1]: (a) The beam charge distributions at each crossing of IP are obtained by assigning macro-particles to the grid points of a uniform mesh in two-dimensional transverse configuration space for each beam using the four-point cloud-in-cell technique. (b) The beam-beam kicks are calculated at the grid points using the pre-calculated Green's functions for the beam-beam kicks. (c) the kicks are then interpolated to the position of every macro-particle. In order to ensure the convergence of the simulation parameters and to avoid any artificial result due to those numerical approximations, the size of mesh, the grid constant (the length between nearest neighboring grid points), and the number of macro-particles have to be carefully tested [1]. In this study, we found that a uniform mesh extending to  $6\sigma_0$  in all directions of the normalized configuration space with a grid constant of  $0.2\sigma_0$  is good enough. To have a reliable beam-beam simulation for hadron beams, on the other hand, the number of macro-particles has to be large enough, typically  $> 10^5$ . In this study, we use  $5 \times 10^5$  macro-particles for each beam. Tracking of particle motion has been done in four-dimensional transverse phase space without synchrotron oscillations and momentum deviations. The beam dynamics has been studied with  $10^6$ -turn tracking that corresponds to about 21 seconds run in Tevatron.

For the simulation of the electron-beam compensation, we considered the case that the electron beam has the same kind of charge distribution of the initial  $p$  beam. The distribution of the electron beam is therefore chosen to be the Gaussian distribution with a standard deviation that changes with the rms beam size of the counter-rotating  $p$  beam during the tracking. The momentum kick exerted by the electron beam can be simply calculated with the standard formula for the beam-beam interaction of a Gaussian beam [6].

### 3 SIMULATION RESULTS

Both full- and half-strength electron-beam compensations were studied. In the full-strength compensation,  $\xi_{\bar{p}e} = -\xi_{\bar{p}p}$  where  $\xi_{\bar{p}e}$  and  $\xi_{\bar{p}p}$  are the beam-beam parameters of the  $\bar{p}$  beam for the  $e$ - $\bar{p}$  collision and  $p$ - $\bar{p}$  collision, respectively. In the half-strength compensation,  $\xi_{\bar{p}e} = -\xi_{\bar{p}p}/2$ . Two different working points were used in the study,  $\nu_x = 20.582$  and  $\nu_y = 20.574$  that is the

nominal working point and  $\nu_x = 20.740$  and  $\nu_y = 20.730$  that is close to the 4th-order resonance. In addition, the effect of the Landau damping on the coherent instability in a slightly unsymmetrical ring was also studied.

#### 3.1 Results with $\nu_x = 20.582$ and $\nu_y = 20.574$

The study of the electron-beam compensation with the nominal working point is to understand how the electron beam would affect the beam dynamics of the  $\bar{p}$  beam in a working point that is far away from major resonances. In this case, both  $p$  and  $\bar{p}$  beams have the same betatron tune of  $\nu_x = 20.582$  and  $\nu_y = 20.574$ . In the simulation, the intensity of the  $\bar{p}$  beam is assumed to be half of that of the  $p$  beam.  $\xi_{\bar{p}p} = 0.01$  and  $\xi_{p\bar{p}} = 0.005$ , where  $\xi_{p\bar{p}}$  is the beam-beam parameter of the  $p$  beam for the  $p$ - $\bar{p}$  collision.

Fig. 1 plots the initial tune spread of the  $\bar{p}$  beam with or without the electron-beam compensation, where the beam tune spread was evaluated with about 500 test particles during the first 2000-turns tracking. It shows that with the electron-beam compensation the beam tune spread was shrunk as expected. In the case of the half compensation ( $\xi_{\bar{p}e} = 0.005$ ), the tune spread of the  $\bar{p}$  beam is shrunk about a half of the original (see Figs. 1a and 1b). In the case of full compensation ( $\xi_{\bar{p}e} = 0.01$ ), a small remaining tune spread of  $\Delta\nu \sim 0.002$  (see Fig. 1c) is the high-order contributions from both  $p$ - $\bar{p}$  and  $e$ - $\bar{p}$  collisions that becomes observable when the lowest-order tune spread is eliminated by the electron-beam compensation. In Fig. 2, the evolution of rms beam size of the  $\bar{p}$  beam was plotted for the cases of Fig. 1. Without the electron beam compensation, the size of the  $\bar{p}$  beam increases less than 1.5% in  $10^6$  turns (see curve a of Fig. 2). With either half- or full-strength of the electron beam compensation, however, the beam-size growth becomes much more severe, with more than 6% and 8% in  $10^6$  turns for the half and full compensation (see curve b and c of Fig. 2), respectively, even though the tune spread is reduced significantly. Since in this case the original tune spread of the  $\bar{p}$  beam does not lead to crossing of any major resonance, the reduction of the tune spread with the electron-beam compensation could not improve the beam dynamics but introduce more nonlinearity ( $\{H_{e\bar{p}}\}$  in Eq. 1) to the beam that is responsible for the increased beam-size growth. For a good working point that is away from major resonances, therefore, the beam-beam tune spread is not necessarily important to the slow beam-size growth and the nonlinear phase-dependent parts of the beam-beam Hamiltonian dominate the beam-beam effect instead.

#### 3.2 Unsymmetrical rings

Simulation was also performed for the  $p$  and  $\bar{p}$  beams with slightly different working points. The working point for the  $\bar{p}$  beam was chosen to be the nominal working point ( $\nu_x = 20.582$ ,  $\nu_y = 20.574$ ) while for the  $p$  beam two different cases were studied, ( $\nu_x = 20.583$ ,  $\nu_y = 20.575$ ) and ( $\nu_x = 20.587$ ,  $\nu_y = 20.579$ ). The tune split of the

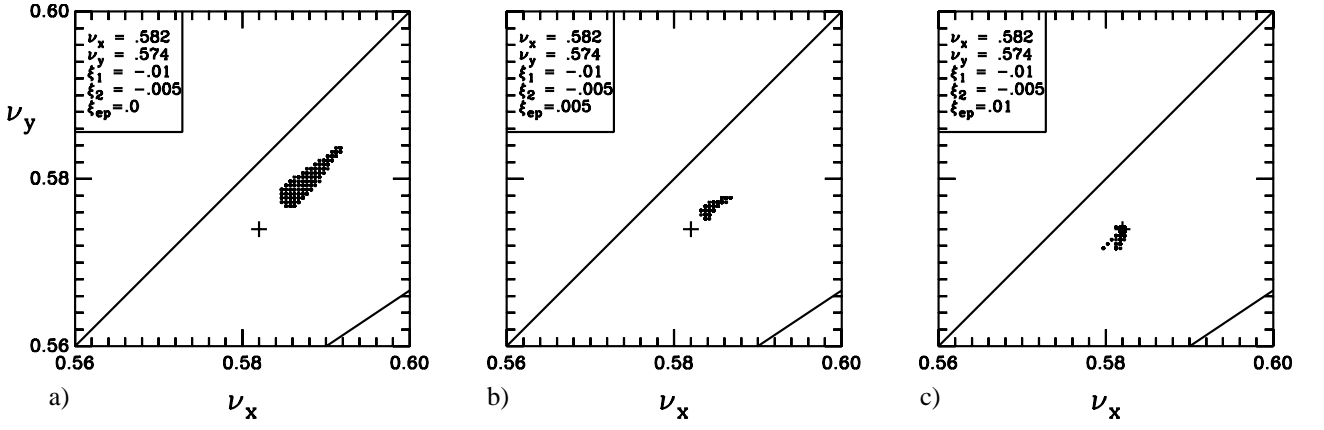


Figure 1: Tune spread of the  $\bar{p}$  beam when  $\nu_x = 20.582$  and  $\nu_y = 20.574$ .  $\xi_{\bar{p}p} = 0.01$  and  $\xi_{p\bar{p}} = 0.005$ . a) Without the electron-beam spread compensation; b) with the half-strength electron-beam compensation; and c) with the full-strength electron-beam compensation. Even-order resonances up to the 10th order are plotted as solid lines, and + indicates the location of the bare tune.

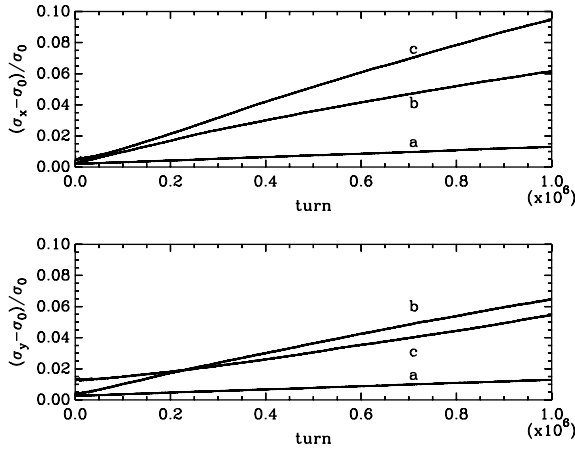


Figure 2: Evolution of rms beam size of the  $\bar{p}$  beam for the cases of Fig. 1. a) without the electron-beam compensation; b) with the half-strength electron-beam compensation; and c) with the full-strength electron-beam compensation.  $\sigma_0$  is the initial beam size.

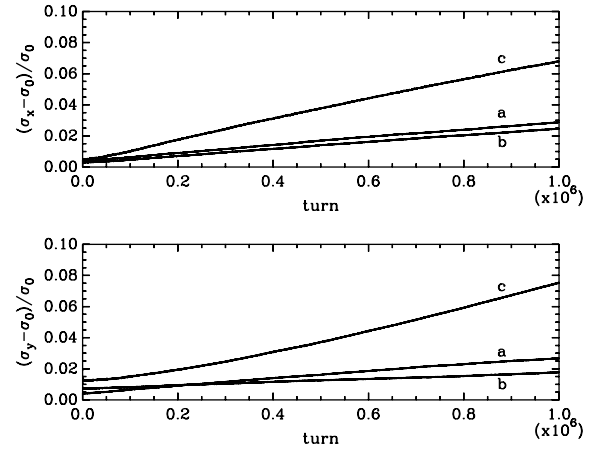


Figure 3: Evolution of rms beam size of the  $\bar{p}$  beam when the tune of the  $p$  and  $\bar{p}$  beams is  $(\nu_x = 20.582, \nu_y = 20.574)$  and  $(\nu_x = 20.587, \nu_y = 20.579)$ , respectively.  $\xi_{\bar{p}p} = 0.01$  and  $\xi_{p\bar{p}} = 0.005$ . a) Without the electron beam compensation; b) with the half-strength electron-beam compensation; and c) with the full-strength electron-beam compensation.

two beams in these two cases is thus  $\delta\nu = 0.001$  and  $\delta\nu = 0.005$ , respectively. In the case of  $\delta\nu = 0.001$ , the result is roughly the same as that in the symmetrical rings (Section 3.1) and the  $e$  beam did more damage than benefit to the  $\bar{p}$  beam with both the full- and half-strength compensation. Fig. 3 plots the beam-size growth in the case of  $\delta\nu = 0.005$ . Without the electron beam, the size of the  $\bar{p}$  beam increases about 3% in  $10^6$  turns. Note that the  $\bar{p}$  beam grows only about 1.5% in  $10^6$  turns in the symmetrical rings. In the case with the full-strength compensation, the collision between the  $e$  and  $\bar{p}$  beams again worsened the performance of the  $\bar{p}$  beam (curve c in Fig. 3) but the half-strength compensation slightly improved the beam dynamics, the growth of the  $\bar{p}$  beam size reduced to 2.5% during  $10^6$  turns (see curve b in Fig. 3).

### 3.3 Results with $\nu_x = 20.740$ and $\nu_y = 20.730$

If the original tune spread of the  $\bar{p}$  beam leads to crossings of major resonances due to either a bad working point or a large beam-beam parameter between  $p$  and  $\bar{p}$  beams, the reduction of the tune spread with the electron-beam compensation could move the beam away from the resonances and improve the beam dynamics. To explore this possible benefit of the electron-beam compensation, we intentionally moved the working point of both the  $p$  and  $\bar{p}$  beams to  $\nu_x = 20.740$  and  $\nu_y = 20.730$  which is close to the 4th-order resonances and used a larger beam-beam parameter between  $p$  and  $\bar{p}$  beams, i.e.  $\xi_{\bar{p}p} = 0.01$  and  $\xi_{p\bar{p}} = 0.02$  for the  $p$  and  $\bar{p}$  beams, respectively.

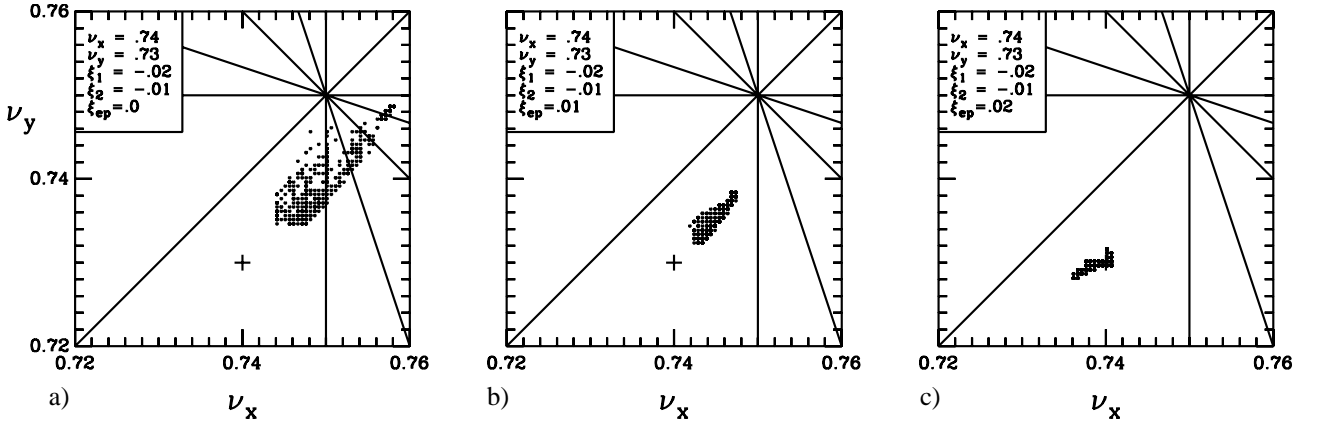


Figure 4: Tune spread of the  $\bar{p}$  beam when  $\nu_x = 20.74$  and  $\nu_y = 20.73$ .  $\xi_{\bar{p}p} = 0.02$  and  $\xi_{p\bar{p}} = 0.01$ . a) Without the electron-beam compensation, the beam core crosses the 4th-order resonances; b) with the half-strength electron-beam compensation; and c) with the full-strength electron-beam compensation. Even-order resonances up to the 10th order are plotted as solid lines and + indicates the location of the bare tune.

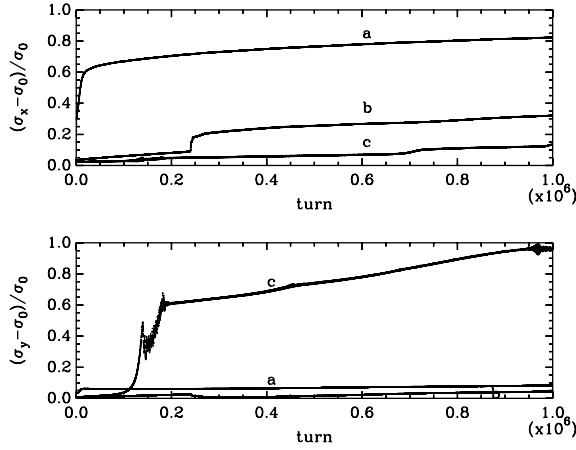


Figure 5: Evolution of rms beam size of the  $\bar{p}$  beam for the cases of Fig. 4. a) Without the electron-beam compensation; b) with the half-strength electron-beam compensation; and c) with the full-strength electron-beam compensation.  $\sigma_0$  is the initial beam size.

In Figs. 4 and 5, the initial tune spread and the beam-size growth of the  $\bar{p}$  beam are plotted with or without the electron-beam compensation. Without the electron-beam compensation, the beam core crosses the 4th-order resonances (see Fig. 4a) and results in a beam blowup in the horizontal plane, an 80% increase in beam size during  $10^6$ -turns tracking (see curve a in Fig. 5). Note that the most of this beam-size growth (the initial jump of the horizontal beam size) is due to the beam filamentation because of the severe deformation of the phase-space area nearby the resonances. With both half- ( $\xi_{\bar{p}e} = -0.01$ ) and full-strength ( $\xi_{\bar{p}e} = -0.02$ ) of the electron-beam compensation, the tune spread of the  $\bar{p}$  beam was shrunk as expected and the crossing of the 4th-order resonances was eliminated completely as shown in Figs. 4b and 4c. Consequently, the initial blowup of the  $\bar{p}$  beam was suppressed in both cases

with the electron-beam compensation (see curve b and c in Fig. 5). In the case of the full-strength compensation, however, a coherent beam-beam instability [1] occurred afterward on the  $\bar{p}$  beam as the vertical beam size jumped suddenly during  $10^5$  to  $2 \times 10^5$  turns (see curve c in Fig. 5) and, meanwhile, the beam-beam interactions between  $p$  and  $\bar{p}$  beams and between  $e$  and  $\bar{p}$  beams induced a spontaneously unstable coherent oscillation on the  $\bar{p}$  beam as shown in Fig. 6c. On the contrary, in the case without

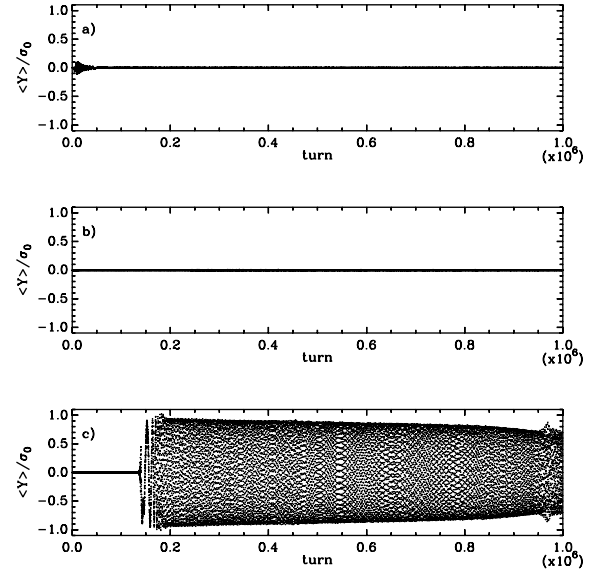


Figure 6: Beam-centroid motion in vertical plane of the  $\bar{p}$  beam for the cases of Fig. 4. a) Without the electron-beam compensation; b) with the half-strength electron-beam compensation; and c) with the full-strength electron-beam compensation.  $\sigma_0$  is the initial beam size. Both  $p$  and  $\bar{p}$  beams are centered initially.

the electron-beam compensation, no spontaneously coherent beam oscillation was observed after the initial beam

filamentation (see Fig. 6a). Due to the unstable coherent beam oscillation in the case of the full-strength compensation, the beam-size growth rate (the slope of curves in Fig. 5) after the sudden jump in the beam size is substantially larger than that without the compensation. With the full-strength compensation, therefore, the nonlinear phase-dependent perturbation ( $\{H_{\bar{p}e}\}$ ) from the  $e$  beam dominates the interaction between the  $e$  and  $\bar{p}$  beams and did significant damage to the  $\bar{p}$  beam even though the  $\bar{p}$  beam benefited initially from the phase-independent perturbation ( $\langle H_{\bar{p}e} \rangle$ ) of the  $e$ - $\bar{p}$  beam-beam interaction. In the case of the half-strength compensation, on the other hand, the original beam blowup due to the beam filamentation near the 4th-order resonances was largely suppressed but no beam-beam instability was excited as shown by curve b in Fig. 5. This result indicates that when the beam is close to major resonances, the electron-beam compensation could improve the beam dynamics if the strength of the  $e$  beam is carefully chosen in such a way that the damage effects of  $\{H_{\bar{p}e}\}$  is insignificant or the benefit of the compensation outweighs the damage effects of  $\{H_{\bar{p}e}\}$ .

## 4 SUMMARY

The effect of electron-beam compensation of beam-beam tune spread on the dynamics of hadron beams depends on the competition between the benefits from the reduction of the beam tune spread and the damaging effects of the additional nonlinear phase-dependent perturbation from the  $e$  beam. At the nominal work point of Tevatron (RUN II) that is away from major resonances, the beam tune spread is not necessarily important to beam-beam effects but the nonlinear phase-dependent perturbation of the beam-beam interactions dominates the beam dynamics. In this case, the electron-beam compensation for the  $\bar{p}$ -beam tune spread was found to damage the dynamics of the  $\bar{p}$  beam with a significantly increased beam-size growth even though the tune spread of the  $\bar{p}$  beam was shrunk as expected. Moreover, when the  $p$  and  $\bar{p}$  beams have slightly different working points with a tune split of  $0.001 \sim 0.005$ , very little improvement on the  $\bar{p}$  beam could be found after the electron-beam compensation of the tune spread. When the working point is close to major resonances such as the 4th-order resonances, on the other hand, the beam-beam interaction between the  $p$  and  $\bar{p}$  beams could lead to the crossing of the resonances and result in a large beam-size growth on the  $\bar{p}$  beam. In this case, the electron-beam compensation of the tune spread can move the beam away from the resonances and suppress the initial beam blowup due to the beam filamentation near the resonances. However, the nonlinear phase-dependent perturbation from the  $e$  beam could still induce the chaotic coherent beam-beam instability that will lead to a beam blowup on the  $\bar{p}$  beam if the  $e$  beam is too strong. This study suggests that the electron-beam compensation of the beam-beam tune spread could improve the beam dynamics only in the cases that the original system is dominated by a few low-order resonances so that the

benefits from the tune-spread compensation outweighs the damaging effects of the nonlinear phase-dependent perturbation from the  $e$  beam.

## ACKNOWLEDGMENTS

This work is supported by the US Department of Energy under Grant No. DE-FG03-00ER41153 and the University of Kansas General Research Fund. We would like to thank the Center for Advanced Scientific Computing at the University of Kansas for the use of the Supercomputer.

## 5 REFERENCES

- [1] J. Shi and D. Yao, "Collective Beam-Beam Effects in Hadron Colliders", *Phys. Rev. E* **62**, 1258 (2000).
- [2] J. Shi and L. Jin "Chaotic Coherent Beam Instability Due to Beam-Beam Interactions in Hadron Colliders", to be submitted to *Phys. Rev. Lett.*, 2001.
- [3] V. Shiltsev, V. Vanilov, D. Finley and A. Sery, "Compensation of Beam-Beam Effects in the Tevatron with Electron Beams", *Phys. Rev. ST Accel. Beams*, **2**, 071001, 1999, and references herein.
- [4] J.-P. Koutchouk, et al., in these proceedings.
- [5] <http://www-ap.fnl.gov/martens/mad/tevatron/run2/lattice.html>.
- [6] J. C. Herrera, "Electromagnetic Interaction of Colliding Beams in Storage Rings", *AIP Conference Proceedings* Number 57, 1979.

# Summary of Coherent Theory and Simulations Session

James A. Ellison and Mathias Vogt  
University of New Mexico

## 1 INTRODUCTION

There were two types of talks which we attempt to summarize. Section 2 discusses the analytical talks and Section 3 the simulation talks. We hope that at least our summary will have the flavor of the session and serve as a reasonable pointer to papers in the proceedings and elsewhere. We take this opportunity to thank the participants of this session for making it an interesting one. The major emphasis in this session was on codes and we have tried to give an overview of basic computational strategies in Section 3 before highlighting the talks.

## 2 ANALYTICAL TALKS

The analytical talks focused on beam–beam equilibria and on perturbation analyses.

Warnock reported on work [1] on the existence of equilibria in the lepton case. Numerical studies indicated the existence of an equilibrium; existence was then proven using a fixed point theorem in an appropriate Banach space for sufficiently small beam–beam parameter. The proof seems to require nonzero damping and so there is no clear generalization to the Hadron case. More information was found by linearizing the beam–beam force, but keeping the nonlinear evolution law. Here the equilibria are found explicitly and in the lepton case it is a unique Gaussian. In the Hadron case there is a large class of equilibria, but even so the existence with full beam–beam force is an open question.

Ellison reported on an averaged Vlasov equation for hadrons [2]. This approximate model has a large class of equilibria, indicating quasi–equilibria for the full model. This was verified in simulations.

Tzenov [3] reported on preliminary work on equilibria in the Hadron case using renormalization group techniques. He found an approximate symplectic beam–beam map with invariant phase space densities.

Shi [4], Warnock [1] and Vogt [5] all reported seeing instabilities with their numerical codes if the beam–beam parameter becomes too large. Shi also presented a detailed study of chaotic behavior of the centroid in this case.

Perturbation theories were discussed. Shi mentioned his projection operator approach [6], Tzenov [3] his renormalization approach and Ellison and Vogt their averaging approach [2].

More work needs to be done on the existence of equilibria and quasi–equilibria and their stability in the Hadron case. However, all analytical and numerical results we are

aware of are consistent with stable equilibria up to a threshold for the beam–beam parameter.

The following need attention.

- Prediction of the threshold for instability.
- A study of the nature of trans–threshold dynamics.
- The study of the linearized equations seems under control. Next it would be nice to develop a weakly nonlinear theory that would show nonlinear mode coupling.
- The long range interaction needs to be incorporated.
- The crossing angle needs to be addressed.

## 3 BEAM–BEAM SIMULATION CODES

### 3.1 Overview of Collective Methods

It is in general impossible to simulate the evolution of 2 or more colliding bunches of typically  $10^9$  to  $10^{12}$  particles each over many turns. Therefore it is mandatory to find an approximate description of the bunches which can be handled computationally. We discuss three general approaches.

The classical approach is to replace each bunch by a significantly smaller but somehow “representative” ensemble of so called macro–particles. Having some notion of a *typical* coarse grained single particle phase space density, which are in principle measurable quantities, one can then create a Monte Carlo (MC) ensemble of  $N$  identical macro–particles at phase space points  $\vec{z}_k$ ,  $1 \leq k \leq N$ . In this approach the charge of the *real* bunch is equally distributed among the macro–particles. The macro–particles are then tracked through the lattice, taking into account the collective beam–beam effect at the IPs. Therefore one obtains  $N$  trajectories  $\vec{\eta}_k(\theta)$ . In the following we will call this approach Monte Carlo Macro–Particle Tracking (MCMPT). At certain view points in the ring, moments and binned densities of the macro–particle ensemble can be computed in a straight forward way. If  $f$  is a function on phase space, then the expectation of  $f$  is approximated by

$$\langle f \rangle \Big|_{\theta} = \sum_{k=1}^N f(\vec{\eta}_k(\theta)) \quad . \quad (1)$$

Another approach is to choose an initial grid  $\{\vec{z}_{\vec{j}}\}$  (uniform or not) in phase space, and assign weights  $\psi_{\vec{j}}(0) w_{\vec{j}}$  to

the grid points. Here the  $\psi_{\vec{j}}(0)$  are the values of the initial density at  $\vec{z}_{\vec{j}}$  and the  $w_{\vec{j}}$  are quadrature weights adapted to the mesh. Then the grid points are used as initial values for trajectories  $\vec{\eta}_{\vec{j}}(\theta)$  whose dynamics is approximated in a similar way as in MCMPT. Expectation values are computed analogously to MCMPT.

$$\langle f \rangle \Big|_{\theta} = \sum_{\vec{j} \in \text{grid}} f(\vec{\eta}_{\vec{j}}(\theta)) \psi_{\vec{j}}(0) w_{\vec{j}}. \quad (2)$$

We will call this approach Weighted Macro-Particle Tracking (WMPT). The basic differences between WMPT and MCMPT are the way in which the initial conditions are constructed and the representation of the expectation values. In fact MCMPT can be seen as an equal weight limit of WMPT with the expectation values being computed with MC quadrature.

The third approach uses the symplecticity of the transport map and the resultant measure preserving property to obtain *explicit* approximations of the density at the consecutive viewpoints. Assume the phase space density is known on a grid  $\{\vec{z}_{\vec{j}}\}$  (typically but not necessarily uniform) at azimuth  $\theta$  and the map from  $\theta$  to  $\theta'$  is known. Then due to conservation of probability the values of the density on the  $\vec{z}_{\vec{j}}$  at  $\theta'$  can be computed by tracking the grid points backwards from  $\theta'$  to  $\theta$ . Since the backward tracking will in general not map grid points to grid points, the updated density has to be obtained by interpolation of the old density between neighboring grid points of the backward tracked grid point. We call this approach [1, 7] the Perron-Frobenius (PF) method. Note that the PF method propagates the discretized density and neither trajectories nor explicitly moments. Thus approximations of the density on the grid can in principle be generated at any time without additional coarsening as in MCMPT and WMPT. Nevertheless, it is unrealistic to write the complete  $2m$  dimensional grid to disk at every viewpoint every turn and so the computation of moments and/or coarsened or projected densities is essential for turn by turn information in PF too. Phase space integrals are represented by

$$\langle f \rangle \Big|_{\theta} = \sum_{\vec{j} \in \text{grid}} f(\vec{z}_{\vec{j}}) \psi_{\vec{j}}(\theta) w_{\vec{j}} \quad (3)$$

where  $\psi_{\vec{j}}(\theta)$  is the approximation of the density at point  $\vec{z}_{\vec{j}}$  and azimuth  $\theta$  and the  $w_{\vec{j}}$  are quadrature weights associated with the grid.

All three approaches mentioned above require an algorithm to compute an approximation of the collective beam-beam kick map. The quickest but least accurate approximation employs a spatial “test” density for which the collective force as a function of the parameters of the density is known explicitly. The force is then calculated by matching the parameters of test density to the moments of the opposing bunch and then evaluating the known function of the parameters. Typically the test density is taken to be a Gaussian and then the method is called either the soft Gaussian approximation or the Gaussian source approximation

(GSA). The GSA is of course not completely selfconsistent.

If only the transverse phase space is treated, a fully self-consistent calculation requires in principle the solution of a Poisson problem with roughly  $N$  charges as source term at the positions of  $N$  spectator charges and applying a kick map to the  $N$  spectator particles.

The treatment in PF in the special case where one half of the grid axes are *in* the coordinate space and the other half of the grid axes are perpendicular to the coordinate space is particularly straight forward. Assume such a grid with  $N = n_g^{2m}$ ,  $m = 1, 2$  points. Then the discretized spatial density on the  $\sqrt{N} = n_g^m$  points of the spatial sub-grid is obtained by quadrature along the momentum axes of the phase space grid. In the worst case the computation of the  $\sqrt{N}$  kicks can be done in  $O(N)$  operations.

The macro-particle tracking methods lose the grid structure after the first application of a transport map (WMPT) or do not have such a structure from the beginning (MCMPT). Naive direct computation of the kicks would be an  $O(N^2)$  process and thus in general prohibitive for long term tracking. The classical way to proceed is to introduce a temporary *spatial* mesh, deposit the weights or charges respectively of the trajectories to the mesh points, compute the kicks on the mesh as explained above and finally redistribute the kicks among the trajectories using a scheme determined by the deposition scheme. These particle in cell (PIC) methods [8] are well established for the simulation of space charge effects. Most PIC methods have an operations count of  $O(N + N_p \log N_p)$  where  $N_p$  is the number of PIC cells.

For not too many macro-particles the Fast Multipole Method (FMM) [9] allows the computation of the collective kicks at a cost of  $O(N)$  but with large order constant and at the expense of a large amount of work space.

The Hybrid FMM (HFMM) method [10, 5], combines PIC and FMM and reduces the operations count even further in that the core regions of phase space are represented by a PIC mesh and only the accumulated charges of the PIC cells *and* the halo particles are finally submitted to the FMM routine.

If the longitudinal phase space is included, one has to take into account the different arrival times of the particles at the IP and in particular the finite length of the interaction region. One way to handle longitudinal phase space is to divide the macro-particle ensemble into several longitudinal slices and then let the slices of both bunches propagate through the slices of the other bunch applying transverse kicks on a slice by slice basis. Note that this method has a cost of  $O(N_s^2)$  with  $N_s$  being the number of slices in use. Another approach, called “ $2 + \frac{1}{2}$  d.o.f.”, is to first compute the binned longitudinal line density, second compute the average transverse phase space distribution of the ensemble by projection of the 6-D coordinates to 4-D coordinates, then compute the average transverse beam-beam kicks and finally weight them with the line density of the opposing beam. The “ $2 + \frac{1}{2}$  d.o.f.” is significantly faster than the

slice method, but it cannot account for transverse longitudinal correlation. Finally it is, of course, possible to extend the PIC methods and possibly even the FMM based methods to cope with the beam-beam force in 3 d.o.f. However, for vanishing crossing angle this approach is maybe overkill.

### 3.2 Collective Codes Presented at the Workshop

**Codes for Hadrons:** We will now attempt to summarize the main features of the strong-strong hadron codes presented the workshop.

#### 1. W. Herr, M.-P. Zorzano and F. W. Jones : MCMPT/HFMM code [10]

- 4-D code.
- Typically, a run with 10,000 particles for 16,000 turns takes 6 hours on a 600 MHz machine.
- The  $\pi$ -mode frequency found in simulations agrees well with the predictions of Yokoya [11] and Alexahin [12] based on linearized Vlasov theory.
- It is planned to implement long range interactions and 6-D phase space (without parallelization).

#### 2. J. Shi and L. Jin : MCMPT/PIC code [4]

- 4-D code.
- Uses typically  $10^6$  particles and a PIC mesh extending to  $\pm 6\sigma$ .
- With  $10^6$  particles the speed is 3 seconds per turn.
- Simulations predict chaotic behavior of the centroid motion above a beam-beam instability threshold.
- Studies on suppression of instability and on the importance of tune spread are ongoing.

#### 3. M. Vogt : BBDeMo $m$ D [5]

- Contain higher order multipole kicks and RF-dipoles.
- BBDeMo1D : WMPT code in 2-D phase space, three limits from 4-D to 2-D [13, 11, 14] implemented. Various Field solvers (direct  $O(N^2)$ , or  $O(N \log N)$  in the case of the Chao-Ruth limit, and GSA) [14].
  - Yokoya factor for the Chao-Ruth limit agrees well with predictions based on averaging and linearized Vlasov theory [2].
  - A typical run with  $201 \times 201$  particles over 130,000 turns takes depending on the 2-D limit and the field solver between 12 and 25 h on a 425 MHz Sun Ultra-80.

- BBDeMo2D : WMPT code in 4-D phase space.
  - Kicks are computed alternatively by GSA, FMM (small  $N$ ) or HFMM.
  - A typical run with  $45^4$  particles per beam over 16,000 turns takes 6 days on a 425 MHz Sun Ultra-80.
  - A parallel version is in progress.
  - It is planned to implement MAD type lattice reader and higher order symplectic integrators [15].

#### 4. M. Vogt : BBPF $m$ D [5]

- Contains higher order multipole kicks and RF-dipoles.
- BBPF1D : PF code in 2-D phase space, three limits from 4-D to 2-D implemented. Various field solvers and interpolation methods (orders) have been implemented.
  - Good agreement between BBPF1D and BBDeMo1D. In 2-D the PF method is normally faster than WMPT and the turn by turn evolution of the moments shows less jitter.
- BBPF2D : PF code in 4-D phase space.
  - The 4-D PF code is still in the development phase.
  - It is planned to implement the same features as in BBDeMo2D.

**Codes with Synchrotron Radiation:** During this workshop various codes that implement the effects of damping and diffusion have been presented. This is an attempt to summarize their main features.

#### 1. R. L. Warnock : PF code for Vlasov-Fokker-Planck [7, 1]

- 2-D phase space.
- Operator splitting : alternating time steps with Vlasov evolution using PF and Fokker-Planck evolution using a finite difference scheme.
- Applications other than beam-beam (sawtooth instability, coherent synchrotron radiation) exist.
- A typical run with  $201 \times 201$  grid takes 6.5 hours for 30,000 turns on a 400 MHz work station.
- With this grid the code conserves probability to 1 part in  $10^5$  over several damping times.

#### 2. J. Rogers and E. Anderson : ODYSSEUS [16]

- Adaptive 6-D MCMPT code for beam-beam.
- Typically 5000 particles in each beam and 15 longitudinal slices.

- Uses different methods for computing the collective transverse kicks on core and on halo particles.
  - In the core the kicks are computed by a PIC method (cloud in cell) and an FFT.
  - The kicks on the halo particles are calculated in the GSA.
  - A typical run takes 3 seconds per turn on a 500 MHz PC.
  - The simulations of the luminosity in CESR show good agreement with the measurements.
  - It is planned to implement machine errors.
3. S. Tzenov and Y. Cai : PIC code with reduced mesh [17]
- 4-D MCMPT code with PIC (triangular shaped cloud, cyclic reduction & FFT [8], numerical differentiation).
  - The effective mesh size is reduced by a Green's function method.
  - The simulations show good agreement with the measured luminosity in PEP-II.
  - In collaboration with Ji Qiang (LANL): the code has been parallelized and a parallel 6-D code is in preparation.

Although not presented in this workshop we should at least mention the code by K. Ohmi [18]. The code uses PIC with an FFT of the derivative of the Green's function and computes the kicks directly.

## 4 REFERENCES

- [1] J. A. Ellison and R. L. Warnock, *Proc.: 2-nd ICFA Workshop on Quantum Aspects of Beam Physics*, Capri, Oct. 2000, to be published by World Scientific.
- [2] J. Ellison and M. Vogt, in these proceedings.
- [3] S. Tzenov, in these proceedings.
- [4] J. Shi and L. Jin, in these proceedings.
- [5] M. Vogt, J. A. Ellison, T. Sen and R. L. Warnock, in these proceedings.
- [6] D. Yao and J. Shi, *Phys. Rev. S.T.-AB* **1**, 084001, (1998).
- [7] R. L. Warnock and J. A. Ellison, *Proc.: 2-nd ICFA WS. on High Brightness Beams, UCLA*, Ed.: J. Rosenzweig and L. Serafini, World Scientific, (2000).
- [8] R. W. Hockney and J. W. Eastwood, *Computer Simulations Using Particles*, Institute of Physics Publishing, Bristol and Philadelphia, (1988).
- [9] L. Greengard, *Thesis*, The MIT Press Cambridge MA London England, (1988).
- [10] F. W. Jones, *Proc.: Workshop on Space Charge Physics in High Intensity Hadron Rings*, Ed.: A. U. Luccio and W. T. Weng, AIP Conf. Proc. **448**, (1998);  
W. Herr, M.-P. Zorzano and F. W. Jones, *Phys. Rev. S.T.-AB* **4** 054402, (2001);  
W. Herr, in these proceedings.
- [11] K. Yokoya and H. Koiso, *Part.Acc.* **27**, pp. 181–186, (1990).
- [12] Y. Alexahin, in the proceedings of the LHC beam-beam workshop, CERN, (1999).
- [13] A. W. Chao and R. D. Ruth, *Part.Acc.* **16**, pp. 201–216, (1985).
- [14] M. Vogt, T. Sen, J. A. Ellison, FNAL Pub-01/096-T, submitted to *Phys. Rev. S.T.-AB*, (2001).
- [15] R. L. Warnock and J. A. Ellison, *Appl.Num.Maths* **29**, pp. 89-98, (1999);  
also: DESY preprint 97-163, (1997).
- [16] J. Rogers, in these proceedings.
- [17] S. Tzenov and Y. Cai, in these proceedings.
- [18] K. Ohmi, *Phys. Rev.* **E62**, 7287, (2000).